Preprint of review published in *Phys. Rep.* **373**, 247-408 (2003).

Zero-Dispersion Phenomena in Oscillatory Systems

S.M. Soskin [a], R. Mannella [b] and P.V.E. McClintock [c]

[a] *Institute of Semiconductor Physics, National Academy of Sciences of Ukraine, Kiev, Ukraine*

[b] *Dipartimento di Fisica, Università di Pisa and Istituto Nazionale Fisica della Materia UdR Pisa, Via F. Buonarroti 2, 56100 Pisa, Italy.*

[c] *Department of Physics, Lancaster University, Lancaster LA1 4YB, UK*

Abstract

Phenomena occurring in a particular class of nonlinear oscillatory systems – *zero-dispersion systems* – are reviewed for cases with and without damping while the system is driven either by random fluctuations (noise), or by a periodic force, or by both together. Zero-dispersion (ZD) systems are those whose frequency of oscillation ω possesses an extremum as a function of energy E. Oscillations at energies close to the extremal energy E_m, where the "frequency dispersion" $d\omega/dE$ is equal to *zero*, correlate with each other for very long times, to some extent like in a harmonic oscillator. But unlike the latter, the correlation time decreases as the energy shifts away from E_m. It is the combination of this local harmonicity, with the fact that a perturbation can cause transitions between strongly and weakly correlated behaviour, that gives rise to the rich manifold of interesting ZD phenomena that are reviewed. A diverse range of physical systems may be expected to exhibit ZD behaviour under particular circumstances. Examples considered in detail include SQUIDs (superconducting quantum interference devices), the 2-D electron gas in a magnetic superlattice, axial molecules, electrical circuits, particle accelerators, impurities in lattices, relativistic oscillators, and the Harper oscillator. The ZD effects to be anticipated in quantum systems are also discussed. Each section ends with a suggested outlook for future research.

Contents

Foreword

The typical reader's information overload is so huge at present that large reviews might seem to be of limited value – because nobody will have enough motivation to read them in their entirety. Nonetheless, this perception can properly be qualified provided:

(i) that the review presents a really general, novel, but non-trivial view of a wide variety of problems linked by a common theme; and
(ii) that it is clearly structured so that non-experts can pick up the general viewpoint and central ideas by reading the introduction and conclusions, while experts can readily choose those sections that are of particular interest to them, to be read almost independently of the rest of the work.

We hope that our review satisfies both conditions. A general overview and guide to content are presented in Section 1. The paper is aimed primarily at experts on fluctuations in dynamical systems (including to some extent quantum systems) and nonlinear dynamicists generally, as well as at those physicists who are interested in the behaviour of the particular systems listed in Section 2.

1 Introduction

Oscillatory behavior is typical of diverse systems in nature and plays a crucial role in many phenomena. This is true, not only of strictly periodic motion, but also of situations where the periodicity is only approximate. Because the latter case is in a sense less fundamental, in that it may often be considered to arise through a weak perturbation of the former case, we first consider a purely periodic motion. We take as an example the one-dimensional Hamiltonian system:

$$\dot{q} = \frac{\partial H(q,p)}{\partial p}, \qquad \dot{p} = -\frac{\partial H(q,p)}{\partial q}, \tag{1.0.1}$$

which can be taken to represent a common class of systems displaying periodic motion. The quantity that is conserved during motion is the energy

$$E = H(q,p). \tag{1.0.2}$$

The motion is periodic and the frequency ω of oscillation generally depends on E (Fig. 1(a)). There is, however, a special case where the frequency is independent of E, i.e. the *harmonic* (or *linear*) oscillator, for which

$$H(q,p) = \frac{\omega_0^2 q^2}{2} + \frac{p^2}{2}. \tag{1.0.3}$$

In this case, $\omega(E) \equiv \omega_0$ [1] (Fig. 1(b)) and

$$q(t) = \frac{\sqrt{2E}}{\omega_0} \cos(\omega_0 t + \phi_0), \tag{1.0.4}$$

where ϕ_0 is an initial angle.

That fact that eigenoscillations at different energies are resonant with each other has many remarkable consequences: if a perturbation is applied that gives rise to a variation of energy, it has almost no effect on the resonant behavior of the angle. Thus, if a periodic force of frequency close to ω_0 is applied, the response is very strong: much stronger than in the general case of an energy-dependent frequency (Fig. 1(a)). Similarly, if noise is applied then, for a harmonic oscillator, the spectrum of fluctuations exhibits a narrow peak around ω_0 whereas, for a nonlinear oscillator, the fluctuation spectrum is typically much broader [2–4] because noise activates a range of energies thus involving a correspondingly wide spectrum of frequencies.

When a harmonic oscillator is subject to a weak perturbation, the energies involved are small (unless the perturbation is exactly periodic at frequency ω_0). For a nonlinear oscillator, on the other hand, a relatively high (resonant) energy may be relevant. The latter condition leads e.g. to the phenomenon of nonlinear resonance [5]. There exists a distinct class of oscillators which, in a sense, combine the *highly resonant* behaviour characteristic of a harmonic oscillator, with the possibility of resonance at *high energies* that is characteristic of nonlinear oscillators. These are the oscillators for which $\omega(E)$ possesses an extremum (Fig. 1(c)): the dispersion at the extremum is equal to zero, i.e.

$$\left.\frac{d\omega(E)}{dE}\right|_{E_m} = 0, \tag{1.0.5}$$

so that, in the close vicinity of E_m, $\omega(E)$ is practically constant. Thus, small variations of energy near E_m distort the resonance to a much smaller extent than in other energy ranges or in a conventional nonlinear oscillator where $d\omega(E)/dE \neq 0$. Such systems were identified as a distinct class by Soskin [1] [6,7]. The title *zero-dispersion* (ZD) was given to them first by Dykman et al [11], since when it has become conventional in the physics literature. The nomenclature originates from solid state physics terminology (see e.g. the book by Ashcroft and Mermin [12]) where the term "dispersion" means $d\omega(k)/dk$ where ω and k are respectively the frequency and wave number of a phonon [2].

We emphasize that ZD behaviour is not restricted to Hamiltonian systems i.e. to systems where the conserved quantity is energy. Similar behavior will be valid for a system which

[1] There were also several works by mathematicians on a structure of local chaos in so called *nonmonotonic twist maps* (e.g. [8,9]) or, equivalently, *area-preserving nontwist maps* (e.g. [10]) which are closely related to periodically driven Hamiltonian systems possessing the property (1.0.5). These works will be briefly discussed in Sec. 4 below in relation to periodically-driven non-dissipative ZD systems.

[2] In a sense, zero-dispersion peaks in fluctuation spectra [6,7] are analogous to Van Hove singularities [12] in solid state physics.

possesses any other integral of motion J and for which the eigenfrequency possesses an extremum as a function of J. Nonetheless, those ZD systems studied to date have all been Hamiltonian ones (several examples are considered in Section 2). This review will consequently be restricted to phenomena associated with perturbations of Hamiltonian ZD systems.

Common types of perturbation consist of (i) noise (together with an associated dissipation [12,13]), or (ii) a periodic force (with or without dissipation), or (iii) a combination of (i) and (ii). Distinctive phenomena occurring in ZD systems under their action are described in Sections 3, 4 and 5 respectively. Such phenomena include: extremely narrow high peaks (ZD peaks) in fluctuation spectra, in the presence of noise; a peculiar kind of nonlinear resonance, zero-dispersion nonlinear resonance (ZDNR); the onset of deterministic chaos at unusually low periodic driving force amplitudes; a characteristic sharp growth of signal-to-noise ratio with noise intensity, called the zero-dispersion stochastic resonance (ZDSR), and a strong enhancement by noise of subharmonic absorption, when the periodic driving force is weak compared to the added noise; and a strong enhancement of escape from a potential well and characteristic features of noise-induced inter-attractor transitions and a characteristic evolution of fluctuation spectra in the opposite limit, where the noise is much weaker than the periodic drive. We present in these sections both the theory and results of analogue electronic experiments as well as discussing possible applications.

These phenomena all arise in classical systems. The distinct differences in the way one would expect them to manifest themselves in quantum ZD systems are discussed in Section 6.

Some concluding remarks are presented in Section 7.

Finally, the Appendix describes the transformation between coordinate-momentum variables and energy-angle (or, equivalently, action-angle) variables. The latter are especially convenient in the theoretical consideration of all ZD phenomena because the energy (or, equivalently, action) varies only slowly with time, whereas the angle changes fast, and their separation significantly facilitates the theoretical consideration of the majority of ZD phenomena.

2 Examples of models and physical systems displaying zero-dispersion behaviour

2.1 Superconducting quantum interference devices (SQUIDs)

A radio-frequency SQUID, in common with other more complicated SQUID devices, includes [14,15] as a basic element a superconductive loop containing a Josephson junction (Fig. 2). The dynamics of the loop may be described in many cases by a resistively-shunted model, in terms of which the time evolution of the phase of the order parameter, or of the magnetic flux Φ threading the loop, can [14,15] be described by the equation

$$LC\frac{d^2q}{d\tau^2}+\frac{L}{R_N}\frac{dq}{d\tau}+q+\beta\sin(q)=q_e,$$
$$q=2\pi\frac{\Phi}{\Phi_0},\qquad q_e=2\pi\frac{\Phi_e}{\Phi_0},\qquad \beta=\frac{2\pi LJ_c}{\Phi_0}. \tag{2.1.1}$$

Here τ is a real time variable; $\Phi\equiv\Phi(\tau)$ is the full magnetic flux through the loop; Φ_e is the flux of the external magnetic field; $\Phi_0=h/2e$ is the flux quantum; L is the inductance of the loop; and C, R_N and J_c are respectively the capacitance, normal resistivity [3] and critical supercurrent of the junction.

In addition to a constant component $\Phi_{\rm dc}$, the external flux often includes a small periodic signal $\Phi_s\cos(\omega_s\tau)$ and a noisy component $\Phi_N(\tau)$ to which thermal fluctuations within the loop itself and noise in the Josephson junction can formally be added (the overall noise term, where present, will for the sake of simplicity be assumed white and of intensity D):

$$\Phi_e=\Phi_{dc}+\Phi_s\cos(\omega_s\tau)+\Phi_N(\tau), \tag{2.1.2}$$
$$\langle\Phi_N(\tau)\rangle=0,\quad \langle\Phi_N(\tau)\Phi_N(\tau')\rangle=2D\delta(\tau-\tau').$$

Taking account of (2.1.2) and introducing the normalised quantities

$$t=\omega_p\tau,\quad \Gamma=\frac{1}{\omega_pR_NC},\quad \Omega=\frac{\omega_s}{\omega_p},$$
$$A=\frac{\Phi_s}{LJ_c},\quad T=\frac{2\pi DR_N}{\Phi_0L^2J_c},\quad \omega_p=\left(\frac{2\pi J_c}{C\Phi_0}\right)^{1/2}, \tag{2.1.3}$$

Eq. (2.1.1) takes the form

$$\ddot{q}+\Gamma\dot{q}+\frac{dU}{dq}=f(t)+A\cos(\Omega t) \tag{2.1.4}$$
$$\langle f(t)\rangle=0,\quad \langle f(t)f(t')\rangle=2\Gamma T\delta(t-t'),$$

where

$$U(q)=\frac{B}{2}(q-q_e)^2-\cos(q),\qquad B\equiv\frac{1}{\beta}. \tag{2.1.5}$$

If the friction, noise and periodic driving amplitude are small they can be neglected in the zeroth-order approximation, and one then derives the unperturbed equation:

$$\ddot{q}+\frac{dU}{dq}=0. \tag{2.1.6}$$

[3] The resistivity may strongly depend on $dq/d\tau$, and it may formally include an external shunt.

It corresponds to the Hamiltonian

$$H(q,p) = U(q) + \frac{p^2}{2} \tag{2.1.7}$$

with the potential $U(q)$ (2.1.5), which may be either single-well (for $B \gtrsim 1$: see Fig. 3(a)) or multi-well (for $B \lesssim 1$: see Fig. 3(b)).

The frequency of oscillation in the system (2.1.6) can be calculated from the formula

$$\omega \equiv \omega(E) = \pi \left(\int_{q_l}^{q_r} \frac{dq}{\sqrt{2(E - U(q))}} \right)^{-1}, \tag{2.1.8}$$

where q_l and q_r are the left and right turning points at a given E (and in a given potential well if the energy level E exists in more than one well), i.e. the relevant roots of the equation

$$E = U(q). \tag{2.1.9}$$

The function $\omega(E)$ possesses extrema, which are most pronounced if $B \sim 1$: see Fig. 4. Consequently, the system (2.1.5)-(2.1.6) is a ZD system.

2.2 2D electron gas in a magnetic superlattice, axial molecules

Our example from the previous sub-section, the *multi-well* SQUID, belongs to a more general class of systems possessing the ZD property. These are the systems that possess two or more separatrices: the time of motion along any separatrix is infinite, so that the frequency of eigenoscillation for each of the energies (or any other relevant integral of motion) corresponding to the separatrices is zero. The frequency must therefore pass through a maximum somewhere in between these energies. In particular, it may be a multi-barrier potential system in which the tops of at least two of the barriers have different potential energies. Apart from SQUIDs, such a situation is typical of periodic potentials that have two or more barriers within the period.

We now consider briefly two examples of such physical systems. The first is a 2D electron gas in a magnetic superlattice (see e.g. [16,17]). In some cases, e.g. in a thin layer of semiconductor where the electrons are of high mobility, the motion of electrons along the layer can be considered as a two-dimensional motion of non-interacting classical particles [18–21]. If a magnetic field $\vec{\mathrm{H}}$ perpendicular to the layer is added, and periodicaly modulated in some direction along the layer,

$$\vec{\mathrm{H}} \equiv (\mathrm{H}_x, \mathrm{H}_y, \mathrm{H}_z), \quad \mathrm{H}_x = \mathrm{H}_y = 0, \quad \mathrm{H}_z = \mathrm{H}_0 \cos(kx), \tag{2.2.1}$$

then the motion of an electron is described by the Hamiltonian [22]

$$H_{\text{magnetic}} \equiv H_{\text{magnetic}}(x, y, p_x, p_y) = \frac{(\vec{p} - \frac{e}{c}\vec{A})^2}{2m^*}, \tag{2.2.2}$$

where $\vec{A}$ is the vector-potential ($\vec{\text{H}} \equiv \text{curl } \vec{A}$), $\vec{p} \equiv (p_x, p_y)$, e and m^* are respectively the charge and the effective mass of the electron, and c is the velocity of light. For the field (2.2.1), $\vec{A}$ may be chosen in such a way that [20,21]

$$H_{\text{magnetic}} = \frac{p_x^2}{2m^*} + \frac{(p_y - \frac{e}{c}\text{H}_0 k^{-1}\sin(kx))^2}{2m^*}. \tag{2.2.3}$$

The Hamiltonian (2.2.3) does not depend on y: hence, $p_y = \text{const}$, and the motion in the x-direction is separated as one-dimensional Hamiltonian motion (1.0.1) with q, p, t representing normalized (dimensionless) coordinate, momentum and time respectively,

$$q \equiv kx, \quad p \equiv p_x \frac{k}{m^*\omega_c}, \quad t \equiv \omega_c \tau, \quad \omega_c = \frac{e\text{H}_0}{m^* c}, \tag{2.2.4}$$

and the Hamiltonian is of the potential type:

$$H(q, p) = U(q) + \frac{p^2}{2}, \tag{2.2.5}$$

with potential

$$U(q) = \frac{1}{2}(\Phi - \sin(q))^2, \qquad \Phi \equiv \frac{p_y k c}{e\text{H}_0}. \tag{2.2.6}$$

The potential (2.2.6) is periodic. If $\Phi < 1$, it possesses two barriers within the period, of different heights (Fig. 5(a)). Correspondingly, the frequency of oscillation ω possesses a local maximum as a function of energy E (Fig. 5(c)). If $\Phi > 1$, then there is only one barrier within the period (Fig. 5(b)), but $\omega(E)$ can still be shown to possess a local maximum provided $\Phi < 4$ (Fig. 5(d)). Thus, if $\Phi < 4$, the system (2.2.5)-(2.2.6) possesses the zero-dispersion property (1.0.5). One may induce a perturbation by e.g. perturbing the magnetic field or applying an electric field along the layer [20,21].

Another example which may be described by a periodic potential with more than one barrier within the period relates to torsional motion within a complex axial molecule (Fig. 6). If such a complex molecule has a rigid axis then an atom (or a group of atoms) beyond the axis may have a few equilibrium positions lying in the plane perpendicular to the axis. The motion of such an atom (group of atoms), often called an isomerisation process [23], may sometimes be considered as an underdamped rotation in the plane (cf. [23,24]), which, neglecting damping and other weak interactions with the surroundings, may be described as Hamiltonian motion in a periodic potential with a few non-equal barriers, thus again providing for the zero-dispersion property.

2.3 Electrical circuits, particle accelerators, impurities in solids: tilted Duffing oscillator

One of the simplest and at the same time non-trivial ZD models is the *tilted Duffing oscillator* (TDO) [11] which may be considered as a conventional Duffing oscillator [1] that is subject to a constant force (which is what leads to the tilt of the Duffing potential):

$$\ddot{q} + \frac{dU}{dq} = 0, \qquad U(q) = \frac{\omega_0^2 q^2}{2} + \frac{\gamma q^4}{4} + Aq, \qquad \gamma > 0. \tag{2.3.1}$$

The potential $U(q)$ (2.3.1) is an asymmetric single well (Fig.7(a)). If $|A|$ exceeds $A_{cr} = 8\omega_0^2/(7\sqrt{7\gamma})$, then $\omega(E)$ possesses a minimum [11] (Fig. 7(b)).

The TDO model may be related to e.g. an oscillatory electrical circuit with a battery [25] (Fig. 8). The charge q on the capacitance obeys the equation

$$\frac{q}{C} = \epsilon - L\frac{d^2q}{dt^2}, \tag{2.3.2}$$

where C is the capacitance, L is the inductance and ϵ is the battery emf; ϵ and L are typically constants. Real capacitors are non-ideal, and the stored charge q is not quite proportional to the potential difference. In many cases, the growth of q with voltage is weaker than linear, and is independent of the sign of the voltage, which means that C is a decreasing function of q^2. At small enough q, it may typically be approximated as $C = C_0/(1 + \alpha q^2)$ where C_0 and α are constants; thus Eq. (2.3.2) reduces to Eq. (2.3.1). A possible small resistance in the circuit, weak Nyquist noise, periodic signals, etc. may be considered as perturbations.

The TDO model may also be relevant to rf acceleration in particle accelerators [26] and to local and resonant vibrations in certain doped crystals [27] when a constant homogeneous electric field or external pressure are applied to the crystal.

It should be noted that the linear term in the TDO potential $U(q)$ (2.3.1) can be converted to a cubic term by a change of origin to the equilibrium position determined by $dU/dq = 0$ i.e. by a root of the equation

$$\gamma q_{eq}^3 + \omega_0^2 q_{eq} + A = 0. \tag{2.3.3}$$

Indeed,

$$U(q) \equiv U(q_{eq}) + \frac{\omega_0^2 + 3\gamma q_{eq}^2}{2}(q - q_{eq})^2 + \gamma q_{eq}(q - q_{eq})^3 + \frac{\gamma(q - q_{eq})^4}{4}. \tag{2.3.4}$$

Such a presentation of the potential is usually more convenient for the analysis. In particular, by using it, one can easily show that the ratio of the maximal decrease of eigenfrequency (as energy varies from the bottom to the energy corresponding to the minimum

in $\omega(E)$) to the eigenfrequency in the bottom is rather small for a potential of the type (2.3.1) (cf. Fig. 7(b)), even at large A.

At the same time, the potential with a cubic nonlinearity,

$$U(q) = \frac{\omega_0^2 q^2}{2} + \frac{\beta q^3}{3} + \frac{\gamma q^4}{4}, \qquad (2.3.5)$$
$$\frac{9}{10} < \frac{\beta^2}{\gamma\omega_0^2} < 4,$$

permits any depth of minimum in $\omega(E)$ (cf. Fig. 9). An oscillator with the potential (2.3.5) is therefore also referred to as a *tilted Duffing oscillator* and it will be used extensively in this review as a simple characteristic model [4].

Finally, we present in this sub-section an explicit expression for $\omega(E)$ [11]:

$$\omega(E) = \frac{\pi}{2K(k)} \left(\frac{1}{2} z^{(1)} z^{(2)}\right)^{\frac{1}{2}}, \qquad (2.3.6)$$
$$k^2 = \frac{1}{4} \frac{(q^{(1)} - q^{(2)})^2 - (z^{(1)} - z^{(2)})^2}{z^{(1)} z^{(2)}},$$
$$z^{(j)} = [(q^{(3)} - q^{(j)})(q^{(4)} - q^{(j)})]^{\frac{1}{2}}, \qquad j = 1, 2,$$

where $K(k)$ is a full elliptic integral of the first kind and k is its modulus; $q^{(1)}, q^{(2)}$ are real roots and $q^{(3)}, q^{(4)} \equiv q^{(3)*}$ are complex conjugate roots of the equation

$$U(q^{(n)} + q_{eq}) - U(q_{eq}) - E = 0; \qquad (2.3.7)$$
$$n = 1, ..., 4; \qquad q^{(1)} > q^{(2)},$$

where $U(q)$ is given either by (2.3.1) or by (2.3.5) while q_{eq} is given by (2.3.3) or equal to zero respectively.

2.4 Relativistic oscillators

A one-dimensional relativistic oscillator can be described as a Hamiltonian system with the following Hamiltonian [28]

$$H(q, p) = \sqrt{p^2 c^2 + m^2 c^4} + U(q), \qquad (2.4.1)$$

[4] It should be noted that, apart from being a convenient model for theoretical studies, the potential (2.3.5) may also serve as an approximation for a variety of real systems.

where c is the velocity of light and m is a mass.

At a given energy E, the system oscillates between the turning points q_l and q_r which are the relevant roots of the equation

$$E = mc^2 + U(q). \tag{2.4.2}$$

The frequency of oscillation is described by the formula [28]

$$\omega(E) = \pi c \left(\int_{q_l}^{q_r} \frac{E - U(q)}{\sqrt{(E - U(q))^2 - m^2c^4}} dq \right)^{-1}. \tag{2.4.3}$$

If $E - mc^2 \ll mc^2$, then $|p|/m \ll c$, so that the Hamiltonian reduces to

$$H_{\text{nonrel}}(q,p) = mc^2 + \frac{p^2}{2m} + U(q), \qquad E - mc^2 \ll mc^2, \tag{2.4.4}$$

and the dynamics reduces to non-relativistic potential motion (cf. (2.1.6), (2.1.7)). In particular, $\omega(E)$ is described by a non-relativistic formula similar to (2.1.8) (in which E should be replaced by $E - mc^2$ while the right-hand side should be divided by $\sqrt{m}$).

In the opposite (strongly relativistic) limit, $E - mc^2 \gg mc^2$, the Hamiltonian reduces to

$$H_{\text{rel}}(q,p) = |p|c + U(q), \qquad E - mc^2 \gg mc^2, \tag{2.4.5}$$

which corresponds to a constant modulus of velocity during the motion [5], $\dot{q} = \pm c$, so that the period of oscillation is equal just to $2(q_r - q_l)/c$ and, given that the distance between turning points grows with E if E is large enough (unless the potential has infinite vertical walls), $\omega(E)$ is a decreasing function at large enough E:

$$\omega(E) \approx \frac{\pi c}{q_r - q_l} \overset{E\to\infty}{\longrightarrow} 0. \tag{2.4.6}$$

Thus, if the potential $U(q)$ provides in the non-relativistic regime an increase of $\omega(E)$ in some range of energies $E - mc^2 \ll mc^2$ (for example, a Duffing oscillator, both single-well and double-well, provides an increasing $\omega(E)$ at E exceeding certain values [2,29,28]),

[5] Obviously, Eq. (2.4.5) is not valid in the close vicinity of turning points, but this has little effect on the period of the motion, which is the main quantity of interest for us in the present context.

then $\omega(E)$ (2.4.3) necessarily possesses a local maximum at some energy in the transition range between the non-relativistic and relativistic limits (cf. Fig. 10). The system therefore manifests zero-dispersion properties [30,31].

It should be noted also that zero-dispersion phenomena may be expected to occur, not only in the simple model relativistic systems considered above, but also in certain more complicated relativistic systems such as driven electron plasma waves [32] and periodically focused intense beams of charged particles [33].

2.5 The Harper oscillator

The kicked Harper model [34] is defined by the time-dependent Hamiltonian

$$H(I,\psi,t) = -V_0\cos(2\pi I) - V_1\cos(2\pi\psi)K(t), \tag{2.5.1}$$

$$K(t) = \tau\sum_{n=-\infty}^{\infty}\delta(t-n\tau),$$

where I and ψ may be considered e.g. as action and angle respectively [1] and t is time.

This model may in some cases be related to real physical systems, e.g., at $V_0 = V_1$, it serves as an approximation for a kicked charge in a magnetic field [35]. More often, however, it is used in theoretical and numerical studies of chaos, being a simple system manifesting very rich chaotic behaviour, both in the classical and quantum cases (see e.g. [36,37] and references therein). We shall explore the non-symmetric case

$$V_1 \ll V_0. \tag{2.5.2}$$

In the zeroth-order approximation, the term $\propto V_1$ may then be omitted and we derive the Hamiltonian

$$H_0 \equiv H_0(I) = -V_0\cos(2\pi I), \tag{2.5.3}$$

which does not depend on angle ψ. Therefore, the system (2.5.3) is integrable: the action I is a constant of motion while the angle ψ oscillates with the frequency [1,35]

$$\omega = \frac{dH_0}{dI} = 2\pi V_0\sin(2\pi I). \tag{2.5.4}$$

As a function of action, ω (2.5.4) possesses extrema at

$$I = I_n \equiv n + \frac{1}{2},$$
$$n = 0, \pm1, \pm2, ...,$$

where the derivative is equal to zero, $d\omega(I_n)/dI_n = 0$. Obviously, the derivative with respect to energy $E \equiv H_0(I)$ also equals zero at $E_n \equiv H_0(I_n)$: $d\omega/dE|_{E_n} = (\omega|_{E_n})^{-1} d\omega/dI|_{I_n} = 0$.

Thus, the zeroth-order approximation (2.5.3) of the Harper model possesses the zero-dispersion property. The kicking (the periodic perturbation term $\propto V_1$ in (2.5.1)) leads to nonlinear resonances, and to associated chaos, which may be especially pronounced under certain conditions related to the zero-dispersion property (see Sec. 4).

3 Zero-dispersion systems subject to noise: zero-dispersion peaks in fluctuation spectra

3.1 Basic equations

For the sake of clarity, we shall consider in this section, as an example of a noise-driven ZD system, a one-dimensional ZD system of the potential type subject to a linear friction and white noise:

$$\begin{aligned} &\dot{q} = p, \qquad \dot{p} = -\Gamma \dot{q} - dU/dq + f(t), \\ &\langle f(t) \rangle = 0, \quad \langle f(t) f(t') \rangle = 2\Gamma T \delta(t - t'). \end{aligned} \tag{3.1.1}$$

Instead of the Langevin description (3.1.1), one may use a description in terms of the time evolution of the probability density in a phase space, $W(p, q, t|p_0, q_0)$, i.e. the density of probability of the coordinate and momentum being equal to q and p respectively, at a given instant t, if at the initial time they were equal to q_0 and p_0. In the case of white noise, W obeys the Fokker-Plank equation (FPE) [38]

$$\frac{\partial W}{\partial t} = -p \frac{\partial W}{\partial q} + \frac{dU}{dq} \frac{\partial W}{\partial p} + \Gamma \frac{\partial}{\partial p} \left(p + T \frac{\partial}{\partial p} \right) W \tag{3.1.2}$$

with the initial condition

$$W(p, q, 0|p_0, q_0) = \delta(p - p_0) \delta(q - q_0). \tag{3.1.3}$$

The stationary solution of the FPE (3.1.2) is the Gibbsian distribution [13,38]

$$\begin{aligned} &W_{st}(p, q) = Z^{-1} \exp(-E/T), \\ &Z = \int_{-\infty}^{\infty} dp \int_{-\infty}^{\infty} dq \, \exp(-E/T), \qquad E = U(q) + p^2/2. \end{aligned} \tag{3.1.4}$$

Thus, T plays the role of temperature (even if the noise is of a non-thermal nature), and it will be referred to as such in what follows.

In many problems, the quantity of interest is the spectrum of fluctuations of a given (real-valued) function of dynamical variables, $\varphi(q,p)$ [13,38]

$$Q_\varphi(\Omega) = \frac{1}{2\pi}\int\limits_{-\infty}^{\infty} dt\ \exp(-i\Omega t)R_\varphi(t) \equiv \frac{1}{\pi}\mathrm{Re}\left[\int\limits_{-\infty}^{\infty} dt\ \exp(-i\Omega t)R_\varphi(t)\right], \qquad (3.1.5)$$
$$R_\varphi(t) \equiv \langle(\varphi(t)-\langle\varphi\rangle)(\varphi(0)-\langle\varphi\rangle)\rangle, \qquad \varphi(t)\equiv\varphi(q(t),p(t)),$$

where the brackets $\langle ...\rangle$ denote averaging both over the equilibrium ensemble (3.1.4) and over realizations of the random force $f(t)$, i.e. respectively over the initial and final states, in the phase space.

The fluctuation spectrum is an important physical quantity which can be determined directly in an experiment. For example, if q is the coordinate of an electrically charged particle, then the spectrum of the classical radiation is proportional to $\Omega^4 Q_q(\Omega)$ [22]. The spectral dependence of the mobility of charged particles is determined by $\Omega^2 Q_q(\Omega)$ [38]. The polarizability of a rotating dipole is proportional to the spectrum of the time-derivative of the correlation function of the corresponding superposition of the sine and cosine of the angle [39]. In some cases, $Q_\varphi(\Omega)$ may characterize the combination scattering spectrum (in this case, φ is a complicated function of coordinate and momentum [40]). There are also many other physical quantities which may be described in terms of fluctuation spectra [38].

It will be convenient to transform from (q,p) to the energy–angle representation (E,ψ) [1]

$$E = U(q) + \frac{p^2}{2}, \qquad \psi = \int dq \frac{\omega(E)}{\sqrt{2(E-U(q))}}, \qquad (3.1.6)$$

since, at small friction (relevant to ZD phenomena), energy is a slow variable whereas the angle is a fast one, so that their dynamics are well separated.

Allowing for the periodicity of φ in ψ,

$$\varphi(q,p) \equiv \tilde\varphi(E,\psi) = \sum_{n=-\infty}^{\infty} \varphi_n(E)\mathrm{e}^{-in\psi}, \qquad \varphi_{-n} = \varphi_n^*, \qquad (3.1.7)$$

one may present the correlation function $R_\varphi(t)$ (3.1.5) as

$$R_\varphi(t) = \int\limits_{U_{\min}}^{\infty} dE_0 \int\limits_0^{2\pi} d\psi_0\ \tilde W_{st}(E_0,\psi_0)(\langle\tilde\varphi(t)\rangle_{E_0,\psi_0} - \langle\tilde\varphi\rangle)(\langle\tilde\varphi(E_0,\psi_0)\rangle - \langle\tilde\varphi\rangle), \qquad (3.1.8)$$

$$U_{\min} \equiv \min\{U(q)\},$$

where

$$\tilde{W}_{st}(E_0, \psi_0) = \frac{W_{st}(p_0, q_0)}{\omega(E_0)} = \frac{\exp(-E_0/T)}{\omega(E_0)Z} \tag{3.1.9}$$

is a stationary distribution in the energy-angle space, while

$$\langle\tilde{\varphi}(t)\rangle_{E_0,\psi_0} \equiv \int_{U_{\min}}^{\infty} dE \int_0^{2\pi} d\psi\ \tilde{\varphi}(E,\psi)\tilde{W}(E,\psi,t|E_0,\psi_0), \tag{3.1.10}$$

where $\tilde{W} = W/\omega(E)$ is the conditional probability density in the $E-\psi$ space normalized to a 2π-band of ψ.

3.2 Zero-frequency-limit

In the zero-friction approximation, energy is conserved whereas the angle changes with a constant speed $\omega(E)$, so that

$$\tilde{W}(E,\psi,t|E_0,\psi_0) = \delta(E-E_0)\sum_{n=-\infty}^{\infty}\delta(\psi-\psi_0-\omega(E_0)t+2\pi n). \tag{3.2.1}$$

Substituting (3.2.1) into (3.1.10), putting the resulting expression and (3.1.9) into (3.1.8), one obtains for the spectrum (3.1.5) at a non-zero frequency

$$Q_\varphi(\Omega) \approx Q_\varphi^{(0)}(\Omega) \equiv \frac{2\pi}{Z}\sum_{n=1}^{\infty}\sum_j \frac{1}{n}\left[\frac{\exp(-E/T)}{\omega(E)}|\varphi_n(E)|^2\frac{1}{|d\omega(E)/dE|}\right]_{E=E_j(\Omega/n)},$$
$$\Omega \neq 0, \tag{3.2.2}$$

where the $E_j(\Omega/n)$ are determined from the equation

$$\omega(E_j(\Omega/n)) = \Omega/n, \tag{3.2.3}$$

and the summation over j in (3.2.2) denotes a summation over all the roots of Eq. (3.2.3).

Near the extremum, $\omega(E)$ takes the form

$$\omega(E) = \Omega_m + \frac{1}{2}\omega''(E-E_m)^2, \qquad \omega'' \equiv \frac{d^2\omega(E_m)}{dE_m^2}. \tag{3.2.4}$$

Thus, the solutions of Eq. (3.2.3) can be written

$$E_{1,2}(\frac{\Omega}{n}) \approx E_m \pm \sqrt{2(\frac{\Omega}{n} - \Omega_m)/\omega''}, \qquad \omega''(\frac{\Omega}{n} - \Omega_m) > 0. \tag{3.2.5}$$

Correspondingly, the zero-friction approximation of the spectrum near $n\Omega_m$ is

$$Q_\varphi^{(0)}(\Omega) \approx \begin{cases} \frac{4\pi|\varphi_n(E_m)|^2 \exp(-E_m/T)}{Z\Omega_m\sqrt{2n\omega''(\Omega - n\Omega_m)}} & \text{at} \quad \omega''(\Omega - n\Omega_m) > 0, \\ 0 & \text{at} \quad \omega''(\Omega - n\Omega_m) < 0, \end{cases} \tag{3.2.6}$$

$$n = 1, 2, 3, ..., \qquad \sqrt{(\Omega/n - \Omega_m)/\omega''} \ll T.$$

Thus, $Q_\varphi^{(0)}(\Omega)$ possesses singularities at Ω_m and its harmonics, indicating the existence of peaks in the exact spectrum $Q_\varphi(\Omega)$ too: they are called *zero-dispersion peaks* (ZDPs). $Q_\varphi^{(0)}(\Omega)$ provides a good approximation for the wing of the ZDP but the description of the peak itself requires more sophisticated approaches, which will be presented in the following sub-sections.

3.3 Asymptotic low-friction theory of ZDP

This sub-section largely follows the treatment given in [7] [6]. Before embarking on a rigorous analysis, we present some simple qualitative estimates relevant to the ZDP at the fundamental frequency, which will facilitate understanding of the rigorous results.

3.3.1 Qualitative estimates

Let us estimate the correlation time t_c for an oscillator whose initial energy E_0 is close to E_m. It may be found approximately from the condition that the diffusion of angle has attained $\sim \pi$:

$$\Delta\psi(t_c) \sim \pi. \tag{3.3.1}$$

Angular diffusion is due to the diffusion of energy, ΔE, which leads to a diffusion of $\omega(E)$, leading in turn to the diffusion of $\dot{\psi} \approx \omega(E)$:

$$\Delta\dot{\psi} \sim |\omega(E_0 \pm \Delta E(t)) - \omega(E_0)| \sim |\omega''\Delta E(t)(2(E_0 - E_m) \pm \Delta E(t))|. \tag{3.3.2}$$

The diffusion of energy $\Delta E(t) \approx (T\overline{p^2}\Gamma t)^{1/2}$ where the overbar denotes an averaging over one period of eigenoscillation $2\pi/\omega(E_0)$ (cf. [38]). Consider first an E_0 such that

[6] Note that there were some misprints in [7]. In particular, in Eq. (2.35) (which is the major result of [7]: it describes the asymptotic shape of ZDP), the factor $\sqrt{2}$ was missed in the scaling factor A.

$|E_0 - E_m| \lesssim \Delta E(t_c)$. Then, $\Delta\dot{\psi}(t_c) \sim |\omega''|(\Delta E(t_c))^2$, while

$$\Delta\psi(t_c) \sim \Delta\dot{\psi}(t_c)t_c \sim |\omega''|T\overline{p^2}t_c^2. \tag{3.3.3}$$

Comparing (3.3.3) with (3.3.1), we conclude that, if $|E_0 - E_m| \lesssim (T\overline{p^2}\Gamma/|\omega''|)^{1/4}$, then $t_c \sim (|\omega''|T\overline{p^2}\Gamma)^{-1/2}$.

If, on the other hand, $|E_0 - E_m| \gg (T\overline{p^2}\Gamma/|\omega''|)^{1/4}$, then $\Delta E(t_c) \ll |E_0 - E_m|$, so that (3.3.2) reduces to $\Delta\dot{\psi}(t_c) \sim |\omega''|\Delta E(t_c)|E_0 - E_m|$. Comparing $\Delta\psi(t_c) \sim \Delta\dot{\psi}(t_c)t_c$ with π, we conclude that $t_c \ll (|\omega''|T\overline{p^2}\Gamma)^{-1/2}$ for such E_0 and, therefore, that the contribution of such energies to the formation of the spectrum at $\Omega \approx \Omega_m$ may be neglected.

Thus, we have found the characteristic scales of time and energy relevant to the ZDP:

$$t_{\rm zdp} = (|\omega''|T\overline{p^2}_m\Gamma)^{-1/2} \propto \Gamma^{-1/2}, \qquad \overline{p^2}_m \equiv \overline{p^2}(E_m), \tag{3.3.4}$$

$$\Delta E_{\rm zdp} \equiv \Delta E(t_{\rm zdp}) = (T\overline{p^2}_m\Gamma/|\omega''|)^{1/4} \propto \Gamma^{1/4}. \tag{3.3.5}$$

The time scale $t_{\rm zdp}$ characterizes the decay time for oscillations of frequency $\approx \Omega_m$. Thus, the width of the ZDP should be

$$\Delta\Omega_{\rm zdp} \sim t_{\rm zdp}^{-1} = \sqrt{|\omega''|T\overline{p^2}_m\Gamma} \propto \sqrt{\Gamma}. \tag{3.3.6}$$

The energy scale $\Delta E_{\rm zdp}$ characterizes the width of the energy band contributing to the formation of the ZDP. It follows from (3.1.5) and (3.1.8) that the magnitude of the ZDP

$$Q_\varphi(\Omega_m) \sim \frac{1}{Z\omega_m}\exp(-\frac{E_m}{T})|\varphi_1(E_m)|^2\Delta E_{\rm zdp}t_{\rm zdp} \propto \frac{1}{\Gamma^{1/4}}. \tag{3.3.7}$$

The qualitative estimates (3.3.6),(3.3.7) are confirmed by the rigorous analysis presented below.

3.3.2 Rigorous asymptotic theory

As already mentioned, it is convenient to transform from (p, q) to (E, ψ) variables. The corresponding dynamical equations are given in the Appendix: see Eq. (A.15). The FPE [38] for $\tilde{W}(E, \psi, t|E_0, \psi_0)$ can be written as

$$\frac{\partial\tilde{W}}{\partial t} = -\omega(E)\frac{\partial\tilde{W}}{\partial\psi} + \Gamma\hat{\tilde{L}}\tilde{W}, \tag{3.3.8}$$

$$\hat{\tilde{L}} = -\frac{\partial}{\partial E}\left[-p^2 + T(pp_E - \omega(E)q_Ep_\psi)\right] - \frac{\partial}{\partial\psi}T\left[\omega^2(E)q_Eq_{E\psi} - p\frac{\partial}{\partial E}(\omega(E)q_E)\right] +$$

$$\frac{\partial^2}{\partial E^2}Tp^2 - 2\frac{\partial^2}{\partial E \partial \psi}T\omega(E)q_E p + \frac{\partial^2}{\partial \psi^2}T\omega^2(E)q_E^2,$$

where the subscripts E, ψ denote the corresponding partial derivatives.

The initial condition for $\tilde{W}$ is

$$\tilde{W}(E, \psi, 0|E_0, \psi_0) = \delta(E - E_0) \sum_{n=-\infty}^{\infty} \delta(\psi - \psi_0 + 2\pi n). \tag{3.3.9}$$

In view of its periodicity in ψ, $\tilde{W}$ can be expanded in a Fourier series. It is convenient to write explicitly the "dissipationless" factor $\exp\{in[\psi_0 + \omega(E_0)t]\}$ in Fourier coefficients,

$$\tilde{W} = \sum_n W_n \exp\{-in[\psi - \psi_0 - \omega(E_0)t]\}. \tag{3.3.10}$$

In the zero-friction limit ($\Gamma = 0$), the coefficients W_n do not depend on time: $W_n(\Gamma = 0) = \delta(E - E_0)/(2\pi)$. At a small (but non-zero) Γ, W_n varies with time *slowly* as compared to $[n\omega(E)]^{-1}$ at $n \neq 0$ or to $\omega^{-1}(E)$ at $n = 0$ (which is, of course, confirmed by the result). Therefore, substituting (3.3.10) into the FPE (3.3.8), one may drop fast-oscillating terms, in accordance with the averaging method [41], so that

$$\begin{aligned}\frac{\partial W_n}{\partial t} = & in[\omega(E) - \omega(E_0)]W_n \\ & + \Gamma \left\{ \frac{\partial}{\partial E}\overline{p^2} \left[\left(1 + T\frac{d\omega(E)/dE}{\omega(E)} \right) W_n + T\frac{\partial W_n}{\partial E} \right] - n^2 T\omega^2(E)\overline{q_E^2}W_n \right\}.\end{aligned} \tag{3.3.11}$$

For $n = 0$, Eq. (3.3.11) coincides with the well-known Kramers equation [42] . For $n = 1$, in the case of the Duffing oscillator, Eq. (3.3.11) may be reduced to the FPE obtained in [43].

Transforming to the dimensionless variables

$$\begin{aligned}\tilde{t} &= \frac{t}{t_{\text{zdp}}}, \\ \tilde{E} &= \frac{E - E_m}{\Delta E_{\text{zdp}}},\end{aligned} \tag{3.3.12}$$

introducing the parameter

$$\tilde{E}_0 = \frac{E_0 - E_m}{\Delta E_{\text{zdp}}}, \tag{3.3.13}$$

and omitting all terms which, at the relevant unit "times" $\tilde{t}$ and "energies" $\tilde{E}, \tilde{E}_0$, tend to zero as [7] $\Gamma \to 0$, we obtain an asymptotic equation for W_n:

$$\frac{\partial W_n}{\partial \tilde{t}} = \frac{1}{2} in \ \mathrm{sgn}(\omega'')(\tilde{E}^2 - \tilde{E}_0^2) W_n + \frac{\partial^2 W_n}{\partial \tilde{E}^2}. \tag{3.3.14}$$

The initial condition is:

$$W_n \xrightarrow{\tilde{t} \to 0} \frac{\delta(\tilde{E} - \tilde{E}_0)}{2\pi \Delta E_{\mathrm{zdp}}}. \tag{3.3.15}$$

An equation similar to (3.3.14) (but without the imaginary i) was obtained in quantum statistical mechanics in relation to the density matrix of the harmonic oscillator [44].

Using the substitution

$$W_n = \exp[a(\tilde{t})\tilde{E}^2 + b(\tilde{t})\tilde{E} + c(\tilde{t})], \tag{3.3.16}$$

we obtain for a, b, c the set of ordinary differential equations,

$$\begin{aligned} \frac{da}{d\tilde{t}} &= \frac{1}{2} in \ \mathrm{sgn}(\omega'') + 4a^2, \\ \frac{db}{d\tilde{t}} &= 4ab, \\ \frac{dc}{d\tilde{t}} &= -\frac{1}{2} in x_0^2 \ \mathrm{sgn}(\omega'') + b^2 + 2a, \end{aligned} \tag{3.3.17}$$

which can be solved explicitly, so that W_n satisfying the initial condition (3.3.15) reads

$$\begin{aligned} W_n &= \frac{1}{\Delta E} \frac{\exp\left[-\frac{\lambda_n (\tilde{E} - \tilde{E}_0 \mathrm{sech}(\lambda_n \tilde{t}))^2}{4 \mathrm{th}(\lambda_n \tilde{t})} - \frac{\tilde{E}_0^2 \lambda_n \mathrm{th}(\lambda_n \tilde{t})}{4} - \frac{in \tilde{E}_0^2 \mathrm{sgn}(\omega'') \tilde{t}}{2} \right]}{4\pi \sqrt{\pi \ \mathrm{sh}(\lambda_n \tilde{t})/\lambda_n}}, \\ \lambda_n &= \sqrt{n \ \mathrm{sgn}(\omega'')}(1 - i), \qquad n \neq 0. \end{aligned} \tag{3.3.18}$$

The solution vanishes exponentially sharply as $\tilde{t}$ or $|\tilde{E} - \tilde{E}_0|$ grow $\gg 1$; if $|\tilde{E}_0| \gg 1$, then W_n oscillates rapidly with $\tilde{t}$ even at $|\tilde{t}|, |\tilde{E} - \tilde{E}_0| \sim 1$. This confirms our original inference that, in the asymptotic limit $\Gamma \to 0$, the ZDP is dominated by an infinitesimal band of energies around E_m.

[7] The upper limit on Γ for which the asymptotic results obtained in this sub-section are valid depends on temperature and on other parameters. This dependence will be derived explicitly in the next sub-section.

Substituting W_n (3.3.18) into $\tilde{W}$ (3.3.10), putting $\tilde{W}$ into $\langle\tilde{\varphi}(t)\rangle_{E_0,\psi_0}$ (3.1.10), substituting the latter into the correlation function (3.1.8), calculating its Fourier transform and omitting all terms which vanish as $\Gamma \to 0$, we obtain for the asymptotic shape of the ZDP (see [7] for details; note however footnote 6 above)

$$
\begin{aligned}
&Q_\varphi(\Omega) = C_{\rm scale} S(\Delta\tilde{\Omega}_n), \qquad (3.3.19)\\
&C_{\rm scale} = \frac{4\sqrt{\pi}\mid \varphi_n(E_m)\mid^2 \exp(-E_m/T)}{\omega_m(\mid \omega''\mid)^{3/4} Z(\Gamma T \overline{p^2}_m)^{1/4}}\,,\\
&\Delta\tilde{\Omega}_n = {\rm sgn}(\omega'')(\Omega - n\Omega_m)t_{\rm zdp}/\sqrt{n}, \quad |\Omega - n\Omega_m| \ll \Omega_m, \quad n = 1,2,3,...,\\
&S(x) = |{\rm Re}[S_c(x)]|\,,\\
&S_c(x) = \int\limits_0^\infty d\tau\, \frac{\exp(-ix\tau)}{\sqrt{(1-i)\,{\rm sh}[(1-i)\tau]}}\,.
\end{aligned}
$$

The universal function $S(x)$ is easily calculated numerically [8] (see Fig. 11). It has the shape of an asymmetric peak with a maximum at $x_m \approx 0.61$ ($S(x_m) \approx 2.5$) and a width ~ 1. The shift of the maximum to the right relative to the $x = 0$ value (corresponding to frequency $n\Omega_m$) for the value ~ 1 is due to the fact that Ω_m is the boundary frequency of the spectrum of eigenfrequencies while, over the major part of the time relevant to formation of the peak, the system has such energy that $\omega(E)$ is shifted from Ω_m for $\sim {\rm sgn}(\omega'')(\sqrt{n}t_{\rm zdp})^{-1}$.

At $|x| \gg 1$, only small τ contribute to the integral, so that

$$
\begin{aligned}
&S(x) \approx \int\limits_0^\infty d\tau\, \frac{\cos(x\tau)+\sin(x\tau)}{2\sqrt{\tau}} = \begin{matrix}\sqrt{\frac{\pi}{2x}} & \text{at} \quad x{>}0,\\ 0 & \text{at} \quad x{<}0,\end{matrix} \qquad (3.3.20)\\
&|x| \gg 1.
\end{aligned}
$$

Thus, $Q_\varphi(\Omega)$ (3.3.19) reduces at $|\Delta\tilde{\Omega}_n| \gg 1$ to the zero-friction expression (3.2.6).

The expression (3.3.19) also confirms the qualitative estimates (3.3.6) and (3.3.7), for the ZDP's width and magnitude respectively.

3.4 Asymptotic theory of the ZDP evolution with temperature

The formula (3.3.19) describes the spectrum near $n\Omega_m$ in the asymptotic limit $\Gamma \to 0$; but what would happen if, at a small but fixed Γ, the temperature became smaller than $\Delta E_{\rm zdp}$? It is intuitively obvious that the spectrum must change, both because the statistical distribution within the relevant band of energies becomes strongly inhomogeneous and

[8] In doing so, one should bear in mind that the argument of the complex expression under the radical in the integrand should vary continuously (from $-\pi/2$ to $-\infty$) as τ increases.

because the influence of the drift of energy on the correlation function during the relevant interval $t_{\rm zdp}$ becomes comparable with the influence of the diffusion. And, indeed, the experimental results obtained in [11] show that, when the spectrum near Ω_m is starting to grow exponentially with temperature, it takes (for the given parameters) the form of a step rather than of a peak, and only gradually transforms into a peak with further increase of temperature. In other works (see e.g. [45–47]), which explored different sets of parameters or different models, the evolution varied: in some cases, the exponentially growing spectrum near $n\Omega_m$ had a distinct peak-like shape from its very first manifestation on the background of a low plateau (cf. the right inset in Fig. 17(a)) while, in other cases, the initial shape was either a step followed by a monotonic growth (cf. Fig. 15(c)) or a step leading to a slight decrease followed by significant growth (cf. Fig. 16(a)). The whole diverse range of evolutions is nicely described by numerical calculations based on the algorithm suggested in [11] and generalized in [47]. However, it is also important to obtain explicit results to reveal the mechanisms responsible for different types of evolution. This problem was solved in [48]. Moreover, the universal nature of the relevant part of the spectral evolution has been demonstrated in analogue experiments [46]: the evolution is described by *universal* function, and the variety of different evolutions mentioned above results merely from different arguments of this universal function as well as from different scaling factors. We review below the major results of [48].

We now introduce two new parameters:

$$\tilde{E}_m \equiv \frac{E_m - U_{\rm min}}{\Delta E_{\rm zdp}} \propto \frac{1}{(\Gamma T)^{1/4}}, \tag{3.4.1}$$

$$\gamma \equiv \frac{\Delta E_{\rm zdp}}{T} \propto \frac{1}{T^{3/4}}. \tag{3.4.2}$$

Note that the ratio of the drift of energy near E_m, $\Delta E_{\rm drift}(t) \approx \Gamma \overline{p^2}_m t$, to the diffusion of energy, $\Delta E_{\rm dif}(t) \approx (\Gamma \overline{p^2}_m T t)^{1/2}$, grows with time,

$$\frac{\Delta E_{\rm drift}}{\Delta E_{\rm dif}} = \gamma \sqrt{\frac{t}{t_{\rm zdp}}}, \tag{3.4.3}$$

and reaches the value γ precisely at $t = t_{\rm zdp}$.

The product $\gamma \tilde{E}_m \equiv (E_m - U_{\rm min})/T$ determines the statistical weight of the energy E_m, $W_{st}(E_0 = E_m) \propto \exp(-\gamma \tilde{E}_m)$. It is obvious that, if $\gamma \tilde{E}_m$ is large enough, the contribution of energies $E \approx E_m$ is negligible in comparison with the contribution from $E \approx U_{\rm min}$. At the same time, the characteristic (step-like or similar) shape of the spectrum near Ω_m is possible only if $\gamma \sim 1$, as follows from (3.4.3). On the other hand, it is obvious that the ZDP may be resolved in the spectrum only if

$$\tilde{E}_m \gg 1. \tag{3.4.4}$$

Thus, an important feature of the problem is that we should work down to temperatures that are small enough for γ to be ~ 1 (so that the effect of drift is comparable with that

of diffusion) but large enough for $W_{st}(E_0 = E_m) \propto \exp(-\gamma \tilde{E}_m)$ not to be negligible. The experimental existence of a step-like (or similar) shape of spectrum constitutes evidence that such a range of temperatures does exist, and the theoretical considerations below confirm this inference.

Thus, we shall consider the case of $\gamma \stackrel{\sim}{<} 1$ (which corresponds to $T \stackrel{\sim}{>} (\Gamma\overline{p^2}/\omega'')^{1/3}$). Transforming the reduced FPE (3.3.11) to a dimensionless equation, we shall keep the drift term ($\propto \gamma$) while omitting all terms $\propto \tilde{E}_m^{-k}$ with $k \geq 1$:

$$\frac{\partial W_n}{\partial \tilde{t}} = \frac{1}{2} in \ \mathrm{sgn}(\omega'')(\tilde{E}^2 - \tilde{E}_0^2) W_n + \gamma \frac{\partial W_n}{\partial \tilde{E}} + \frac{\partial^2 W_n}{\partial \tilde{E}^2}. \tag{3.4.5}$$

The explicit solution for W_n (with the same initial condition as before: see Eq. (3.3.15)) can be obtained in a similar manner to the case for $\gamma = 0$ described in the previous sub-section (though it is more cumbersome). But the evaluation of the spectrum is more complicated.

Let us present the spectrum in the following form:

$$Q_\varphi(\Omega) \equiv \int\limits_{U_{\min}}^{\infty} dE_0 \, Q_\varphi^{(\mathrm{partial})}(E_0, \Omega) \equiv \int\limits_{-\tilde{E}_m}^{\infty} d\tilde{E}_0 \, \tilde{Q}_\varphi^{(\mathrm{partial})}(\tilde{E}_0, \Omega), \tag{3.4.6}$$

where

$$\begin{aligned} Q_\varphi^{(\mathrm{partial})}(E_0, \Omega) &= \frac{1}{\pi} \mathrm{Re} \Bigg(\int\limits_0^\infty dt \ \mathrm{e}^{-i\Omega t} \int\limits_0^{2\pi} d\psi_0 \ W_{st}(E_0, \psi_0) [\langle \tilde{\varphi}(t) \rangle_{E_0, \psi_0} \\ &\qquad - \langle \tilde{\varphi} \rangle] [\langle \tilde{\varphi}(E_0, \psi_0) \rangle - \langle \tilde{\varphi} \rangle] \Bigg), \\ \tilde{Q}_\varphi^{(\mathrm{partial})}(\tilde{E}_0, \Omega) &= \Delta E_{\mathrm{zdp}} Q_\varphi^{(\mathrm{partial})}(E_0, \Omega). \end{aligned} \tag{3.4.7}$$

The partial spectrum $Q_\varphi^{(\mathrm{partial})}(E_0, \Omega)$ characterizes the Fourier spectrum of oscillations with initial energy E_0. Correspondingly, it has the form of a peak whose absolute maximum is near $\omega(E_0) \approx \Omega_m + \omega''(E_0 - E_m)^2/2$ and whose width is $\sim t_{\mathrm{zdp}}^{-1}$, while (see Appendix of [48]) the ratio of its absolute value near Ω_m to $|Q_\varphi^{(\mathrm{partial})}(E_m, \Omega_m)|$ is

$$\Big| \frac{\tilde{Q}_\varphi^{(\mathrm{partial})}(\tilde{E}_0, \Omega_m)}{\tilde{Q}_\varphi^{(\mathrm{partial})}(0, \Omega_m)} \Big| \sim \begin{cases} 1 & \text{at} \quad |\tilde{E}_0| \stackrel{\sim}{<} 1, \\ \exp(-\gamma \tilde{E}_0) \max(1, \gamma |\tilde{E}_0|)/\tilde{E}_0^6 & \text{at} \quad |\tilde{E}_0| \gg 1, \end{cases} \tag{3.4.8}$$

i.e., if $\gamma \tilde{E}_m \equiv (E_m - U_{\min})/T$ is not too large, then the main contribution to the ZDP (i.e. to the integral in (3.4.6) at $\Omega \approx \Omega_m$) is made by energies near the extremal one ($|\tilde{E}_0| \stackrel{\sim}{<} 1$). On the contrary, if $(E_m - U_{\min})/T$ is large enough, then the main contribution is made by the lowest energies ($E_0 \approx U_{\min}$). At the same time, for $E_0 \approx U_{\min}$, the conditions under

which Eq. (3.4.5) was obtained are not satisfied, so that the contribution of energies close to E_0 must be described in a different way. We resolve these two different cases below, in sub-sections 3.4.1 and 3.4.2

3.4.1 ZDP at high and moderately small temperatures

There is a paradox in the calculation of the spectrum for $\gamma \neq 0$, as follows. On the one hand, $Q_\varphi(\Omega \approx \Omega_m)$ is dominated by the contributions from energies $E \approx E_m$ and, therefore, should not depend on the actual value of $\tilde{E}_m$ within the relevant wide range (see below) but, on the other hand, replacement of the $\tilde{E}_m$ in (3.4.6) with a minus infinity would be invalid, unlike in the case of $\gamma = 0$, because the result would then diverge [9]. Thus, we should keep the finite $-\tilde{E}_m$ for the lower limit in (3.4.6). At the same time, in the calculation of $\langle\tilde{\varphi}(t)\rangle_{E_0,\psi_0}$ (3.1.10), we may still change the lower energy boundary to $-\infty$, as in the case when $\gamma = 0$.

With account taken of the above remarks and using the explicit solution of the reduced FPE (3.4.5), one can obtain for the spectrum [48]:

$$
\begin{aligned}
&Q_\varphi(\Omega) = C_{\rm scale}\tilde{S}(\Delta\tilde{\Omega}_n, \frac{\gamma}{2n^{1/4}}, \frac{\tilde{E}_m n^{1/4}}{2}), \qquad (3.4.9)\\
&\tilde{S}(x,y,z) = \left|{\rm Re}\left[\tilde{S}_c(x,y,z)\right]\right|,\\
&\tilde{S}_c(x,y,z) = \int\limits_0^\infty d\tau\ \frac{\exp\left[-ix\tau + y^2\left(\frac{2/(1-i)}{{\rm th}[(1-i)\tau/2]} - \tau\right)\right]}{2\sqrt{(1-i)\ {\rm sh}[(1-i)\tau]}}\\
&\qquad\qquad \times{\rm erfc}\left(-z\sqrt{(1-i)\ {\rm th}[(1-i)\tau]} + y\frac{1+{\rm sech}[(1-i)\tau]}{\sqrt{(1-i)\ {\rm th}[(1-i)\tau]}}\right),\\
&\gamma\tilde{E}_m < 5\ln(\tilde{E}_m n^{1/4}/2),
\end{aligned}
$$

where $C_{\rm scale}$ and $\Delta\tilde{\Omega}_n$ are defined in (3.3.19), ${\rm erfc}(z) \equiv \sqrt{2/\pi}\int_z^\infty dy\ \exp(-y^2)$ is the complement of the error function with respect to 1 in the complex plane [49], and the origin of the last inequality in (3.4.9) will be clear from Eq. (3.4.10) below.

If $\gamma = 0$ and $\tilde{E}_m \gg 1$, then $Q_\varphi(\Omega)$ (3.4.9) reduces to Eq. (3.3.19) and, in particular, the shape $\tilde{S}(x,y,z)$ reduces at $|x| \sim 1$ to $S(x)$ (see also Fig. 12(a)).

Analysis of the partial spectrum near Ω_m shows [48] that the structure of $\tilde{S}(x,y,z)$ at $z \gg 1$ is as follows:

---

[9] Allowing for $\gamma \ll 1$ in the present case ($T \gtrsim E_m$), one could alternatively try to use perturbation theory, i.e. to expand the term $\exp(\gamma\tilde{E}_0...)$ in the partial correlation function in a Taylor series over γ so that its integration down to $-\infty$ would give a convergent result for $R_\varphi(\tilde{t})$. However, the resultant correction to $R_\varphi(\tilde{t})$ is $\propto \tilde{t}^{-3/2}$ at small $\tilde{t}$, resulting in the divergence of its Fourier transform. This divergence indicates that $Q_\varphi(\Omega)$ depends on γ non-analytically.

$$\tilde{S}(x,y,z) = \tilde{S}_{\rm zdp}(x,y) + \frac{\epsilon}{8\sqrt{\pi}}\frac{\exp(4yz)}{z^5}, \tag{3.4.10}$$
$$\epsilon = \begin{cases} \sim 1 & \text{at} \quad yz \lesssim 1, \\ 1 & \text{at} \quad yz \gg 1, \end{cases}$$
$$\tilde{S}_{\rm zdp}(x,y) \sim 1, \qquad z \gg 1, \qquad |x| \lesssim 1, \qquad y \lesssim 1.$$

As can be seen from (3.4.10), at $4yz \equiv E_m/T < 5\ln(z)$ the second term on the right-hand side of (3.4.10) (which is determined by the low energies) is exponentially small in comparison with the first term (which is determined by energies near E_m). This confirms the independence of $Q_\varphi(\Omega)$ on $\tilde{E}_m$ in the range defined in (3.4.9). The independence of $\tilde{S}(x,y,z)$ on z in the corresponding range is also confirmed by numerical calculations (Fig. 12(b)).

Properly speaking, just the function $\tilde{S}_{\rm zdp}(x,y)$ describes the shape of the ZDP itself. Both the qualitative analysis and numerical calculations (see Fig. 12(a)) show that, at $y \ll 1$, $\tilde{S}_{\rm zdp}(x,y)$ has the shape of a peak reducing to $S(x)$ as $y \to 0$; as y grows to ~ 1, the right wing of the peak lifts (creating a minimum after which the function grow sharply as x increases); at some $y \sim 1$, the peak transforms into a step followed by rapid growth as x increases. Finally, at $y \gg 1$, $\tilde{S}_{\rm zdp}(x,y)$ is a monotonically (and sharply) increasing function of x but $\tilde{S}$ on the whole becomes exponentially large while the concept of the ZDP loses its physical meaning.

3.4.2 ZDPs at low temperatures

Strictly speaking, the contribution from the lowest energies ($E \approx U_{\rm min}$, i.e. $\tilde{E} \approx -\tilde{E}_m$) has not been correctly taken into account in the previous section. But, given that this contribution is negligible at $T \gtrsim E_m - U_{\rm min}$, Eq. (3.4.9) nonetheless describes the spectrum correctly at such temperatures. On the contrary, however, for $T \ll E_m - U_{\rm min}$, which is the most relevant range of temperatures for $\gamma \sim 1$, the contribution of low energies may become dominant and it should be evaluated differently from Sec. 3.4.1.

Let us first divide the whole integration range in (3.4.6) into three sub-ranges:

$$Q_\varphi(\Omega) = \int\limits_{U_{\rm min}}^{U_{\rm min}+\alpha T} dE_0 ... + \int\limits_{U_{\rm min}+\alpha T}^{E_m-\beta(E_m-U_{\rm min})} dE_0 ... + \int\limits_{E_m-\beta(E_m-U_{\rm min})}^{\infty} dE_0 ... \tag{3.4.11}$$
$$\equiv Q_\varphi^{\rm (low)}(\Omega) + Q_\varphi^{\rm (int)}(\Omega) + Q_\varphi^{\rm (zdp)}(\Omega),$$
$$\tilde{E}_m^{-1} \ll \beta < 1, \quad 1 \ll \alpha < (E_m - \beta(E_m - U_{\rm min}))/T, \quad T/(E_m - U_{\rm min}) \ll 1.$$

The contribution of the intermediate range, $Q_\varphi^{\rm (int)}(\Omega)$, can easily be shown [48] to be negligible in comparison with the either first or third term in (3.4.11).

The third term, $Q_\varphi^{\rm (zdp)}(\Omega)$, is described similarly to the case for $T \gtrsim E_m$, the only difference being that $\tilde{E}_m$ in Eq. (3.4.9) should be exchanged for $\beta\tilde{E}_m$.

The first term, $Q_\varphi^{(\mathrm{low})}(\Omega)$, is determined by weakly nonlinear oscillations in the minimum of the potential and has a narrow peak near $\Omega_0 \equiv \omega(E = U_{\min})$ while Ω_m is located on its far wing. It may easily be shown [10] that the far wings of $Q_\varphi^{(\mathrm{low})}(\Omega)$ coincide with the spectrum calculated in the harmonic approximation, $Q_\varphi^{(\mathrm{harmonic})}(\Omega, \Omega_0)$; e.g. for $\varphi = q$, the relevant spectrum is

$$Q_\varphi^{(\mathrm{harmonic})}(\Omega, \Omega_0) = \frac{\Gamma T(\Omega^2 + \Omega_0^2)}{2\pi\Omega_0^2(\Omega^2 - \Omega_0^2)}. \tag{3.4.12}$$

Thus, ultimately, we obtain for the spectrum in the vicinity of Ω_m:

$$\begin{aligned} &Q_\varphi(\Omega \approx \Omega_m) = C_{\mathrm{scale}}\tilde{S}(\Delta\tilde{\Omega}_n, \frac{\gamma}{2n^{1/4}}, \frac{\beta\tilde{E}_m n^{1/4}}{2}) + Q_\varphi^{(\mathrm{harmonic})}(\Omega, \Omega_0), \qquad (3.4.13)\\ &\beta \gg \tilde{E}_m^{-1}, \qquad 1 - \beta \gg T/(E_m - U_{\min}), \qquad |\Omega - n\Omega_m| \ll \Omega_m, |\Omega_0 - n\Omega_m|,\\ &n = 1, 2, 3... \end{aligned}$$

The first (ZDP) term in (3.4.13) depends on T exponentially strongly, whereas the second term (the low-energy tail) depends on T relatively weakly (in a power-like way: cf. (3.4.12)). Thus, there is some critical temperature $T_c^{(n)}$ below which the ZDP is not manifested while, above $T_c^{(n)}$, the ZDP dominates. Furthermore, in order to be definite, we shall consider the spectrum of fluctuations of the coordinate; but the main results will be valid for arbitrary φ.

In order to find $T_c^{(n)}$ to logarithmic accuracy, one should equate the orders of magnitude of C_{scale} (3.3.19) and $Q_q^{(\mathrm{harmonic})}(n\Omega_m, \Omega_0)$ (3.4.12), so that

$$T_c^{(n)} \approx \frac{E_m}{5\ln(\tilde{E}_m + 2\ln(|q_n/q_1|))}, \qquad T_c^{(n)} \ll E_m. \tag{3.4.14}$$

It is seen from (3.4.14) that the number of ZDPs is finite because, at large enough n, q_n decreases exponentially as n grows. Thus $T_c^{(n)}$ reaches infinity at the critical value $n = n_c$ which can be determined approximately from the equation:

$$|\frac{q_n}{q_1}| \sim (\frac{\Gamma}{\Omega_m})^{5/8}. \tag{3.4.15}$$

It is seen also from (3.4.14) that the minimal critical temperature $T_c \approx E_m/(5\ln(\tilde{E}_m)$ corresponds to $n = 1$. In the asymptotic limit $\Gamma \to 0$,

$$T_c = \frac{E_m}{\frac{5}{4}\ln(\frac{\Omega_m}{\Gamma})}. \tag{3.4.16}$$

[10] To the lowest order in $\Delta\Omega_0/|\Omega - \Omega_0|$, where $\Delta\Omega_0$ is the width of the peak $Q_\varphi^{(\mathrm{low})}(\Omega)$, the spectrum on the wings is entirely determined by the $dR_\varphi(t = 0)/dt$ which, in turn, coincides with the expression calculated in the harmonic approximation.

The coefficient $\gamma(T = T_c) \equiv \gamma_c$ is

$$\gamma_c = \left[\frac{5\ln(\tilde{E}_m)}{\tilde{E}_m}\right]_{T_c}. \tag{3.4.17}$$

In the asymptotic limit $\Gamma \to 0$, γ_c goes to zero too. Hence, at small enough Γ, the shape of the ZDP is close to the universal shape (3.3.19) from the very manifestation of the ZDP, at $T \approx T_c$.

At the same time, if Γ is not small enough, so that the inequality (3.4.4) is not too strong, then the shape of the ZDP at $T \approx T_c$ is step-like and only gradually evolves to the universal peak shape as T grows. Just this type of the evolution was observed in [11] (see Fig. 14) where $\tilde{E}_m \approx 3$ at $T \approx T_c$.

In order to demonstrate the two different types of ZDP evolution with temperature, we calculate $Q_q(\Omega)$ from Eqs. (3.4.13), (3.4.12) for the same system as in [11] (the tilted Duffing oscillator [11]: see also sub-section 2.3 above), at two different values of Γ. The results are shown in Fig. 13.

3.5 General theory

The explicit description of ZDPs given in the previous sub-sections is important for an understanding of the relevant physical mechanisms and of the characteristic features of ZDPs. At the same time, quantitative agreement with real spectra is restricted to the very low friction and very narrow frequency ranges.

In order to provide an accurate theoretical description of spectra in a broad frequency range and in the whole range of small (rather than just ultra-small) friction, a special method [11] was developed and later generalized for multi-well potentials [47]. Note that the method is not restricted to ZD systems: it facilitates the calculation of fluctuation spectra for any underdamped system. We illustrate below the major features of this method using as an example the fluctuation spectrum of a generalized coordinate (magnetic flux) in a multi-well SQUID potential (Fig. 3(b)).

Let us present the correlation function $R_q(t)$ (3.1.5) in the following form:

$$R_q(t) = \int_{-\infty}^{\infty} dp \int_{-\infty}^{\infty} dq\ (q - \langle q \rangle)\tilde{\tilde{W}}(p, q, t), \tag{3.5.1}$$

[11] In fact, the TDO is far from being the best model for illustrating the ZDP evolution with temperature: it typically requires a very small value of Γ. Historically, however, the TDO was the first system in which ZDPs and their evolution were observed, which is why we consider it here. In sub-section 3.6, describing analogue experiments, we shall illustrate ZDP evolution for the SQUID model as well.

$$\tilde{\tilde{W}}(p,q,t) = \int\limits_{-\infty}^{\infty} dp_0 \int\limits_{-\infty}^{\infty} dq_0 \; (q_0 - \langle q \rangle) W(p,q,t|p_0,q_0) W_{st}(p_0,q_0).$$

The function $\tilde{\tilde{W}}$ satisfies the same FPE as W (see (3.1.2)) but with a different initial condition:

$$\tilde{\tilde{W}}(p,q,0) = (q - \langle q \rangle) W_{st}(p,q). \tag{3.5.2}$$

For further analysis, it is convenient to rewrite the FPE (3.1.2) in the energy-angle representation [12] and to make a half-Fourier-transform with respect to time. For the sake of generality, we assume a multi-well potential (a single-well potential may be considered as a particular case), so that the energy-angle representation must be differently defined in different regions of the phase space, divided by separatrices corresponding to the barrier energy levels (cf. Fig. 3(b)).

Tagging each such region with an index j, we can write the equation for the half-Fourier transform W_F in the j-th phase space region as

$$\begin{aligned}
&-i\Omega W_F + \omega \frac{\partial W_F}{\partial \psi} = \Gamma \hat{L} W_F + (q - \langle q \rangle) W_{st}(q,p), \qquad (3.5.3)\\
&\hat{L} \equiv \hat{L}^{(j)}(E,\psi) = \\
&\qquad \left[p \frac{\partial}{\partial E} - \omega q_E \frac{\partial}{\partial \psi} \right] \left[p \left(1 + T \frac{\partial}{\partial E} \right) - T \omega q_E \frac{\partial}{\partial \psi} \right] , \\
&\omega \equiv \omega^{(j)}(E), \quad q \equiv q^{(j)}(E,\psi), \quad p \equiv p^{(j)}(E,\psi), \\
&W_F \equiv W_F^{(j)}(E,\psi,\Omega) = \int\limits_0^{\infty} dt \; \exp(i\Omega t) \tilde{\tilde{W}}(p,q,t).
\end{aligned}$$

Allowing for the periodicity of W_F in ψ, we may expand it in a Fourier series,

$$W_F^{(j)}(E,\psi;\Omega) = \sum_{n=-\infty}^{\infty} W_n^{(j)}(E,\Omega) \exp(in\psi). \tag{3.5.4}$$

Substituting (3.5.4) into (3.5.3), we obtain

$$\begin{aligned}
&-(\Omega - n\omega^{(j)}) W_n^{(j)} = \Gamma \sum_m \hat{L}_{nm}^{(j)} W_m^{(j)} + (q_n^{(j)} - \langle q \rangle \delta_{n0}) W_{st}, \qquad (3.5.5)\\
&\hat{L}_{nm}^{(j)} = \frac{1}{2\pi} \int\limits_0^{2\pi} d\psi \; \exp(-in\psi) \hat{L}^{(j)} \exp(im\psi),
\end{aligned}$$

[12] Note that the result differs slightly from the FPE (3.3.8) for $\tilde{W}(E,\psi,t)$ since these equations relate to differently normalized functions: $\tilde{W}/W = \partial(p,q)/\partial(E,\psi) = \omega^{-1}(E)$ [1].

$$q_n^{(j)} = \frac{1}{2\pi} \int_0^{2\pi} d\psi \, \exp(-in\psi) q^{(j)}(E, \psi),$$

where δ_{n0} is a Kronecker delta ($\delta_{n0} = 1$ for $n = 0$, whereas $\delta_{n0} = 0$ for $n \neq 0$). Our aim is to find the $W_n^{(j)}$, since the fluctuation spectrum can be written in terms of them as

$$Q_q(\Omega) = \sum_j 2 \, \mathrm{Re} \Big[\int_{E_{\min}^{(j)}}^{E_{\max}^{(j)}} \frac{dE}{\omega^{(j)}(E)} \times \sum_{n=0}^{\infty} \left((q_n^{(j)}(E))^* - \delta_{n0} \langle q \rangle \right) W_n^{(j)}(E, \Omega) \Big], \tag{3.5.6}$$

where $E_{\min}^{(j)}$ and $E_{\max}^{(j)}$ are respectively the minimum and maximum energies of the j-th region and the star * denotes the operation of complex conjugation.

Assuming that the friction is small and that we are interested in peaks of the spectrum rather than in low fluctuational plateaus, we retain in Eq. (3.5.5) only diagonal terms since the influence of different resonances on each other is negligible [13] [11]. Thus, we obtain for each $W_n^{(j)}$ a closed equation:

$$-i(\Omega - n\omega) W_n^{(j)} = \Gamma \left(1 + \overline{p^2} \frac{d}{dE} \right) \left(1 + T \frac{d}{dE} \right) W_n^{(j)} - \Gamma T n^2 \omega^2 \overline{q_E^2} W_n^{(j)} + (q_n - \delta_{n0} \langle q \rangle) W_{st} \, , \tag{3.5.7}$$

where the bar, as before, implies averaging over the angle ($\frac{1}{2\pi} \int_0^{2\pi} d\psi \ldots$).

In order to solve Eq. (3.5.7), we also need to know the boundary conditions at $E_{\min}^{(j)}$ and $E_{\max}^{(j)}$ for each region. We now show that if $n \neq 0$ [14], then $W_n^{(j)}$ vanishes at the boundaries:

$$W_n^{(j)}(E_{\min}^{(j)}, \Omega) = W_n^{(j)}(E_{\max}^{(j)}, \Omega) = 0. \tag{3.5.8}$$

The condition at $E_{\max}^{(j)} \equiv \infty$ immediately follows from the vanishing of the probability density as $E \to \infty$. The derivation for other boundaries is less trivial.

Consider first those $E_{\min}^{(j)}$ which correspond to local minima of the potential $U_{\min}^{(j)}$. Near

[13] This procedure is equivalent to neglecting the nonresonant terms in the original FPE in the energy-angle representation (3.3.8), in accordance with the averaging method: cf. (3.3.11).
[14] The boundary conditions for the case $n = 0$ require separate analysis [50,51] but, given that ZDPs are located at distinctly non-zero frequencies, the case $n = 0$ is not relevant in the present context.

these local minima, the self-oscillations are approximately harmonic, so that

$$\overline{p^2} \approx E - U_{\min}^{(j)}, \quad \overline{q_E^2} \approx \frac{1}{4\omega_0^2(E - U_{\min}^{(j)})}, \quad q_1 \approx \frac{\sqrt{2}\omega_0}{\sqrt{E - U_{\min}^{(j)}}}. \tag{3.5.9}$$

The solutions of (3.5.7), (3.5.9) can be seen to be either $\propto (E-U_{\min}^{(j)})^{1/2}$ or $\propto (E-U_{\min}^{(j)})^{-1/2}$. Allowing for the finiteness of the probability density (and therefore also of $W_n^{(j)}$), one chooses the convergent solution and thus arrives at the condition $W_n^{(j)}(E_{\min}^{(j)}, \Omega) = 0$.

Similarly, for boundaries corresponding to the levels of potential barriers, $E_b^{(j)}$,

$$\overline{q_E^2} \propto \frac{1}{(\mid E - E_b^{(j)} \mid)^2}, \tag{3.5.10}$$

so that the solution of (3.5.7), (3.5.10) may be either convergent ($\propto \mid E - E_b^{(j)} \mid$) or divergent ($\propto (\mid E - E_b^{(j)} \mid)^{-1}$). Choosing the convergent solution, one arrives at the condition $W_n^{(j)}(E_b^{(j)}, \Omega) = 0$.

Eq. (3.5.7), together with the boundary conditions (3.5.8) is easily solved numerically by a standard method (the coefficients in the equation are easily calculated from their definition: see [11,46]). Results for several examples will be presented in the next sub-section (see Figs. 14-17).

3.6 Analogue electronic experiments

A valuable method for studying fluctuational phenomena in dynamical systems is to model the dynamics and the noise by means of analogue electrical circuits, electronic chips and noise generators (for reviews see [52–54]). ZDPs were observed in several such experiments and studied in various aspects [11,45–47,55–57]. We present below some typical experimental results together with their comparison with calculations based on the theory described in the previous sub-sections.

The first experimental results [55] were obtained, in fact, as a wholly unexpected by-product of the search for the zero-frequency peak in the TDO model [50]. Later [11], they were developed and compared with the theory. Fig. 14 presents the evolution with increasing T of the spectrum in the TDO model, with $U(q)$ as given in (2.3.1) and drawn in Fig. 7. First of all, we see that the theoretical calculations nicely match the experimental results. Secondly, it is seen that, at low temperatures (curve (a)), the spectrum is centred close to the bottom eigenfrequency $\Omega_0 = 2$ (cf. Fig.7) while, at the high temperature (curve (c)), the spectrum is centred close to the minimal eigenfrequency $\Omega_m \approx 1.76$. For the given intermediate temperature (curve (b)), the spectrum has the shape of a wide nearly rectangular peak with a flat top, from $\approx \Omega_m$ to $\approx \Omega_0$. Thus, as the temperature increases from (b) to (c), the spectral peak becomes significantly *narrower*, quite unlike the conventional case with a monotonic $\omega(E)$ when the increase of noise necessarily results

in a broadening of the spectrum. The narrowing is related to the onset of the ZDP, which is narrow and becomes dominant at high enough temperature. At the same time, the spectrum retains a single-peaked structure at all temperatures just because the friction is not small enough for two peaks to be resolved: the parameter γ at $T = T_c$ (i.e. at the onset of the ZDP) is ~ 1 and the ZDP is step-shaped while merging, at the same time, with the peak determined by the low energy range. In the case of the TDO, the friction parameter should be at least a few times smaller in order for the ZDP to be resolved from the low-energy peak. In [45], an approximately 11 times smaller value of the friction parameter was achieved [15] ($\Gamma \approx 1.7 \times 10^{-3}$): see Fig. 15. Agreement with the theoretical calculations using the algorithm described in sub-section 3.5 is excellent [45].

In [46], the spectra were studied experimentally for two different models, the TDO and SQUID, and compared with the explicit expressions [48] described in sub-section 3.4 above with the aim of demonstrating the universality of the ZDP shape and its evolution with temperature. The agreement obtained was reasonably satisfactory: see Figs. 16,17. The observed deviations of about 30% in Fig. 16(a,b) are partly due to the exponential sensitivity to parameters, and partly because the small parameter in the theory (x_m^{-1}) is in reality not very small in these cases. The absence of the plateau in the theoretical curves in the right-hand insets in Fig. 17(a,b) is because the theoretical curves account only for the ZDP contribution while the low-energy contribution is not included [16] (cf. Eq. (3.4.13), which includes both contributions).

Figs. 16,17 provide a clear experimental verification of the universality of the ZDP evolution, showing both types of ZDP onset: step-wise (Figs. 16(a,b)) and peak-wise (Figs. 17(a,b)). In addition, they demonstrate that the SQUID model provides a much more pronounced manifestation of ZDPs than the TDO, because of the better resolution between the frequency and energy ranges responsible for the ZDP and for the low-energy peak. This has allowed observation of a pronounced manifestation of *zero-dispesion stochastic resonance* (ZDSR) [47,56,57] in the SQUID model but not in the TDO (cf. [58], where noise-induced growth of the signal/noise ratio was not achieved because it would have required unrealistically small values of Γ). Fig. 18 presents the results from [47], where the spectra of the SQUID model were studied most thoroughly. The spectral evolution with temperature demonstrates very nicely the sequential "firing" of ZDPs corresponding to the different extrema of $\omega(E)$ (see Fig. 4). Fig. 18 also demonstrates excellent agreement between the measured spectra and spectra calculated by the algorithm described above in sub-section 3.5, over the whole relevant range of frequencies [17].

[15] In order to provide the required extremely small value of Γ, the corresponding feedback resistor on the first integrator was necessarily made rather larger ($\sim 100\text{M}\Omega$) than would normally [52–54] be used in circuit-modelling experiments, thereby exacerbating the effect of leakage currents, stray capacitance and other non-idealities of the components.

[16] The low-energy contribution is not included since it is not universal. The major aim of [46] was to demonstrate the universality of the evolution of the ZDP shape as T varies.

[17] The theoretical calculations did not include the zero-frequency peak since it was not relevant to ZDSR and would have required special consideration [50,51].

Although most of the fundamental issues related to ZDPs seem already to have been solved, there still remain some interesting open questions.

One of the hitherto unstudied problems relates to the hierarchy of ZDPs related to the order of an extremum $\omega(E)$. The explicit expressions for the asymptotic ZDP shape and its evolution with temperature, derived above in sub-sections 3.3 and 3.4 (Eqs. (3.3.19) and (3.4.9) respectively), assume that $d^2\omega(E_m)/dE_m^2 \neq 0$, which is the most frequently occurring case in real systems. At the same time, it is possible in principle that the order of the lowest nonzero derivative at the extremum is higher than 2 (as for an inflection point, for instance). In this case, the shape of the ZDP will differ from (3.3.19), while still being universal, i.e. described by a function that is independent of any parameter. Thus the hierarchy of universal shapes of the ZDP depends on the order of the extremum of the functions $\omega(E)$. The quantitative analysis of this hierarchy, based on the reduction of the full Fokker-Planck equation to the asymptotic dimensionless one, and its further solution has yet to be tackled. Following [46], we now present some qualitative estimates.

We shall suppose in this sub-section that the dependence $\omega(E)$ is power-law-like near the extremum:

$$\omega(E) = \Omega_m + \frac{1}{(1+k)!}\omega^{(1+k)}(E - E_m)^{1+k}, \qquad k = 1, 2, 3, ... \tag{3.7.1}$$

The characteristic time $t_{\mathrm{zdp}}^{(k)}$ for the decay of the angle correlation is determined by the fluctuations of energy, giving rise in turn to fluctuations of the angle derivative with respect to time $d\psi/dt \approx \omega(E)$ and, correspondingly, to a loss of the angle correlation. As in sub-section 3.3, in order to estimate $t_{\mathrm{zdp}}^{(k)}$, we need to take into account the diffusion-like growth with time of the energy distribution (for an initially definite value of energy) [38]: $\Delta E(t) \sim \sqrt{\Gamma T \overline{p^2} t}$. Correspondingly, within the relevant range of energies, the characteristic width of the fluctuational distribution of angles is of the order of $\Delta\psi(t) \sim |\omega(E_m \pm \Delta E(t)) - \omega(E_m)|t$. Allowing for $\Delta\psi(t_{\mathrm{zdp}}^{(k)}) \sim \pi$, we arrive at

$$t_{\mathrm{zdp}}^{(k)} \sim \frac{1}{|\omega^{(1+k)}/(1+k)!|^{\frac{2}{3+k}}(\Gamma T \overline{p^2})^{\frac{1+k}{3+k}}} \propto \frac{1}{\Gamma^{\frac{1+k}{3+k}}} \quad . \tag{3.7.2}$$

Thus, the width of the ZDP is

$$\Delta\Omega^{(k)} \sim \frac{1}{t_{\mathrm{zdp}}^{(k)}} \propto \Gamma^{\frac{1+k}{3+k}} \quad . \tag{3.7.3}$$

The characteristic width $\Delta E_{\mathrm{zdp}}^{(k)}$ of the band of energies near E_m that are responsible for

the ZDP is $\sim \Delta E(t^{(k)}_{\rm zdp})$, i.e.

$$\Delta E^{(k)}_{\rm zdp} \sim \left(\frac{\Gamma T \overline{p^2}}{|\omega^{(1+k)}|/(1+k)!} \right)^{\frac{1}{3+k}} \propto \Gamma^{\frac{1}{3+k}} \quad . \tag{3.7.4}$$

The scaling factor for the magnitude of the fundamental (i.e. at $\Omega = \Omega_m$) ZDP is:

$$C^{(k)}_{\rm scale} \sim \frac{1}{Z\Omega_m} {\rm e}^{-\frac{E_m}{T}} |\varphi_1|^2 \Delta E^{(k)}_{\rm zdp} t^{(k)}_{\rm zdp} \propto \Gamma^{-\frac{k}{3+k}} \quad . \tag{3.7.5}$$

For the particular case $k = 1$, the above expressions reduce to the corresponding equations in sub-section 3.3.

Another so far unstudied problem is the shape of the ZDP in case of coloured noise of long correlation time t_N [18] . The ZDP should typically persist but its shape may be expected to change. But the linearity of the friction is not crucial. It is important only that the net loss of energy within one period of oscillation should be much smaller than E_m, while details of the dependence of friction on velocity and coordinate are not very important.

Similarly, the case of multiplicative noise in ZD systems has not yet been studied.

We anticipate that the major emphasis of further investigations related to ZDPs will be on applications to real systems, and on using ZDPs as a non-destructive method for the determination of parameters. Given the strong sensitivity of the ZDP magnitude to E_m and T ($\propto \exp(-E_m/T)$), as well as their narrowness ($\propto \sqrt{\Gamma}$) and height ($\propto \Gamma^{-1/4}$), ZDPs are likely to provide a convenient tool for the determination of T and/or other parameters affecting E_m or Ω_m.

3.8 Conclusions

To summarize, if a ZD system is subject to noise and weak friction, then the spectrum of its fluctuations may possess a high narrow peak (ZDP) near the extremal eigenfrequency $\Omega_m = \omega(E_m)$, as well as peaks at its harmonics. The origin of the ZDPs lies in a long correlation in the angle dynamics during the motion within the narrow band of energies near E_m: diffusion of energy in this band nearly does not affect the angle ($\psi \approx \int dt\, \omega(E)$ while $d\omega(E_m)/dE_m = 0$).

In the asymptotic limit of small friction Γ, the peaks become infinitely high and infinites-

[18] Note that conventionally understood coloured noise, i.e. the noise with a correlation time comparable with a characteristic period of eigenoscillation (Ω_m^{-1}, in our case), may still be considered as a white noise in the context of the ZDP. In order for the colour to affect the ZDP shape, it is necessary that $t_N \gtrsim t_{\rm zdp}$ where $t_{\rm zdp}$ is given by Eq. (3.3.4) in which the product ΓT means, in general, the noise intensity.

imally narrow:

$$Q_{\rm zdp} \propto \frac{1}{\Gamma^{1/4}}, \tag{3.8.1}$$

$$\Delta\Omega_{\rm zdp} \propto \Gamma^{1/2}, \tag{3.8.2}$$

while the scaled shape reduces to the universal form $S(x)$ (3.3.19).

The influence of temperature on ZDPs is mainly due to the activation-like dependence of the statistical weight of the relevant energies about E_m:

$$Q_{\rm zdp} \propto {\rm e}^{-\frac{E_m}{T}}, \tag{3.8.3}$$

Thus, at too small temperatures, ZDPs are not manifested at all on the background of the smooth fluctuational plateau ($\propto \Gamma T$) which is formed by low-energy oscillations with the frequency Ω_0, and the onset of the fundamental (at $\Omega \approx \Omega_m$) ZDP occurs at

$$T = T_c \approx \frac{E_m}{\frac{5}{4}\ln(\frac{|\Omega_0-\Omega_m|}{\Gamma})}\ , \qquad \ln(\frac{|\Omega_0-\Omega_m|}{\Gamma} \gg 1\ . \tag{3.8.4}$$

As the temperature grows, the ZDP becomes dominant over the low-energy tail in the relevant range of $\Omega \approx \Omega_m$.

ZDPs are also manifested at a finite number of higher harmonics, such that $|q_n/q_1| \gg (\Gamma/\Omega_m)^{5/8}$. As the temperature grows from T_c to $T \stackrel{\sim}{>} E_m$, the shape of the ZDP evolves towards the universal form $S(x)$. This evolution is governed by only one parameter γ (3.4.2), which is a monotonically decreasing function of temperature: $\gamma \sim [(\Gamma/|\Omega_m - \Omega_0|)(E_m/T)^3]^{1/4} \propto T^{-3/4}$. If $\gamma \ll 1$, then the shape is close to the universal one while, if γ increases to ~ 1, the shape becomes step-like; with further growth of γ, the ZDP concept loses physical sense because the low-energy contribution becomes dominant.

In the asymptotic limit $\Gamma \to 0$, $\gamma_c \equiv \gamma(T_c) \to 0$ so that the ZDP possesses the universal shape S from its very onset.

The explicit expressions (3.3.19), (3.4.9) and (3.4.13) provide a qualitative understanding of the ZDPs' formation as well as a quantitative description in the relevant (narrow) range of frequencies near Ω_m, provided the friction parameter is very small. For an accurate description of spectra over a broad range of frequencies, and for the full range of small frictions ($\Gamma/\Omega_m \ll 1$), one may use a simple numerical method based on an averaging technique (see sub-section 3.5).

The theory provides a satisfactory description of the results of experiments on analogue electronic circuits.

The phenomenon of ZDPs may be used for the non-destructive determination of parameters as well as providing the underlying physical basis for the phenomenon of the zero-dispersion stochastic resonance (see sub-section 5.1. below).

4 Periodically-driven zero-dispersion systems

Periodically driven dynamical systems are of long-standing interest both to mathematicians and to other scientists, forming a subject that is fundamental and also of importance in numerous applications.

The concept of *nonlinear resonance* in periodically-driven Hamiltonian systems was introduced by Chirikov while studying magnetic traps [59]. It has become of seminal importance in studies of Hamiltonian systems, especially in the context of chaos [5,35,60]. One of its most important features is that the behaviour of a periodically driven Hamiltonian system is to a large extent universal and described approximately by the so-called *standard map* [5,35,60].

At the same time, conventional nonlinear resonance (NR) as above, and the standard map, are valid only if they relate to the energy range where $d\omega(E)/dE \neq 0$. The dynamics become drastically different if the resonance occurs close to an extremal energy E_m where $d\omega(E)/dE = 0$. Probably the first study of such a situation was that in [26], where the problem of rf acceleration in particle accelerators was studied numerically and the occurrence of a characteristic *separatrix reconnection* in the phase space with variation of the parameters of the corresponding map was observed. Separatrix reconnection was also found in relation to some other physical problems, e.g. motion of magnetic field lines [61], wave-particle interactions [62] and laser-plasma coupling [63]. The identification of such maps as a general class, and some analytic studies of their separatrix reconnection, were first reported in [8]. Later, two alternative titles were established for such maps: *nonmonotonic twist maps* [9] and *area preserving nontwist maps* [10]. They were used in a number of papers in the context of a variety of physical problems, e.g. transport and mixing in fluids [64,65] and dynamics of rays in optical waveguides [66]. A detailed classification [19] of this class of maps was presented in [9,10] together with some analytic and numerical studies of their properties, especially in the context of the breakage of KAM trajectories and onset of global chaos.

Independently of the studies of maps, the concept of *zero-dispersion nonlinear resonance* (ZDNR) was introduced in [67] via an averaging method [41]. The evolution of the phase space (via separatrix reconnection) as the frequency of the driving force varied was then studied analytically and numerically [68]. The authors of [67,68] were unaware of the studies of the maps described above, so that there was a significant overlap between the results. At the same time, even in these initial papers on ZDNR, features were found that were not present in the earlier papers on maps. In particular, it was shown [67] that ZDNR occured, not only within the spectrum of eigenfrequencies, but also within a restricted band of frequencies beyond the extremal eigenfrequency [20].

The subsequent studies of ZDNR evolved mainly in four directions that were distinctly different from those on area preserving nontwist maps. One of these was a generalization

[19] The classification relates to different types of extremum in $\omega(E)$. The analogous classification in relation to ZDPs was done earlier in [46] (cf. also Sec. 3.7 above).
[20] Nearly simultaneously, a similar feature was found [66] for maps.

of the concept of ZDNR to the *weakly dissipative* case [69]. This has provided a powerful tool for the analysis of both non-chaotic and chaotic dynamics in such systems, including in particular a thorough local and global bifurcation analysis [70] and the generalization of the Chirikov resonance-overlap criterion for the onset of chaos to the dissipative case [71–73] [21] . The second direction is the study of the *chaos* associated with ZDNR in *non-dissipative* systems: this includes both the derivation of the corresponding separatrix map [75,71] (which is distinctly different from the conventional separatrix map [60]) and the dramatic facilitation of the onset of global chaos in systems with more than one separatrix [21,76]. The third direction involves the inclusion of *fluctuations* [77,71,78]. Finally, applications to various *particular models* which had not been studied previously in this context were considered, such as the TDO [67–75], relativistic oscillators [30,31], SQUIDs [79] and the 2D electron gas in a one-dimensional magnetic superlattice [20,21,76].

The material that follows in this section is based mainly on the studies of ZDNR reported in [67–77,79,30,31,20,21].

4.1 Slow-oscillating dynamics and zero-dispersion nonlinear resonance

Consider the general case of a one-dimensional periodically driven oscillator:

$$\begin{aligned}
&\dot{p} = -\frac{\partial H}{\partial q} - \Gamma f_p(q,p), \\
&\dot{q} = \frac{\partial H}{\partial p} - \Gamma f_q(q,p), \\
&H = H_0(p,q) + hV(p,q,t), \quad V(p,q,t) = \sum_{l=1}^{\infty} V_l(p,q)\cos(\mathrm{l}\omega_f t + \alpha_l),
\end{aligned} \tag{4.1.1}$$

where, if $\Gamma = 0$, the system is Hamiltonian whereas, if $\Gamma > 0$, then the terms proportional to f_q and f_p provide the dissipation condition, i.e. a volume contraction of the phase space with time on average.

It is convenient to transform to the canonically conjugate variables action I and angle ψ [1,35,60] (see also eqs.(A.2)-(A.4) in Appendix):

$$I \equiv I(E) = \left[\int_{E_{\min}}^{E} \frac{d\tilde{E}}{\omega(\tilde{E})}\right]_{E=H_0(p,q)}, \quad \psi = \left[\omega(E)\int_{q_{\min}(E)}^{q} \frac{d\tilde{q}}{p(\tilde{q},E)}\right]_{E=H_0(p,q)}, \tag{4.1.2}$$

where

$$E = H_0(p,q) \tag{4.1.3}$$

[21] The latter is still under active study [74].

is the energy in conservative motion ($\Gamma = 0, h = 0$),

$$\omega \equiv \omega(E) = dH_0/dI \tag{4.1.4}$$

is the frequency of conservative motion at a given energy E; $E_{\min}$ is the minimal (over all q, p) energy $E \equiv H_0(p, q)$ and $q_{\min} \equiv q_{\min}(E)$ is the minimal (for given E) coordinate $q \equiv q(E, p)$, and $q(E, p)$ and $p(E, q)$ are determined from (4.1.3).

By definition, the unperturbed part of the Hamiltonian does not depend on angle, and the periodic perturbation can be expanded into a Fourier series over ψ,

$$\begin{aligned} &H \equiv \tilde{H}_0(I) + h\tilde{V}(I, \psi, t), \\ &\tilde{V}(I, \psi, t) = \sum_{l=1}^{\infty} \sum_{n=0}^{\infty} V_l^{(n)}(I) \cos(n\psi + \beta_n) \cos(l\omega_f t + \alpha_l). \end{aligned} \tag{4.1.5}$$

Note that $V_l^{(n)}$ is twice larger than a conventionally defined Fourier harmonic (cf. (A.5) in Appendix); this non-conventional definition was used in [70], and we retain it here to avoid confusion.

The dynamics (4.1.1) are expressed in $I - \psi$ variables in the following way (cf. Appendix):

$$\begin{aligned} \dot{I} &= -\frac{\partial H}{\partial \psi} - \frac{\Gamma}{\omega}\left(\frac{\partial H_0}{\partial p} f_p + \frac{\partial H_0}{\partial q} f_q\right), \\ \dot{\psi} &= \frac{\partial H}{\partial I} + \Gamma\omega(-p_E f_q + q_E f_p). \end{aligned} \tag{4.1.6}$$

It is assumed in what follows that both the dissipation and the periodic perturbation are small. If this were not the case, nonlinear resonance would not occur: the undriven motion would be non-oscillatory for strong damping; and it could change its period or become chaotic if the periodic perturbation was large.

Let us consider the range of actions (or energies, equivalently) where the resonance condition holds approximately for some integers n and l,

$$n\omega(I) \approx l\omega_f. \tag{4.1.7}$$

Introducing the slow angle

$$\tilde{\psi} = n\psi - l\omega_f t + \beta_n - \alpha_l, \tag{4.1.8}$$

using a standard averaging method [41] and some formal transformations, one can obtain a closed set of dynamical equations for $I, \tilde{\psi}$ (cf. the non-dissipative case [5,35,59,60,67,68] and some partial dissipative cases [69–73]),

$$
\begin{aligned}
&\dot{I} = -\frac{\partial \overline{H}}{\partial \tilde{\psi}} - \Gamma f_I, \\
&\dot{\tilde{\psi}} = \frac{\partial \overline{H}}{\partial I} - \Gamma f_{\tilde{\psi}}, \\
&\overline{H} \equiv \overline{H}(I, \tilde{\psi}) = \int_0^I d\tilde{I}\ (n\omega(\tilde{I}) - l\omega_f) + \frac{h}{2} n V_l^{(n)}(I)\cos(\tilde{\psi}), \\
&f_I \equiv f_I(I) = \frac{1}{2\pi} \int_0^{2\pi} d\psi\ \left(f_p \frac{\partial q}{\partial \psi} - f_q \frac{\partial p}{\partial \psi} \right), \\
&f_{\tilde{\psi}} \equiv f_{\tilde{\psi}}(I) = \frac{1}{2\pi} \int_0^{2\pi} d\psi\ n \left(-f_p \frac{\partial q}{\partial I} + f_q \frac{\partial p}{\partial I} \right).
\end{aligned}
\tag{4.1.9}
$$

The system (4.1.9) is necessarily non-chaotic and describes slow dynamics in the vicinity of nonlinear resonance. Note also that if the original system (4.1.1) is dissipative ($\Gamma > 0$), then the averaged system (4.1.9) obviously displays dissipative behaviour too.

In that case, if $\Gamma = 0$ and $d\omega/dI$ is distinctly non-zero in the relevant range of actions/energies near the resonant one (see the criterion below or, e.g., in [35]), the integrand in the auxiliary Hamiltonian $\overline{H}$ (4.1.9) may be linearized so that the slow dynamics reduce to pendulum motion in the space of the slow variables $\tilde{I} - \tilde{\psi}$:

$$
\begin{aligned}
&\overline{H} \approx \frac{1}{2} \frac{d\omega(I_r)}{dI_r} \tilde{I}^2 + \frac{h}{2} n V_l^{(n)}(I_r)\cos(\tilde{\psi}), \\
&\tilde{I} \equiv I - I_r, \quad n\omega(I_r) \approx l\omega_f, \\
&d\omega(I_r)/dI_r \neq 0,
\end{aligned}
\tag{4.1.10}
$$

which describes the slow dynamics of conventional nonlinear resonance (NR) [5,35,59,60]. There are regions of the phase space where the slow angle is *trapped* (Fig. 19(a)), which means that the angle of the oscillator approximately follows the angle of the external periodic perturbation, slowly and weakly oscillating around it, while the action/energy slowly and weakly oscillates around the resonant action/energy. The regions of trapped $\tilde{\psi}$ are separated from regions of running $\tilde{\psi}$ by the separatrix of the *heteroclinic* topology. The maximal variation of the slow angle within the trapped region is equal to 2π while the variation of action/energy is $\propto \sqrt{h}$.

On the other hand, if the system is of the ZD type and the driving frequency is close to the extremal eigenfrequency $\omega_m \equiv \omega(I = I_m)$, then the integrand in $\overline{H}$ (4.1.9) cannot be linearized and the slow dynamics are far different from those in the pendulum-like auxiliary system (4.1.10). The asymptotic form of the auxiliary Hamiltonian $\overline{H}$ is then as follows [68] (assuming the asymptotic limits $\omega_f \to \omega_m$, $I \to I_m$ and $h \to 0$):

$$\overline{H} \approx (\omega_m - \omega_f)(I - I_m) + \frac{1}{6}\omega''_m(I - I_m)^3 + \frac{h}{2}nV_l^{(n)}(I_m)\cos(\tilde{\psi}), \qquad (4.1.11)$$
$$d\omega(I_m)/dI_m = 0, \quad \omega''_m \equiv d^2\omega(I_m)/dI_m^2.$$

The separatrix separating the regions of the trapped and running angle possesses the *homoclinic* topology (Fig. 19(b)). The maximal variation of the slow angle within the trapped region is typically $\ll 2\pi$ while the variation of action is typically $\propto h^{1/3}$, and hence is larger than in the conventional case (4.1.10). In order to distinguish this behaviour from the conventional type, it was called [67] *zero-dispersion nonlinear resonance* (ZDNR). The physical reason for its being so different from NR behaviour is as follows: the variation of action/energy in the vicinity of the extremum does not break the resonance with the external periodic driving, because $d\omega/dI \approx 0$ in the relevant range of actions/energies. Consequently, the oscillation of action/energy is typically significantly larger than in the conventional case $d\omega/dI \neq 0$ while the oscillation of angle, on the contrary, is significantly smaller.

As parameters (e.g. the frequency or amplitude of the external periodic driving) vary, the transition between ZDNR and NR occurs [68] via the global bifurcation known as *separatrix reconnection* [26,8] (Fig. 20).

A further important step was the generalization of the concept of nonlinear resonance to the (weakly) dissipative case. Though the constrained vibrations of dissipative systems had been widely studied over many years (see e.g. [1,25]), their investigation by means of the nonlinear resonance technique, including in particular the topological analysis of basins of attraction, was introduced more recently in [77,69]. Such an analysis has proved to be highly informative and important for a variety of applications [69–74,77–79].

In the dissipative case, a 2D dynamical system possesses *attractors* so that the phase space is divided into different *basins of attraction*, unlike the non-dissipative case (in which elliptic points and separatrices are relevant). At the same time, similarly to the non-dissipative case, the difference in angle between the corresponding stable and unstable points (attractor and saddle respectively) is ≈ 0 and $\approx \pi$, for ZDNR and NR respectively (cf. Figs. 21(a,b) and Figs. 21(c-e) respectively). The dissipative analogue of the ZDNR/NR transition occurs [77,69] via the global bifurcation known as *saddle connection* [80], which is illustrated in Figs. 21(b,c).

Typically, there are also other global bifurcations in the system. A detailed bifurcation analysis for one characteristic example is presented in the next sub-section (mainly following [70]). It should be noted that the global bifurcations may become particularly important if external noise is added, as indicated in [77,69,71] (see also sub-section 5.5 below). The ZDNR/NR transition also seems to play an important role in the onset of certain chaotic attractors [73,74] (see also sub-section 4.4. below).

4.2 Bifurcation analysis

Our goal will be to find and classify all the local and global bifurcations of (4.1.9) in the space of the driving force parameters (h and ω_f), keeping all other parameters fixed, including Γ. We shall illustrate our general qualitative analysis by making numerical calculations for a concrete example of a ZD system with particular types of periodic perturbation and dissipative terms. Strictly, the analysis is applicable only for small h where the averaging method is valid and (4.1.9) therefore provides an adequate approximation for (4.1.1). In order that the most interesting bifurcations of (4.1.9) should occur in this range, we must choose an example ZD system for which the variation of eigenfrequency in the range of energies between $E_{\min}$ and the extremal energy (or, equivalently, for actions between zero and the extremal action) is much less than the frequency itself. We emphasize, however, that the qualitative features of our analysis – and some of the quantitative ones too in the range of small h – remain valid even if the latter condition is not satisfied.

We choose to consider the archetypal example of a ZD system provided by the tilted Duffing oscillator (see sub-section 2.3),

$$\begin{aligned} &H_0(p,q) = \frac{p^2}{2} + U(q), \\ &U(q) = \frac{1}{2}\omega_0^2 q^2 + \frac{1}{3}\beta q^3 + \frac{1}{4}\gamma q^4, \quad \frac{9}{10} < \frac{\beta^2}{\gamma\omega_0^2} < 4, \end{aligned} \tag{4.2.1}$$

with $\omega_0 = 1$, $\beta = 5/3$, $\gamma = 1$ (cf. a similar $U(q)$ in Fig. 9(a)). The dependence of ω on I is shown in Fig. 22: it exhibits a minimum of $\omega_m = 0.805$ at $I_m = 0.187$. As required, the variation of eigenfrequency in the range $I \lesssim I_m$ is much less than the eigenfrequency itself in this range. The perturbation and the dissipative [22] terms, that we will consider are respectively

$$\begin{aligned} &V = -q\cos(\omega_f t), \\ &f_q = 0, \quad f_p = p. \end{aligned} \tag{4.2.2}$$

Thus, the original system becomes a nonlinear oscillator with cubic and quartic nonlinearities subject to a cosine driving force and a linear friction,

$$\ddot{q} + \Gamma\dot{q} + \omega_0^2 q + \beta q^2 + \gamma q^4 = h\cos(\omega_f t). \tag{4.2.3}$$

[22] A linear friction reflects the most general properties of dissipation. We comment, however, that more complicated behaviour is possible for dissipative terms of greater complexity, e.g. the coexistence of attractors, repellers and regions of conservative motion [81]. We do not consider such cases here, because they lack generality, but it would be interesting to investigate them in the future.

We shall consider w_f close to ω_m and the range of actions $I \sim I_m$ so that $n = 1$ in (4.1.7) is relevant ($l = 1$ from the definition of the perturbation V in (4.2.2)) i.e. we shall consider the nonlinear resonance of the 1st order. The equations (4.1.9) for the averaged system may then be reduced for the system (4.2.3) to the following form:

$$\dot{I} = -\frac{\partial \overline{H}}{\partial \tilde{\psi}} - \Gamma I, \quad \dot{\tilde{\psi}} = \frac{\partial \overline{H}}{\partial I}, \tag{4.2.4}$$
$$\overline{H} = \int_0^I d\tilde{I}\ (\omega(\tilde{I}) - \omega_f) - h q_1(I)\cos(\tilde{\psi}),$$

where q_1 is a modulus of the first Fourier component in the expansion (A.5) of q as a function of action and angle (note that the normalization of components in the expansion (A.5) differs by a factor of 2 from that in the expansion (4.1.5)).

4.2.1 Local bifurcation analysis

Allowing for the fact that

$$q_1(0) = 0, \tag{4.2.5}$$

the stationary points of (4.2.4) can be of the four types

$$I_{\rm st}^{(1,2)} = 0, \quad \tilde{\psi_{\rm st}}^{(1)} = \frac{\pi}{2}, \quad \tilde{\psi_{\rm st}}^{(2)} = -\frac{\pi}{2},$$
$$\tilde{\psi_{\rm st}}^{(3)} = -\arcsin\left(\frac{\Gamma I_{\rm st}^{(3)}}{h q_1(I_{\rm st}^{(3)})}\right), \quad \tilde{\psi_{\rm st}}^{(4)} = \arcsin\left(\frac{\Gamma I_{\rm st}^{(4)}}{h q_1(I_{\rm st}^{(4)})}\right) - \pi, \tag{4.2.6}$$

where $I_{\rm st}^{(3,4)}$ are determined by the equations

$$\omega(I_{\rm st}^{(3,4)}) - \omega_f = \pm h \frac{dq_1(I_{\rm st}^{(3,4)})}{dI_{\rm st}^{(3,4)}} \sqrt{1 - \left(\frac{\Gamma I_{\rm st}^{(3,4)}}{h q_1(I_{\rm st}^{(3,4)})}\right)^2}, \tag{4.2.7}$$

and the + and − correspond to $I_{\rm st}^{(3)}$ and $I_{\rm st}^{(4)}$ respectively.

The 1st and 2nd types of stationary point are unstable; the stability of the 3rd and 4th ones is determined by the condition (cf. [68])

$$\pm \left[\frac{d}{dI}\left(\omega - \omega_f \mp h \frac{dq_1}{dI}\sqrt{1 - \left(\frac{\Gamma I}{h q_1}\right)^2}\right)\right]_{I_{\rm st}} > 0, \tag{4.2.8}$$

where the + and – again correspond to $I_{\rm st}^{(3)}$ and $I_{\rm st}^{(4)}$ respectively (see Fig. 23).

Typically, the maximum (for any choice of driving force parameters) number of solutions for equations (4.2.7) is five [23], three of which are stable and two unstable.

Figs. 24(a) and 24(b) plot the bifurcation diagrams for the non-dissipative (Γ=0) and dissipative ($\Gamma \neq 0$) cases respectively. The black lines indicate the onset/disappearance of stable points. They have been obtained from the condition that the curves corresponding to the left-hand and right-hand sides of (4.2.7) touch, rather than cross, each other (cf. Fig. 23). After some manipulation, they can be written in parametric form as

$$\begin{aligned}
&\omega_f = \omega - \frac{1}{2}\frac{(dq_1/dI)(d\omega/dI)}{d^2q_1/dI^2}\left(1 \pm \sqrt{1 + \frac{2(dq_1/dI)(d^2q_1/dI^2)\Gamma^2[d(I/q_1)^2/dI]}{(d\omega/dI)^2}}\right), \\
&h = \sqrt{\left(\frac{\omega-\omega_f}{dq_1/dI}\right)^2 + \left(\frac{\Gamma I}{q_1}\right)^2}, \\
&\frac{dq_1}{dI}\frac{d^2\omega}{dI^2}(\omega-\omega_f) \gtrless 0.
\end{aligned} \tag{4.2.9}$$

Here, I plays the role of the parameter and $>$ and $<$ correspond to the full and dashed lines respectively. The analysis demonstrates (cf. Fig. 24(b)) that, for $\Gamma \neq 0$, the full line has two cusps, whereas the dashed line has only one cusp. One can derive asymptotic formulae for the positions of the cusps. Those for the full line are

$$\begin{aligned}
&\omega_f^{(1)} \approx \omega_0 - \frac{\sqrt{3}}{2}\Gamma, \quad h^{(1)} \approx \frac{2\Gamma^{3/2}}{\sqrt{3\sqrt{3}\,|[d\omega/dI]_{I=0}|}}, \\
&\omega_f^{(2)} \approx \left[\omega - \frac{(dq_1/dI)(d\omega/dI}{d^2q_1/dI^2}\right]_{I_e}, \quad h^{(2)} \approx \left[\frac{d\omega/dI}{d^2q_1/dI^2}\right]_{I_e}
\end{aligned} \tag{4.2.10}$$

where I_e is a solution of the equation

$$\frac{d\omega}{dI} = \left(\frac{dq_1/dI}{d^2q_1/dI^2}\right)\frac{d^2\omega}{dI^2}. \tag{4.2.11}$$

For the dashed line, the cusp occurs at

[23] We do not consider here the particular (in practice, rare) case where there are oscillations near the extremum or other complicated behaviour of $\omega(I)$, when the number of solutions of (4.2.7) can be larger. Such a sophisticated $\omega(I)$ is not valid for the relevant example (4.2.1) anyway.

$$\omega_f^{(3)} \approx \omega_m + \frac{1}{2^{5/3}} \left(\left[\frac{(dq_1/dI)\sqrt{|d(I/q_1)^2/dI|}}{(|d^2\omega/dI^2|)^{1/4}} \right]_{I_m} \Gamma \right)^{4/3},$$
$$h^{(3)} \approx \left[\frac{\Gamma I}{q_1} \left(1 + \frac{1}{2} \left(\frac{\omega_f^{(3)} - \omega_m}{dq_1/dI} \frac{q_1}{\Gamma I} \right)^2 \right) \right]_{I_m}. \tag{4.2.12}$$

There is a separation $\Delta\omega, \Delta h$ between the full line and the cusp of the dashed line, as shown by the inset of Fig. 24 (b),

$$\Delta\omega \sim \omega_f^{(3)} - \omega_m \propto \Gamma^{4/3},$$
$$\Delta h \sim \frac{(\Delta\omega)^2}{\Gamma} \left[\frac{q_1}{I(dq_1/dI)^2} \right]_{I_m} \propto \Gamma^{5/3}. \tag{4.2.13}$$

This separation tends to zero as $\Gamma \to 0$ (cf. Fig. 24(a)).

Within the region bounded by the full line (except *very* close to its right and left cusps), point S1 in Fig. 2 is well separated in action from S2 and S3. The responses corresponding to S2 and S3 are always strongly nonlinear. The response corresponding to S1 is linear in the region far below the upper part of the full line, although it becomes nonlinear as the line is approached. However, it remains significantly smaller than S2/S3 and, in order to distinguish S1 from S2/S3, we shall refer to it as "linear" within the whole area within the full line.

The full line of Fig. 24 bounds the region within which both the linear, and one or both of the nonlinear, responses can exist: the upper part marks the boundary of linear response; and the lower part that of the nonlinear ones. The area between the upper and lower parts of the dashed line is the region where both nonlinear responses coexist. Note that, for Γ=0, the lower part of the dashed line merges into the part of the abscissa axis lying to the right of ω_m, while part of the full line merges into the segment of abscissa axis lying between ω_m and ω_0.

We now carry out a global bifurcation analysis, treating the non-dissipative and dissipative cases separately in Secs. 4.2.2 and 4.2.3 respectively.

4.2.2 Global bifurcation analysis for the non-dissipative case

In the non-dissipative case, equations (4.2.4) are purely Hamiltonian, so that the quasi-energy $\overline{H}$ is conserved. Consequently, trajectories in the vicinity of stable points are closed (elliptic) orbits. Such regions are separated from each other, or from regions with open trajectories, by separatrices that include unstable fixed points.

Figure 25 shows an example of how the phase space evolves with increase of the driving force frequency. One can see the consequences of two global bifurcations: the topology of the separatrices changes between (a) and (b), and again between (b) and (c). These bifurcations are of the *separatrix reconnection* type [8]. The first one, which results from a reconnection of the separatrices passing through the unstable fixed points marked [24] as g and o, respectively, is the ZDNR/NR transition [68]: Fig. 25(a) represents the ZDNR stage, and Fig. 25(b) the NR one. This transition is indicated by the full green line on the bifurcation diagram, Fig. 24(a). The second bifurcation, between Figs. 25(b) and 25(c), results from a reconnection of the separatrices passing through the points marked as g and o respectively. It is indicated by the yellow line in Fig. 24(a). Yet another possible reconnection may occur between the separatrices passing through the points marked as g and y respectively. It is indicated by the brown line in Fig. 24(a).

These three types of separatrix reconnection exhaust all possible types in the present case: the maximum number of reconnections is equal to [25]

$$n_{\max}^{(\mathrm{nondis})} = C_3^2 \equiv 3, \tag{4.2.14}$$

using[82] the binomial coefficient $C_j^i = \frac{j!}{i!(j-i)!}$.

4.2.3 Global bifurcation analysis for the dissipative case

In the dissipative case, the stable points are true attractors. Consequently, we have boundaries of basins of attraction (see Fig. 26) in place of the separatrices of the non-dissipative case. These boundaries include unstable fixed points (either saddles or similar, but non-hyperbolic, points). Correspondingly, the separatrix reconnection of the non-dissipative case is exchanged for the more general *heteroclinic orbit* [80], connecting unstable points.

It follows from the analysis of sub-section 4.2.1 (see eqs.(4.2.6)–(4.2.8) and footnote 23) that the maximum number of unstable fixed points is equal to 4. Note, however, that as in the non-dissipative case, the two unstable points with I=0 (see (4.2.6)) are always connected to each other and, moreover, that the direction of their connection is always the same. Thus, in the classification of heteroclinic orbits they should be considered a single unit. Note also that, unlike a separatrix reconnection, a heteroclinic orbit is characterised both by a pair of connected points and by the direction of the connection. Thus, the maximum number of different types of heteroclinic orbit in the system is

$$n_{\max}^{(\mathrm{dis})} = 2 \times C_3^2 \equiv 6. \tag{4.2.15}$$

[24] In the original paper [70], on which the present sub-section is based, the unstable points were marked in the corresponding figure by different colours. Here, being restricted financially, we present the figure in black-and-white, using instead of the green, orange and yellow colours the markers g, o and y respectively.

[25] Although there are formally 4 types of unstable fixed point, the lower index of the binomial coefficient in (4.2.15) is taken as 3 because both types of points marked as y ($I = 0$, $\tilde{\psi} = \pm\pi/2$) are always connected by a separatrix and cannot be reconnected with other unstable points independently of each other.

Using the notation o, g respectively for the unstable fixed points corresponding to U1, U2 in Fig. 23 (which are indicated in Fig. 26 by orange and green dots respectively), y for points with I=0 (yellow dots in Fig. 26), and indicating the direction of a connection with an arrow, the set of possible heteroclinic orbits can be classified [26] as

$$\begin{array}{ll} (1)\, o \to g; & (2)\, g \to o; \\ (3)\, o \to y; & (4)\, y \to o; \\ (5)\, g \to y; & (6)\, y \to g. \end{array} \tag{4.2.16}$$

We now discuss each of them separately –

(1) $o \to g$ corresponds to the ZDNR/NR transition [77,69,71], analogous to the corresponding transition in the non-dissipative case. This bifurcation is indicated by the full green line in the bifurcation diagram Fig. 24(b).

(2) $g \to o$ corresponds to the bifurcation between configurations where the basin of attraction of one of the nonlinear resonances encompasses the other one, or where it passes around it [77,69,71]. This type of bifurcation is indicated by the orange lines in Fig. 24(b) [27] . It has no analogue in the non-dissipative case.

(3) $o \to y$ corresponds to the jump by 2π of the end of the trajectory emerging from the orange saddle, i.e. the jump between adjacent linear response attractors: see e.g. Figs. 26(a) and (b). This type of bifurcation is indicated by red lines in Fig. 24(b). It has no analogue in the non-dissipative case.

(4) $y \to o$ corresponds to the change between the boundary including the orange saddle (Fig. 26) encompassing either the nonlinear attractor(s) or linear attractor: see e.g. the change between Figs. 26(b) and 26(c). This type of bifurcation is indicated by the yellow line in Fig. 24(b). The analogous bifurcation for the non-dissipative case is shown by the yellow line in Fig. 24(a).

(5) $g \to y$ corresponds to the jump by 2π of the end of the trajectory emerging from the green saddle. The trajectory can end *either* in a linear response attractor, if the latter exists and if the trajectory is not trapped by the nonlinear response attractor (full blue lines in the bifurcation diagram Fig. 24(b)), *or* in a nonlinear one when linear response is encompassed by a red boundary (cf. Fig. 26(c)), or does not exist at all (dashed blue lines) [28] . This type of bifurcation has no analogue in the non-dissipative case.

(6) $y \to g$ is analogous to $y \to o$. It is indicated in Fig. 24(b) by the brown line which starts where the ZDNR/NR line crosses the yellow line. Its non-dissipative analogue is shown by the brown line in Fig. 24(a).

Points where global bifurcation lines intersect or meet each other correspond to more complicated connections. These and other interesting features of the diagram (e.g. the

[26] We should note that the *o, g* points are saddles while the y points are non-hyperbolic unstable fixed points.

[27] For small enough Γ, there will be additional orange lines in the ZDNR region, i.e. above the full green line, but below the upper parts of the dashed and full black lines.

[28] For small enough Γ, additional blue lines can exist above the green and brown lines, but below the upper part of the dashed black line.

yellow staircase) would be interesting to study in the future in more detail.

4.2.4 Discussion

We now discuss the characteristic differences between the bifurcation diagrams of ZD systems, and those of the conventionally considered kind of system in which there is no extremum in the variation of eigenfrequency with energy or, equivalently, action. We also consider the physical consequences that may be expected to result from the bifurcations of the averaged system discussed above.

It is immediately evident that a system with an extremum in $\omega(I)$ is much richer in terms of bifurcations than a system without one. In fact, the only global bifurcation in the standard system with monotonic $\omega(I)$ is the one corresponding to the yellow lines of Fig. 24 (cf. [83]). Most features of the local bifurcation lines (the cusps, separatrices, etc) are peculiar to the system with an extremum – the exception being the cusp near $\omega_0 \equiv \omega(0)$, which also exists for systems with monotonic $\omega(I)$.

We now consider the physical significance of the various bifurcations.

Local bifurcations are important because they correspond to the onset/disappearance of the different regimes of oscillation and, unlike the case of monotonic $\omega(I)$, three rather than two regimes are typically possible. The overlap of resonances of different order leads to the onset of global chaos in the non-dissipative case [5] (see also sub-section 4.3 below) and may lead to the onset of chaotic attractors in the dissipative case [72–74] (see also sub-section 4.4 below).

Global bifurcations in the absence of dissipation have two main effects. On the one hand, they change certain topological properties of the slow dynamics (an example of such changes in the Poincaré section is shown in Fig. 27); and, on the other hand, they result in changes in the structure of the chaotic layers associated with nonlinear resonances (cf. [75,71] as well as sub-section 4.3.1 below) and facilitate chaotic transport (cf. [76] as well as subsection 4.3.2 below).

Global bifurcations in the presence of dissipation may play some role in the onset of chaotic attractors [73,74] (see also sub-section 4.4 below). They also play an important role in the case when the system is additionally driven by a weak noise [29]. Indeed, if the noise is weak, then fluctuational transitions occur with overwhelming probability via unstable fixed points (see e.g. [2–4] as well as sub-section 5.4 below). Thus their connections should influence profoundly the fluctuational transitions between attractors of the dynamical system. Those that occur via yellow points (Fig. 26), however, result only in a change of the angle by 2π which is usually not observable in physical systems [30]. In

[29] Given that noise in real systems is always associated with dissipation, only the dissipative (rather than the non-dissipative) case is relevant to the problem of fluctuations.

[30] There are, however, circumstances in which these transitions could be both observable and important. For example, phase slips of this kind represent highly undesirable events in voltage standards based on SQUIDs, and in memory cells [15], so that it is important to understand their probability.

relation to fluctuational transitions, therefore, the most important global bifurcations are those that do not involve the yellow points, i.e. the ZDNR/NR transition ($o \to g$) and the encompassing/passing-around transition ($g \to o$). Of these two, the ZDNR/NR transition is of particular interest: first because the most pronounced change in fluctuational transition rates is to be expected; and, secondly, because the associated repopulation of the nonlinear resonances for small h gives rise to dramatic characteristic changes in the fluctuation spectra [77,71] (see also sub-section 5.5 below).

Given the importance of the ZDNR/NR transition, we present below the asymptotic formula for the frequency $\omega_f^{(tr)} \equiv \omega_f^{(tr)}(h)$ at which the transition occurs [69] (valid both for the dissipative and non-dissipative cases, beyond the close vicinity of the cusp):

$$\omega_f^{(tr)} = \omega_m + \mathrm{sgn}(\omega_m'')(|\omega_m''|/2)^{\frac{1}{3}} \left[\frac{3}{2} h q_1(I_m)\{(1-\eta^2)^{\frac{1}{2}} - \eta(\frac{\pi}{2} - \arcsin(\eta))\}\right]^{\frac{2}{3}}, \quad (4.2.17)$$

$$\eta \equiv \frac{\Gamma I_m}{h q_1(I_m)} < 1, \quad \left[\frac{\Gamma}{|\omega_m''| I_m^2}\right]^{\frac{2}{3}} \ll \left[\frac{\omega_f^{(tr)} - \omega_m}{\omega_m'' I_m^2}\right]^{\frac{1}{2}} \ll 1.$$

4.3 Chaos in the absence of dissipation

Describing in the previous sub-sections of Sec. 4 the slow dynamics of the periodically driven system, we neglected fast-oscillating terms in dynamical equations for action I and for the shift of the angle from the angle of the periodic driving, $\tilde{\psi}$. Provided the periodic driving (perturbation) is weak, such neglect is justified throughout the major part of the phase space: the fast-oscillating terms have only a slight effect on the motion [41]. However in the absence of dissipation, there are necessarily regions in the phase space where the influence of the fast-oscillating terms is inherently important, however weak the periodic perturbation is: the thin layers around the separatrices of the slow dynamics are necessarily chaotic [5,35,60]: it is called *local chaos* [5,35,60]. The width and some other features of the layer are described by the corresponding *separatrix map*. However, the separatrix maps for conventional NR [5,35,60] and ZDNR [75,71] are quite different. Correspondingly, the widths of the layers and their structure on the whole are different as well. Some initial analytic and numerical study of local chaos in ZDNR has been reported [75,71] and is described below in sub-section 4.3.1.

If the amplitude of the perturbation grows the width of the layers grows as well and, at some stage, different layers merge, which typically marks the onset of *global chaos* [5,35,60], characterized by a chaotic motion within a large region of the phase space. However the onset of global chaos in ZD systems has distinct differences [75,71,76] from this scenario, which are described below in sub-section 4.3.2.

4.3.1 Local chaos in ZDNR

We shall derive the separatrix maps for ZDNR by following the same scheme as was used in [35] for the case of the conventional NR. For the sake of brevity and clarity, we shall

assume some simplification for the periodic perturbation. Namely, we shall consider the case when $\tilde{V}$ in (4.1.5) has only the term corresponding to $l = n = 1$. Moreover, we shall assume that $V_1^{(1)}$ does not depend on I. In fact, these simplifications are often still valid in a more general case (at least if one considers the 1st-order resonance, i.e. the range of I where (4.1.7) holds for $l = n = 1$). As for other cases, the results can readily be generalized and, at the end of the present sub-section, we shall outline how this may be done.

So, let us now consider the perturbed Hamiltonian (cf. (4.1.5))

$$H = \tilde{H}_0(I) + hV_1^{(1)}\cos(\psi + \beta_1)\cos(\omega_f t + \alpha_1), \tag{4.3.1}$$

where $\tilde{H}_0(I)$ is a Hamiltonian of some ZD system, i.e. the eigenfrequency $\omega(I) \equiv \partial\tilde{H}_0/\partial I$ possesses a maximum or a minimum at some action I_m.

The dynamics of the action I and slow angle (4.1.8) (note that $l = n = 1$ in our case) are also Hamiltonian:

$$\begin{aligned}
\dot{I} &= -\frac{\partial(\overline{H} + V)}{\partial\tilde{\psi}}, \\
\dot{\tilde{\psi}} &= \frac{\partial(\overline{H} + V)}{\partial I}, \\
\overline{H} &= \int_0^I d\tilde{I}\ (\omega(\tilde{I}) - \omega_f) + \frac{h}{2}V_1^{(1)}\cos(\tilde{\psi}), \\
V &= \frac{1}{2}hV_1^{(1)}\cos(\tilde{\psi} + 2\omega_f t + 2\alpha_1).
\end{aligned} \tag{4.3.2}$$

It should be emphasized that, unlike (4.1.9) (where averaging was used), the Hamiltonian $\overline{H} + V$ (4.3.2) is strictly equivalent to (4.3.1).

Let us consider the dynamics of the averaged energy $\overline{E} \equiv \overline{H}$,

$$\dot{\overline{E}} = [\overline{H}, (\overline{H} + V)] = [\overline{H}, V] = -\frac{\partial\overline{H}}{\partial I}\frac{\partial V}{\partial\tilde{\psi}}. \tag{4.3.3}$$

The brackets [...] imply Poisson brackets [1], and $\tilde{\psi}$, I are respectively the generalized coordinate and momentum for the system (4.3.2).

Let us consider the motion near one of the separatrices related to the averaged Hamiltonian $\overline{H}(I, \tilde{\psi})$ (4.3.2). Typical "unperturbed" (i.e. at $V = 0$) trajectories are shown in Fig. 19(b). Apart from the separatrix itself, there are three different types of such unperturbed trajectory: (i) trajectories *inside* any of the loops of the separatrix; (ii) those *outside* the loops, passing the part of the separatrix connecting saddles on the side *opposite* to the

loops (in the case shown in Fig. 19(b), such trajectories pass *below* the loops); and (iii) those *outside* the loops, passing the part of the separatrix connecting saddles on the *same* side as the loops (in the case shown in Fig. 19(b), such trajectories pass *above* the loops). The most important feature of such trajectories in the present context is that the system remains near the saddles for most of time , where $\partial\overline{H}/\partial I = 0$ by definition. Characteristic examples of the dependence of $\partial\overline{H}/\partial I$ on time along a *perturbed* trajectory are shown in Fig. 28. Such a dependence consists of a succession of relatively short pulses between which $\partial\overline{H}/\partial I$ rests nearly at zero. The pulses repeat each other and the corresponding pulses on the "unperturbed" trajectories nearly identically [31] . The duration of each pulse, T_p, is of the order of the period of eigenoscillation in the local minimum of the averaged Hamiltonian $\overline{H}(I, \tilde{\psi})$,

$$T_p \sim \tilde{\omega}_0^{-1}, \qquad (4.3.4)$$
$$\tilde{\omega}_0 \equiv \sqrt{hV_1^{(1)}\sqrt{\omega_m''(\omega_f - \omega_m)/2}}.$$

The intervals between successive pulses are much longer than their duration, and depend strongly on the "energy" $\overline{E}$, which almost does not change during the intervals between pulses: it follows from (4.3.3) that the major change of $\overline{E}$ occurs during a pulse of $\partial\overline{H}/\partial I$. As $\overline{E}$ approaches its value on the separatrix, which is equal in the case of $\overline{H}$ to

$$\overline{E}_s = \int_0^{I_r} d\tilde{I}\ (\omega(\tilde{I}) - \omega_f) \pm \frac{h}{2} V_1^{(1)} \cos(\tilde{\psi}), \qquad \omega(I_r) \equiv \omega_f, \qquad (4.3.5)$$

then the interval between the pulses on the unperturbed trajectory (i.e. at $V = 0$ in (4.3.2)) diverges, being described by the asymptotic formula [32]

$$T_{\rm int} \equiv T_{\rm int}(|\overline{E} - \overline{E}_s|) \approx (\pi\tilde{\omega}_0)^{-1} \ln\left(\frac{hV_1^{(1)}}{|\overline{E} - \overline{E}_s|}\right), \qquad (4.3.6)$$
$$|\overline{E} - \overline{E}_s|/(hV_1^{(1)}) \ll 1.$$

Let us now turn namely to the construction of the separatrix map. With this aim, we shall transform from the description of the system in terms of $I - \tilde{\psi}$ to the equivalent description in terms of "energy" $\overline{E}$ and time t. Let us characterize the dynamics by a series of pairs of these quantities $(\overline{E}_k, t_k)$ chosen just before pulses of $\partial\overline{H}/\partial I$ and enumerated in increasing time: see Fig. 28. The map relating each pair to the previous one is different for different regions in the vicinity of the separatrix.

[31] In the case of motion similar to type (iii) described above, two different types of the pulse alternate: cf. Fig. 28(c).

[32] In the range of non-small $|\overline{E} - \overline{E}_s|/(hV_1^{(1)})$, the dependence of $T_{\rm int}$ on $\overline{E}$ is different for the different types of trajectory described above. The dependences reduce to the same asymptote, however, as $\overline{E} \to \overline{E}_s$.

1. For the trajectories inside or below [33] the loop (Figs. 28(a) and 28(b) respectively),

$$\begin{aligned} \overline{E}_{k+1} &\approx \overline{E}_k + \Delta\overline{E}_k^{(1,2)}, \\ t_{k+1} &\approx t_k + T_{\rm int}|_{\overline{E}=\overline{E}_{k+1}}\,, \end{aligned} \tag{4.3.7}$$

where

$$\Delta\overline{E}_k^{(1,2)} = -\int_{t_k}^{t_k+\Delta t} dt\, \left(\frac{\partial\overline{H}}{\partial I}\right)^{(1,2)} \left(\frac{\partial V}{\partial\tilde{\psi}}\right)^{(1,2)}, \tag{4.3.8}$$

and the superscripts $^{(1)}$ and $^{(2)}$ relate to the trajectories respectively inside and below the loops, while Δt is chosen so that

$$T_p \le \Delta t \le T_{\rm int}|_{\overline{E}=\overline{E}_{k+1}}\,. \tag{4.3.9}$$

$\Delta\overline{E}_k$ is almost independent of Δt within the range (4.3.9). The dependence on $\overline{E}_k$ is also very weak, so that it may be calculated approximately along the corresponding piece of separatrix: along the loop, for the trajectories inside the loop; and along the section connecting adjacent saddles, for the trajectories below the loops. We now substitute V (4.3.2) into (4.3.8), allow for the fact that, on the separatrix, $\partial\overline{H}/\partial I$ and $\tilde{\psi}$ are respectively even and odd functions of $t-(t_k+T_p/2)$ [34] (see Figs. 28(a,b)), and introduce the auxiliary variable

$$\varphi_k \equiv 2\omega_f(t_k + T_p/2) + 2\alpha_1 \tag{4.3.10}$$

(which represents twice the angle of the perturbation taken at the instant when the pulse of $\partial\overline{H}/\partial I$ passes its centre). We thus obtain

$$\begin{aligned} \Delta\overline{E}_k^{(1,2)} &= \Delta\overline{E}_s^{(1,2)}\sin(\varphi_k), \\ \Delta\overline{E}_s^{(1,2)} &= \frac{h}{2}V_1^{(1)}\int_{-\infty}^{\infty} dt\, \left(\frac{\partial\overline{H}}{\partial I}\right)_s^{(1,2)} \cos(\tilde{\psi}_s^{(1,2)}(t) + 2\omega_f t), \end{aligned} \tag{4.3.11}$$

where the s subscript means that all dynamical functions are to be evaluated on the separatrix, while the zero of t is chosen so that it marks the centre of the corresponding pulse of $\partial\overline{H}/\partial I$ which implies, in particular, that $\tilde{\psi}_s(0) = 0$ or $\tilde{\psi}_s(0) = \pi$, for the superscript $^{(1)}$ or $^{(2)}$ respectively. Given that the characteristic time-scale of the pulse $T_p \sim \tilde{\omega}_0^{-1} \gg \omega_f^{-1}$, the quantities $\Delta\overline{E}_s^{(1,2)}$ are exponentially small, i.e. $\propto \exp(-a\omega_f/\tilde{\omega}_0)$ where a is some positive number ~ 1 (cf. the case of the chaotic layer for the pendulum [5,35,60]). The explicit expressions have not so far been found.

[33] Here and in the rest of sub-section 4.3.1, we shall refer for the sake of clarity just to the separatrix shown in Fig. 19(b), in which the loops are directed "up"; correspondingly, the types of trajectory referred to above as "(ii)" or "(iii)" will be described for the sake of brevity as being *below* or *above* the loops respectively.

[34] The instant $t-(t_k+T_p/2)$ relates to the centre of the corresponding pulse $\partial\overline{H}/\partial I(t)$ and, at the same time, to $\tilde{\psi}$ being equal to either 0 or π, depending on the type of separatrix and on the relevant bit of the separatrix (cf. Fig. 19(b)).

Using also the asymptotic expression (4.3.6) for $T_{\rm int}$, we derive the final representation of the ZDNR separatrix map for trajectories either inside or below any of the separatrix loops, they are distinguished below by means of the superscripts, (1) and (2) respectively:

$$\overline{E}_{k+1}^{(1,2)} = \overline{E}_k^{(1,2)} + \Delta\overline{E}_s^{(1,2)} \sin(\varphi_k^{(1,2)}),$$
$$\varphi_{k+1}^{(1,2)} = \varphi_k^{(1,2)} + A \ln\left(\frac{B}{\left|\overline{E}_k^{(1,2)} - \overline{E}_s + \Delta\overline{E}_s^{(1,2)} \sin(\varphi_k^{(1,2)})\right|}\right), \tag{4.3.12}$$
$$A = \frac{2\omega_f}{\pi\tilde{\omega}_0}, \qquad B = hV_1^{(1)}.$$

The general form of these maps coincides with the conventional separatrix map [5,35,60]. The difference lies only in the coefficients $\Delta\overline{E}_s^{(1,2)}$, A, B. It is well known [5,35,60] that, if $|\overline{E} - \overline{E}_s|$ is large enough, then all iterations of the map are rather regular. But if $\overline{E}$ lies within a layer around $\overline{E}_s$ of width $\sim \Delta\overline{E}_s^{(1,2)}$ then the motion becomes chaotic i.e. $(\overline{E}_k, \varphi_k)$ change from one iteration to the next in a seemingly random manner.

2. For the trajectories above the loop, the two different shapes of pulses of $\partial\overline{H}/\partial I$ alternate (Fig. 28(c)). Correspondingly, it is convenient to consider two series, $(\overline{E}_k^{(1)}, \varphi_k^{(1)})$ and $(\overline{E}_k^{(2)}, \varphi_k^{(2)})$, relating to the different types of pulses. In order to obtain a closed map for each of the series, one should make two iterations, unlike the case of trajectories inside or below the loops (where just one iteration was enough). As a result, one obtains the following maps for $(\overline{E}_k^{(1,2)}, \varphi_k^{(1,2)})$.

$$\overline{E}_{k+1}^{(1,2)} = \overline{E}_k^{(1,2)} + \Delta\overline{E}_s^{(1,2)} \sin(\varphi_k^{(1,2)}) + \Delta\overline{E}_s^{(2,1)} \sin\left(\varphi_k^{(1,2)} + A \ln\left(\frac{B}{\left|\overline{E}_k^{(1,2)} - \overline{E}_{sep} + \Delta\overline{E}_s^{(1,2)} \sin(\varphi_k^{(1,2)})\right|}\right)\right), \tag{4.3.13}$$
$$\varphi_{k+1}^{(1,2)} = \varphi_k^{(1,2)} + A \ln\left(\frac{B^2}{\left|\overline{E}_k^{(1,2)} - \overline{E}_s + \Delta\overline{E}_s^{(1,2)} \sin(\varphi_k)\right| \left|\overline{E}_{k+1}^{(1,2)} - \overline{E}_s\right|}\right).$$

Though these maps are more complicated than the maps (4.3.12), their major qualitative feature, namely chaos in a thin layer near the separatrix, is similar: the series $(\overline{E}_k^{(1,2)}, \varphi_k^{(1,2)})$ change in a random-like fashion if $\overline{E}$ deviates from $\overline{E}_s$ for values smaller than some critical value $\sim \max(\Delta\overline{E}_s^{(1)}, \Delta\overline{E}_s^{(2)})$.

It is obvious that the derivation of the separatrix maps (4.3.12), (4.3.13) for the system (4.3.1) can be easily generalized for a more general perturbation. Indeed, the perturbation's independence of I is not fundamental: if $V_1^{(1)}$ depends on I, the corrections to the maps can be shown to be typically exponentially smaller than principal terms. For a perturbation that has more than one harmonic, a situation can arise such that the term which makes the major contribution to the slow dynamics, and the term playing the major role

in the formation of the chaotic layer, are not the same. To obtain the correct map, one should keep in the non-resonant perturbation V the term of smallest possible frequency since other terms result only in exponentially smaller contributions: cf. the estimation of $\Delta\overline{E}_s^{(1,2)}(\omega_f)$ above. For example, if the original perturbation (i.e. the perturbation in (4.3.1)) had also a 2nd harmonic, $hV_1^{(2)}(I)\cos(2\psi+\beta_2)\cos(\omega_f t+\alpha_1)$, then the perturbation in the representation (4.3.2) would have in particular a term $\propto \cos(2\tilde{\psi}+\omega_f t)$. The frequency of oscillation of this term is less than half that of the term $\propto V_1^{(1)}$ (cf. (4.3.2)), and hence its effect on the formation of the chaotic layer would be exponentially larger.

We emphasize at the same time that the general forms of the ZDNR separatrix maps (i.e. (4.3.13) and two first lines in (4.3.12)) are the same for all types of perturbation; only the coefficients (i.e. A, B, $\Delta\overline{E}_s^{(1,2)}$) depend on the detailed form of the perturbation.

Thus, we may conclude from this sub-section that, though there is much in common in the origins of the local chaos in ZDNR and NR, the chaotic layers are very different: the dependences of their widths on the parameters of perturbation are significantly different in the cases of NR and ZDNR. Unlike the conventional (NR) case, the layers in ZDNR are strongly asymmetric, and probably strongly inhomogeneous, because their different parts are described by different maps. It would be interesting to study them in detail, both analytically and numerically.

Some very preliminary studies of the chaotic layers associated with ZDNR were reported in [75,71]. Numerical studies of local chaos in nonmonotonic twist maps are described in [8–10,64–66].

4.3.2 Global chaos

Global chaos, i.e. chaos throughout a large region of the phase space, is conventionally taken to occur when at least two nonlinear resonances overlap in energy: this is the essence of the celebrated empirical Chirikov resonance-overlap criterion [5,35,60]. However, global chaos may arise differently in ZD systems: if the resonances are of the same order, then neither their overlap in energy, nor even their overlap in phase space, need necessarily result in the onset of global chaos; rather, the overlap in phase space results in reconnection of the thin chaotic layers associated with the resonances while, as the amplitude of the periodic perturbation grows further, the layers separate again but with a different topology: cf. Fig. 29(a).

For global chaos to occur in a ZD system, nonlinear resonances of *different* order should overlap (in energy), which typically requires a much stronger perturbation than for the overlap of resonances of the same order: cf. Fig. 29(a) and Fig. 29(b).

On the other hand, it can happen in a ZD system that the overlap in energy between different-order resonances, and the overlap in the phase space between resonances of the same order, are *combined* resulting in the onset of global chaos, either in a very pronounced form, or at unusually small amplitudes of perturbation. We demonstrate this in detail for a system with *more than one separatrix*, since the effect is at its most pronounced in

precisely such systems. Moreover, if the system is periodic, then the effect provides a drastic increase of the accessible energy range in unbounded chaotic transport.

Our presentation mostly follows the work [76]. So, as an example of a Hamiltonian system possessing more than one separatrix, consider (2.2.5)-(2.2.6) with $\Phi < 1$ (Fig. 5(a)), which describes e.g. a 2D electron gas in a one-dimensional periodic magnetic field [20,21] (see also sub-section 2.2 above). The separatrices in the momentum-coordinate plane are shown in Fig. 30: they correspond to motion with energies equal to the corresponding barrier heights. The eigenfrequency possesses a local maximum ($\omega_m \approx 0.43$) as a function of energy/action: see Fig. 5(c). If, additionally, a periodic electric force is applied in the same direction as that in which the magnetic field is periodic, then the system is equivalent to a Hamiltonian one with an additive time-periodic perturbation,

$$\begin{aligned} &\dot{p} = -\frac{\partial(H+V)}{\partial q}, \qquad \dot{q} = \frac{\partial(H+V)}{\partial p}, \\ &H = p^2/2 + (\Phi - \sin(q))^2/2, \qquad \Phi = 0.2, \\ &V = -hq\cos(\omega_f t). \end{aligned} \tag{4.3.14}$$

Let us first consider the evolution of chaos as h grows while ω_f remains fixed at some arbitrarily chosen value beyond the immediate vicinity of ω_m and its harmonics. It is well illustrated by Fig. 31. At small h, there are two thin chaotic layers, around the inner and outer separatrices of the undriven system. Note that unbounded chaotic transport takes place only in the outer chaotic layer i.e. in a *narrow* energy range. As h grows, so also do the layers until, at some (typically non-small) critical value $h_{gc} \equiv h_{gc}(\omega_f)$, they merge. This event may be considered as the onset of global chaos: the whole range of energies between the barriers heights then becomes involved in unbounded chaotic transport. Note that the states $\{I^{(l)}\} \equiv \{p = 0, q = \pi/2 + 2\pi l\}$ and $\{O^{(l)}\} \equiv \{p = 0, q = -\pi/2 + 2\pi l\}$ (where $l = 0, \pm 1, \pm 2, ...$) in the stroboscopic (for instants $n2\pi/\omega_f$ with $n = 0, 1, 2, ...$) Poincaré section are associated respectively with the inner and outer saddles of the undriven system, and necessarily belong to the inner and outer chaotic layers respectively. Thus, the necessary and sufficient condition for global chaos to arise in our system may be formulated e.g. as the possibility of the system placed initially in the state $\{I^{(0)}\}$ passing beyond the neighbouring "outer" states, $\{O^{(0)}\}$ and $\{O^{(1)}\}$, i.e. the possibility of $q(t \gg 2\pi/\omega_f)$ becoming smaller than $-\pi/2$ or larger than $3\pi/2$.

A diagram in the $h - \omega_f$ plane, based on the above criterion, is shown in Fig. 32. The lower boundary of the shaded area represents the function $h_{gc}(\omega_f)$. It has deep cusp-like minima (*spikes*) at frequencies $\omega_f = \omega_s^{(n)}$ that are slightly less than the odd multiples of ω_m,

$$\omega_s^{(n)} \approx \omega_m(2n-1), \qquad n = 1, 2, ... \tag{4.3.15}$$

The deepest minimum occurs at $\omega_s^{(1)} \approx \omega_m$: $h_{gc}(\omega_s^{(1)})$ is approximately 40 times smaller than in the neighbouring pronounced local maximum of $h_{gc}(\omega_f)$ at $\omega_f \approx 1$. As n increases, the corresponding minimum becomes less deep. The origin of the spikes becomes obvious from the analysis of the evolution of the Poincaré section as h grows while $\omega_f \approx \omega_s^{(1)}$. For

$h = 0.001$, one can see in Fig. 33(a) four chaotic trajectories: those associated with the inner and outer separatrices of the undriven system [5,35,60] are coloured green and blue respectively, while the trajectories associated with the nonlinear resonances of the 1st order [5,35,60] (cf. sub-section 4.3.1) are indicated [35] by red and cyan (the corresponding attractors are indicated respectively by crosses of the same colours). Examples of non-chaotic (often called KAM [5,35,60]) trajectories separating the chaotic ones are shown in brown. As h increases to $h = 0.003$ (Fig. 33(b)), the blue and red chaotic trajectories merge: the resulting trajectory is shown in blue. As h increases further (see Fig. 33(c), where $h = 0.00475$), the latter trajectory merges with the cyan chaotic trajectory (the resulting trajectory is shown by blue) and, finally, as h increases slightly more (see Fig. 33(d), where $h = 0.0055$), the latter trajectory merges with the green trajectory [36], so that the inner well becomes involved in unbounded chaotic transport, thereby marking the onset of global chaos in our system, as defined above.

The chaotic character of motion on the trajectory associated with the separatrix of the undriven system can be considered [60] to be a consequence of the overlap of high-order resonances (in the case shown in Fig. 33(a), the relevant orders are 3, 5, 7, ...). The scenario described above for the onset of global chaos therefore corresponds exactly to the *combination* of an overlap between resonances of different orders (1, 3, 5, ...) and an overlap between resonances of the same (1st) order. The latter overlap is also illustrated by Fig. 34 showing the evolution of the separatrices of the 1st-order resonances calculated in the resonance approximation (cf. sub-sections 4.1, 4.2).

Near the spikes, the function $h_{gc}(\omega_f)$ may be quite well approximated using the resonance approximation. The explicit asymptotic (for $\Phi \to 0$) formulae for the minima themselves, in the lowest order of the parameters of smallness, are as follows:

$$\omega_s^{(n)} \approx (2n-1)\omega_m \approx \frac{(2n-1)\pi}{2\ln(\frac{8}{\Phi})}, \qquad n = 1, 2, ..., \qquad \Phi \ll 1, \tag{4.3.16}$$

$$h_{gc}(\omega_s^{(n)}) \approx \frac{(2n-1)}{24}\Phi^3 \ln(\frac{8}{\Phi}), \qquad n = 1, 2, ..., \qquad 2n-1 \ll \ln(\frac{8}{\Phi}). \tag{4.3.17}$$

The values of $\omega_s^{(n)}$ obtained from simulations at $\Phi = 0.2$ (see Fig. 32) are in a good agreement with the formula (4.3.16). As concerns the values of $h_{gc}(\omega_s^{(n)})$, the value $\Phi = 0.2$ is too large for Eq. (4.3.17) to be valid but, even so, Eq. (4.3.17) provides the correct order of magnitude for $h_{gc}(\omega_s^{(1)})$ and $h_{gc}(\omega_s^{(2)})$ (see Fig. 32). More accurate numerical calculations within the resonance approximation yield the value $h_{gc}(\omega_s^{(1)}) \approx 0.005$, which practically coincides with the value measured in simulations.

It is worth mentioning two examples of physical applications

[35] The chaotic layers associated with nonlinear resonances are extremely narrow at the given parameters, so that their width is much less than the diameters of dots indicating the trajectories in the figure.

[36] In the figure, we still use two colours for the different parts of this trajectory in order to demonstrate that their mixing occurs very slowly, which indicates that the given h is just slightly above the critical value h_{gc}.

(1) The jump-wise increases of the range of energies involved in the unbounded chaotic transport of electric charge carriers in a magnetic superlattice result in jump-wise increases of the *dc conductivity* [20].
(2) A significant decrease of the *activation energy* for noise-induced multi-barrier escape in the presence of periodic driving is associated with the onset of the possibility of *noise-free* transport from the lower barrier to beyond the upper barrier (cf. [119] and sub-sections 5.3.2,5.3.3 above).

There are two immediate generalizations:

(1) The absence of pronounced spikes at the *even* harmonics (i.e. at $2n\omega_m$) in the case considered above is explained by the fact that $q_{2n} = 0$ due to the symmetry of the potential (2.2.6) and, correspondingly, that there are no resonances of even order; for a non-symmetric potential, even-order resonances do exist so that spikes in $h_{gc}(\omega_f)$ at $\omega_f \approx 2n\omega_m$ exist also.
(2) If the time-periodic driving is multiplicative rather than additive, then the resonances become *parametric* (cf. [1]). Parametric resonance is more complicated and much less studied than nonlinear resonance. But, still, the major mechanism for the onset of global chaos remains the same, namely the combination of the reconnection between resonances of the same order and of their overlap in energy with the chaotic layers associated with the barriers. At the same time, the frequencies of the major spikes in $h_{gc}(\omega_f)$ are twice as large as those of the corresponding spikes in the case of the additive driving: this is because the characteristic frequencies of parametric resonance are typically doubled as compared with the nonlinear resonance (cf. [1]). Thus, if the parameter Φ in $U(q)$ (2.2.6) is periodically driven (which may correspond e.g. to the time-periodic electric force being *perpendicular* to the direction of the periodicity of the magnetic field [21]) i.e. if the full Hamiltonian is

$$H = p^2/2 + (\Phi - \sin(q))^2/2, \quad \Phi = \Phi_0 + h\cos(\omega_f t), \quad \Phi_0 = \text{const}, \tag{4.3.18}$$

then one may expect for major spikes in $h_{gc}(\omega_f)$ to occur at the frequencies

$$\omega_{sp}^{(n)} \approx 2\omega_s^{(n)} \approx 2(2n-1)\omega_m, \qquad n = 1, 2, ..., \tag{4.3.19}$$

which agrees well with results of simulations [76].

4.4 Chaos in the presence of dissipation

4.4.1 Introduction

The system (4.2.3) has 1.5 degrees of freedom and, therefore [80,60], it can be chaotic if the driving amplitude h is large enough . It has indeed been established that there are many regions in the plane of the driving force parameters where the motion is chaotic i.e. where positive Lyapunov exponents exist at least within some part of the phase space: see Fig. 35 [71]. Chaotic attractors corresponding to the chaotic motion are strange [80,60] attractors and, as in many other (not necessarily ZD) periodically driven systems, they may look quite different depending on the region of the parameter space and of the

phase space (see examples e.g. below in Fig. 39(a.8,b.7)). But the remarkable feature of the ZD system (4.2.3) is that there is a chaotic band at unusually small amplitudes of the driving force. It was noticed in [71] that this chaotic band lies within the 1st-order resonance region [37] (see Fig. 35). It was further noticed in [72] that the chaotic band lies within the intersection between the 1st-order and 2nd-order regions. Furthermore, the evolution of Poincaré sections in the relevant region of the driving force parameters was studied thoroughly, leading to the inference that chaos in this parameter range could be attributed to some rather simple empirical criteria for the onset of chaos in weakly dissipative systems being met [73]. These criteria may be considered as being, in a sense, a generalization to weakly dissipative systems of the Chirikov resonance-overlap criterion in Hamiltonian systems [5,35,60]. The criteria constitute a very remarkable result. They are applicable to an arbitrary system, not just to ZD systems [38]. However, our very recent (though incomplete) studies [74] have shown that, as the damping (dissipation) parameter becomes *very* small, the criteria fail: the chaotic regions in the parameter plane shrink notwithstanding that the bifurcations (period-doubling, etc.) which precede the onset to chaos at moderately small damping are still well described by our criteria. Given the generality and potential importance of these criteria, it will be necessary to study them over a wider range of damping and to establish their limits of validity. The fundamental origins of the criteria may be explicable by mathematicians and we hope, therefore, that this section will attract their attention.

We now present in sub-section 4.4.2 the major results of [73], for the case of some moderately small damping, while sub-section 4.4.3 is devoted to more recent results [74] for the case of very small damping and outlines possible future directions of the research.

4.4.2 Empirical criteria for the onset of chaos in weakly dissipative periodically driven systems. The case of moderately small damping

Let us first consider the resonance approximation (4.2.4) for $n = 1, 2$ (i.e. the resonances of the 1st and 2nd orders) for the system (4.2.3) with Γ =0.05, ω_0 =0.5924, β =1.026, γ =1. Fig. 36 shows the relevant bifurcation lines in the relevant area of the $h - \omega_f$ plane. Fig. 37 illustrates the ZDNR/NR transition for the 2nd-order resonance (the dashed line in Fig. 36): the figures (a) and (b) correspond to the NR and ZDNR stages respectively. Analogously to the 1st-order resonance, the basin of attraction of the larger-action attractor encompasses that of the smaller-action attractor, in the ZDNR stage, while it is vice versa in the NR stage.

Let us now turn to the full system (4.2.3) to study its chaos (in the lowest chaotic band

[37] It was wrongly suggested, though, that the chaos probably related to global bifurcations of the 1st-order resonance regime.

[38] But the range of their validity is probably at its largest precisely in ZD systems. Furthermore, the criteria work most efficiently in ZD systems, because the amplitudes of the driving force at which the different-order resonances overlap in energy, either with each other or with a linear response, are typically much smaller in ZD systems than in other systems. Thus the accuracy of the resonance and linear response approximations (which are used in the criteria) is larger in ZD systems than in others.

in the $h - \omega_f$ plane) and the routes to its onset. Fig. 38 shows the relevant chaotic band together with various bifurcation lines, as well as lines found in the resonance approximations and lines related to the interaction between resonances. There are two different types of chaotic attractor [39] (cf. Fig. 39). The corresponding regions of parameters practically do not overlap. For the sake of brevity, we will refer to them as to *chaos-1* and *chaos-2*.

As h increases, the chaotic attractor corresponding to chaos-1 (cf. Fig. 39(a.7)) is born via a sequence of period-doubling bifurcations from the *larger-amplitude* period-2 attractor (which corresponds to the larger-action 2nd-order resonance). With further increase of h, the chaotic attractor grows and, when h reaches the crisis line, the attractor touches the boundary of attraction of the 1st-order resonance and vanishes discontinuously (Figs. 39(a.8,9)).

The chaotic attractor corresponding to chaos-2 (cf. Fig. 39(b.6)) is born via a sequence of period-doubling bifurcations from the *smaller-amplitude* period-2 attractor (the smaller-action 2nd-order resonance). With further increase of h, destruction of the chaotic attractor and a reverse sequence of period-doubling bifurcations occur (Figs. 39(b.8,9)).

It is seen that the chaos-1 and chaos-2 regions can be roughly delineated using simple criteria related to interactions between oscillatory regimes of different frequencies calculated either in the resonance or in the linear response approximations.

Chaos-1 is bounded by the lines 1-2-3-1. It is based on the inference that the origin of chaos-1 lies in a strong interaction between the larger-amplitude period-1 and period-2 regimes of oscillation (larger-action nonlinear resonances of the 1st and 2nd order respectively), which seems to correlate with the evolution of the Poincaré section. The line 1-2 corresponds to a Chirikov-like overlap in energy between the larger-action 2nd-order resonance and the 1st-order nonlinear resonance. The line 1-3 corresponds to the lowest action on the boundary of the 1st-order nonlinear resonance becoming equal to the action of the larger-action attractor of the 2nd-order resonance: this line approximately bounds the crisis of the chaotic attractor. The line 2-3 (ZDNR/NR) bounds the chaos-1 region from the right. The seeming relevance of this line is based on the following argument. In the nearby parameter region, an overlap between the larger-action 2nd-order and 1st-order resonances is possible only in the ZDNR stage: in the NR stage, the basin of the larger-action 2nd-order resonance is encompassed by the basin of the smaller-action 2nd-order resonance (see Fig. 37(a) and Fig. 39(a.3)) which prevents an overlap of the former basin with that of the 1st-order resonance. We note that, as the parameter β decreases so that the minimum of $\omega(E)$ becomes shallower, disappearing at $\beta \approx 0.562$, the area of the delineated region quickly decreases (cf. Fig. 40) until it vanishes, which nicely correlates with shrinkage of the chaos-1 region and with its ultimate disappearance at $\beta \approx 0.8$.

Chaos-2 is bounded very roughly by the lines 4-5-6-7-4. Though the delineation is much less accurate than for chaos-1, it still seems to provide a good guess as to approximately where chaos-2 may be expected and, moreover, the shrinking of the delineated region

[39] It should be mentioned that one of these was observed in experiments on electrical circuits and also obtained by numerical integration of the equation of motion [85]. However, no attempt was made in [85] to relate the attractor to the overlap of nonlinear resonances.

as β decreases correlates quite well with the shrinkage of the chaos-2 area and its final disappearance at $\beta \approx 0.9$. The line is based on the inference (which seems to correlate also with the evolution of the Poincaré section) that the origin of chaos-2 lies in a strong interaction between the smaller-amplitude period-2 oscillation (the smaller-action 2nd-order resonance) and the smaller-amplitude period-1 oscillation, which may be roughly described as a linear response:

$$q_{LR} \approx \frac{h}{\omega_0^2 - \omega_f^2} \cos(\omega_f t), \qquad \omega_f - \omega_0 \gg \Gamma, \omega(I = \frac{h^2 \omega_0}{(\omega_0^2 - \omega_f^2)^2}) - \omega_0. \tag{4.4.1}$$

The line 4-7, bounding chaos-2 from the left, is just the ZDNR/NR line: in the region to the right of it, the larger-action 2nd-order resonance does not prevent an interaction between the smaller-action 2nd-order resonance and linear response. The lines 6-7 and 4-5 bound (from below, and from above, respectively) the region where both linear response and the smaller-action 2nd-order resonance are to occur in approximately one and the same energy range: 6-7 and 4-5 correspond to equality of the energy of the attractor of the 2nd-order resonance with the largest and smallest energies respectively of the linear response. The line 5-6, roughly bounding chaos-2 from the right, is just the line $\omega_f = 2\omega_0$: nearly everywhere to the right of it, the smaller-action 2nd-order resonance is suppressed by linear response so that, if our inference about the origin of chaos-2 is true, chaos should not arise in this region.

It should be noted that we have also studied [74] the case when the damping is larger, $\Gamma = 0.08$, and the chaotic areas still match very well the areas delineated by lines derived as described above.

4.4.3 The case of very small damping

The results of [73,74] described in the previous sub-section allowed us to infer that we had found a powerful empirical criterion valid in the asymptotic limit $\Gamma \to 0$. To test this, we have been considering [74] the same system as in [73], but with an even smaller damping parameter: $\Gamma = 0.01$. The results have turned out to be rather disappointing. Fig. 41 shows a diagram similar to Fig. 38 but for $\Gamma = 0.01$. The lines calculated by our empirical criterion are almost unshifted, naturally. But the real chaotic areas have significantly shrunk: the upper boundary has shifted almost to the lower boundary, both for chaos-1 and chaos-2. Moreover, for chaos-2, the upper boundary becomes of the crisis type rather than a reverse period-doubling sequence as it was in the case of $\Gamma = 0.05$.

Thus, we may draw two major conclusions from the results [73,74]. On one hand, the fact that the lower, left and right boundaries of chaos-1 and chaos-2 correlate well with the empirical criteria, both for $\Gamma = 0.05, 0.08$ and $\Gamma = 0.01$, confirms the validity of the inference about the origins of chaos in the relevant regions of the $h - \omega_f$ plane. On the other hand, an understanding of why and how chaotic attractors evolve as h grows, and of how they could be delineated by means of a simple criterion (if any) is absent so far. It will be necessary to study in more detail the evolution of chaotic attractors as Γ, h and ω_f vary (in the underdamped range and in the relevant range of the $h - \omega_f$ plane,

respectively) and to try to understand the underlying reasons for the observed behaviour.

4.5 Unsolved problems

Item 1-3 below summarize three major unsolved problems related to periodically driven ZD systems considered in detail above; items 4-6 introduce issues not so far discussed.

1. Although the major features of the *slow dynamics* in the case of an additive periodic force – at least in systems like the TDO, i.e. in monostable systems whose $\omega(E)$ possesses a local minimum – have already been understood and described, there are still some interesting problems: (i) to study some of the global bifurcations in more detail (e.g. the yellow line in Fig. 24(b)); (ii) to study in more detail the higher-order resonances, following the initial study carried out in [72,73] which demonstrated the existence of certain differences from the case of the 1st-order resonance; (iii) to study characteristic features of the bifurcation diagram for the slow dynamics in periodically-driven ZD systems with local maxima in $\omega(E)$ and, especially, in those ZD systems which possess separatrices e.g. SQUIDs; (iv) to consider more complicated types of friction and its influence on the slow dynamics.
2. As for *chaos in the non-dissipative* case, it would be interesting to study, both numerically and analytically (if possible), the chaotic layer associated with ZDNR, including the structure of the layer, chaotic transport within it, statistics of the Poincaré returns, long flights, traps, etc. (cf. [90]; for a numerical study of the statistics of Poincaré returns in the chaotic layer of conventional NR and its qualitative analysis see [91] as well as [92] and references therein).

   It would also be desirable to develop a more accurate numerical description of the spikes in the dependence $h_{gc}(\omega_f)$ using resonance approximations of different order. A development of an explicit resonant approximation theory for analogous spikes in the case of parametric perturbation is another important and challenging problem (see also item 6 below).
3. Studies of *chaos in weakly dissipative* ZD systems are actively developing. The nearest empirical task is to find for the same potential as in [73] the value of Γ at which the chaotic areas in the $h - \omega_f$ plane start to shrink significantly, while the major fundamental problem is to understand the underlying reasons for the evolution of the relevant chaotic attractors as the damping parameter decreases. This would hopefully allow us to derive, more efficiently than at present, simple criteria for delineation of the corresponding chaotic regions in the parameter space. A further stage would be to test the criteria over a wide range of weakly dissipative systems, also including non-ZD systems.
4. It would be interesting to study the problem of *synchronization* in arrays of ZD systems, e.g. underdamped SQUIDs. A similar problem in overdamped SQUIDs was studied intensively a few years ago (e.g. [86–89]) but synchronization between underdamped SQUIDs in the ZD regime may be much more pronounced.
5. Resonance at *subharmonics* and/or subharmonic absorption may occur because the non-resonant response at the driving frequency (subharmonic) possesses harmonics at multiple frequencies, due to the nonlinearity. These, in turn, may resonate with one or more of the eigenfrequencies (cf. [1]). Such a mechanism in ZD systems is likely to

be much more pronounced than in the conventional case, provided that the driving frequency is close to a subharmonic of the extremal eigenfrequency.

6. *Parametric* resonance, where the periodic driving affects one or more of the parameters of the non-driven system (i.e. as a multiplicative rather than additive perturbation), has not yet been investigated in any detail for ZD systems, although there have been some numerical studies in the context of chaos in certain non-dissipative ZD systems [20,21,76]. The significant difference between conventional parametric and nonlinear (i.e. additive) resonances suggests that much the same distinction will relate to the ZD case too.

4.6 Conclusions

ZD systems under periodic driving may manifest very characteristic properties both in their non-chaotic and chaotic dynamics.

Thus, if the driving is weak enough, the motion is non-chaotic. The slow dynamics in the nonlinear resonances arising in ZD systems may be distinctly different from those in conventional systems. The topology of the corresponding nonlinear resonance, referred to as ZDNR, is different from that for conventional nonlinear resonance (NR). The variation of energy is typically larger than in the conventional NR whereas the variation of angle, on the contrary, is smaller. As the driving amplitude and frequency vary, the slow dynamics in periodically driven ZD systems undergo a variety of local and global bifurcations most of which do not have analogues in conventional systems. The most important global bifurcation is the so-called ZDNR/NR transition, which may be also interpreted as an overlap between nonlinear resonances of the same order. The most important unsolved problem concerning the slow dynamics in periodically driven ZD systems is the analysis of the corresponding bifurcation diagramme for the case when the non-driven ZD system possesses separatrices.

Chaotic layers associated with ZDNRs in the non-dissipative case also exhibit many differences from the layers associated with NRs. They are strongly inhomogeneous, different parts being described by different maps. Their dependences on driving amplitude and frequency also differ from those in the conventional case. A detailed study of chaotic layers in ZDNR has yet to be undertaken.

In case of the non-dissipative systems with more than one separatrix, the amplitude of periodic driving sufficient for the chaotic transport to connect the separatrices becomes very small if the drving frequency lies close to the extremal eigenfrequency or/and its harmonics.

In the presence of weak dissipation, chaos may arise in periodically driven ZD systems at unusually small driving amplitudes, because the overlap of different-order resonances requires smaller amplitudes than conventionally. An attempt was made to construct a set of rather simple empirical criteria, based on the resonance and linear response approximations, aiming to delineate the chaotic regions in the plane of the driving force parameters. These criteria require further study and clarification.

5 Zero-dispersion systems subject to periodic driving and noise

The interplay between noise and periodic driving in dynamical systems is a very broad subject that has been studied in numerous papers and books (see e.g. [2–4,38,**?**,84,93–95] and references therein). There may be three distinctly different cases –

(a) *Strong or moderate periodic driving*, so that chaotic or quasi-chaotic attractors may arise [60], i.e. the phase space of the noise-free system differs markedly from that in the absence of the driving. In this case, the motion occurs over a broad range of energies so that the peculiarity of the extremal ("zero-dispersion") energy is largely lost, which is why we do not consider this case here [40] .
(b) *Weak periodic driving with relatively large noise intensity*, so that the statistical distribution differs only slightly from that found in equilibrium without driving. Phenomena peculiar to ZD systems under these conditions are discussed in sub-sections 5.1-5.2.
(c) *Moderately weak driving with relatively weak noise.* In this case, the distribution in the regions of resonant energies differs strongly from equilibrium. Given that the widths of these resonant regions are typically much larger in ZD systems than in conventional ones, noisy phenomena in periodically driven ZD systems become especially pronounced and phenomena peculiar to ZD systems may then arise. Phenomena corresponding to this type of interplay between noise and periodic driving are described in sub-sections 5.3-5.5.

5.1 Weak periodic driving: zero-dispersion stochastic resonance

Stochastic resonance (SR) has been the subject of intensive investigation over the last decade: for recent reviews see [93,94]. The idea of SR was originally introduced [98] in relation to a noise-induced enhancement of the amplitude of a low frequency periodic signal in a bistable system. It was subsequently realised [99,100], however, that a stronger definition of SR in the same system was also possible: it was shown that, for small enough signals, not only the signal amplitude but also the signal-to-noise ratio (SNR) could increase with noise intensity (temperature) within a certain range. It is this latter definition of SR that is probably now the more widely used and accepted, and which we will apply below.

A general theory of SR, not confined to the conventional bistable case [100] was introduced in [101,102]. It was predicted [103,58] on this basis that SR could also occur in monostable systems. In this perception of the phenomenon, SR is to be anticipated in any system whose fluctuation spectrum in the absence of a periodic signal displays at least one narrow peak that grows quickly enough with increasing noise intensity. In the particular case considered in [103,58], the SR was associated with *zero-dispersion peaks* (see Sec. 3):

[40] The only ZD consequence is an indirect one: the onset of chaos may in some cases occur at driving force amplitudes much smaller than those typical of conventional systems (see section 4 above). Noise-induced escape from the chaotic attractor in one such system (TDO) was recently studied by means of simulations [96,97].

to distinguish it from conventional bistable SR, it was named *zero-dispersion stochastic resonance* (ZDSR).

The original works [103,58] that identified ZDSR theoretically did so on the basis of the TDO model; but it has turned out that this is not actually the best system for observation of ZDSR. This is because adequate resolution between the ZDP and the peak coming from low energies requires extremely small values of the damping parameter (cf. sub-section 3.6 and Figs. 14-16). Hence only *signal* growth with noise was observed in the analogue experiments [58]. The observation of noise-induced growth of the SNR, which came later [56], was based on a SQUID model in which the resolution between the ZDP and the low-energy peak is excellent (Fig. 17). A detailed theoretical description of ZDSR, including both its asymptotic theory and the necessary numerical algorithm, together with detailed analogue experiments for the SQUID model, were presented in [47]. It has become apparent since the latter work that ZDSR can in principle be used to enhance the output SNR of a SQUID at moderate and high frequencies, in very much the same way as conventional SR has already been used to enhance the output SNR of multistable SQUIDs [104] in the low frequency range.

We present the general theory of ZDSR in sub-section 5.1.1. The corresponding analogue experiments are discussed in sub-section 5.1.2.

5.1.1 General theory

Let us consider a one-dimensional oscillator subject to a weak periodic force, and to friction and noise which, for the sake of convenience, we take to be linear and white respectively,

$$\begin{aligned} &\ddot{q} + \Gamma\dot{q} + \frac{dU}{dq} = f(t) + A\cos(\Omega t) \\ &\langle f(t)\rangle = 0, \quad \langle f(t)f(t')\rangle = 2\Gamma T\delta(t-t'), \end{aligned} \tag{5.1.1}$$

where $U(q)$ is a potential. The noise intensity T corresponds to temperature in cases where the noise is of thermal origin. We introduce the SNR [100] in terms of the power spectrum,

$$Q(\omega) = \lim_{\tau\to\infty} (4\pi\tau)^{-1} \left| \int_{-\tau}^{\tau} dt\, q(t)\exp(i\omega t) \right|^2 . \tag{5.1.2}$$

$Q(\omega)$ consists of δ-spikes at the frequency Ω of the periodic force, and its harmonics, superimposed on a smooth fluctuational background that corresponds to the power spectrum $Q_q(\omega)$ in the absence of the periodic force, defined in Eq. (3.1.5). The SNR is then defined as the ratio of the intensity (the square) of the δ-spike at Ω to the fluctuational

background at Ω [100],

$$\mathrm{SNR} = \frac{I_\delta(\Omega)}{Q_q(\Omega)}. \tag{5.1.3}$$

As shown in [101,102] (see [93] for further details), the SNR can be written in terms of a complex susceptibility $\chi(\Omega)$ which, in turn, can be expressed in terms of $Q_q(\Omega)$ using the fluctuation dissipation theorem and the Kramers-Krönig relations [13]

$$\begin{aligned}
&\mathrm{SNR} = \frac{1}{4}A^2 \mid \chi(\Omega) \mid^2 / Q_q(\Omega), \\
&\mathrm{Re}\,[\chi(\Omega)] = \frac{2}{T}\,\mathrm{P}\int_0^\infty d\alpha \left(\frac{\alpha^2}{\alpha^2 - \Omega^2}\right) Q_q(\alpha), \\
&\mathrm{Im}\,[\chi(\Omega)] = \frac{\pi\Omega}{T} Q_q(\Omega),
\end{aligned} \tag{5.1.4}$$

where P denotes the Cauchy principal part.

It was shown [101,102] within this framework that SR in the conventional bistable system [99,100] is due to the high, narrow peak in $Q_q(\Omega)$ centred at $\Omega = 0$ [3,29], which in turn is attributable to noise-induced inter-well transitions.

This picture, based on (5.1.4), led immediately to a more general perception of SR: intuitively, it must be anticipated in *any* system whose fluctuation spectrum in the absence of periodic driving exhibits sharp peaks that rise swiftly enough with increasing noise intensity [105]. McClintock therefore suggested in 1991 that SR-like behaviour might be sought in ZD systems, despite their lack of bistability, provided Ω lay close to the frequency of the ZDP. It was quickly confirmed in simulations [58] that, at least on the weaker definition of SR (i.e. occurrence of a noise-induced increase of *signal* only) SR occurs in the TDO. It was then realised that SR-like phenomena might occur in an even broader range of systems, in particular in *any* underdamped nonlinear oscillator: as T increases, the average frequency of oscillations changes and, if it moves closer to the driving frequency Ω, then the amplitude of the response obviously grows. In ZD systems, this growth is especially pronounced provided the driving frequency is close enough to the extremal eigenfrequency [58]. But an increase of the *signal-to-noise ratio* was not observed in [58]. This was explained in [103], which derived theoretically the conditions for which an SNR increase would be observed in the ZD system (the TDO) used in [58]. In addition, [103] analysed rigorously the earlier intuitive inference [58,105] about the range of occurrence of SR [41]. We follow [103] in the few next paragraphs.

Let us suppose that $Q_q(\omega)$ has a high, narrow peak at $\omega \approx \omega_m$, i.e. that we can present the spectrum as a sum of the two following terms:

$$Q_q(\omega) = Q_{\mathrm{peak}}(\omega) + Q_{\mathrm{far}}(\omega), \tag{5.1.5}$$

[41] Note that, chronologically, [103] was published before either [58] or [105]. In fact, however, the central ideas of [58] had been reported earlier at the 1992 SR conference in San-Diego [105].

where $Q_{\rm peak}(\omega)$ has a maximum of magnitude Q_m at $\omega \approx \omega_m$ and width $\Delta\omega \ll \omega_m$, while $Q_{\rm far}(\omega)$ is negligible at $\omega \approx \omega_m$ though it may still be substantial at frequencies far from ω_m in comparison to $\Delta\omega$. If the signal frequency $\Omega \approx \omega_m$, then absolute values of the contributions to $\mathrm{Re}\,[\chi(\Omega)]$, i.e. to the integral in (5.1.4), from frequencies close to ω_m (i.e. for $|\alpha - \omega_m| \lesssim \Delta\omega$) and from those far from it are respectively

$$F_{\rm close} \sim \frac{1}{T}\omega_m \mid \frac{dQ_q(\omega \approx \omega_m)}{d\omega} \mid \Delta\omega \sim \frac{\omega_m Q_m}{T}, \tag{5.1.6}$$

$$F_{\rm far} \sim \frac{1}{T}\frac{\omega_f^2}{|\omega_f^2 - \omega_m^2|} S_{\rm f}, \tag{5.1.7}$$

where $S_{\rm f} = \int d\omega Q_{\rm far}(\omega)$ is the area under $Q_{\rm far}(\omega)$, and ω_f lies within the range of the maximum of $Q_{\rm far}(\omega)$. If $Q_{\rm far}(\omega)$ possesses more than one distinct maximum, then $F_{\rm far}$ should be a sum of analogous terms for each maximum.

It can be seen from (5.1.6) that the order of magnitude of the contribution to the real part of the susceptibility from frequencies close to ω_m does not depend on the width $\Delta\omega$ of the peak $Q_{\rm peak}$ while, if the maximum Q_m of this peak is high enough, then this contribution dominates over $F_{\rm far}$ (5.1.7). Correspondingly, given the last equality in (5.1.4), i.e. that $\mathrm{Im}\,[\chi(\Omega \approx \omega_m)] \sim Q_m\omega_m/T$, the absolute magnitude of the susceptibility at $\Omega \approx \omega_m$ is given by

$$|\chi(\Omega \approx \omega_m)| = \sqrt{(\mathrm{Re}\,[\chi(\Omega \approx \omega_m)])^2 + (\mathrm{Im}\,[\chi(\Omega \approx \omega_m)])^2} \sim \frac{Q_m\omega_m}{T}. \tag{5.1.8}$$

Thus, if Q_m increases faster than T, then the response of the system to a weak periodic force of frequency close to ω_m will also increase with T. Moreover, if this increase of Q_m is faster than T^2, then the SNR increases too, as must follow from Eqs. (5.1.4),(5.1.8).

Zero-dispersion peaks ideally fit the framework described above, and the corresponding SR-like phenomenon (which was historically the first among high-frequency SR-phenomena: cf. e.g. [106]) was called *zero-dispersion stochastic resonance* (ZDSR) [103].

Obviously, the smaller the damping parameter Γ is, the higher and narrower the ZDP is and, therefore, the more pronounced the ZDSR becomes. Moreover, the SNR can be described in the asymptotic limit $\Gamma \to 0$ by a universal function, which is not difficult to derive by substitution of $Q_q(\Omega)$ (3.3.19) into (5.1.4) (cf. [47]):

$$\begin{aligned} &\mathrm{SNR} = \mathrm{SNR}^{(\mathrm{zd})} \equiv \frac{1}{4}A^2\frac{\pi^2 n^2 \Omega_m^2}{T^2}\, C_{\rm scale}\, R\left(\frac{\Omega - n\Omega_m}{\Delta\tilde{\Omega}_n}\right), \\ &R(x) = \frac{|\, S_c(x)\,|^2}{S(x)}. \end{aligned} \tag{5.1.9}$$

The conditions for validity of (5.1.9) are (cf. [47]):

$$\left|\frac{\Delta\tilde{\Omega}_n}{\min(n\Omega_m, |n\Omega_m - \omega_i|)}\right|, \left|\frac{\Delta\tilde{\Omega}_n}{\omega'' T^2}\right|^{1/2} \ll 1,$$
$$-\left|\Delta\tilde{\Omega}_n\right| \lesssim \mathrm{sgn}(\omega'')(\Omega - n\Omega_m) \ll |\omega''|\, T^2,$$
$$T > \frac{0.4\, E_m}{\ln\left|\omega'' E_m^2/\Delta\tilde{\Omega}_n\right|}, \tag{5.1.10}$$

where ω_i denotes the frequency of any other characteristic peak of the spectrum. These conditions are always satisfied in the asympototic limit of small Γ when Ω is close enough to $n\Omega_m$.

The function $R(x)$, plotted in Fig. 42 characterises the frequency dependence of the SNR. It decreases monotonically with x (cf. the harmonic oscillator for which SNR $\propto \Omega^{-2}$), but the form of the decrease changes with x: it can be shown that the SNR $\propto (-x)^{3/2}$ for large negative x, and that the SNR $\propto x^{-1/2}$ for large positive x.

Of greater interest in the present context is that the SNR is proportional to C_{scale}, which increases sharply with T for $T \ll E_m$. Consequently, the SNR must increase with T within some range [42], just as in the case of SR in conventional bistable systems [93,94,99–102]. The activation-law type dependence of the SNR on T arises because both the susceptibility and fluctuation spectrum are determined by those oscillator vibrations whose energies lie within a narrow band around the extremal frequency, whose population increases rapidly with T.

The frequency dependence of the SNR is well-described by the universal function R, but only for very small values of Γ and in the close vicinity of $n\Omega_m$; the same restrictions apply also to the shape of the ZDP itself (see Sec. 3). In order to calculate the SNR over a wider range of parameters, it is necessary to compute the fluctuation spectrum numerically. The algorithm [11,47] has been described by us in sub-section 3.5 above and the results for the SNR based on it are discussed below in sub-section 5.1.2.

5.1.2 Applications to the TDO and SQUID models and analogue electronic experiments

In [103], the numerical algorithm [11] (see also sub-section 3.5) was applied to the calculation of the spectrum $Q_q(\Omega)$, which could then be substituted into Eq. (5.1.4) to find the SNR. As expected, there was a range within which the SNR increased with T provided that Γ was small enough and Ω was close enough to Ω_m. At the same time, because the minimal eigenfrequency, Ω_m, and the eigenfrequency in the bottom of the well, Ω_0, are typically very close to each other in the TDO model, separation of the ZDP from the low-energy peak requires very small values of Γ: for the parameters of the model [58], it needed to be $\lesssim 10^{-3}$ [103]. That is why, the noise-induced growth of SNR was not achieved in [58], in which the analogue circuit had $\Gamma \sim 10^{-2}$.

[42] Strictly, $R([\Omega - n\Omega_m]/\Delta\tilde{\Omega}_n)$ also depends on T because $\Delta\tilde{\Omega}_n \propto T^{1/2}$. This dependence is much weaker, however, than the activation-law type dependence of C_{scale} on T, and therefore has only a minor influence.

At the same time, the response ($\propto |\chi|$) did grow dramatically with T [58]. Of course, this phenomenon is not restricted to ZD systems (though it is more pronounced in ZD systems than in conventional ones: cf. [58]). The mechanism of such growth is related to the tuning (by means of noise) of the statistically averaged eigenfrequency $\omega(\langle E \rangle)$ to the frequency of the driving force (provided Ω lies within the spectrum of eigenfrequencies). Recently, this idea was also applied to the conventional bistable oscillator [107].

A much more pronounced manifestation of ZDSR occurs in the SQUID model [56,57,47] (Fig. 43). The frequency dependence of the SNR in ZD oscillators quite generally displays a resonant-like behaviour (Fig. 44), in contrast to the behaviour of the SNR in conventional systems (cf. [99–102]). At the same time, the width of each resonance is generally much larger than the band of frequencies within which conventional SR is manifested in overdamped SQUIDs. This is especially clear from Fig. 45, in which one can see that the noise-induced growth of SNR may occur in a rather broad range of frequencies. Moreover, there is typically more than one maximum in the frequency dependence: this is due to the multiple extrema in $\omega(E)$ (see Fig. 4). In the case of many wells in the SQUID potential (2.1.5) ($B \ll 1$), the extremal eigenfrequencies are very close to each other and, in addition, the energy ranges responsible for the "adjacent" ZDPs become very narrow and close to each other. Consequently, the noise-induced growth of SNR smears or even disappears altogether. In the opposite limit, $B \gg 1$, the extrema of $\omega(E)$ are very shallow: the system reduces to the harmonic oscillator, where growth of the SNR with temperature is absent [93]. Thus, the optimal range for ZDSR in SQUIDs is $B \sim 1$ [43]. Thus, together with the condition of being underdamped $\Gamma \ll \Omega_m \sim \sqrt{B}$, the optimal conditions for the manifestation of ZDSR in SQUIDs are

$$\Gamma \ll B^{1/2} \sim 1, \tag{5.1.11}$$

or, in terms of SQUID parameters (see sub-section 2.1),

$$\begin{aligned} R_N &\gg (L/C)^{1/2}, \\ \beta &\sim 1. \end{aligned} \tag{5.1.12}$$

For a more detailed discussion of ZDSR in SQUIDs, see [47].

5.1.3 Unsolved problems

(1) The theory of ZDSR for a single oscillator has been quite well elaborated and tested in analogue and computer experiments in many details, especially for the SQUID model. Thus, the most important problem for the future is, in our opinion, a realization of ZDSR in real systems and its uses in various applications.

[43] It does not matter whether B is above or below the critical value $B_c \sim 1$ dividing the boundary between multi-stability ($B < B_c$) and monostability ($B > B_c$) of the SQUID.

The most probable candidate for such a realization is a SQUID loop. The major difficulty which may occur at this is that, typically [47], the relevant extremal eigenfrequency ω_m is of the order of a plasma frequency of the Josephson junction, which is very high (of the order of 1-10 GHz [15]). This difficulty could be removed in two ways. One of them is to make the extremal eigenfrequency significantly smaller by means of a proper choice of the loop and junction parameters (note however that the ZDSR becomes less pronounced if one uses the extremum of $\omega(E)$ with too small extremal eigenfrequency [108]; a maximal decrease at which the ZDSR is still pronounced is of the order of 10 typically [108]). Another way is [109] to increase the frequency of the relevant (low-frequency) signal to the range of a (high) plasma frequency, to enhance it by means of the ZDSR and then to decrease the frequency back to the low-frequency range, in analogy with conventional radio technique [110].

(2) Another interesting problem for the future is to study ZDSR in arrays of ZD oscillators. Conventional SR in an array of overdamped bistable systems was shown [111] to be enhanced in comparison with the single system. It was recently shown [112,113] that, in an array of conventional (non-ZD) monostable underdamped oscillators, the signal may be enhanced by the application of noise, similarly to the case of the single oscillator [58] but in a more pronounced way. In addition, the dependence of such an enhancement on noise intensity exhibits more than one peak, unlike the case of the single oscillator [58]. This is because the degeneracy of the eigenfrequency in a system of identical non-interacting oscillators is lifted if a coupling is introduced. These considerations have allowed us to suggest [47,114] studies of arrays of ZD oscillators. Unlike the case of conventional oscillators, they should exhibit a very pronounced increase of SNR, rather than just of the signal, and the signal enhancement should be much stronger than for the case of conventional oscillators. On the other hand, compared to single ZD oscillators, arrays promise to provide much stronger manifestations of ZDSR, and the dependence of the SNR on noise intensity promises to possess several peaks, unlike the single one in the case of a single oscillator.

5.2 Weak periodic driving: subharmonic absorption

The resonant response of a nonlinear oscillator to periodic driving at a subharmonic frequency, and the related resonant subharmonic absorption, are well known phenomena [1] that are relevant to many areas of physics, for example mechanics [1] and nonlinear optics [115]. The theory of these phenomena in a weakly nonlinear *noise-free* oscillator is quite well established [44]. Their mechanism is as follows: the sub-harmonic driving (e.g. at 1/2 of the frequency ω_0 of a small-amplitude eigenoscillation of the oscillator) causes a non-resonant, approximately linear, response. Due to the nonlinearity, this response also possesses higher harmonics; one of these harmonics – the 2nd one, in the case of the driving at the frequency $\omega_0/2$ – turns out to be resonant to the eigenoscillation, so that this harmonic provides for *resonant* absorption if there is friction in the system. Such resonant nonlinear absorption may turn out to be stronger than the linear non-resonant absorption, provided that the driving amplitude is not too small.

[44] We note however that, as mentioned in sub-section 4.5, the case of ZD systems was not studied and it would be interesting to study it.

However the frequency ranges where such phenomena may occur are typically limited to the close vicinity of the subharmonics of ω_0. The situation changes drastically if noise is added [116]: it populates a relatively broad range of energies, thereby significantly widening the range of eigenfrequencies that are relevant (typically, $\delta\omega \sim |\omega(0) - \omega(T)|$, where $\omega(0) \equiv \omega_0$ and T is temperature). If the noise is too large, on the other hand, so that the relevant range of eigenfrequencies becomes too broad, then the resonance is smeared out. Thus, for a given driving frequency that is distinctly inside the spectrum of eigenfrequencies, there is typically a distinct peak in the resonant nonlinear absorption and higher-harmonic generation as functions of temperature. In a sense, this may be considered as a kind of stochastic resonance (cf. sub-section 5.1), but for a nonlinear rather than linear response, and at the subharmonic rather than at the main/multiple frequency.

In a conventional (non-ZD) system, such peaks in the dependences on temperature of the absorption and of the 2nd-harmonic intensity do not depend on the damping parameter Γ, provided that Γ is small (i.e. $\Gamma \ll \omega_0, \delta\omega$) [116]. In contrast, in ZD systems, if the driving frequency is close to a subharmonic of the extreme eigenfrequency ω_m, the magnitudes of the peaks should become extremely high as $\Gamma \to 0$ (infinitely high if the frequency is exactly equal to the subharmonic of ω_m), closely analogous to zero-dispersion peaks in the linear response at the main/multiple frequency (see Sec. 3).

To the best of our knowledge, the only paper on resonant nonlinear absorption in the presence of noise is [116]. It concentrates mostly on the conventional case i.e. where the ZD property is not relevant. At the same time, the authors of [116] did notice some interesting features that may arise in the case of a ZD system: they presented some illustrative examples, though for a particular model (the TDO) which, as already mentioned, is far from being the best choice for demonstration of the relevant ZD phenomena. Thus, it would be both interesting and important to study resonant nonlinear absorption experimentally in other ZD models, e.g. in the SQUID model, and to develop the corresponding general theory – which is, however, far from being a trivial problem.

Below, following [116], we present in sub-section 5.2.1 the theory of 2nd harmonic generation and of subharmonic absorption for the TDO model where the extreme frequency $\omega_m \equiv \omega(E_m)$ is close to ω_0, so that the nonlinearity of the eigenoscillation in the relevant range of energies $E \lesssim E_m$ is weak. Subsection 5.2.2 presents some experimental results. In sub-section 5.2.3, we present a brief discussion of the results and identify some remaining unsolved problems.

5.2.1 Theory

The non-driven oscillator that we consider is the TDO (4.2.1) (see also Sec. 2.3) with $\omega_0 = \gamma = 1$, $\beta = 5/3$; the eigenfrequency ω as a function of action is shown in Fig. 22. As can be seen from the figure, the minimal eigenfrequency $\omega_m \approx 0.805$ i.e. only slightly less than ω_0. The corresponding energy $E_m \approx 0.1635$ is also rather small so that, in the range of relevant energies $E \lesssim E_m$, the anharmonic corrections in the potential $U(q)$ (i.e. $\beta q^3/3$

and $\gamma q^4/4$) are small in comparison with the parabolic term $\omega_0^2 q^2/2$:

$$E_m \ll \frac{\omega_0^4}{\gamma}, \frac{\omega_0^6}{\beta^2}. \tag{5.2.1}$$

This allows us to use in the theory below the harmonic approximation as the lowest-order approximation.

The equation of motion which we study is formally similar to that considered earlier in the context of stochastic resonance (cf. (5.1.1)),

$$\begin{aligned} &\ddot{q} + \Gamma\dot{q} + \omega_0^2 q + \beta q^2 + \gamma q^3 = f(t) + A\cos(\Omega t), \\ &\langle f(t)\rangle = 0, \quad \langle f(t)f(t')\rangle = 2\Gamma T\delta(t-t'), \\ &\Gamma \ll \omega(E), \Omega, \end{aligned} \tag{5.2.2}$$

but the relevant range of frequencies Ω is different: we assume that the doubled frequency of the driving force, 2Ω, is close to the band of thermally excited vibrations of the oscillator,

$$|2\Omega - \omega(E)| \ll \omega(E) \qquad \text{for} \quad E \lesssim T, \tag{5.2.3}$$

while

$$T \lesssim E_m \ll \frac{\omega_0^4}{\gamma}, \frac{\omega_0^6}{\beta^2}. \tag{5.2.4}$$

The quantity of major interest in the present context also differs from that in stochastic resonance problems, namely it is the absorption coefficient:

$$\kappa = A^{-2}\overline{\langle \dot{q}(t) A\cos(\Omega t)\rangle} \tag{5.2.5}$$

where the overbar denotes averaging over the period $2\pi/\Omega$.

For small amplitudes of the driving force and for moderately weak noise intensities (5.2.4), the analysis of the resonant nonlinear response of the oscillator may be done in two steps familiar from [1]: (i) one first ignores the oscillator nonlinearity, so that a sinusoidal external force results in nonresonant vibrations at the force frequency Ω (the perturbation parameter is the force amplitude A weighted by nonlinearity constants); and (ii) in the next iteration one substitutes the corresponding oscillating term in the oscillator coordinate into the nonlinear terms in the restoring force on the oscillator. These terms then oscillate at the overtones of Ω, and act as an effective force that drives the oscillator. The resonant linear response to this force may then be analysed.

Thus, to lowest order in A, *nonresonant* forced vibrations may be described in the harmonic approximation,

$$q^{(1)}(t) \approx \frac{A}{\omega_0^2 - \Omega^2} \cos(\Omega t + \phi^{(1)}), \qquad \phi^{(1)} \approx -\frac{\Gamma\Omega}{\omega_0^2 - \Omega^2}. \tag{5.2.6}$$

The angular shift $\phi^{(1)}$ allows for a weak linear absorption by the oscillator. The corresponding linear nonresonant absorption coefficient is

$$\kappa^{(1)} = \frac{\Gamma\Omega^2}{2(\omega_0^2 - \Omega^2)^2}. \tag{5.2.7}$$

The equation of motion for the vibrations at frequency 2Ω in the range of moderately small noise intensities (5.2.4) can be obtained by seeking the solution of Eq. (5.2.2) in the form $q(t) \approx q^{(1)}(t) + q^{(2)}(t)$. The equation of motion for $q^{(2)}(t)$ may be written as

$$\begin{aligned} &\ddot{q}^{(2)} + \Gamma\dot{q}^{(2)} + \omega_0^2 q^{(2)} + \beta[q^{(2)}]^2 + \gamma[q^{(2)}]^3 \\ &\qquad \approx f(t) - \frac{A^2}{2(\omega_0^2 - \Omega^2)^2}\beta[\cos(2\Omega t + 2\phi^{(1)}) + 1]. \end{aligned} \tag{5.2.8}$$

We have neglected terms of higher order in A as well as the terms $\beta A q^{(2)}, \gamma A[q^{(2)}]^2, \gamma A^2 q^{(2)}$. In the range (5.2.4), they contain, in addition to A, a small factor proportional to the amplitude of fluctuational vibrations. The nonresonant time-independent term on the right-hand side of (5.2.8) is retained for the sake of clarity; it gives rise to a shift of the equilibrium position of the nonlinear oscillator due to the periodic driving.

Equation (5.2.8) is the equation of motion for a nearly resonantly driven weakly nonlinear oscillator. For small A the response of the oscillator to the force $\propto \beta A^2$ can be described by linear response theory [13]:

$$\begin{aligned} \langle q^{(2)} \rangle \approx &-\frac{\beta A^2}{2\omega_0^2(\omega_0^2 - \Omega^2)^2} - \\ &\frac{\beta A^2}{4(\omega_0^2 - \Omega^2)^2}[\chi(2\Omega)\mathrm{e}^{-i(2\Omega t + 2\phi^{(1)})} + \chi^*(2\Omega)\mathrm{e}^{i(2\Omega t + 2\phi^{(1)})}], \end{aligned} \tag{5.2.9}$$

where $\chi(2\Omega)$ is the susceptibility of the system at 2Ω.

In terms of nonlinear optics, the onset of vibrations at twice the frequency of the driving force corresponds to *second-harmonic generation* (SHG). Equation (5.2.9) fully describes resonant SHG in an underdamped fluctuating nonlinear oscillator.

In the frequency range (5.2.3) the susceptibility $\chi(2\Omega)$ is resonantly large. In the absence of noise, $\chi(2\Omega) \approx (4\Omega^2 - \omega_0^2 - i2\Gamma\Omega)^{-1}$. In the presence of noise, χ is related to the spectrum

of fluctuations Q_q (3.1.5) by means of fluctuation-dissipation theorem and the Kramers-Krönig relation: see (5.1.4). At $T \ll E_m$, the spectrum can be evaluated analytically [2,43] while, in general, it can be readily calculated by means of the numerical algorithm [11] descibed in sub-section 3.5 above. The latter was used in Figs. 46-48.

Figs. 46 and 47 show the dependence of $|\chi(\omega)|^2$ as a function of T for five values of $\omega = 2\Omega$, and as a function of ω for three values of T, respectively. Fig. 48 shows the dependence on T of the real and imaginary parts of $\chi(\omega)$. It is clear from Figs. 46 and 48 that, for $\omega \approx \omega_0$, the functions $\chi'(\omega), \chi''(\omega)$, and $|\chi(\omega)|^2$ display nonmonotonic dependences on T. The peaks in $|\chi''(\omega)|$ and $|\chi(\omega)|^2$ vs T are due to the fact that the noise "tunes" an underdamped oscillator to a given frequency. As ω decreases the peaks become lower and broader (see the curves (a)-(d) in Fig. 46): this is due to the fact that, if the frequency lies in the the range of a monotonic decrease of $\omega(E)$, then the smaller the frequency the larger is the T that is required to tune the oscillator to this frequency, while the larger T is the larger the fluctuational smearing $\delta\omega$ of the oscillator frequency so that the oscillator displays a less resonant response. However, as ω reaches the close vicinity of ω_m, the peaks again rise (to infinity if $\Gamma \to 0$): see the curve (e) in Fig. 46. The latter effect is due to the ZD property, which provides an enhancement of the resonant properties of the oscillations as T becomes comparable with E_m.

Equation (5.2.9) also makes it possible to analyze resonant absorption at frequency 2Ω, i.e. *two-photon absorption* (TPA), in the language of nonlinear optics. To do this one has to iterate Eq. (5.2.2) once more and to find the term $q^{(3)}(t)$ (i.e. the term $\propto A^3$): this term contains components oscillating with frequency Ω and thereby contributes to the absorption coefficient κ (5.2.5). The resultant overall expression for κ allows both for the nonresonant linear (in A) absorption due to oscillator damping, and for a resonant nonlinear (in A) absorption. It takes the form

$$\kappa \approx \kappa_1 + \kappa_2,$$
$$\kappa_2 = \frac{\Omega}{4(\omega_0^2 - \Omega^2)^2} \left(\frac{\beta A}{\omega_0^2 - \Omega^2} \right)^2 \chi''(2\Omega), \tag{5.2.10}$$

where κ_1 and κ_2 are respectively the coefficients of linear and nonlinear absorption. The coefficient κ_1 for small noise intensities is given by (5.2.7).

It follows from (5.2.10) that, in the range (5.2.4), TPA as a function of frequency and temperature should display behaviour similar to that displayed by linear resonant absorption of a nonlinear oscillator at the frequency 2Ω, which is described by the imaginary part [45] of the susceptibility, $\chi''(2\Omega)$. Thus, like $\chi''(2\Omega)$, the TPA has a distinct peak as a function of T provided 2Ω is close to ω_0; the peak decreases and broadens as Ω decreases until the the close vicinity of $\omega_m/2$ is reached, when it again rises due to the ZD property.

[45] We note that the proportionality factor between κ_2 and $\chi''(2\Omega)$ is the squared coefficient of the cubic nonlinearity β, in agreement with the well-known fact that TPA occurs in noncentrosymmetric systems.

5.2.2 Experiment

To test these theoretical predictions, the authors of [116] performed analogue electronic experiments and digital simulations. We describe them briefly below; further details may be found in [116].

5.2.2.1 Circuit

The analogue model was of a standard design, constructed on the basis of the principles described in detail elsewhere [52–54], using operational amplifiers, multipliers, and other standard analog components to perform the required mathematical operations of addition, substraction, multiplication, division, integration, etc. (cf. also sub-section 3.6). After proper rescalings, the circuit modeled the parameters of Eq. (5.2.2) in the following way:

$$\omega_0 = 1, \qquad \beta = 5/3, \qquad \gamma = 1. \tag{5.2.11}$$

The nominal value of Γ was 0.0142. However, for such small damping, the actual value usually differs from the nominal one due to the effects of stray capacitances and resistances in the circuit. In the present case, the actual value, measured experimentally by two independent methods (cf. [46]) was found to be $\Gamma = 0.0122$.

The intensity of the second harmonic of the signal was measured directly from the ensemble-averaged signal in the circuit at frequency 2Ω. It follows from (5.2.9) that this intensity divided by $\beta^2 A^4/(16(\omega_0^2-\Omega^2)^4)$ gives us $|\chi(2\Omega)|^2$, provided A is small ($A = 0.0176$ in the relevant experiment).

The two-photon absorption coefficient was determined from measurements of the angular shift ϕ, relative to the driving force, of the ensemble-averaged signal at frequency Ω. In the range of moderately weak noise intensities (5.2.4) the expression for the angular shift can be obtained in a way similar to that used to derive Eq. (5.2.10) for the absorption coefficient. In the limit of weak absorption the angular shift is given by a sum of the contributions $\phi^{(1)}$ and $\phi^{(2)}$ that correspond, respectively, to linear absorption and to TPA:

$$\phi \approx \phi^{(1)} + \phi^{(2)}, \qquad \phi^{(2)} = -\frac{1}{2}\frac{\beta^2 A^2}{(\omega_0^2 - \Omega^2)^3}\chi''(2\Omega), \tag{5.2.12}$$

where the angular shift $\phi^{(1)}$ is given by Eq. (5.2.6) with higher-order corrections in T [116].

The digital simulation was based on the algorithm described in [117]. The spectra of fluctuations in the absence of periodic driving obtained by two alternative algorithms [117] and [118] coincided with each other.

5.2.2.2 Results

A. Second harmonic generation.

Measurements of the intensity of the signal at the second harmonic of the forcing frequency are shown for two frequencies by the data points in Figs. 49(a) and 49(b). In the range of force amplitudes A investigated, the intensity of the second-harmonic signal (SHS) was proportional to A^4, and the data in Fig. 49 have been appropriately scaled for comparison with the relevant theoretical susceptibility curves from Fig. 46. Also included in Fig. 49 are theoretical values of $|\chi|^2$ from (5.1.4) derived from fluctuation spectra obtained via digital simulations of the dynamics. It is evident that all the results agree well within experimental error. Direct measurements of the linear response to a weak force at the resonant frequency $\Omega \approx \omega_0$ were also found to be in a good agreement with theory. It is clear that the dependence of the SHS intensity on the noise intensity is strongly nonmonotonic, the peak of the SHS intensity being particularly tall and narrow for $\Omega \approx \omega_0/2$. The *noise-induced enhancement*, defined as the ratio of the maximal intensity of the signal at a given frequency to the intensity for $T = 0$, was found to exceed a factor of 4.5 under the experimental conditions.

It can be seen from Fig. 49(b) that, for $\Omega \approx \omega_m/2$, there is a distinct peak too. For the given model and given parameters, it is a bit smaller and broader than the peak in the case $\Omega \approx \omega_0/2$ but, if one further decreased Γ while shifting Ω yet closer to $\omega_m/2$, then the magnitude of the peak would grow (to infinity, in the limits $\Gamma \to 0$ and $\Omega \to \omega_m/2$). Note also that the *noise-induced enhancement* in the case $\Omega \approx \omega_m/2$ is incomparably larger than in the case $\Omega \approx \omega_0/2$ (cf. Fig. 49).

B. Nonlinear absorption.

As explained above in sub-section 5.2.2.1, a convenient way to investigate the absorption of a periodic driving force $A\cos(\Omega t)$ in an analog experiment is to determine the angular shift between the ensemble-averaged signal at frequency Ω and the force itself. It follows from the theory (see Eqs. (5.2.10) and (5.2.12)) that the absorption coefficient and the angular shift are each made up of a sum of two components, representing linear and nonlinear contributions. In Figs. 50(a) and 51(a) we compare the measured and calculated dependences of the total angular shift ϕ on the noise intensity. The theoretical curves (solid lines) were calculated using Eq. (5.2.12) with $\phi^{(1)}$ given by (5.2.6) with the T-dependent corrections [116] and $\phi^{(2)}$ given by (5.2.12) with $\chi(2\Omega)$ from (5.1.4). To evaluate the spectrum of fluctuations, the algorithm [11] was used.

An additional numerical experiment was performed in which the angular lag at the frequency of the weak periodic force was found directly (see [116] for details) and the spectrum of fluctuations in the absence of periodic driving, $Q_q(\omega)$, was obtained by Monte Carlo simulation of the dynamics. The resultant values of $Q_q(\omega)$ were used to evaluate the angular shift according to Eqs. (5.1.4) and (5.2.12), with $\phi^{(1)}$ given by $-\arctan[\chi''(\Omega)/\chi'(\Omega)]$. In Figs. 50 and 51 these results are compared with those derived from theory and from analog experiment. All the results - including those from theory, direct analog simulations, and numerical simulations, both direct and in the absence of force - are in good agreement with each other.

The contribution of the linear nonresonant angular shift to the total angular shift is

important when the nonlinear resonant effect is relatively small. It is especially true for the relatively broad peak at $\Omega \approx \omega_m/2$. For this reason, the angular shift was measured for very small force amplitudes when $\phi \approx \phi^{(1)}$. The temperature dependences of the measured angular shift ϕ and the calculated linear angular shift $\phi^{(1)}$ are shown, for two different frequencies, in Figs. 50(b) and 51(b). It can be seen that $\phi^{(1)}$, as given by (5.2.6) with the T-dependent corrections, is in reasonable agreement with both the measured $\phi \approx \phi^{(1)}$ and with the values of $\phi^{(1)} = -\arctan[\chi''(\Omega)/\chi'(\Omega)]$ obtained by computer simulation of $Q_q(\omega)$. The results were clearly very different from those of Figs. 50(a) and 51(a).

5.2.3 Discussion and unsolved problems

Thus, the addition of noise may strongly enhance the generation of harmonics of order higher than 1, as well as the nonlinear absorption at subharmonics of eigenfrequencies (the classical analogue of many-photon absorption). It has been demonstrated both theoretically and experimentally that the intensity of the second harmonic and two-photon absorption coefficients as functions of temperature (which characterises noise intensity: see (5.2.2)) are strongly peaked, provided that the frequency of the driving force Ω is close either to the eigenfrequency of small-amplitude oscillations or to the extremal eigenfrequency (where the dispesion is equal to zero: $d\omega/dE = 0$). These phenomena may be considered as a generalization of stochastic resonance (cf. e.g. sub-section 5.1) for the *nonlinear* response. It should be emphasized in connection with this that, if one assumes the strong definition of SR i.e. a noise-induced increase of the signal-to-noise ratio rather than signal only, then such an increase in relation to the *nonlinear* response to the subharmonic driving may occur only in a ZD system provided also that Ω is close to a subharmonic of the extreme eigenfrequency (cf. sub-section 5.1 related to the linear response to the driving on the main/multiple frequency).

The quantitative theory presented above is valid only in the range of small T (5.2.4), when the anharmonicity of the vibrations involved is weak. At the same time, it is intuitively obvious that the effect of SHG and TPA should still exist for frequencies 2Ω significantly different from ω_0 (while still lying within the spectrum of eigenfrequencies) provided T is large enough to tune the oscillator to such a frequency. Obviously, the theory would then require generalization to allow for the strong nonlinearity of the oscillations. Such a generalization for the *conventional* case of a monotonic $\omega(E)$ was developed in [116]: it is based on the iterative perturbation scheme applied to the Fokker-Plank equation i.e. to the equation of motion of the *probability density* rather than the coordinate itself. However this theory is not valid in the ZD case where it gives rise to singularities.

As already mentioned, the ZDP and the spectral peak at the main frequency are much more widely separated in a strongly nonlinear oscillator than in the moderately nonlinear TDO. The noise-induced increase of SHG, and especially of the corresponding signal-to-noise ratio, and the TPA at subharmonics of the extremal eigenfrequency in the strongly nonlinear oscillator (cf. SQUIDs: see sub-section 2.1) may be expected to be much more pronounced than in the TDO with $\omega_0 - \omega_m \ll \omega_0$, in analogy with the linear response at the main frequency (see sub-section 5.1). It will thus be important to test this inference experimentally and to develop the corresponding theory.

5.3 Weak noise: escape rates and directed diffusion

In the previous subsections (5.1 and 5.2), we discussed the interplay between noise and periodic driving mainly in the context of spectral densities, signal-to-noise ratio, and noise-induced absorption. In doing so, we assumed the periodic driving to be much weaker than the noise, in the sense that the distortion of thermal equilibrium by the periodic driving was taken as negligible.

In contrast, in the three sub-sections that follow, the noise is assumed to be weaker than the periodic driving, in the sense that the equilibrium/quasiequilibrium is significantly distorted by the driving force, at least within the relevant ranges of phase space.

Furthermore, the present sub-section relates to quantities that differ from those discussed in sub-sections 5.1, 5.2: the major quantities of interest here are the escape rate from a potential well, and the noise-induced net flux in periodically-driven periodic potentials (ratchets).

In sub-section 5.3.1 below, we describe briefly the results of [95] on the influence of non-adiabatic periodic driving on the noise-induced escape rate, and we consider the associated ratchet effect in periodic potentials. In sub-section 5.3.2, the underdamped limit is considered, based on the results of [84,119]. In sub-section 5.3.3, we discuss particular features of the effects in zero-dispersion systems [119]. Finally, in sub-section 5.3.4, we draw conclusions and identify major unsolved problems.

5.3.1 Escape rates and resonant directed diffusion in nonadiabatically driven systems at moderately weak damping

The influence of a weak *nonadiabatic* periodic driving force on noise-induced escape is a fundamental problem whose solution is far from complete, despite numerous studies (see e.g. [120–125,95,126,84,119] and references therein). It is also relevant to many applications, e.g. to the destruction of metastable states in devices based on Josephson junctions [120,125] or in mechanical electrometers [127], and to directed diffusion [95,126].

Unlike most of the work on stochastic resonance (see e.g. [99–102]) and early works on directed diffusion (e.g. [128]), which relate to adiabatic driving where the escape rates are determined by the instantaneous value of the driving force, the escape rate for nonadiabatic driving does not manage to follow changes of the driving force. If the driving force is very small, its main effect on the escape was shown [122–124] to be an enhancement of the diffusion over energy, which increases only the *prefactor* in the escape rate and does so relatively weakly: the correction is quadratic in the driving amplitude. But if the amplitude of non-adiabatic driving exceeds the properly weighted temperature, its effect was recently shown [95] to be much stronger: the corresponding mechanism relies on positive work by the force in pushing the system resonantly with the eigenoscillation at the resonant energy, thus freeing the noise from some of this work within the range of energies close to the resonant one, and thereby reducing the activation energy. Moreover, in a periodic potential, the driving-induced correction to the activation energy for

escape over the left barrier may differ from that over the right barrier, provided that a certain space-time symmetry [95,131] is broken, e.g. the potential is asymmetric within one period. This difference of activation energies leads to a net flux that strongly (in an activation-like way) depends on temperature. Here we consider briefly the driving-induced reduction of the activation energy and the associated noise-induced directed diffusion in periodic potentials ("ratchets"), following majorly [95].

A. Escape rate

Consider first the escape rate from a potential well. As a simple example of a system possessing a barrier, we shall use the double-well Duffing oscillator (Fig. 52). The external periodic force is assumed sinusoidal, for the sake of simplicity. Thus, the equation of motion is [46]

$$\Pi(\ddot{q},\dot{q},q,t)=\xi(t),\quad \Pi=\ddot{q}+2\Gamma\dot{q}+U'(q)-A\cos(\Omega t), \tag{5.3.1}$$
$$\langle\xi(t)\xi(t')\rangle=4\Gamma T\delta(t-t'),\qquad U(q)=-q^2/2+q^4/4,\qquad T\ll\Delta U\equiv 1/4.$$

Using the concept of *optimal fluctuation* (for complementary reviews of its various modifications, see [132,54]; see also some details in the sub-section 5.4.1 below), one can show that the transition rate W between steady regimes $q_{st}^{(1,2)}(t)$ of forced vibration around the minima of the potential $U(q)$ can be described by an activation law, $W\propto\exp(-S_a/T)$, where the activation energy S_a is some functional minimized over the end state $\vec{\mathrm{s}}_e$, over the end time t_e and over the path $[q(t)]\equiv[q_{st}^{(1)}\overset{t_e}{\to}\vec{\mathrm{s}}_e]$:

$$S_a=\min_{[q(t)],\vec{\mathrm{s}}_e,t_e}S,\quad S=\frac{1}{8\Gamma}\int\limits_{-\infty}^{t_e}dt\;\Pi^2(\ddot{q},\dot{q},q,t), \tag{5.3.2}$$
$$q(t\to-\infty)\to q_{st}^{(1)}(t),\quad \{q(t_e),\dot{q}(t_e)\}=\vec{\mathrm{s}}_e\overset{nf}{\to}q_{st}^{(1,2)}(t),$$
$$q_{st}^{(1,2)}(t)\approx q_0^{(1,2)}+\frac{A}{2-\Omega^2}\cos(\Omega t),\quad \Gamma\ll|\Omega-\sqrt{2}|.$$

Here, the end state $\vec{\mathrm{s}}_e$ is any state in the phase space from which the noise-free system can relax either into $q_{st}^{(2)}(t)$ or into $q_{st}^{(1)}(t)$.

If $A=0$, then all states $\{q,\dot{q}\}$ corresponding to $q_{st}^{(1,2)}(t)$ reduce to the *stationary* stable states $\vec{\mathrm{s}}_{1,2}$ of the undriven system, whereas the *exit state* $\vec{\mathrm{s}}_{ex}$, i.e. $\vec{\mathrm{s}}_e$ minimizing S, reduces to the *unstable* stationary state $\vec{\mathrm{u}}$ at the top of the barrier; the exit time t_{ex}, i.e. t_e minimizing S, becomes infinite. The path $[q(t)]$ yielding S_a for the transition $\vec{\mathrm{s}}_1\to\vec{\mathrm{u}}$, called the most probable escape path (MPEP), is the time-reversed noise-free relaxational trajectory $[\vec{\mathrm{u}}\overset{nf}{\to}\vec{\mathrm{s}}_1]$ (see e.g. [133,3]):

[46] It is similar to Eqs. (5.1.1) and (5.2.2) but we have to use a different normalization of the damping parameter corresponding to that in [84,95] since we reproduce below the figure from [95] in which the relevant value of Γ is indicated directly in the figure.

$$\mathrm{MPEP}(A=0)\equiv[Q(t)],\qquad \ddot{Q}-2\Gamma\dot{Q}+U'(Q)=0, \tag{5.3.3}$$
$$Q(-\infty)=q_0^{(1)},\dot{Q}(-\infty)=0,\quad Q(\infty)=q_b,\dot{Q}(\infty)=0.$$

The path $[Q(t)]$ provides $S_a=\Delta U\equiv U_b-U_0$, which obviously agrees with the classical result for the escape rate [42].

In the asymptotic limit $A\to 0$, the leading-order correction to the $\mathrm{MPEP}(A=0)\equiv[Q(t)]$ is linear in A [95]; in particular, this concerns $q_{st}^{(1)}$ and $\overrightarrow{\mathrm{s}}_{ex}$. It follows from the definition of the MPEP [132,54] that its variation [134] is equal to zero in the linear approximation, so that corrections to $S_a(A=0)\equiv\Delta U$ from a linear correction of the MPEP are weaker than linear. Hence [95], to calculate the leading-order (linear) term in $\delta S_a\equiv S_a-\Delta U$, one may use $[Q(t)]$:

$$\delta S_a\approx-|\tilde{\chi}|A,\quad \tilde{\chi}\equiv\tilde{\chi}(\Omega)=-\int\limits_{-\infty}^{\infty}dt\mathrm{e}^{\mathrm{i}\Omega t}\dot{Q}(t), \tag{5.3.4}$$

where $\tilde{\chi}(\Omega)$ may be called the spectral density of the *logarithmic susceptibility* [95].

In the static limit $\Omega\to 0$, the modulus of the spectral density $|\tilde{\chi}(\Omega)|$ approaches $q_b-q_0^{(1)}$ so that S_a approaches the minimum value taken by the instantaneous potential barrier during one period of the driving force, as one would expect. In general, the shape of $|\tilde{\chi}(\Omega)|$ depends on the interrelation between the damping parameter Γ and the characteristic eigenfrequencies. For small damping, the function $|\tilde{\chi}(\Omega)|$ displays sharp peaks; and for some potentials $U(q)$ it may in fact have a distinctly multi-peaked structure (cf. Fig. 54 corresponding to the $U(q)$ shown in Fig. 53). This structure can be understood if one expands the velocity along the MPEP into a Fourier series in angle (cf. (3.1.7))

$$\dot{Q}(t)\equiv\sum_{n=1}^{\infty}(\dot{Q}_n\{E(t)\}\mathrm{e}^{-in\psi(t)}+\mathrm{c.c.}), \tag{5.3.5}$$

where E and ψ are respectively the energy and angle: see (3.1.6). Now, for small damping, energy and angle are respectively slow and fast variables: see (A.15) in the Appendix, with $f(t)=0$ and allow for the additional factor of 2 in the normalization of the damping parameter in (5.3.1). Hence

$$\dot{E}\approx 2\Gamma\omega(E)I(E),\qquad \dot{\psi}\approx\omega(E), \tag{5.3.6}$$

where $\omega(E)$ is the eigenfrequency as a function of energy (cf. (2.1.8)), $I(E)$ is the action as a function of energy (see (A.4)), and we dropped the terms $\propto\Gamma$ in the equation of motion (A.15) for angle, and the fast-oscillating terms in that for energy.

It follows from (5.3.4)-(5.3.6) that the major contributions to $\tilde{\chi}(\Omega)$ are provided by those sections of $[Q(t)]$ that correspond to energies $E(t)\equiv(\dot{Q}(t))^2/2+U(Q(t))$ close to the *resonant* energies $E_n(\Omega)$, implicitly defined as $n\omega(E_n)=\Omega$ where n is an integer. Labelling

with N the resonance which provides the largest contribution to δS_a, and allowing for that $\omega(E)$ is approximated near E_N as

$$\omega(E) \approx \omega(E_N) + \frac{d\omega(E_N)}{dE_N}(E - E_N),$$

one then obtains

$$|\tilde{\chi}| \approx |\tilde{\chi}_N| \equiv |\dot{Q}_N(E_N)| \sqrt{\left(\int_{-\infty}^{\infty} dt \cos(at^2)\right)^2 + \left(\int_{-\infty}^{\infty} dt \sin(at^2)\right)^2} \tag{5.3.7}$$
$$= |\dot{Q}_N(E_N)| \sqrt{\frac{\pi}{a}},$$
$$a = \Gamma\Omega |d\omega(E_N)/dE_N| I(E_N).$$

In deriving the final expression for $|\tilde{\chi}_N|$, we have used the fact that each of the integrals in the upper line of (5.3.7) is equal to $\sqrt{\pi/(2a)}$ [135].

There are three important conclusions to be drawn from (5.3.7).

(1) If Ω is only slightly less than the eigenfrequency in the bottom $\omega_0 \equiv \omega(E_m)$ (note that unlike in other sections, E_m here denotes the *minimal* energy [47]), then the main contribution comes from the 1st-order resonance i.e. for $N = 1$, and $|\tilde{\chi}_1(\Omega)|$ has a sharp tooth-like shape near ω_0 [95] (cf. Fig. 54):

$$|\tilde{\chi}_1(\Omega)| = A(1 - Bx)\theta(x), \qquad x = \omega_0 - \Omega, \qquad 0 < 1 - Bx \lesssim 1, \tag{5.3.8}$$
$$A = [\pi/(2\Gamma|\omega'|)]^{1/2}, \qquad B = -(2\omega')^{-1}[(|\dot{Q}_2/\dot{Q}_1|^2)' + \omega''/\omega'].$$

The derivatives over E are to be evaluated at $E = E_m$. Similar, but much broader and lower, peaks arise at harmonics of ω_0.

(2) The divergence which would arise in (5.3.7) if we considered a ZD system, and Ω went to the extremal eigenfrequency Ω_m, indicates that for a ZD system $|\tilde{\chi}|$ possesses peaks at Ω_m and at its harmonics provided that Γ is small enough. The shape of the peaks has to be evaluated a bit differently from (5.3.7), as shown below in sub-section 5.3.3.1.

(3) The divergence in (5.3.7) as $\Gamma \to 0$ indicates that, on one hand, the reduction in the activation energy by the above *resonant* mechanism may grow as Γ decreases but that, on the other hand, the range of very small Γ should be treated differently. It is this latter range that is the most interesting in the present context, and it will be considered below in sub-section 5.3.2.

B. Directed diffusion

[47] We are obliged to use this notation here because it was used in the figure taken from [95] which we reproduce as Fig. 54.

Let us now discuss briefly how the resonant mechanism for reduction of the activation energies provides for directed diffusion within a periodic potential [95]. As an example of a periodic potential possessing an asymmetry within a period, let us consider the potential shown in Fig. 53

$$U(q) = \sin(q) + 0.3\sin(2q + 0.4). \tag{5.3.9}$$

Without driving, the system is in thermal equilibrium so that, for low temperatures ($T \ll \Delta U$), the system stays with overwhelming probability near the bottom of one of the wells, equally distributed between all wells. Moreover, because detailed balance holds [38], the probabilities of escape from the bottom over the adjacent barriers to the left and to the right are equal each other. Consequently, there is no net flux.

The situation may become radically different if a periodic driving force is applied [95]. Detailed balance need no longer be satisfied. The driving-induced corrections to the activation energy may differ, depending on whether the escape occurs over the left barrier or over the right one. This effect is most pronounced in the range where the contributions from several overtones are substantial so that their mutual *interference* comes into play (cf. (5.3.4), (5.3.5)). This is well demonstrated by Fig. 54, where the spectral densities for escapes to the left and to the right differ markedly except at a few values of Ω. A detailed study of the spectroscopy of $|\tilde{\chi}^{\pm}|$ has not been carried out and it would be very interesting to study it, especially in the ZD case: cf. sub-section 5.3.3 below. But even Fig. 54 demonstrates that, by changing the frequency, one can control the direction of the diffusion:

$$\begin{aligned} J &= l(W^{(+)} - W^{(-)}) \\ &\propto \operatorname{sgn}(|\tilde{\chi}^{+}(\Omega)| - |\tilde{\chi}^{-}(\Omega)|) \exp\left(-\frac{\Delta U - A\max\{|\tilde{\chi}^{+}(\Omega)|, |\tilde{\chi}^{-}(\Omega)|\}}{T}\right). \end{aligned} \tag{5.3.10}$$

Here l is a period of the potential, which is equal to 4π in case of $U(q)$ (5.3.9).

It should be noted also that a net flux may arise even in a symmetric potential in cases when the periodic driving force contains more than one harmonic [95]: the direction of the diffusion is then controlled by the relative initial angles of relevant harmonics.

For high and moderate damping, the influence of non-adiabatic periodic driving on escape rates, and the net flux in non-adiabatically driven periodic potentials, were observed in analogue experiments [126] and found to be in satisfactory agreement with theory [95].

5.3.2 Underdamped limit

As can be seen from Eq. (5.3.7), the theory [95] implies an increasing escape rate that diverges as $\Gamma \to 0$. Theories [122–124] based on the mechanism of diffusion over energy also diverge as $\Gamma \to 0$. These divergences suggest that the system should be *underdamped* in order for the escape rate to reach the maximum value possible. On the other hand, the

theories in question can predict neither (i) the maximum increase, nor (ii) the conditions under which it occurs, and nor (iii) can they illuminate the underlying mechanism. Thus, it is extremely important to study the problem in the underdamped limit. This is the major purpose of the present sub-section, which to a large extent follows [84] completed by the most recent results from [119].

Let us again consider Eq. (5.3.1) but, unlike the previous sub-section, we shall not assume that A is necessarily the smallest parameter in the problem after the temperature. At the same time, A is still assumed to be small. Contributions to the decrease in activation energy that are $\propto A^n$ with $n > 1$ will therefore be neglected.

The presence of the periodic driving affects S_a in three different ways: (1) by shifting the starting energy E_{st}, i.e. the energy of the starting state $\vec{\mathrm{s}}_{st}$ (belonging to $q_{st}^{(1)}$), away from $E(\vec{\mathrm{s}}_1) = U_0$; (2) by shifting the exit energy $E_{ex} \equiv E(\vec{\mathrm{s}}_{ex}) \equiv \dot{q}_{ex}^2/2 + U(q_{ex})$ away from $E(\vec{\mathrm{u}}) = U_b$; and (3) by causing a breakdown of the relation $S_a = E_{ex} - E_{st}$. Correspondingly, we divide $\delta S_a \equiv S_a - \Delta U$ formally into three parts:

$$\begin{aligned} &\delta S_a \equiv \delta S_a^{(st)} + \delta S_a^{(ex)} + \delta S_a^{(r)}, \\ &\delta S_a^{(st)} \equiv U_0 - E_{st}, \quad \delta S_a^{(ex)} \equiv E_{ex} - U_b, \quad \delta S_a^{(r)} \equiv S_a - (E_{ex} - E_{st}). \end{aligned} \tag{5.3.11}$$

The maximum deviation of energy on the attractor $q_{st}^{(1)}(t)$ from U_0 is $\approx \{A \max(\Omega, \sqrt{2})/(2 - \Omega^2)\}^2/2$. Thus,

$$-\delta S_a^{(st)} \equiv E_{st} - U_0 < \frac{1}{2} \left(\frac{\max(\Omega, \sqrt{2})}{2 - \Omega^2} \right)^2 A^2, \tag{5.3.12}$$

and may be neglected in comparison with the other two terms in (5.3.11) (see below) unless Ω is very close to $\sqrt{2}$; the latter narrow range will be considered neither here nor in what follows.

While evaluating two other terms in (5.3.11), it is convenient to resolve the cases of vanishingly and moderately small A.

5.3.2.1 Asymptotic limit $A \to 0$.

Obviously, the limit of a vanishingly small driving amplitude is not of practical interest, because the decrease of S_a is then negligible; at the same time, its consideration allows us to resolve best of all different physical mechanisms by which the driving affects S_a. In turn, this provides a better understanding of the case of moderately small A, which is potentially important in situations of practical importance. We shall evaluate the terms $\delta S_a^{(ex)}$ and $\delta S_a^{(r)}$ separately, respectively in stages (1) and (2) below.

(1) To evaluate $\delta S_a^{(ex)}$ we note first that $\delta S_a^{(r)}$ is dominated by contributions from the narrow range of resonant energies, and therefore its dependence on $\vec{\mathrm{s}}_e$ from the relevant range of energies $\approx U_b$ is weak (cf. (5.3.4), (5.3.7) as well as stage (2)

below). We shall assume that the latter dependence is weak enough for one to be able to derive $\delta S_a^{(ex)}$ merely from the minimization of $E(\vec{s}_e)$ over $\vec{s}_e$, independently of $\delta S_a^{(r)}$. So, when this assumption is true [48], then, to leading order in A, $\vec{s}_{ex}$ is the state which, among all possible $\vec{s}_e$, has the minimal energy, E_{min}:

$$\delta S_a^{(ex)} \approx E_{min} - U_b. \tag{5.3.13}$$

For $A/\Gamma \to 0$, $\vec{s}_{ex}$ belongs to the unstable periodic orbit near the top of the barrier [95]. So, $U_b - E_{min} \approx A^2/(2(1+\Omega^2)^2)$, and $-\delta S_a^{(ex)}$ can be neglected in comparison with $-\delta S_a^{(r)} \approx -|\tilde{\chi}|A$ (see Eq. (5.3.4)).
On the other hand, if

$$A > A_c \approx \mu_l \Gamma, \qquad \mu_l = \frac{4\sqrt{2}\cosh(\pi\Omega/2)}{3\pi\Omega}, \tag{5.3.14}$$

($\mu_l \sim 1$ at $\Omega \sim 1$, so that $A_c \sim \Gamma$), then a *homoclinic tangle* arises in the *noise-free* system [60] leading, in Poincaré section, to a complex mixing of the basins of attraction of $q_{st}^{(1,2)}$ in a layer around the boundary separating the attracting basins of the stable states of the undriven system (Fig. 55). To first order in A, E_{min} may be approximated by the minimum energy in that part of the basin of attraction of $q_{st}^{(2)}$ where $q < q_b = 0$, additionally minimized over the angle of the Poincaré section. It can be shown (in the same way as (5.3.14) is derived in [60]) that, to first order in A, $E_{min} < U_b$ if and only if the condition (5.3.14) holds. If (5.3.14) holds and $\Omega \sim 1$, then $(U_b - E_{min})/A \sim 1$.

One can readily find E_{min} numerically, just by integrating the dissipative equation (5.3.1) in the absence of noise ($T = 0$). This should be done for a variety of initial driving force angles in the interval $[0, 2\pi]$ and on a grid of initial states with $q < 0$, choosing from them that state which has the minimum energy among those states from which the system relaxes to the attractor $q_{st}^{(2)}$: this energy approximates E_{min}, to first order in A.

For $A \gg A_c \sim \Gamma$, the numerical search for E_{min} can significantly be simplified: the lower-energy boundary of the layer then coincides approximately with the lower-energy boundary of the corresponding chaotic layer of the *non-dissipative* system, namely, of the chaotic layer which includes the state $\{q = q_b, \quad \dot{q} = 0\}$. At the same time it can be shown that the minimal energy in a Poincaré section of the chaotic layer, $E_m^{(nd)}$, is independent of the angle at which the section is taken; so, $E_{min} \approx E_m^{(nd)}$. The explicit formula for $E_m^{(nd)}$ is unknown [136] but, in the light of the above remarks, the chaotic layer is readily generated by computer, using $\{q = q_b, \quad \dot{q} = 0\}$ as the initial state of the system while an initial angle for the driving force may be chosen arbitrarily. Thus, $E_m^{(nd)}$ can very easily be found numerically. Its detailed analysis will be presented elsewhere; here, we present characteristic examples of the dependence of $U_b - E_m^{(nd)}$ on the amplitude and frequency of the driving force. The

[48] We shall indicate in the last paragraph of the item (2) below the ranges of A where this assumption fails. But even in those ranges, eq.(5.3.13) provides for $-\delta S_a^{(ex)}$ the estimation from above, which will turn out quite enough for it to be neglected in the asymptotic limit $A \to 0$. At the same time, $\delta S_a^{(ex)}$ (5.3.13) will provide the major contribution in the range of moderately small A, as shown in Sec. 5.3.2.2 below.

amplitude dependence is ladder-like (Fig. 56(a)); the frequency dependence exhibits sharp peaks (Fig. 56(b)). The jumps in the first case and the peaks in the latter correspond to the occurrence of overlap/separation between nonlinear resonances. Let us first demonstrate it for the frequency dependence.

For very small Ω, the relevant chaotic layer relates only to the separatrix of the undriven system and $U_b - E_m^{(nd)} \propto \Omega A$ [35]. As Ω grows, the resonant energy $E_1(\Omega)$ sharply decreases and, starting from $\Omega = \Omega_1 \approx 2\pi/\ln(1/A)$, the lower part of the chaotic layer relates to the lower part of the nonlinear resonance [5,35,60,136] while the upper part of the layer still relates to the separatrix of the *undriven* system. Both parts are clearly resolved in Poincaré section: Fig. 57(a); cf. also sub-section 4.3.2. Thus, $U_b - E_m^{(nd)}$ grows rapidly and reaches the first maximum for Ω slightly larger than Ω_1. As Ω grows further, the layer related to the nonlinear resonance separates from the layer around the original separatrix. It can then no longer provide inter-well chaotic transport (Fig. 57(b)). Consequently, $U_b - E_m^{(nd)}$ drops abruptly. The peaks at multiple frequencies correspond to higher-order resonances.

Similarly, as A grows, $U_b - E_m^{(nd)}$ undergoes large jumps at $A_n \sim \exp(-2\pi n/\Omega)$, related to successive overlaps between the layer associated with the original separatrix and the layers associated with nonlinear resonances. Note however that the largest A_n, namely $A_{[\Omega/\sqrt{2}]+1}$, is typically still quite small – unless Ω is only slightly less than the eigenfrequency at the bottom, $\sqrt{2}$. Further growth of $U_b - E_m^{(nd)}$ with A is approximately linear, provided $A \ll 1$. Thus, for most of the range $A \ll 1$, the quantity $(U_b - E_m^{(nd)})/A$ plays a role similar to that of $|\tilde{\chi}|$ in (5.3.4).

The question of the relevance/non-relevance of the above peaks and jumps to the frequency and amplitude dependences of δS_a respectively will be discussed at the end of the (2) below.

(2) We next wish to evaluate, or at least to estimate, the last term in δS_a (5.3.11) i.e. $\delta S_a^{(r)}$.

Let us first try to generalize the evaluation of this part [95] corresponding to the case when the homoclinic tangle and related reduction in the exit energy are absent (described in part A of Sec. 5.3.1 above) for the more general case in which the tangle and reduction may be present. Using arguments similar to those of [95], $\delta S_a^{(r)}$ may be described by the formula

$$\delta S_a^{(r)} \approx -|\tilde{\tilde{\chi}}|A, \quad \tilde{\tilde{\chi}} = -\int_{-\infty}^{t_{ex}} dt \mathrm{e}^{\mathrm{i}\Omega t}\dot{\tilde{Q}}(t), \tag{5.3.15}$$

where $\tilde{Q}(t)$ is the time-reversal of the noise-free relaxation from $\vec{\mathrm{s}}_{ex}$. As when the homoclinic tangle is absent, the main mechanism contributing to $\tilde{\tilde{\chi}}$ at small Γ is the resonant one, so that $|\tilde{\tilde{\chi}}| \approx |\tilde{\chi}_N|$ as in (5.3.7).

We now consider how to estimate the value of Γ at which the resonant mechanism saturates and where (5.3.15) is no longer valid. It is a difficult problem: it requires us to find the next term in $\delta S_a^{(r)}$, after the term $\propto A$, while the latter requires us to find the correction $\propto A$ in the MPEP and then to find the corresponding correction to the activation energy; moreover, as is obvious from (5.3.1) and (5.3.2), the part of the second-order (i.e. $\propto A^2$) correction to the activation energy that comes from the

second-order correction in the integrand Π^2 of (5.3.2) *diverges*[49]. Altogether, there are enormous technical difficulties and we have failed to overcome them. Instead, we suggest below a way of estimating a quantity Γ_r such that Eq. (5.3.15) is definitely invalid for all $\Gamma < \Gamma_r$. The most straightforward way would be to use the fact that $-\delta S_a^{(r)}$ cannot exceed $E_{ex} - E_{st}$. This would give rise to an estimate $\Gamma_r \propto A^2$. However, it is possible to find much higher Γ_r. Indeed, the main contribution to the integrals in (5.3.7) comes from the range of t within which the absolute value of the argument of the trigonometric functions is $\lesssim \pi/2$, i.e. $|t| \lesssim t_r \equiv \sqrt{\pi/(2a)} \propto \Gamma^{-1/2}$. In this range, the energy along the MPEP, $E \approx \dot{\tilde{Q}}^2/2 + U(\tilde{Q})$, increases from $E_N - \Delta E_r/2$ to $E_N + \Delta E_r/2$ where

$$\Delta E_r \approx 2\Gamma\omega(E_N)I(E_N)2t_r \propto \sqrt{\Gamma}. \tag{5.3.16}$$

The unperturbed part of the activation energy associated with a noise-induced increase of energy for ΔE_r is equal to ΔE_r. Thus, the perturbative formula (5.3.15) (as well as its partial case (5.3.4)) is valid as long as the absolute value of the negative correction due to the resonant mechanism in the range $[-t_r, t_r]$, which is $\sim |\dot{Q}_N(E_N)|t_r A$, is less than ΔE_r. Hence,

$$\Gamma_r \sim A/\mu_r, \qquad \mu_r = [\omega I/|\dot{Q}_N|]_{E=E_N}. \tag{5.3.17}$$

Typically, $\mu_r \sim |\ \dot{Q}_1^2/\dot{Q}_N\ |$. Thus, typically, $\mu_r \sim 1$ if the relevant resonance number N is 1 while $\mu_r \gg 1$ otherwise.

Of course, it cannot be guaranteed that the resonant mechanism (and the corresponding Eq. (3.5.15)) is valid for all $\Gamma \gg \Gamma_r$ but this is quite likely and, if it is valid indeed, then the saturation of the growth of $-\delta S_a^{(r)}$ as Γ decreases occurs at $\Gamma \sim \Gamma_r$, typically at the level

$$-\delta S_a^{(r)} \sim \sqrt{\frac{|\dot{Q}_N|A}{|d\omega(E_N)/dE_N|}} \propto \sqrt{A}, \tag{5.3.18}$$

i.e. it greatly exceeds $-\delta S_a^{(ex)} \propto A$, given that $A \to 0$.

The next question is: what is $\delta S_a^{(r)}$ for $\Gamma \ll \Gamma_r$? A rigorous treatment of this difficult problem has not yet been achieved. The authors of [84] suggested an intuitive argument in favour of a vanishing $\delta S_a^{(r)}$ as $\Gamma \to 0$: the resonant mechanism affects mainly the "resonant" energies i.e. those in the band $[E_N - \Delta E_r/2, E_N + \Delta E_r/2]$; hence, $-\delta S_a^{(r)}$ is not likely to exceed the width of this band significantly,

$$-\delta S_a^{(r)} \lesssim \Delta E_r \propto \sqrt{\Gamma} \overset{\Gamma\to 0}{\longrightarrow} 0, \qquad \Gamma \lesssim A. \tag{5.3.19}$$

The results of computer simulations[50] [84] seemed to support this hypothesis: as seen from Fig. 58, δS_a reduces to $\delta S_a^{(ex)}$ as $\Gamma/A \to 0$. However recent simulations in

[49] In fact, this divergence indicates that the next-order (after the first-order) correction in $\delta S_a^{(r)}$ is probably non-analytic, i.e. that its second derivative is likely to diverge at $A = 0$.

[50] Eq. (5.3.1) was simulated numerically, and the transition flux from $q_{st}^{(1)}(t)$ to $q_{st}^{(2)}(t)$, $J \equiv J(A,T) \equiv P(A,T)\exp(-S_a(A)/T)$, was measured at two slightly different low temperatures, both for a given A and for $A = 0$. The activation energy was then calculated as $S_a \approx [T_1 T_2/(T_1 -$

some other system [119] (see the Sec. 5.3.3 below, in particular Fig. 64) and more careful qualitative theoretical analysis [119] have shown that the hypothesis about the vanishing of $\delta S_a^{(r)}$ in the underdamped limit is not valid in general, while the argument [84] about the vanishing of ΔE_r (5.3.16) as $\Gamma \to 0$ is irrelevant because the perturbation theory on which Eq. (5.3.16) is based becomes inapplicable at $\Gamma \lesssim \Gamma_r$.

It is still not clear how to solve the problem quantitatively but some qualitative understanding may be gained from [129] (see also the review [2]). This paper considers fluctuational transitions in a weakly nonlinear single-well oscillator driven by a nearly resonant periodic force. In the absence of noise, such a system possesses two stable states which, in the asymptotic limit of vanishing damping, correspond to a linear response and nonlinear resonance respectively (cf. Sec. 4 above). To solve the problem of fluctuational transitions between these two states, the authors of [129] transform to slow variables (cf. the transformation to slow action and slow angle in Sec. 4), and then consider by the method of optimal fluctuation transitions from each of the two states to the saddle on the boundary between their basins of attraction in the plane of the slow variables. In the asymptotic limit of a small driving amplitude A (but with the damping parameter still assumed to be much smaller), the linear response attractor corresponds to energies close to the very bottom of the potential well (i.e. U_0) while both the saddle and the attractor of the nonlinear resonance correspond approximately to the resonance energy E_r i.e. to such an energy for which the eigenoscillation and driving frequencies are equal: $\omega(E_r) = \Omega$. In the asymptotic limit $A \to 0$, the activation energy S_{lrs} for the transition from the linear response attractor to the saddle can be found explicitly [129]

$$S_{lrs} = (E_r - U_0) - \frac{\xi}{\sqrt{2}} \Delta E_{nr}, \tag{5.3.20}$$

$$\Delta E_{nr} = 2\sqrt{\frac{A\sqrt{E_r/2}}{d\omega/dE}} \propto \sqrt{A}, \qquad \xi \approx 0.98.$$

Thus, the deviation of S_{lrs} from just the difference in energy between the starting and ending states, $E_r - U_0$, which is similar to $\delta S_a^{(r)}$ in our problem, is of the order of ΔE_{nr} in absolute value. As in the case of $\Gamma \gg A$ [95], this deviation is yielded mainly in the narrow ($\sim \Delta E_{nr}$) band of energies near E_r, though the mechanism is different.

Of course, the method of [129] is not immediately applicable to our case where the eigenfrequency varies over a broad range (from 0 to ω_0) and it is impossible to introduce slow variables which would be valid in the whole relevant range of energies. The same is true of the method used in [130], which in particular considers the same problem as in [129] and also uses a transformation to slow variables but the consideration is done in terms of the Fokker-Plank equation rather than by means of the method of optimal fluctuation. On the other hand, the results of [129] indicate that $-\delta S_a^{(r)}$ does not vanish as $\Gamma \to 0$; rather it is of the order of the width of the

$T_2)] \ln[\tilde{J}(A,T_1)/\tilde{J}(A,T_2)]$, where $\tilde{J}(A,T) \equiv J(A,T)/J(A=0,T)$ (comparison with the case $A = 0$ was made in order to reduce as much as possible the influence of the prefactor P in the determination of S_a; note that T_1 and T_2 were chosen such that $T_1 \ll \Delta U$ while $|T_1 - T_2| \sim T_1^2/\Delta U$).

broadest nonlinear resonance. Note that it is of the same order as the value $-\delta S_a^{(r)}$ (5.3.18) (the latter corresponds to the saturation of the resonant mechanism [95] at $\Gamma \sim A/\mu_r$; besides, we obviously assume that $N = 1$ in (5.3.18), otherwise the comparison with (5.3.20) would not make sense).

It is also obvious from the above discussion that the jumps and peaks in the amplitude and frequency dependences of $U_b - E_m^{(nd)}$ are not manifested in the corresponding dependences of $-\delta S_a$: apart from the fact that $-\delta S_a^{(ex)}$ is on the whole much smaller than the major nonlinear resonance contribution $\propto \sqrt{A}$, there are no jumps/peaks even in $-\delta S_a^{(ex)}$ itself. Indeed, the jumps/peaks in $U_b - E_m^{(nd)}$ are related to the reconnection of the chaotic layer around the original separatrix with the thin chaotic layers around the separatrices of nonlinear resonances of a high order while – as is obvious from results [129] and from the discussion above – the end state in the problem of a fluctuational transition from a state of low energy towards the separatrix of a nonlinear resonance is the saddle, rather than the lowest energy state of the separatrix. Furthermore, the corresponding activation energy is not just the difference in energy between the final and initial states. Note that the resonance width constitutes a jump in $U_b - E_m^{(nd)}$ at a relevant value of A. Thus, it may be expected that the contribution to $-\delta S_a$ from the range of energies close to the barrier can be described by $U_b - E_m^{(nd)}$ *smoothed* over the jumps, i.e. this contribution coincides with $U_b - E_m^{(nd)}$ only if A lies beyond the vicinity of jumps in the corresponding amplitude dependence in Fig. 56(a) (cf. also Fig. 58 and the discussion in Sec. 5.3.2.2 below). In any case, in the limit $A \to 0$ considered, this contribution may be neglected in comparison with the contribution from the major nonlinear resonance.

Thus, it seems that, in the asymptotic limit $A \to 0$, the evolution of $-\delta S_a$ as Γ decreases should occur in the following manner: for $\Gamma \gg A/\mu_r$, it grows due to the resonant mechanism [95], i.e. $\propto \Gamma^{-1/2}$ according to Eqs. (5.3.4) and (5.3.7); this growth starts to saturate at $\Gamma \sim A/\mu_r$ while a relatively small addition $\sim A$ arises at $\Gamma \sim A/\mu_l$ (these ranges often coincide) due to the reduction in the exit energy caused by the homoclinic tangle [84] as described by Eq. (5.3.13); with further decrease of Γ, when it becomes $\ll A/\max(\mu_r, \mu_l)$, the reduction in exit energy saturates at the level $\sim A$ [84], while the contribution from the range of resonant energies remains dominant and of the same order (i.e. $\propto \sqrt{A}$) as at $\Gamma \sim A/\mu_r$, though by a different mechanism. The latter involves a large fluctuation through the range of the broadest nonlinear resonance in the plane of the slow variables [129,119], i.e. it is associated with a characteristic change of the MPEP in the vicinity of the major nonlinear resonance.

We may conclude that, in the asymptotic limit $A \to 0$, the largest decrease in activation energy occurs at $\Gamma \lesssim A/\mu_r$, the major contribution to it comes from the range of the broadest nonlinear resonance, the decrease being of the order of the resonance width in energy.

5.3.2.2 The range of moderately small A.

An obvious question which may arise in relation to Sec. 5.3.2.1 is: how does its conclusion about the dominance of the nonlinear resonance contribution (rather than of the reduction in exit energy) in the decrease of S_a in the underdamped limit agree with the results of the

simulations [84] presented in Fig. 58? Indeed, one can clearly see in both Fig. 58(a) and Fig. 58(b) that, in those ranges of A and Γ where $\Gamma/A \ll 1$ (i.e. in the distinctly underdapmed regime), the decrease of the activation energy in simulations is nearly exactly equal to $U_b - E_m$ i.e. to the lowering of the minimal energy in the layer of transient chaos (i.e. layer of mixed basins), which appears at first sight to contradict the conclusion of Sec. 5.3.2.1.

To resolve the paradox we note that the conclusion of Sec. 5.3.2.1 relates to the asymptotic limit $A \to 0$, when the layer of transient chaos is distinctly separated from the lowest nonlinear resonance. But, if the latter is much closer to the barrier level U_b than to the bottom U_0, then there exists a range of *moderately weak* driving amplitudes which are weak enough for a linear response to exist but, at the same time, large enough to provide a complete absorption of the energy range of the lowest nonlinear resonance by the layer of transient chaos. When such an absorption takes place, then obviously only one mechanism of the decrease of S_a remains relevant – the lowering of the exit energy due to the layer of transient chaos.

Note that, in the case of a conventional potential well like that of the Duffing or multi-well SQUID potentials, $\omega(E)$ decreases *monotonically* from ω_0 to 0, with the major decrease occurring in a narrow vicinity of the barrier level: cf. e.g. those branches of $\omega(E)$ in Fig. 4(b) which correspond to wells of the multi-well SQUID potential shown in Fig. 3(b). For ω_0 of such type, the absorption described in the previous paragraph is valid in the major part of the relevant [51] driving frequency range $\Omega \lesssim \omega_0$, namely in the whole range $\Omega \lesssim \omega_0$ except the close vicinity of the bottom eigenfrequency ω_0 or of any of its harmonics of moderate order, i.e.

$$\left(\left[\frac{\Omega}{\omega_0} \right] + 1 \right) \omega_0 - \Omega \sim \omega_0, \qquad \Omega \lesssim \omega_0, \tag{5.3.21}$$

where the square brackets imply taking the integer part. Indeed, the order of the lowest nonlinear resonance, which in the case (5.3.21) is also the broadest one, is $N = [\Omega/\omega_0] + 1$. Allowing for (5.3.21), the deviation of the relevant resonant energy E_N from U_b is much less than the barrier height ΔU: e.g. for the Duffing oscillator used in [84] (see (5.3.1) above), it may be described by the following asymptotic formula [29]

$$U_b - E_N \approx 64 \Delta U \exp\left(-\frac{\sqrt{2}\pi}{\Omega/N} \right) \ll 1. \tag{5.3.22}$$

Correspondingly, if the driving is *moderately weak*, namely

$$\Delta U \gg A \gg U_b - E_N, \tag{5.3.23}$$

[51] When $\Omega \gg \omega_0$, the layer of transient chaos is exponentially narrow [35,60,136] while the relevant nonlinear resonances are of a high order and therefore are very narrow too. The effect of driving on the activation energy is therefore negligible.

then the nonlinear resonance mechanism for the decrease of S_a is irrelevant, so that

$$S_a \approx \delta S_a^{(ex)} \approx U_b - E_m. \tag{5.3.24}$$

Just such a situation relates to Fig. 58: $\Omega = 1.7$ while $\omega_0 = \sqrt{2}$, so that the lowest nonlinear resonance has the order $N = 2$ and the deviation of the corresponding resonant energy from the barrier level $U_b - E_2 \approx 0.01$ is much less than both $\Delta U = 0.25$ and relevant values of A. Thus, (5.3.23) is satisfied and, hence, Eq. (5.3.24) holds.

Let us now briefly discuss the narrow frequency range that remains, namely that just below ω_0,

$$0 < \omega_0 - \Omega \ll \omega_0, \tag{5.3.25}$$

and its harmonics of a moderate order,

$$\begin{aligned} &\left(\left[\frac{\Omega}{\omega_0}\right] + 1\right)\omega_0 - \Omega \ll \omega_0, \\ &1 \leq [\Omega/\omega_0], \qquad \Omega \sim \omega_0. \end{aligned} \tag{5.3.26}$$

In the frequency range (5.3.25), the regime of moderately weak driving is usually impossible: the lowest nonlinear resonance occurs close to the bottom providing that the driving is really weak; while, as the driving amplitude increases, linear response typically disappears before the layer of transient chaos reaches the energy range of the resonance.

In the frequency range (5.3.26), the lowest possible nonlinear resonance has the order $N = [\Omega/\omega_0] + 1 > 1$ and corresponds to energies close to the bottom of the well. The corresponding harmonic $q_N(E_N)$ is very small (E_N lies in the range of nearly harmonic eigenoscillation) so that the corresponding resonance is either very narrow or even nonexistent, being suppressed by the linear response. Thus, the broadest nonlinear resonance in this case, that of order $N + 1$: $\Omega/(N + 1)$, is distinctly lower than ω_0 and the relevant harmonic $q_{N+1}(E_{N+1})$ is much larger than $q_N(E_N)$ since E_N is close to U_0 while E_{N+1} is not (cf. [29]). Thus, there exists a range of driving which plays a role similar to that of *moderately weak* driving in the range (5.3.21), i.e. the layer of transient chaos absorbs the broadest nonlinear resonance and thus remains the only mechanism that decreases the activation energy.

5.3.2.3 Discussion in the contexts of directed diffusion and of the interplay between chaos and noise.

Let us discuss briefly the application of the results [84,119] reviewed above to the problem of directed diffusion in periodic potentials with weak damping [95] (cf. item B in subsection 5.3.1). The theory [95] predicts that the activation energies for escape to adjacent wells to the left and right typically differ: thus the fluxes to the left and to the right may differ exponentially strongly. Moreover, this difference grows as $\Gamma \to 0$. It follows from

the results of [84], however, that this growth saturates at least at $\Gamma \sim A/\mu_r$, i.e. well before the correction [95] to the activation energy becomes comparable with the potential barrier, which occurs at $\Gamma \sim A^2$. Furthermore, if Γ/A becomes smaller than $\mu_l^{-1} \sim 1$ (see Eq. (5.3.13)), then the difference between the activation energies disappears: a layer with mixed basins (transient chaos) is formed. As soon as the system reaches any point within this layer, it may be transported either towards the well on the left, or towards that on the right, with probabilities of the same order. But if certain space-time symmetries [131] are broken, noise-free transport within the layer may be asymmetric, at least on finite time scales, so that the pre-exponential factors may differ and a net flux may still be present despite the onset of the layer.

Finally, we set the results [84,119] in the context of studies of the interplay between chaos and noise (cf. [60]). Most of such works have studied the effect of noise on transport properties *within* a chaotic attractor/layer/web. In [137], the dependence on noise intensity for noise-induced inter-attractor hoppings in a multi-attractor map with transient chaos was studied in simulations. But neither of these works studied how transient chaos affects noise-induced escape.

5.3.3 Particular features of escape and directed diffusion in ZD systems

If, instead of the Duffing potential, we consider in Eq. (5.3.1) a potential $U(q)$ which possesses the zero-dispersion property, i.e. such that the corresponding $\omega(E)$ possesses an extremum at some energy E_e [52], then the major resonance near the extreme eigenfrequency $\omega(E_e)$ is very broad in energy and, therefore, the effect of driving of the frequency $\Omega \approx \omega(E_e)$ on the escape rate and the related directed diffusion may be expected to be especially pronounced. This expectation has been confirmed by both a theoretical analysis and simulations carried out in [119], whose results are reviewed in this sub-section.

5.3.3.1 Peaks in the spectral density of the logarithmic susceptibility.

The asymptotic formula (5.3.7), valid for $A \ll \Gamma \ll \omega(E_N)$, diverges as $d\omega(E_N)/dE_N \to 0$. To obtain the correct asymptote for this case, one needs to take account of the first non-zero term in the Taylor expansion of $\omega(E)$ in powers of $(E - E_e)$. Typically, an extremum is a maximum or a minimum, with a non-zero 2nd derivative associated with it. Near the extremum, one may use the parabolic approximation:

$$\omega(E) \approx \Omega_m + \frac{1}{2}\frac{d^2\omega(E_e)}{dE_e^2}(E - E_e)^2. \tag{5.3.27}$$

So, if the driving frequency Ω is close to $N\Omega_m$, one obtains from (5.3.4)-(5.3.6),(5.3.27)

[52] In other sections, such an energy was denoted E_m (see e.g. Eq. (1.0.5)), but we cannot use the latter in sub-section 5.3 since we had to use this notation in 5.3.1 in a different context (see footnote 47 above and the text preceding its citation) following [95] whose figure, using this notation, is reproduced here as Fig. 54.

$$
\begin{aligned}
&|\tilde{\chi}(\Omega)| \approx |\tilde{\chi}^{(ZD)}(\Omega)| \qquad (5.3.28)\\
&\equiv |\dot{Q}_N(E_e) \int\limits_{-\infty}^{\infty} dt \cos\left((\Omega - N\Omega_m)t - \frac{2d^2\omega(E_e)/dE_e^2[\Gamma\Omega_m I(E_e)]^2}{3N}t^3\right)|\\
&= C_{\rm scale}^{(ls)}|{\rm Ai}(-\Delta\Omega_N^{(ls)})|,\\
&C_{\rm scale}^{(ls)} = \frac{2\pi|\dot{Q}_N(E_e)|}{\Delta\Omega_N^{(ZD)}},\\
&\Delta\Omega_N^{(ls)} = {\rm sgn}(d^2\omega(E_e)/dE_e^2)\frac{\Omega - N\Omega_m}{\Delta\Omega_N^{(ZD)}},\\
&\Delta\Omega_N^{(ZD)} = \left(\frac{2|d^2\omega(E_e)/dE_e^2|[\Gamma\Omega_m I(E_e)]^2}{N}\right)^{1/3},
\end{aligned}
$$

where ${\rm Ai}(x)$ is the Airy function [49]; we have used an explicit expression [135] for the integral in the 2nd line of (5.3.28).

Eq. (5.3.28) provides a universal description of zero-dispersion peaks in the spectra of the *logarithmic* susceptibility; cf. Eq. (3.3.19) which provides a universal description of ZDPs in spectra of the conventional susceptibility [7,46].

The shape of the peak, given by the modulus of the Airy function, is shown in Fig. 59. It is strongly asymmetric: one of its wings decays rather fast while the other wing oscillates between some slowly decaying upper limit and zero, which is a consequence of an interference between relevant contributions from different parts along the MPEP.

The magnitude of the peak, $C_{\rm scale}^{(ls)}$, is proportional to $\Gamma^{-2/3}$. It therefore grows with decrease of Γ slightly faster than the conventional peak related to oscillations in the bottom of the potential well [95] (which $\propto \Gamma^{-1/2}$: see Eq. (5.3.8)). The widths of each sub-peak, as well as of the peak as a whole, are $\propto \Gamma^{2/3}$, and thus tend to zero as $\Gamma \to 0$, unlike the width of the "bottom" peak (which remains finite in the underdamped limit: cf. Figs. 54, 60).

Obviously, Eq. (5.3.28) assumes: (i) that the width of the peak is much less than the frequency of the maximum; and (ii) that the peak is well separated from other peaks in the spectrum. Both of these requirements are satisfied in the asymptotic limit $\Gamma \to 0$, which is well demonstrated by the insets in Fig. 60, presenting $|\tilde{\chi}(\Omega)|$ for the escapes to the left and to the right (denoted $\tilde{\chi}^{(-)}$ and $\tilde{\chi}^{(+)}$ respectively) in the periodic potential shown in Fig. 61(a). The relevant peak relates to $N = 1$ and to the local maximum [53] Ω_m in $\omega(E)$ shown in Fig. 61(b). At $\Gamma = 10^{-3}$ (Fig. 60(c)), the asymptotic formula nicely describes the first two sub-peaks. Sub-peaks with higher ordinal number are lower than the corresponding sub-peaks according to the asymptotic formula since the shape of the latter assumes a purely parabolic shape of $\omega(E)$ within a broader range of energies than occurs in reality. At $\Gamma = 10^{-2}$ (Fig. 60(b)), the width of each sub-peak becomes about 5

[53] The local minimum at $\Omega_m^{(1)}$ is so sharp that the relevant range of energies is very narrow and, given that $\Omega_m^{(1)}$ is rather close to Ω_m, the contribution from this range of energies at the values of Γ explored in Fig. 60 is negligible in comparison with that from the range related to the local maximum.

times larger and only the first few of them can be manifested in the spectrum since those of higher ordinal number would involve energy ranges which, in reality, are much beyond the range relevant to the local maximum in $\omega(E)$. Nonetheless, the description of the first (i.e. highest) sub-peak by the asymptotic formula is satisfactory. The value related to Fig. 60(a), $\Gamma = 10^{-1}$, definitely exceeds the upper limit for the validity of Eq. (5.3.28) but, even at this Γ, the peak in $|\tilde{\chi}^{(-)}(\Omega)|$ still exists and, moreover, is qualitatively described by Eq. (5.3.28).

One can also see some manifestation of ZDPs on the 2nd and 3rd harmonics, especially in Fig. 60(c). However, at the given range of Γ they interfere strongly with contributions from other energy ranges, as we now discuss.

5.3.3.2 Directed diffusion in the asymptotic limit $A \to 0$.

As was briefly demonstrated in sub-section 5.3.1, the interference between different harmonics of $|\tilde{\chi}|$ (5.3.4)-(5.3.6) for asymmetric [54] periodic potentials may give rise to inequality of the spectral densities related to escape to the left or to the right, leading in turn to the onset of directed diffusion.

We demonstrate below both qualitatively and by means of numerical calculations that, similarly to the non-ZD case, the difference between $|\tilde{\chi}^{(-)}|$ and $|\tilde{\chi}^{(+)}|$ under ZD conditions also oscillates as $\Gamma \to 0$, but the amplitude of the oscillations is typically larger. Indeed, as shown in section A above, the ZD contribution $\tilde{\chi}^{(ZD)}$ into $\tilde{\chi}(\Omega = N\Omega_m)$ (5.3.4)-(5.3.6) (i.e. the contribution made to the integral (5.3.4) by the Nth harmonic in the range of t close to t_e where t_e corresponds in (5.3.5) to $E(t_e) = E_e$) is $\propto \Gamma^{-2/3} \overset{\Gamma \to 0}{\to} \infty$. Contributions from other energy ranges, including in particular those related to other harmonics, are typically $\propto \Gamma^{-1/2}$ (see Eq. (5.3.7)), i.e. they grow slower as $\Gamma \to 0$. Therefore, the ZD contribution dominates as $\Gamma \to 0$. Let the second largest (absolute) contribution to $\tilde{\chi}(N\Omega_m)$ correspond to some harmonic $n = n_s$ while the range of t is close to t_{n_s}, where t_{n_s} corresponds to such $E(t_{n_s})$ in (5.3.5) that $n_s\omega(E(t_{n_s})) = N\Omega_m$. As $\Gamma \to 0$, the relevant angle differences projected onto the 2π range, namely

$$\Delta\psi^{(\pm)} \equiv N\psi^{(\pm)}(t_e) - n_s\psi^{(\pm)}(t_{n_s}) + N\Omega_m(t_{n_s} - t_e) \\ -2\pi\left[\frac{N\psi^{(\pm)}(t_e) - n_s\psi^{(\pm)}(t_{n_s}) + N\Omega_m(t_{n_s} - t_e)}{2\pi}\right],$$

oscillate between 0 and 2π, and the smaller Γ is, the faster these oscillations in Γ become, with a period $\propto \Gamma^2$. Moreover, if the potential is asymmetric, then the difference between $\Delta\psi^{(+)}$ and $\Delta\psi^{(-)}$ also oscillates; and the smaller Γ, the faster the oscillations become.

Thus, as Γ decreases, the situation when the (relatively small) non-ZD contribution is extracted from the (much larger) ZD one alternates with the situation when the contributions are added to each other. Moreover, in the asymmetric potential this alternation

[54] The asymmetry is essential only for the case of a *monochromatic* periodic force while, in case of a multi-harmonic periodic force, directed diffusion may also arise in symmetric potentials [95].

occurs differently for escape to the left and to the right. So, the direction of the diffusion alternates as well provided that A is still $\ll \Gamma$. In fact, this conclusion is not restricted to the ZD case but is valid generally: some evidence in support of it was contained earlier in [95] (see Fig. 54 above, reproducing Fig. 1 from [95]). But, in the ZD case, the amplitude of the oscillations of $|\tilde{\chi}^{(+)}| - |\tilde{\chi}^{(-)}|$ may be larger. Indeed, this amplitude is equal to the doubled contribution from the time range near t_{n_s} in the n_s harmonic, $2|\tilde{\chi}_{n_s}|$, while a similar contribution in the non-ZD case dominates in $\tilde{\chi}$. Thus the difference between $|\tilde{\chi}^{(+)}|$ and $|\tilde{\chi}^{(-)}|$, which arises because of the different results of interference with the next (by absolute value) contribution, is obviously smaller than $2|\tilde{\chi}_{n_s}|$.

The strong interference between the 2nd ZDP harmonic and the fundamental, and between the 3rd ZDP harmonic and the fundamental, are well seen [55] in Fig. 60. The alternation of the sign of $|\tilde{\chi}^{(+)}| - |\tilde{\chi}^{(-)}|$ (as Ω or Γ vary) is also obvious from Fig. 60.

5.3.3.3 Underdamped limit.

Consider first the asymptotic limit $A \to 0$. Similarly to the conventional case, the decrease of activation energy caused by the resonant mechanism as A increases, or Γ decreases, may be expected to saturate at $A \sim \Gamma$: Eq. (5.3.17) is valid in the ZD case too if we exchange E_N for E_e. However the characteristic width ΔE_r of the energy band which makes the major contribution to the resonant mechanism is larger than in the conventional case: as in all zero-dispersion phenomena, the resonance covers a broader band of energies than in the conventional case. More concretely, ΔE_r is larger due to the time t_r during which $\dot{Q}(t)$ stays in resonance with the relevant harmonic of the periodic driving force, i.e. the time during which the argument of the cosine in the integral in (5.3.28) has an absolute value $\stackrel{\sim}{<} \pi$, is larger: $t_r \sim (\Delta\Omega_N^{(ZD)})^{-1} \propto \Gamma^{-2/3}$. Correspondingly,

$$\Delta E_r \sim \Gamma\Omega_m I(E_e) t_r \propto \Gamma^{1/3}. \tag{5.3.29}$$

The width of the nonlinear resonance ΔE_{nr} which comes into play as $\Gamma/A \to 0$, is of the same order of magnitude as ΔE_r (5.3.29) at the onset of saturation (i.e. at $\Gamma \sim A$): cf. [67,68], or Sec. 4.1 above. Thus, in the asymptotic limit $A \to 0$, the maximal decrease in activation energy as Γ varies is larger than in the conventional case: $(-\delta S_a)_{\max} \sim \Delta E_{nr} \sim \Delta E_r(\Gamma \sim A) \propto A^{1/3}$ (cf. the conventional case, where it is $\propto A^{1/2}$).

The most important difference between the ZD and conventional cases is manifested in the range of *moderately* weak damping. Unlike the conventional case, the variation of eigenfrequency over a broad band of energies far from the bottom may be very small: cf. Fig. 61. Correspondingly, the energy width of a nonlinear resonance may be very large (it may be comparable with the barrier height) while the linear response still exists. Moreover, if the driving frequency is close to the relevant extremal eigenfrequency Ω_m, then the relevant layer of transient chaos goes down very deep into the well while the

[55] The interference between the 1st ZDP harmonic and the fundamental are seen only in Fig. 60(a) while, at smaller values of Γ which relate to the figures (b) and (c), the range of energies close to E_e is the only range which contributes to the frequency range close to Ω_m so that the ZDP contribution has nothing to interfere with.

driving amplitude is still quite small. This is attributable to the reconnection between the chaotic layer around the original separatrix and the layers around separatrices of the nonlinear resonances (cf. Sec. 4.3.2 above). Altogether, the mixed mechanisms of nonlinear resonance and the chaotic layer give rise to a very significant reduction of the activation energy even for rather weak driving. Let us now examine this in more detail.

Consider first the evolution of the layer of transient chaos as A increases. Generalizing the derivation of the asymptotic expression for μ_l (5.3.14) related to the Duffing oscillator [60], one can derive the following formula for the critical value A/Γ at which a homoclinic tangle arises in an *arbitrary* potential system perturbed by a linear friction and sinusoidal force,

$$\mu_l \equiv \left(\frac{A}{\Gamma}\right)_c = \frac{2\int_{-\infty}^{\infty} dt\ \dot{q}_s^2(t)}{\sqrt{\left(\int_{-\infty}^{\infty} dt\ \dot{q}_s(t)\cos(\Omega t)\right)^2 + \left(\int_{-\infty}^{\infty} dt\ \dot{q}_s(t)\sin(\Omega t)\right)^2}}, \tag{5.3.30}$$

where $\dot{q}_s(t)$ is the velocity on the separatrix for unperturbed motion in the potential, i.e. without friction or periodic driving; the origin of time axis t may be chosen arbitrarily. For the periodic potential drawn in Fig. 61(a), the dependence $\mu_l(\Omega)$ (5.3.30) is shown in Fig. 62. Though it possesses distinct differences from the case of the Duffing oscillator (unlike the latter case, $\mu_l(\Omega)$ for a periodic potential does not diverge as $\Omega \to 0$), its major property in the present context remains the same: $\mu_l(\Omega) \sim 1$ in the relevant range $\Omega \sim \Omega_m \sim \omega_0$.

Though the onset of the homoclinic tangle is not related to the ZD property, its further evolution, as the driving amplitude increases, possesses in a ZD system a remarkable feature that is not typical of a conventional system: the reconnection between the chaotic layer around the barrier level with the layers around the separatrices of the ZDNRs starts at a very small driving amplitude provided that $\Omega \approx \Omega_m$ (cf. Sec. 4.3.2 above). It causes a drastic lowering of the minimal energy in the layer of transient chaos which provides transport beyond the barriers. Fig. 63 clearly demonstrates this feature for the ZD system shown in Fig. 61: if the driving frequency is far from the extremal eigenfrequency $\Omega_m \approx 0.658$ and its harmonics, then a significant decrease in activation energy (for a value $\sim \Delta U$) requires a relatively large driving amplitude, $A \sim 0.1$; whereas, if Ω is only slightly smaller than Ω_m, then such a decrease occurs in a jump-wise manner at a much smaller amplitude, $A = 0.005$.

But, as discussed in the last paragraph of item (2) of Sec. 5.3.2.1 above, the jumps in E_m do not result in jumps of either δS_a or even of E_{ex}. On the other hand, the value of A at which the jump in $U_b - E_m^{(nd)}$ (or in $U_b - E_m$ if Γ is not small enough) occurs due to the reconnection with the major ZDNRs indicates the range of A in which the growth of $-\delta S_a(A)$ saturates or significantly slows. The value of $U_b - E_m^{(nd)}$ after the jump indicates the order of magnitude of $-\delta S_a(A)$ in the range of A where its growth is saturated. These qualitative conclusions are in a good agreement with the results of simulations, presented in Fig. 64. We stress also that, despite the equality (in the relevant range of A) of the activation energies for escape to the left and to the right, the prefactors are still different due to the asymmetry of noise-free transport in the chaotic layer (cf. [131]), so that the directed diffusion is still present and, obviously, the significant decrease of the activation

energy results in a drastic increase of the net flux.

5.3.4 Conclusions and unsolved problems

Thus, the initial work [119] has shown immediately that the decrease in activation energy caused by periodic driving is strongest in ZD systems. The effect is especially pronounced if the driving frequency is close to the relevant extreme eigenfrequency while the driving is moderately weak: the major nonlinear resonances (ZDNRs) are then very wide in energy and, in addition, chaotic layers associated with their separatrices reconnect the chaotic layer associated with the barrier level. Consequently, the activation energy may be substantially reduced, even by periodic driving that is relatively weak.

But there obviously remain many interesting unsolved problems and barely studied issues. We mention, in particular that –

(1) Given that the largest decrease of the activation energy under the action of periodic driving occurs in strongly underdamped ZD systems, the most important task is to create a theoretical method to describe δS_a quantitatively for the ZD case in the *underdamped limit*. Given that the major contribution comes from the energy range of the major ZDNRs, where the variation of eigenfrequency is small, we hope it may be possible to introduce a proper pair of slow variables (e.g. slow action–slow angle) and to use the method of optimal fluctuations in the plane of these variables.
(2) It is a challenging problem to create a quantitative theory for the range $\Gamma \sim A$, where neither of the approximations described above can be used for a quantitative description. At present, we cannot even suggest an approach to the solution of this problem.
(3) Explicit formulae that would estimate quantitatively the overlap of the ZDNRs with the chaotic layer associated with the barrier level are desirable. They would allow one to estimate even more easily the value of A at which the growth of $-\delta S_a$ with A saturates, as well as the order of magnitude of the, in a sense, optimal driving amplitude. They would also allow one to calculate more accurately the optimal difference between the driving frequency and the extremal eigenfrequency, and to estimate the corresponding decrease in activation energy.
(4) A theoretical evaluation of the prefactor in the escape rate is obviously important, but this problem appears to be a very difficult one.
(5) It is certainly necessary to undertake more detailed experimental studies, in a wide range of systems and driving force parameters, both for the escape rate and for directed diffusion. This seems to be especially important, given that a quantitative theoretical description exists so far only for some of the regimes.
(6) It would be interesting to study characteristic features of escape and directed diffusion under periodic driving in periodic potentials that have more than one barrier within the period (cf. various related aspects in [138] and in subsubsection 4.3.2). These nearly always possess the ZD property: cf. subsections 2.1 and 2.2.

5.4 Weak noise: noise-induced escapes from nonlinear resonances

We now consider noise-induced escape from nonlinear resonances, i.e. from metastable states generated by the periodic driving itself; note the distinction from the previous sub-section 5.3, where we considered the influence of periodic driving on noise-induced escape from a metastable potential well that exists independently of the driving. Provided the driving force is weak, slow motion within the nonlinear resonance reduces to the motion of the auxiliary autonomous Hamiltonian system (see Sec. 4). Similarly, the original escape problem in the non-autonomous system also reduces to the escape problem in the autonomous one. The most interesting case arises when more than one nonlinear resonance is involved, which is precisely the situation for ZDNR. In contrast to motion in a multi-well potential, subject to linear friction and white noise, where the escape problem has been well understood and a unique solution can be rigorously found [133,138], the possibilities for finding a rigorous solution in the search for the most probable escape path from a non-potential multi-basin state are much more limited. The work [139] presents a profound study of caustics, cusps and other singularities encountered by the flow of optimal paths. However, the conclusions of [139] are not directly applicable to the present problem of an escape to beyond the *boundary of a multi-basin state*. So, we hope that, apart from applications to the particular model investigated by us, our initial numerical results [78] may stimulate an extension of the general analysis carried out in [139].

The sub-section is arranged in the following way. Sec. 5.4.1 presents the reduction of the original non-autonomous stochastic equations to the corresponding autonomous ones for slow variables, and it describes the method of optimal fluctuation in application to this problem. Sec. 5.4.2 provides numerical results for the most probable escape path in the case of the TDO, taken as a typical example of a ZD system, and compares them with the results of simulations. Concluding remarks and a discussion of unsolved problems are given in Sec. 5.4.3.

5.4.1 Fluctuational transitions in a ZD oscillator driven by a quasi-periodic force with fluctuating angle

As described above in Sec. 4, a nonlinear oscillator subject to a periodic force generally possesses nonlinear resonances, i.e. stable states generated by the periodic force itself; in the case of a ZD oscillator, slow motion within these resonances is essentially different from that of a conventional oscillator. If, in addition, the system is perturbed by weak noise, the states generated by the periodic force become metastable: escape may then occur under the influence of the noise. The most general features of such an escape are qualitatively similar for any type of noise. However, it is easiest to study them for the case when noise is applied to the angle of the driving force [56] rather than being additive as in the previous sub-sections 5.1–5.3. Apart from being convenient for theoretical studies in the present context, a fluctuating angle is typical of the fields generated by a variety of real sources including e.g. lasers and electromagnetic generators [141].

[56] The escape problem in the presence of such noise was studied in [140] for the case of a conventional (i.e. non-ZD) weakly nonlinear oscillator.

Thus, we shall consider the following model:

$$\begin{aligned} &\ddot{q} + \Gamma\dot{q} + dU/dq = h\cos(\omega_f t + \varphi(t)), \\ &\dot{\varphi} = -f(t), \\ &\langle f(t)\rangle = 0, \qquad \langle f(t)f(0)\rangle = 2D\delta(t), \end{aligned} \tag{5.4.1}$$

where $U \equiv U(q)$ is the potential of a ZD oscillator, i.e. the eigenfrequency ω possesses one or more extrema as a function of energy (or, correspondingly, as a function of action).

This model differs from those considered in Sec. 4 (cf. for example Eq. (4.2.3)) through the presence of the noise term in the equation for the angle, namely the instantaneous frequency of the sinusoidal driving force is subject to white noise. Similarly to the noise-free case, we may separate the slow and fast variables, so that the dynamics of the slow variables of the oscillator, the action I and the slow angle $\tilde{\psi} \equiv \psi - \omega_f t - \varphi(t)$, are described by the following equations

$$\begin{aligned} &\dot{I} = -\frac{\partial\overline{H}}{\partial\tilde{\psi}} - \Gamma I, \quad \dot{\tilde{\psi}} = \frac{\partial\overline{H}}{\partial I} + f(t), \\ &\overline{H} \equiv \overline{H}(I,\tilde{\psi}) = \int_0^I d\tilde{I}\ (\omega(\tilde{I}) - \omega_f) - hq_1(I)\cos(\tilde{\psi}), \end{aligned} \tag{5.4.2}$$

which differ from (4.2.4) only through the noise term in the equation for $\dot{\tilde{\psi}}$. It causes the stable states of the noise-free system (the most relevant of which correspond to nonlinear resonances of the original system) to become metastable.

As in the problem of field-enhanced escape from a potential well, considered above in sub-section 5.3, we shall consider here only the exponential factors in the escape probabilities. We shall again use the method of optimal fluctuation (for complementary reviews of its various modifications, see [132,54]) but in a variant that differs slightly from the one used in sub-section 5.3.

The method of optimal fluctuation makes use of the fact that the probability density functional $\mathrm{P}[f]$, characterizing the probabilities of different realizations of the random force $f(t)$, depends on noise intensity D in an activation-like manner:

$$\mathrm{P}[f] = \exp\left(-\frac{S[f]}{D}\right), \tag{5.4.3}$$

where the functional S does not depend on D. In the particular case of white noise, the functional $S[f]$ is of the following form [142]

$$S[f] = \frac{1}{4}\int_0^\infty dt f^2(t). \tag{5.4.4}$$

The escape probability is the path integral [142] over all trajectories starting in the attractor and ending on the relevant boundary (e.g. the boundary of its basin of attraction), taken with the statistical weight (5.4.3)-(5.4.4):

$$W = \int \tilde{D}f(t)\mathrm{e}^{-\frac{S[f]}{D}}. \tag{5.4.5}$$

Because of the smallness of D, the functional $\mathrm{P}[f]$ is very sharp, so that

$$W = F_{\mathrm{pre}}(D)\mathrm{e}^{-\frac{S_{\min}}{D}}, \tag{5.4.6}$$

where the so called prefactor F_{pre} depends on D relatively weakly (typically as a power law), while the major dependence is determined by the exponential (activation) factor. The so called *activation energy* $S_{\min}$ is the minimum of $S[f]$ over all relevant trajectories and over the time t. Given that the dynamical variables are related to $f(t)$ via the equations of motion (Eqs. (5.4.2) in our case), the minimization of $S[f]$ may be formulated as a variational problem [134]: cf. for example sub-section 5.3 above. However, unlike the potential case – where $f(t)$ may easily be expressed from the equations of motion via the generalized coordinate and its first and second time derivatives, so that one may seek the absolute minimum of the corresponding functional (cf. Eq. (5.3.2)) – the dynamical variable $\tilde{\psi}$ in the present case is expressed in terms of the conjugated variable I, and its derivative $\dot{I}$, in a rather complicated manner. Correspondingly, the Euler equation turns out very complicated and inconvenient for numerical analysis. An alternative approach is to formulate the minimization problem as a *conditional* one [134]. Namely, it follows from (5.4.2), (5.4.4)-(5.4.6) that

$$\begin{aligned} &S_{\min} = \min_{[I(\tau),\tilde{\psi}(\tau)],t} S, \qquad S = \int_0^t d\tau\ L(I,\tilde{\psi},\dot{\tilde{\psi}}), \\ &L = \frac{1}{4}(\dot{\tilde{\psi}} - \frac{\partial\overline{H}}{\partial I})^2 = \frac{1}{4}(\dot{\tilde{\psi}} + \omega_f - \omega(I) + h\frac{dq_1}{dI}\cos(\tilde{\psi}))^2, \end{aligned} \tag{5.4.7}$$

with the additional condition, following from the first equation in (5.4.2),

$$\dot{I} + \frac{\partial\overline{H}(I,\tilde{\psi})}{\partial\tilde{\psi}} + \Gamma I = 0. \tag{5.4.8}$$

The most probable escape path (MPEP) $[I(\tau),\tilde{\psi}(\tau)]$ should satisfy the following initial conditions [57],

$$I(0) \approx I_f, \qquad \tilde{\psi}(0) \approx \tilde{\psi}_f, \tag{5.4.9}$$

[57] We use in (5.4.9) the notation "$\approx$" instead of the exact equality because, in reality, the MPEP may emerge from the focus itself *infinitely slowly*. Thus, in real calculations, one should slightly shift the starting point of the MPEP.

where the subscript f denotes the relevant focus of the system (5.4.2) in the absence of noise ($f(t) = 0$).

The condition for an ending point of the MPEP may vary. Typically, one solves the problem of escape to beyond some boundary [58], so that S should be minimized over the position of the ending point on the boundary. Such a minimization can often be done explicitly: see Sec. 5.4.2 below.

The necessary condition for the minimum over time is:

$$\frac{\partial S}{\partial t} = 0. \tag{5.4.10}$$

The minimization over a path (with a given t) with an additional condition may be formulated as the variational problem for an *absolute* minimum, by the introduction of an additional auxiliary function $\lambda(t)$ (sometimes called an "indefinite multiplier") [134]. One therefore has to seek the absolute minimum for the auxiliary functional

$$\begin{aligned} \tilde{S} &= \int_0^t d\tau\ \tilde{L}(I, \tilde{\psi}, \dot{\tilde{\psi}}), \\ \tilde{L} &= L + \lambda(\tau)(\dot{I} + \frac{\partial \overline{H}}{\partial \tilde{\psi}} + \Gamma I), \end{aligned} \tag{5.4.11}$$

where the auxiliary Lagrangian function $\tilde{L}$ differs from the original function L (5.4.7) through the product of an unknown auxiliary function $\lambda(\tau)$ and the left-hand side of the Eq. (5.4.8). The MPEP $[I(\tau), \tilde{\psi}(\tau)]$ and the auxiliary function $\lambda(\tau)$ may be found from the corresponding Euler equations together with the condition (5.4.8). We use an alternative Hamiltonian method, however, in close analogy with [140]. As is well known from mechanics [1], an alternative way to describe the dynamics of a system governed by the minimum principle is to use Hamiltonian equations: for more than one degree of freedom, the Hamiltonian method is often more convenient than the Lagrangian (Euler) one. With this aim, one has to introduce the Hamiltonian function $\tilde{H}(p_i, x_i)$, which is written in terms of generalized coordinates x_i and momenta p_i [1]:

$$\begin{aligned} p_i &= \frac{\partial \tilde{L}}{\partial \dot{x}_i}, \\ \tilde{H} &= \sum_i \dot{x}_i \frac{\partial \tilde{L}}{\partial \dot{x}_i} - \tilde{L}, \end{aligned} \tag{5.4.12}$$

where the velocities $\dot{x}_i$ in the second equation in (5.4.12) are assumed to be expressed via the sets of coordinates $\{x_j\}$ and momenta $\{p_j\}$ from the first equation in (5.4.12).

[58] In mathematical literature, it is often called the *first-passge* problem.

In the case of the Lagrangian $\tilde{L}$ (5.4.11), the generalized coordinates are I and $\tilde{\psi}$. After substituting $\tilde{L}$ (5.4.11) into (5.4.12), we end up with a Hamiltonian which does not depend explicitly on λ:

$$\tilde{H} \equiv \tilde{H}(I, \tilde{\psi}, p_I, p_{\tilde{\psi}}) = p_{\tilde{\psi}}^2 + p_{\tilde{\psi}} \frac{\partial \overline{H}}{\partial I} - p_I (\frac{\partial \overline{H}}{\partial \tilde{\psi}} + \Gamma I), \tag{5.4.13}$$

where $\overline{H} \equiv \overline{H}(I, \tilde{\psi})$ is given in (5.4.2).

The condition (5.4.10) can be shown (cf. e.g. [138,140]) to be equivalent to

$$\tilde{H}(I, \tilde{\psi}, p_I, p_{\tilde{\psi}}) = 0. \tag{5.4.14}$$

Thus, the problem of the MPEP reduces to the solution of the Hamiltonian equations

$$\dot{p}_I = -\partial \tilde{H}/\partial I, \qquad \dot{p}_{\tilde{\psi}} = -\partial \tilde{H}/\partial \tilde{\psi}, \qquad \dot{I} = \partial \tilde{H}/\partial p_I, \qquad \dot{\tilde{\psi}} = \partial \tilde{H}/\partial p_{\tilde{\psi}}, \tag{5.4.15}$$

on the zero-$\tilde{H}$ surface (5.4.14) while I and $\tilde{\psi}$ at the beginning and end of the MPEP lie respectively at the focus and at the proper state on the relevant boundary.

Generally, such an MPEP and the action S (5.4.7) along it, which constitutes the activation energy $S_{\min}$, should be found numerically by a shooting method [59]. A major difficulty which may arise in a numerical search for $S_{\min}$ is that there are typically *many*, often infinitely many, extremals i.e. solutions of the Hamiltonian equations lying on the zero-$\tilde{H}$ surface and providing for the connection between given states in the $I - \tilde{\psi}$ plane. Correspondingly, there are many values of the shooting parameter which provide for an extremal. So far, unfortunately, there are no rigorous rules in the non-potential case [60] that would allow one to single out the range of the shooting parameter in which lies only one value corresponding to an extremal, namely to that extremal whose projection onto the $I - \tilde{\psi}$ plane provides the *absolute* minimum of action. At the same time, there are some rigorous rules which significantly reduce the number of extremals whose projections may pretend to be the MPEP, or may even provide for the unique choice. Examples will be presented in Sec. 5.4.2 below.

[59] Two of the initial conditions required for the four differential equations (5.4.15) are fixed by the conditions (5.4.9) (note however footnote 57). If one of the other initial conditions can be determined, then the remaining initial condition will also be fixed due to the condition (5.4.14). Integrating equations (5.4.15), one should check whether the projection of the trajectory onto the $I - \tilde{\psi}$ plane passes (at any time) close to the given final state. Typically one does not fix a time of integration. Rather the equations are integrated until the projection of the trajectory either reaches a close vicinity of the given final state or, on the contrary, goes far away from the relevant region. Thus there is only one parameter (any combination of the initial conditions) that needs to be matched. Usually, it is possible to choose this parameter as some angle whose full range of variation is 2π. So, one needs to try a large number of values from this range. Their choice is, in a sense, arbitrary: they are effectively "shot", whence the terminology of *shooting method* and *shooting parameter* respectively.

[60] For the potential case, such rules have been derived in [138].

If the damping parameter Γ is sufficiently small that, not only is the original motion (5.4.1) underdamped, but even the motion of the averaged system (5.4.2) is underdamped, then the activation energy may be found explicitly by a different method, using the averaged Fokker-Plank equation. So also can the prefactor (cf. the case of a non-ZD weakly nonlinear oscillator [140]). However, an explicit calculation of this kind for the present (ZD) case has not yet been achieved. In the next sub-section we concentrate instead on the case of a basin of attraction with two saddles, inner and outer, a situation that is of greatest interest when the slow motion is *not* underdamped.

5.4.2 Numerical calculations and simulations for the case of the tilted Duffing oscillator

As an example of a periodically driven weakly dissipative ZD system, we shall again use the tilted Duffing oscillator (TDO) driven by a sinusoidal force and subject to linear friction, with parameters as in Fig. 21(b). As can be seen from this figure, the basin of attraction of one of the nonlinear resonances is encompassed by the basin of the other resonance. We shall be interested in two kinds of escape, which we consider in turn –

(a) Escape from a single basin of attraction and transition to a neighbouring attractor.

The activation energy related to the transition from an attractor to its neighbouring attractor is equal to that related to the escape beyond the boundary dividing their basins of attraction. Indeed, as soon as the system reaches the boundary, the further transition to the neighbouring attractor can follow a noise-free trajectory towards it, so that S (5.4.4) is not being increased any more. We shall consider further only MPEPs beyond boundaries of basins of attraction, while bearing in mind that they constitute the activation energies both for the escapes and for the transitions between the corresponding attractors.

It can be shown [129] that the action S, as a function of the ending state on the boundary of the basin of attraction, decreases as the ending state moves towards the saddle, reaching its minimum on the saddle itself. In the case of a single basin, the saddle is for certain reachable for the flow of optimal paths since the caustic emanates just from the saddle [139]. Thus the MPEP from a single basin of attraction ends on the saddle of the basin (in real calculations, one should slightly shift it from the very saddle since the latter is approached by the MPEP infinitely slowly [139]):

$$I(t) \approx I_s, \qquad \tilde{\psi}(t) \approx \tilde{\psi}_s. \tag{5.4.16}$$

Fig. 65 shows the corresponding MPEPs $[f_1 \to s_1]$, $[f_2 \to s_1]$,$[f_2 \to s_2]$, calculated by means of Eqs. (5.4.13)-(5.4.15) with the corresponding initial and final conditions (5.4.9), (5.4.16). The activation energy $S_{\min}$ (5.4.7) along the MPEPs is equal respectively

$$S_{\min}^{(12)} \approx 0.00293, \qquad S_{\min}^{(21)} \approx 0.0118, \qquad S_{\min}^{(23)} \approx 0.01. \tag{5.4.17}$$

It is worth pointing out that the activation energies differ from the difference between the values of the resonance's Hamiltonian $\overline{H}$ at the corresponding saddle and focus: for example, $\overline{H}(I_{s_1}, \tilde{\psi}_{s_1}) - \overline{H}(I_{f_1}, \tilde{\psi}_{f_1}) \approx 0.0021$, which clearly differs from $S_{\min}^{(12)}$. This is

in contrast to the case of a Hamiltonian of the potential type [61], where the activation energy is simply equal to the height of the potential barrier (i.e. to the difference between the corresponding values of the Hamiltonian).

(b) Escape from the nonlinear resonance area as a whole and direct transition from the inner nonlinear resonance to the linear response attractor.

Mathematical aspects of the problem of noise-induced escapes/transitions in multi-attractor systems have been considered in the monograph [132]. The most important result in the present context is that, if the noise is sufficiently weak, then the dynamics of inter-attractor transitions may be described on exponentially long time-scales by simple kinetic equations with constant inter-attractor rates $\alpha_{ij} \propto \exp(-S_{\min}^{(ij)}/D)$. If one restricts oneself to the evaluation of exponential factors only, one may equivalently consider the problem with an *absorbing* boundary around the basin of attraction of the final attractor. A detailed analysis of the flux dynamics in a 3-state system with an absorbing 3rd state is presented in [138]. Let us denote the basins of attraction of f_1 and f_2 in our system as states 1 and 2 respectively, and let the former basin be encompassed by the latter. The remaining phase space may be denoted as 3. The activation energies $S_{\min}^{(13)}$ and $S_{\min}^{(23)}$ in such a formal problem with an absorbing state 3 ("first-passage" problem) are equal to those for the inter-attractor transitions respectively from the the nonlinear resonances f_1 and f_2 towards the linear response, because the noise-free trajectory that exits through the boundary of the $(1+2)$-area reaches just the linear response attractor. We shall consider further only the first-passage problem, while bearing in mind its direct relation to the problem of inter-attractor transitions.

Consider, for example, the case when the system stays initially in 1. Typically, and in particular for the parameters considered here, the time t_s for the formation of quasi-equilibrium within the nonlinear resonance area as the whole $(1+2)$ is *much* shorter than the average time t_{qs} over which the area $1+2$ is depleted; the latter may be considered as the lifetime within the nonlinear resonance area $1+2$. Then, after a short initial interval t_{in} of the order of the relaxation time during which quasi-equilibrium is established in the initial state, the dynamics of the flux into 3 is described [138] (cf. also [143] where the theory is illustrated by simulations in an example potential system) by

$$J(t) \equiv J_{13}(t) \approx \alpha_{13} e^{-\frac{t}{t_s}} + \frac{1}{t_{qs}}(e^{-\frac{t}{t_{qs}}} - e^{-\frac{t}{t_s}}), \qquad (5.4.18)$$
$$t_s \ll t_{qs}, \qquad t \gg t_{in},$$

The time-scales t_s and t_{qs} can be expressed via the α_{ij}, and both are exponentially longer than t_{in} provided that the noise intensity is small: for example, for the system shown in Fig. 65, the relations $\alpha_{13} \ll \alpha_{12}$ and $\alpha_{21} \ll \alpha_{23} \ll \alpha_{12}$ are satisfied, so that [138] $t_s \approx \alpha_{12}^{-1}$ and $t_{qs} \approx \alpha_{23}^{-1}$. The first term in the expression (5.4.18) for the flux is determined by the direct transitions $1 \to 3$, while the second term is due to indirect transitions i.e. those that involve attractor 2 as an intermediate state. It follows from (5.4.18) that, at relatively small times $t < t_s \ln(t_{qs}/t_s)$, the flux is entirely due to direct transitions, $J(t) \approx \alpha_{13} \exp(-t/t_s)$; in particular, $J \approx \alpha_{13}$ if $t \ll t_s$. For times $t > t_s \ln(t_{qs}/t_s)$, indirect transitions prevail and the flux becomes quasi-stationary, $J(t) \approx t_{qs}^{-1} \exp(-t/t_{qs})$; in particular, $J \approx t_{qs}^{-1}$ if $t_s \ln(t_{qs}/t_s) < t \ll t_{qs}$.

[61] Where the friction and noise are assumed to be linear and white respectively, both entering only the equation for the generalized momentum.

We emphasize that, as the noise intensity decreases, the time-scale t_s becomes exponentially long, so that the quasi-stationary stage becomes unattainable in practice while $J \approx \alpha_{13}$ over the major part of the attainable time-scale. Thus, it is important to know the rates α_{ij}, of which α_{13} for the direct transition $1 \to 3$ is especially important.

The technique described in the previous sub-section, 5.4.1, facilitates calculation of the activation energies $S_{\min}^{(ij)}$ related to α_{ij}. It allows us: (i) to determine strong inequalities between the $\alpha_{ij} \propto \exp(-S_{\min}^{(ij)}/D)$, which in turn determine many important properties of the flux dynamics [138]; and (ii) to determine the major dependence of the flux on noise intensity, which is often quite sufficient for practical purposes.

For the set of parameters corresponding to Fig. 65, the activation energies related to α_{12}, α_{21} and α_{23} are given in Eq. (5.4.17) above. The rest of this sub-section will be devoted to the direct transition $1 \to 3$, i.e. to the search of the corresponding MPEP and $S_{\min}^{(13)}$.

It can be shown by a standard method [134] that the MPEP should either be a projection onto the plane $I - \tilde{\psi}$ of a smooth solution of Eqs. (5.4.13)-(5.4.15), or a combination of the projections of two smooth solutions for which a saddle (a singularity point for projections of the smooth solutions) provides the end point of one solution and the starting point of the other one. It should be emphasized that, for the escape $1 \to 3$, the former option may be realized in contrast to the potential case, where the MPEP from the inner attractor to a state lying beyond its basin of attraction *necessarily* follows the saddle of an inner basin of attraction [133,138,143]. Even without the concrete calculations [138], this latter property of the MPEP in multi-well potential systems can easily be proved using the property of detailed balance, which holds in the potential systems [38]. Indeed, let us prove this by *reductio ad absurdam*. Suppose that the MPEP $[f_1 \to b]$, where b is a state beyond the basin of attraction of f_1, does *not* pass through the saddle s_1. Then, on account of detailed balance, the MPEP $[b \to f_1]$ is the time-reversal of the MPEP $[f_1 \to b]$ and therefore it should not pass through s_1 either, i.e. it should cross the boundary of the basin of attraction of f_1 at some point p_1 which differs from s_1. On the other hand, as soon as the system reaches the basin of attraction of f_1, it then most probably relaxes to f_1, independent of noise. But the noise-free trajectory from p_1, which belongs to the boundary of the basin of attraction, first relaxes to s_1 and only from there to f_1. This contradicts the initial assumption, thereby proving that the saddle s_1 is necessarily followed by the MPEP $[f_1 \to b]$.

In non-potential systems, detailed balance generally does not hold – so proofs like that in the previous paragraph are invalid. On the other hand, we have not met in the literature any example of such avoidance of an inner saddle by an MPEP [62], and one of the incentives for the work [78] was the hope of finding evidence of such saddle point avoidance. However, none has yet been found: though the projections of the smooth solutions do typically avoid the inner saddle s_1 (see the lower inset in Fig. 65), the MPEP is realized by means of the alternative option (i.e. it follows s_1), at least for the present set of parameters (Fig. 65). Given that the search for the MPEP in a non-

[62] This should be resolved from a series of works (see [144] and references therein) on the exit location distribution from a single-basin. In the latter case, deviations of the exit point from the saddle are small in the sense that they go to zero as the noise intensity goes to zero. In contrast, in the present case, the deviation of the exit point on the boundary of the inner basin from the inner saddle is assumed to be *non-zero*, however small the noise intensity.

potential system is far from trivial, we present below a more detailed description and discussion of our numerical results.

Consider first the projection of the flow of such smooth solutions of (5.4.13)-(5.4.15) whose projections emanate from f_1 while ending on the outer boundary (OB) of the basin of attraction of f_2. It turns out that a projection of any solution of such a kind hits the OB at some finite distance from s_2 (i.e. the projection of the flow of the smooth solutions encounters caustics which leaves the saddle s_2 beyond them). It can be shown (cf. [129]) that, the closer the end point on a basin boundary is to its saddle, the smaller the action along the projection of the smooth solution. Hence, we may keep as pretenders to being the MPEP only the two "edge" paths (i.e. those whose end points are as close to s_2 as possible, from the left and from the right respectively). These paths are shown in the lower inset in Fig. 65. However, even without an explicit calculation of actions, it is obvious from the figure itself that neither of these paths can be the MPEP, e.g. because both of them intersect the noise-free path $[s_1 \to f_2]$ while any path intersecting the noise-free path cannot provide a minimal action for a transition $1 \to 3$. Indeed, if such an intersection occurs in some state i, then one may construct a path that necessarily possesses an action smaller than that along the path $[f_1 \to OB]$: the auxiliary path with a smaller action may be put together from (i) $[f_1 \to s_1]$, (ii) the noise-free path from s_1 till the intersection i with the path $[f_1 \to OB]$ and, (iii) the remaining part of the latter path i.e. $[i \to OB]$. Given that $[f_1 \to s_1]$ provides minimal action for the transition from the inner attractor (i.e. f_1) to the boundary of its attraction, part (i) of the auxiliary path provides a smaller action than that along the segment $[f_1 \to OB]$ between f_1 and its intersection with the inner boundary; part (ii) contributes zero action, which must obviously be smaller than the action along the segment $[f_1 \to OB]$ between the intersection with the inner boundary and the state i; finally, part (iii) merely coincides with the remaining part of the path $[f_1 \to OB]$. Similarly, it can be shown that a path $[f_1 \to OB]$ intersecting the outer MPEP $[f_2 \to s_2]$ cannot provide the minimal action either. Similar considerations apply to selfintersecting paths.

Thus, the MPEP for the transition $1 \to 3$ should be constructed from the inner MPEP $[f_1 \to s_1]$ and the projection of a smooth solution of Eqs. (5.4.13)-(5.4.15) such that its projection starts on s_1 and ends on the OB as close to the saddle s_2 as possible, while avoiding selfintersections and intersections with the noise-free path $[s_1 \to f_2]$ or with the outer MPEP $[f_2 \to s_2]$. We have found only one path satisfying all these requirements [63] (see Fig. 65): it joins smoothly onto $[s_1 \to f_2]$ and $[f_2 \to s_2]$, analogously to the potential case [138,143]. This path must be the MPEP. The action along it, i.e. the activation energy related to α_{13},

$$S_{\min}^{(13)} \approx 0.007, \tag{5.4.19}$$

is smaller than action along either of the smooth edge paths (0.173 and 0.0376 for the left and right path respectively).

The upper inset in Fig. 65 presents a few paths $[f_1 \to OB]$ simulated *sequentially* (rather than artificially selected from a larger group of simulated paths $[f_1 \to OB]$) by computer for the noise intensity D=0.0007. They nicely concentrate near the MPEP found theoretically above. Some small regular deviations from the inner and outer

[63] Note that there are many (probably, infinitely many) solutions of Eqs. (5.4.13)-(5.4.15) whose projections connect s_1 to s_2.

saddles are due to the diffusion [144] and they vanish as $D \to 0$.

5.4.3 Concluding remarks and unsolved problems

We have reviewed the initial studies [78] of noise-induced escape from ZDNRs. Similarly to the noise-free case, the non-autonomous system has been reduced to an autonomous auxiliary one. The method of optimal fluctuation has been applied to the escape problem in the latter system, and the activation energies and the most probable escape paths (MPEPs) have been studied, theoretically and by simulations, for two characteristic types of escape: from a single nonlinear resonance and from the ZDNR area as a whole in the situation when the initial nonlinear resonance is encompassed by the other one. In the latter case, the most interesting result is that, although we had reason to anticipate avoidance of the inner saddle by the MPEP from the inner focus to the outer boundary of the outer basin, the MPEP does in fact pass through that saddle, after which it goes to the outer saddle, smoothly turning round both the noise-free trajectory from the inner saddle to the outer focus and the MPEP from the outer focus to the outer saddle.

Problems that it would be interesting to consider in the future include the following –

(1) To study escape for other sets of parameters, seeking a situation when the MPEP from the inner basin beyond the outer boundary of the outer basin is realized along a smooth path, avoiding the inner saddle rather than along two smooth paths connected at the inner saddle.
(2) To try to prove rigorously that there exists a unique extreme path connecting saddles of the multi-basin state, while avoiding selfintersections and intersections with the noise-free path emanating from the inner saddle to the outer focus, and with the MPEP from the outer focus to the outer boundary (cf. the potential case [138,143]): this would make a search of the relevant MPEP much more reliable and simple.
(3) To extend the analysis [139] of caustics and other singularities in the flow of extreme paths to the case when two (rather than one) boundaries of basins of attraction are relevant.
(4) It was found in [138,143] that the activation energy for escape from the multi-basin state of a potential system oscillates as the dissipation parameter varies, a phenomenon related to the occurence of saddle connections in the noise-free system as the parameter varies. Given that the presently used periodically driven weakly dissipative ZD oscillator also encounters numerous saddle connections as the driving frequency or other parameters vary (see Sec. 4 above), one may expect the occurrence of comparable oscillations in the activation energy, in analogy with the potential case. It would be interesting to study this.
(5) To calculate explicitly both the activation energy and the prefactor for the escape rate in the underdamped limit, using a method similar to that of [140].
(6) To consider characteristic features of the escape problem under additive noise (rather than noise applied to angle, as above).
(7) To carry out simulations of the original system, rather than just of the reduced one, which might reveal interesting new features that are absent in the reduced (slow) dynamics.

For noise-driven systems possessing a stationary distribution, the fluctuation spectrum is defined above by Eq. (3.1.5). However, periodically driven systems do not possess a stationary distribution, so that the definition of the fluctuation spectrum of any dynamical quantity φ in such systems needs to be generalized (see e.g. [141,3,106]):

$$Q_\varphi(\Omega) = \frac{1}{\pi}\mathrm{Re}\left[\int\limits_{-\infty}^{\infty} dt\ \exp(-i\Omega t)R_\varphi(t)\right], \tag{5.5.1}$$

$$R_\varphi(t) \equiv \lim_{\tau_l\to\infty}\frac{1}{2\tau_l}\int\limits_{-\tau_l}^{\tau_l} d\tau\ \langle(\varphi(t+\tau)-\langle\varphi(t+\tau)\rangle)(\varphi(\tau)-\langle\varphi(\tau)\rangle)\rangle,$$

$$\varphi(t) \equiv \varphi(q(t),p(t)).$$

Here, $\langle\varphi(t)\rangle$ is the quantity $\varphi(t)$ averaged over the steady distribution in the system [64] while the brackets $\langle ...\rangle$ in the pair correlator denote averaging both over the steady distribution at the instant τ and over realizations of the random force at the interval $[\tau, \tau+t]$.

To our knowledge, there have only been two brief studies of the fluctuation spectra of periodically driven ZD systems, [77,71]. They presented the results of analogue experiments and discussed them qualitatively. We now review these initial studies, providing rather more detail than in the original papers, and we discuss briefly some as yet unsolved problems.

We consider the model (5.2.2) (considered in sub-section 5.2 above in a different context). It can be shown [3,106] that, provided the noise is weak, the fluctuation spectrum in *multi-stable* systems driven by noise has the following structure:

$$Q = Q_{tr} + \sum_j \mathrm{P}_j Q_j, \tag{5.5.2}$$

where Q_{tr} is an exponentially narrow high peak due to noise-induced transitions between stable states of the noise-free system, and Q_j is a relatively broad spectral contribution from small fluctuations about the j-th stable state while P_j is its population. A theoretical description of this kind is supported by analogue experiments: see e.g. Fig. 66 reproducing a figure from [71].

It is demonstrated in Sec. 4 above that, if the driving frequency lies in the most relevant range, i.e. in the vicinity of the extremal eigenfrequency or one of its harmonics, then a periodically driven ZD system typically possesses more than one stable state. The structure of its spectrum of fluctuations therefore takes the form of (5.5.2). We shall demonstrate its characteristic features on the periodically driven TDO, as an example. Its noise-free

[64] We emphasize that the distribution is not stationary; rather it oscillates with time but the character of the oscillations is steady.

dynamics is considered in detail in Sec. 4 above; the actual parameters used are given in the caption to Fig. 21. If the driving frequency ω_f lies in between the minimal eigenfrequency ω_m and the eigenfrequency ω_0 of an oscillation in the bottom of the potential well, and the driving amplitude h is rather small, then there are three attractors in the system: see the bifurcation diagram in Fig. 24(b). Each of them is periodic in time with the period $2\pi/\omega_f$; they differ in terms of their amplitude of oscillation and by the shift of the angle from that of the driving force: the attractor with the smallest amplitude corresponds to linear response, whereas the two other attractors correspond to nonlinear resonances of the 1st order (cf. Fig. 26). We shall also need to expand $\varphi(t) \equiv \varphi(q(t), p(t))$ for each of the attractors into Fourier series:

$$\varphi^{(j)}(t) = \sum_n \varphi_n^{(j)} \exp(in\omega_f t), \tag{5.5.3}$$
$$i \equiv \sqrt{-1}, \qquad \varphi_{-n}^{(j)} = \left(\varphi_n^{(j)}\right)^*, \qquad j = 1, 2, 3.$$

Thus, all three states oscillate with the frequency ω_f and, therefore, $Q_{tr}(\Omega)$ is a narrow peak centered at $\Omega = \omega_f$. As for the spectral contributions $Q_j(\Omega)$ from small fluctuations about the stable states, it is typical for only one of them to be manifested in the spectrum because the populations P_j of two other states are exponentially smaller. Only in exceptional cases are the populations of all three states comparable with each other, so that all terms in the sum in (5.5.2) contribute significantly (cf. the middle sub-figure in Fig. 66).

Typically, the spectral contributions from small fluctuations about the stable states are well resolved from the transition peak [65] and it is convenient to study them separately, which is done below in sub-sections 5.5.1 and 5.5.2. In sub-section 5.5.3, we briefly discuss some unsolved problems.

5.5.1 Transition peak

A theoretical description of the transition peak in a bistable system is presented in [3] in a rather general context: the only limitation is that noise should be weak. The paper [106] studies such a peak in more detail, both theoretically and in analogue experiments, for the nearly resonantly perturbed symmetric single-well Duffing oscillator. Using the terminology of the present review, the transition peak in [106] may be ascribed to the transitions between the (conventional) nonlinear resonance and linear response.

[65] The only exception may concern the far wings of the transition peak, or even the whole peak if the noise is weak enough. Indeed, if oscillations about a stable state are asymmetric, which is typically the case in a multi-stable system, then small fluctuations about the stable state cause slow fluctuations of a coordinate (or any other relevant quantity) averaged over a non-dissipative oscillation around the stable state. The latter fluctuations result in the onset of a peak in the spectrum centred at ω_f. It dominates over the transition peak at least at the far wings of the latter, or even throughout the whole frequency range if the intensity of the transition peak is small: cf. the zero-frequency peak [145,50,51] in the spectrum for a system possessing a stationary distribution.

In the case of a periodically driven *zero-dispersion* oscillator, the number of coexisting stable states may be larger than two: e.g. in the TDO used as an illustration in the present sub-section, it is often three. However, when the system is subject to *weak* noise, the hierarchy of populations of the states is typically exponentially sharp. Hence, the transition peak is mostly due to transitions between the most populated state and a state which has the second largest population, while transitions involving the third state may be neglected since its population is negligible [66] . Thus, the description of the peak is nearly identical to that in [3] and rather close to the description in [106]. We present it below in brief.

Let us denote the indices of the two most populated states by k and l. The dynamics of their populations is described by a simple kinetic equation:

$$\begin{aligned} &\frac{d\mathrm{P}_k}{dt} = -(W_{kl} + W_{lk})\mathrm{P}_k + W_{lk}\mathrm{P}_l, \\ &\mathrm{P}_l = 1 - \mathrm{P}_k, \end{aligned} \tag{5.5.4}$$

where W_{kl} and W_{lk} are the transition rates $k \to l$ and $l \to k$ respectively. The initial conditions correspond to the initially populated either kth or lth state, respectively

$$\mathrm{P}_k(t=0) = 1 \qquad \text{or} \qquad \mathrm{P}_l(t=0) = 1. \tag{5.5.5}$$

The stationary solutions of Eqs. (5.5.4),(5.5.5) are

$$\mathrm{P}_k^{(st)} = \frac{W_{lk}}{W_{kl} + W_{lk}}, \qquad \mathrm{P}_l^{(st)} = 1 - \mathrm{P}_k^{(st)}. \tag{5.5.6}$$

Using (5.5.3), (5.5.6) and solutions of (5.5.4) for each of the initial conditions (5.5.5), one can obtain for the spectrum (5.5.1) (cf. [3]):

$$Q_\varphi(\Omega) = \frac{1}{\pi}\frac{W_{kl}W_{lk}}{W_{kl} + W_{lk}} \sum_n \frac{\mid \varphi_n^{(k)} - \varphi_n^{(l)} \mid^2}{(W_{kl} + W_{lk})^2 + (\Omega - n\omega_f)^2} \quad . \tag{5.5.7}$$

Given that the transition rates W_{ij} are much smaller than Ω, the partial peaks corresponding to different harmonics of ω_f practically do not overlap, so that the spectrum in the close vicinity of any of the harmonics is just a Lorenzian of halfwidth

$$\Delta\Omega = W_{kl} + W_{lk} \ll \Omega. \tag{5.5.8}$$

The transition rates depend on the noise intensity (or, equivalently, on temperature T) in an activation-like manner (see sub-section 5.4),

$$W_{kl,lk} \propto \exp(-S_{kl,lk}/T), \tag{5.5.9}$$

[66] At exceptional sets of parameters, the populations of all three states may be comparable, but we do not consider such a case here because it is, in practice, rare.

where S_{kl} and S_{lk} are the corresponding activation energies. If $T \ll S_{kl}, S_{lk}$, then the transition peaks are extremely narrow, which is why they were named [106] *supernarrow* spectral peaks.

One of the most important characteristics of the supernarrow peak is its intensity

$$
\begin{aligned}
& I_{\varphi}^{(n)} \equiv \int\limits_{n\Omega-a\Delta\Omega}^{n\Omega+a\Delta\Omega} d\tilde{\Omega}\; Q_{\varphi}(\tilde{\Omega}) \\
& \approx \frac{W_{kl}W_{lk}}{(W_{kl}+W_{lk})^2} \mid \varphi_n^{(k)} - \varphi_n^{(l)} \mid^2 \equiv \mathrm{P}_k^{(st)}\mathrm{P}_l^{(st)} \mid \varphi_n^{(k)} - \varphi_n^{(l)} \mid^2, \\
& 1 \ll a \ll \Omega/\Delta\Omega.
\end{aligned}
\tag{5.5.10}
$$

The factor a in the definition of $I_{\varphi}^{(n)}$ may be chosen arbitrarily within the range indicated in the last line of Eq. (5.5.10).

Allowing for the activation-like dependences (5.5.9) of the transition rates and for the expressions (5.5.6) for the stationary populations, one obtains

$$
I_{\varphi}^{(n)} \propto \mathrm{P}_k^{(st)}\mathrm{P}_l^{(st)} \propto (2 + x + x^{-1})^{-1}, \qquad x = \exp\left(\frac{S_{lk} - S_{kl}}{T}\right). \tag{5.5.11}
$$

The exponential x in Eq. (5.5.11) is either very small or very large, except when $\mid S_{lk} - S_{kl} \mid \lesssim T$. Beyond the latter narrow range, the intensity of the peak may be written as $I_{\varphi}^{(n)} \propto \exp(- \mid S_{lk} - S_{kl} \mid /T)$. As any parameter r (e.g. a frequency or amplitude of the driving force) varies, the activation energies typically change in opposite directions i.e. the derivatives $\partial S_{kl}/\partial r$ and $\partial S_{lk}/\partial r$ have opposite signs (cf. [106,140]). At some value of the parameter which we will denote r_0, S_{kl} and S_{lk} become equal to each other. In the vicinity of, but not too close to, r_0

$$
\begin{aligned}
& I_{\varphi}^{(n)} \equiv I_{\varphi}^{(n)}(r) \propto \exp\left(-y\right), \\
& y = \frac{\mid \partial S_{kl}(r_0)/\partial r_0 - \partial S_{lk}(r_0)/\partial r_0 \mid}{T} \mid r - r_0 \mid, \qquad y \gg 1.
\end{aligned}
\tag{5.5.12}
$$

Thus, provided T is small enough, the dependence of intensity on the parameter r is a sharp nearly cusp-like peak with a maximum at $r = r_0$; it is only "nearly cusp-like" in that it is smeared at the extreme maximum. This dependence on parameters is a characteristic feature of a *kinetic phase transition* in bistable systems [129,3,146,106], a phenomenon that was predicted theoretically in [129] and observed for the first time in [146].

Unlike the conventional case [106], when the dependence of the intensity of the transition peak on a parameter (e.g. the driving frequency) possesses just one peak, the analogous dependence in the ZD case often possesses more than one peak. This is because there may be three kinetic phase transitions corresponding to repopulation between linear response and either one of the two nonlinear resonances, as well as between the nonlinear resonances

themselves. For example, a two-peaked structure in such a dependence was observed in [77]. A detailed study of kinetic phase transitions in the ZD case and of the corresponding dependences of the intensities of supernarrow transition peaks on parameters has not yet been undertaken.

5.5.2 Partial spectra due to small fluctuations about stable states.

A detailed study of the partial spectra due to fluctuations about stable states of the periodically driven ZD system has not yet been reported. At the same time, the major characteristic features of such spectra, and of their evolution as parameters vary, seem to have been understood [77]. We present below the qualitative and semiquantitative arguments that provide such an understanding.

If the temperature is small enough, then the hierarchy of populations is typically very sharp so that only the state that possesses the largest activation energy is populated. If it corresponds to the linear response state, then the corresponding partial spectrum is a peak about the eigenfrequency in the bottom of the potential well, $\omega_0 \equiv \omega(E = E_{min})$. If the temperature T is extremely small (see below), then the shape of the peak is approximately Lorenzian with a halfwidth $\sim \Gamma$ (cf. [106]), corresponding to eigenoscillation in the bottom of the well. If T increases so that $\mid d\omega(E = E_{min})/dE \mid T \gtrsim \Gamma$, then the peak broadens and its shape changes, reflecting the broadening of the spectrum of relevant eigenfrequences $\omega(E)$ due to the growth in the energy range involved. The shapes of such broadened peaks have not yet been analyzed.

If the most populated state is one of the nonlinear resonances, then the partial spectrum consists typically of two peaks shifted from the driving frequency ω_f by some small value $\Delta\omega$ to the right and to the left respectively, so that by analogy with optics [115] they may be called Stokes and anti-Stokes peaks (centered on $\omega_f + \Delta\omega$ and $\omega_f - \Delta\omega$ respectively). Their magnitudes usually differ significantly. Furthermore, as parameters vary, so that repopulation of the nonlinear resonances occurs (associated approximately with the crossing of the ZDNR/NR line), the relative magnitudes of the Stokes and anti-Stokes peaks are reversed. In order to understand the origins of these characteristic features, let us evaluate the dependence $q(t)$ in the non-dissipative approximation.

For the sake of simplicity, we shall assume that the nonlinearity in the relevant resonant range of energies is small, so that q as a function of action I and angle ψ may be approximated just by the cosine term [67] while higher harmonics in the expansion (A.5) may be neglected:

$$q(t) \approx 2q_1(I(t))\cos(\psi(t)). \tag{5.5.13}$$

In the absence of noise, the action $I(t)$ would relax to one of the stable stationary states, $I^{(st)}$, and the angle would change with the constant speed ω_f while maintaining a certain shift $\tilde{\psi}^{(st)}$ from the angle of the driving force $\omega_f t$ (see sub-section 4.2):

[67] For the sake of convenience, we choose the origin of the angle ψ such that q_1 is real and positive.

$$I(t\to\infty)\longrightarrow I^{(st)},\qquad \psi(t\to\infty)\longrightarrow \omega_f t+\tilde{\psi}^{(st)},\qquad (5.5.14)$$
$$T=0.$$

In the presence of noise, there is an approximately stationary distribution of action I in the vicinity of $I^{(st)}$. For further analysis we assume that the dissipation is very weak, so that the *non-dissipative* equations of motion for $\{I,\tilde{\psi}\}$ may be analyzed (i.e. Γ in (4.2.4) may be put zero), and that the temperature T is small so that only the close vicinity of the state $\{I^{(st)},\tilde{\psi}^{(st)}\}$ is relevant. The right-hand sides of the equations in (4.2.4) may then be *linearized* near this state.

Thus, introducing the deviations of slow variables I and $\tilde{\psi}\equiv\psi-\omega_f t$ from their relevant stable stationary values,

$$\Delta I\equiv I-I^{(st)},\qquad (5.5.15)$$
$$\Delta\tilde{\psi}\equiv\psi-\omega_f t-\tilde{\psi}^{(st)},$$

and linearizing (4.2.4) near the stable stationary state, one arrives at the following dynamical equations:

$$\frac{d(\Delta I)}{dt}=-\alpha_\psi\Delta\tilde{\psi},\qquad (5.5.16)$$
$$\frac{d(\Delta\tilde{\psi})}{dt}=\alpha_I\Delta I,$$
$$\alpha_\psi\equiv\left.\frac{\partial^2\overline{H}}{\partial\tilde{\psi}^2}\right|_{I^{(st)},\tilde{\psi}^{(st)}},\qquad \alpha_I\equiv\left.\frac{\partial^2\overline{H}}{\partial I^2}\right|_{I^{(st)},\tilde{\psi}^{(st)}},\qquad \alpha_\psi\alpha_I>0,$$

where $\overline{H}\equiv\overline{H}(I,\tilde{\psi})$ is given in (4.2.4) (note that $\left.\partial^2\overline{H}/\partial I\partial\tilde{\psi}\right|_{I^{(st)},\tilde{\psi}^{(st)}}=0$) and the last inequality is equivalent [68] to the requirement that the state $\{I^{(st)},\tilde{\psi}^{(st)}\}$ be stable.

The solution of (5.5.16) is

$$\Delta I=\Delta I_0\cos(\Delta\omega t+\varphi_0),$$
$$\Delta\tilde{\psi}=\mathrm{sgn}(\alpha_I)\sqrt{\frac{\alpha_I}{\alpha_\psi}}\Delta I_0\sin(\Delta\omega t+\varphi_0),\qquad (5.5.17)$$
$$\Delta\omega\equiv\sqrt{\alpha_\psi\alpha_I},$$

where ΔI_0 and φ_0 are the auxiliary "amplitude" and "phase" corresponding to given initial conditions; note that ΔI_0 is necessarily small due to the requirement of the smallness of ΔI and $\Delta\tilde{\psi}$ which we have imposed, because only small values of ΔI and $\Delta\tilde{\psi}$ are relevant at small T.

Expanding $q_1(I)$ and $\cos(\psi)$ in Taylor series over ΔI and $\Delta\tilde{\psi}$ respectively, and omitting from the resultant expression for $q(t)$ (5.5.13) those terms which are proportional to $(\Delta I_0)^m$ with $m \geq 2$, one obtains

$$
\begin{aligned}
q(t) \approx\ & 2q_1^{(st)} \cos(\omega_f t + \Delta\tilde{\psi}^{(st)}) + \\
& \Delta I_0 \left[\left(q_1' + \mathrm{sgn}(\alpha_I) \sqrt{\frac{\alpha_I}{\alpha_\psi}} q_1^{(st)} \right) \cos(\{\omega_f + \Delta\omega\} t + \Delta\tilde{\psi}^{(st)} + \varphi_0) + \right. \\
& \left. \left(q_1' - \mathrm{sgn}(\alpha_I) \sqrt{\frac{\alpha_I}{\alpha_\psi}} q_1^{(st)} \right) \cos(\{\omega_f - \Delta\omega\} t + \Delta\tilde{\psi}^{(st)} - \varphi_0) \right], \\
q_1^{(st)} \equiv\ & q_1(I^{(st)}), \qquad q_1' \equiv dq_1(I^{(st)})/dI^{(st)}.
\end{aligned}
\tag{5.5.18}
$$

The first term in the above expression for $q(t)$ represents the oscillation at the driving frequency, and it does not contribute to the spectrum of fluctuations since it arises in $q(t)$ even in the absence of noise; note that $\langle q(t) \rangle$ is extracted from $q(t)$ when $Q_q(\Omega)$ is calculated: see the definition (5.5.1).

The terms representing the mixed frequencies $\omega_f + \Delta\omega$ and $\omega_f - \Delta\omega$, i.e. the Stokes and anti-Stokes components respectively, are proportional to ΔI_0 and hence are entirely due to noise: it is just noise that causes deviations of I from its stationary (approximately resonant) value $I^{(st)}$; the latter deviations give rise to persistent slow oscillations of I and $\tilde{\psi}$ which, in turn, modulate the fast oscillation of q at the driving frequency thus bringing the mixed frequencies into play.

Furthermore, it can be seen from (5.5.18) that the modulations of angle and action interfere with each other differently for the Stokes and anti-Stokes components. This interference depends on the sign of α_I which, in the ZD case, differs between the nonlinear resonances whose stable point possess the larger and smaller actions [68] (cf. also sub-section 4.2). The repopulation of the nonlinear resonances therefore reverses the relative intensities of the Stokes and anti-Stokes peaks in the fluctuation spectrum. For the TDO results shown in Fig. 66 (see also Fig. 21), the Stokes component prevails over the anti-Stokes one for the larger-action nonlinear resonance, while it is vice versa for the smaller-action resonance.

In the asymptotic limit of weak driving ($h \to 0$), slow motion in the different nonlinear resonances is nearly identical if the driving force parameters lie on the ZDNR/NR line; the only difference is in the sign of α_I so that, in the different resonances, the corresponding trajectories in the $I - \tilde{\psi}$ plane rotate in opposite directions. Therefore, the activation energies are identical as well. Hence, the repopulation of the resonances occurs right at the ZDNR/NR transition [68]. If we move higher than the ZDNR/NR line in the plane of the driving force parameters (h, ω_f), the smaller-action resonance becomes [68] shallower than the larger-action one and, at high enough h, it disappears altogether (see sub-sections 4.1, 4.2 and, in particular, the bifurcation diagram of Fig. 24(a)). Hence,

[68] Roughly, this statement holds true for the whole range of small (rather than just for vanishingly small) h.

the population of the larger-action resonance dominates if the working point $\{h, \omega_f\}$ lies above the ZDNR/NR line (i.e. in the ZDNR region) while the smaller-action resonance dominates below the ZDNR/NR line (i.e. in the NR region). This means that the intensity of the Stokes peak in the fluctuation spectrum is larger than the intensity of the anti-Stokes peak if the parameters of the driving force correspond to ZDNR while it is vice versa if parameters correspond to the NR. Just such an evolution is seen in Fig. 66: for the top sub-figure, which corresponds to the ZDNR stage, the Stokes peak is a few times larger than the anti-Stokes one (note that the large peak on the far right corresponds to linear response, whose population dominates within this parameter range); in the middle sub-figure, which corresponds approximately to the ZDNR/NR transition, all states are approximately equally populated and the peaks under discussion are approximately equal as well; in the bottom sub-figure, which corresponds to the NR stage, the ratio between the Stokes and anti-Stokes components is reversed.

Finally, let us estimate the shift of the peaks away from the driving frequency, $\Delta\omega \equiv \sqrt{\alpha_\psi \alpha_I}$, and the ratio between the intensities of the peaks; we also compare these estimates with those for the conventional (non-ZD) case.

It follows from Eq. (4.1.11) with $n = 1$ and $V_l^{(1)} \equiv 2q_1$, which approximates the Hamiltonian $\overline{H}$ (4.2.4) in the most relevant range of I, that $\mid \alpha_I \mid \approx \mid \omega_m''(I^{(st)} - I_m) \mid$ while $\mid \alpha_\psi \mid \approx hq_1(I_m)$, so that $\Delta\omega \approx \sqrt{hq_1(I_m) \mid \omega_m'' \mid\mid I^{(st)} - I_m \mid}$. At the ZDNR/NR transition, which is the most characteristic case, it can easily be shown [68] (cf. also Eqs. (4.1.11) and (4.2.17) above) that $\mid I^{(st)} - I_m \mid \approx (3hq_1(I_m)/ \mid \omega_m'' \mid)^{1/3}$, so that

$$\Delta\omega \approx 3^{1/6}(hq_1(I_m))^{2/3} \mid \omega_m'' \mid^{1/3} \propto h^{2/3}. \tag{5.5.19}$$

It is typically less than in the conventional case [5], where the frequency of eigenoscillation in a nonlinear resonance is $\approx \sqrt{hq_1(I_r) \mid d\omega(I_r)/dI_r \mid} \propto h^{1/2}$ (see Eq. (4.1.10)).

The ratio between the intensities of the Stokes and anti-Stokes peaks depends strongly on the parameter $\sqrt{\alpha_I/\alpha_\psi}$. It follows from the above estimates for α_I and α_ψ that this parameter is

$$\sqrt{\alpha_I/\alpha_\psi} \propto h^{-1/3}. \tag{5.5.20}$$

Thus, in the asymptotic limit $h \to 0$, it diverges, which indicates (see Eq. (5.5.18)) that the modulation of angle is far more important for the formation of the Stokes and anti-Stokes components in the fluctuation spectrum than the modulation of action. As a consequence, the magnitudes of the Stokes and anti-Stokes peaks should be nearly equal in the asymptotic limit $h \to 0$. At the same time, the divergence in Eq. (5.5.20) is rather weak so that, at *moderately* small h, this factor is not large. The contributions from the action and angle modulations are therefore comparable, resulting in their strong interference and hence in a significant difference between the intensities of the Stokes and anti-Stokes peaks. The latter expectation is well confirmed by the top and bottom sub-figures of Fig. 66.

For the conventional case, the factor $\sqrt{\alpha_I/\alpha_\psi}$ is proportional to $h^{-1/2}$, therefore diverging in the asymptotic limit $h \to 0$ even more strongly than for the ZD case. However, provided h is not too small, the factor $\sqrt{\alpha_I/\alpha_\psi} q_1^{(st)} \omega_f / \mid q_1' \mid$ is still of the order of unity typically, so that the absolute values of the contributions to $q(t)$ from modulations of the action and angle are comparable with each other, as follows from Eq. (5.5.18). The interference between these contributions is therefore strong, which causes the Stokes and anti-Stokes peaks in the fluctuation spectrum to differ strongly in intensity: cf. Fig. 12 from [106].

5.5.3 Unsolved problems

As is obvious from the above discussion, the study of fluctuation spectra in periodically driven ZD systems is far from complete. We formulate below some unsolved problems that seem to us to be of interest.

1. Supernarrow transition peaks.

(a) It is necessary to study in more detail the lines of kinetic phase transitions (KPTs) for at least two characteristic examples of ZD systems: (i) the TDO, which represents a relatively simple example and typically possesses no more than three stable states under periodic driving; and (ii) the multistable SQUID, which represents an example of a strongly nonlinear ZD system and which possesses a separatrix even in the absence of driving.

The most straightforward way to address such problems is to calculate the activation energies by the method of large fluctuations, as in sub-section 5.4. A drawback of this method is that it often ends with heavy numerics and it is not easy to single out general features from such numerical results.

An alternative way might be to reduce the Fokker-Plank equation (FPE) in the $I - \tilde{\psi}$ plane to a one-dimensional FPE, through a separation of the relatively slow auxiliary action from the relatively fast auxiliary angle (cf. ΔI_0 and $\Delta\omega t + \varphi_0$ in Eq. (5.5.17) above), and then to seek a steady-flux solution of the one-dimensional FPE. It may sometimes be possible to find the latter in explicit form (cf. [130], which uses a similar method for the case of a conventional weakly nonlinear oscillator).

After the KPT lines are found theoretically, it will then be necessary to compare them with experimental measurements of the intensity of the supernarrow transition peak as a function of driving parameters.

(b) It would be interesting to study the shape of the supernarrow peak in cases where more than two states are significantly involved. Such a situation occurs in the vicinity of intersections between KPT lines, where populations of more than two (three, typically) most populated states are comparable with each other.

2. Partial spectra due to small fluctuations.

(a) The results presented above in sub-section 5.5.2 provide only a qualitative understanding of some major features of the partial spectra, while the quantitative theoretical description still remains to be tackled. A major problem that may arise will be the explicit evaluation of the stationary distribution within a given state. For small temperatures, when the equations of slow motion may be linearized, such distributions can be derived relatively easily; a similar calculation was used in [106] for the case of a weakly nonlinear conventional oscillator. But in general it is a non-trivial problem,

even for the case of ultra-low friction. Possibly, it may be solved, or at least simplified, by reduction of the corresponding auxiliary FPE in the $I - \tilde{\psi}$ plane to a one dimensional FPE through a separation of an auxiliary action for this motion from the relatively fast auxiliary angle, with a further search for its quasi-stationary solution (cf. the item 1(a) above and [130]).

(b) In case of a strongly nonlinear ZD system (like a multistable SQUID), or even in the case of a relatively weakly nonlinear TDO but for higher temperatures, harmonics with $n \neq 1$ should come into play (cf. the weak second-harmonic Stokes and anti-Stokes peaks in Fig. 12 in [106]). The most interesting among them is the harmonic with $n = 0$: it gives rise to the onset of a narrow peak (of the width $\sim \Gamma$) centered at $\Omega = \omega_f$, which may be confused sometimes with the supernarrow peak. The method for studying it theoretically could be analogous to that used for the zero-frequency peak in the case of a stationary system [145,50,51] but, as in the previous item, the most difficult part of the explicit calculation will probably be related to the explicit calculation of the stationary distribution within the state.

5.5.4 Conclusions

As in any other multi-stable system, the spectrum of fluctuations in a periodically driven ZD system may consist of a "supernarrow" peak at the driving frequency ω_f, arising from inter-state fluctuational transitions, together with a relatively broad multi-peaked structure attributable to relatively small fluctuations about each of the stable states.

At small temperatures, the supernarrow (transition) peak is manifested only in the vicinity of kinetic phase transition (KPT) lines in the parameter space, and its intensity is exponentially small beyond these regions. Unlike the case of a conventional (i.e. non-ZD) single-well oscillator, where there is typically only one KPT line, there are at least three KPT lines in the ZD case. The shape of the supernarrow peak is typically Lorenzian, except in the vicinity of intersections between KPT lines. Detailed studies of KPT lines in the ZD case, as well as of the shape of the peak in the vicinity of intersections of KPT lines, have not yet been reported.

Small fluctuations about a stable state of a periodically driven system cause approximately periodic small oscillations, of relatively low frequency $\Delta\omega$, in the action and angle about their values in the stable state. These give rise to spectral peaks at the mixed frequencies, $\omega_f + \Delta\omega$ and $\omega_f - \Delta\omega$, sometimes called Stokes and anti-Stokes peaks respectively. The ratio between their intensities is reversed if the direction of rotation of trajectories within the nonlinear resonance in the plane $I - \tilde{\psi}$ changes: such a reversal is due to the different interference between action and angle modulations for different directions of the rotation. Given that the ZDNR/NR transition results in a repopulation between resonances in which the directions of rotation are opposite, it also results in the reversal of the relative intensities of the Stokes and anti-Stokes peaks. A quantitative study of partial spectra due to small fluctuations about stable states of a periodically driven ZD system has yet to be attempted.

A combination of noise and periodic driving in ZD systems provides a wide variety of characteristic phenomena. In Sec. 5, we have described five distinctly different types of such phenomena known by the present time. We group the conclusions below according to the same classification.

1. When the periodic driving is weak, so that it does not significantly affect the thermal equilibrium, and one is interested in the influence of noise intensity (temperature) on the response to periodic driving (signal) and on the signal-to-noise ratio (SNR), then the possibility of *zero-dispersion stochastic resonance* (ZDSR) should be considered provided the driving frequency is close to the extremal eigenfrequency of a ZD system or to one of its harmonics. ZDSR is said to occur when the SNR possesses a local maximum as a function of temperature. It should be emphasized that ZDSR does not require bistability, unlike conventional stochastic resonance. The signal itself is also strongly enhanced by noise, and much more strongly than in conventional (non-ZD) systems.

   The phenomenon of ZDSR is closely related to the zero-dispersion peak in the fluctuation spectrum (see Sec. 3 above), and the better the separation of this peak from other peaks in the spectrum, the more pronounced ZDSR is, i.e. the higher the SNR in its local maximum as a function of temperature. Such separation is always provided if the dissipation vanishes: then the local maximum in the SNR goes to infinity provided the driving frequency is exactly equal to the extremal eigenfrequency or a harmonic. At a given dissipation, the best separation of the zero-dispersion peak is provided in systems with more than one separatrix, e.g. such as a SQUID, so that the ZDSR is then at its most pronounced.

   The theory of ZDSR has been well elaborated and tested by analogue experiments and computer simulations in many details. Thus, the major problem for the future seems to be a realization of the ZDSR in real SQUIDs and using it in various applications.

   It would also be interesting [47,114] and potentially important to seek ZDSR in *arrays* of ZD systems since it promises [114] to be even more pronounced than in a single ZD system as well as possibly providing an enhancement of a *signal propagation* (cf. [112,113]).
2. If the frequency of a weak periodic driving is close to a subharmonic of the extreme eigenfrequency ω_m, then the noise-enhancement of the second harmonic generation and nonlinear absorption become very pronounced, and much more so than in conventional systems or for frequency ranges beyond the vicinity of subharmonics of ω_m. In a sense, it is an analogue of the ZDSR but for a nonlinear rather than linear response and at subharmonics rather than at the main or multiple frequencies. Similar to ZDSR, the above phenomena promise to be most pronounced for strongly nonlinear models, where the ZDP in the fluctuation spectrum is well separated from other peaks; however neither has the theory been developed for such strongly nonlinear systems nor has the corresponding experimental study yet been done. It seems important to carry out such studies in future.
3. If the periodic driving is weak, but the noise is even weaker in the sense that the thermal equilibrium is strongly disturbed by the periodic driving, then the enhancement of

noise-induced escape from a potential well due to the periodic driving is typically much stronger in ZD potentials than in similar conventional ones. The enhancement is especially pronounced if the driving frequency is close to the extremal eigenfrequency and the damping parameter is smaller than, or of the same order as, the driving amplitude while the latter may remain moderately weak: the major nonlinear resonances (ZDNRs) are then very wide in energy and, in addition, chaotic layers associated with their separatrices reconnect the chaotic layer associated with the barrier level. Consequently, the activation energy may be substantially reduced, even by periodic driving that is relatively weak. Such a strong reduction may have many important applications, in particular for the the creation of a pronounced ratchet effect in periodic potentials. The subject has only recently started to be investigated, so that many important theoretical and experimental details still need to be elucidated; the most important task appears to be the development of a quantitative theory describing the decrease of activation energy for the ZD case in the underdamped limit.

4. The most general features of noise-induced escapes from ZDNRs are similar to those for a noise-induced escape/transition in any other multi-stable system. The initial work [78] reduces the non-autonomous problem to the autonomous one, and then studies the relevant most probable escape paths (MPEPs) and the corresponding activation energies by means of the optimal fluctuation method. The most interesting result is that, although there was a reason to anticipate avoidance of the inner saddle by the MPEP from the inner focus to the outer boundary of the outer basin, the MPEP does in fact pass through that saddle, after which it goes to the outer saddle, smoothly turning around both the noise-free trajectory from the inner saddle to the outer focus and the MPEP from the outer focus to the outer saddle. We have also suggested (and proved) some simple auxiliary rules which help in identifying the MPEP among the other extremals prior to a calculation of the action along them. There are still many interesting unsolved problems in the subject, of which the most important in a general context seem to us: (i) the search for rigorous rules allowing one to select the range of the shooting parameter in which there lies only one value corresponding to an extremal, namely to that extremal whose projection onto the $I - \tilde{\psi}$ plane provides the absolute minimum of the action, i.e. constitutes the MPEP itself; and (ii) the search for sets of parameters at which the MPEP from the inner focus beyond the outer encompassing basin forms a smooth trajectory avoiding the inner saddle, rather than a trajectory possessing a cusp in the inner saddle.
5. The spectrum of fluctuations in a ZD system subject to weak periodic driving and to a yet weaker noise consists typically of peaks that are due to small fluctuations about the most populated stable state of the noise-free system. If this is a linear response, then there is just one peak, centered at the frequency of eigenoscillation in the non-driven ZD system. If the most populated state is one of the nonlinear resonances, then the spectrum consists of: (i) two peaks shifted from the driving frequency ω_f respectively up or down for a frequency $\Delta\omega$ of small oscillations about the stable state of the noise-free system; and (ii) possibly a narrow ($\sim \Gamma$) peak centered at ω_f. The former peaks arise due to the periodic (with the frequency $\Delta\omega$) modulation of the amplitude and angle of the stable constrained oscillations (at the frequency ω_f), while the latter peak arises in cases when small oscillations about the stable state are asymmetric, its origin being analogous to the origin of the zero-frequency peak in stationary systems [145,50,51]. In rare cases, when the populations of the two or more most populated states are

comparable, all the corresponding peaks are present in the spectrum.

Though the origins of all the major features of the spectral contributions due to small fluctuations about the stable states have now been understood, a quantitative description of the spectrum has yet to be achieved.

In case, when the populations of the two most populated states are comparable, an extremely high and narrow ("supernarrow") peak arises at the driving frequency: it is due to very rare noise-induced transitions between the stable states of the noise-free system. The supernarrow peak in the ZD case is quite similar to that in the conventional case, except when the populations of three or more (rather than two only) most populated states are comparable: in the latter case, the shape of the peak differs from the conventional Lorenzian and it has not yet been studied.

6 Quantum zero-dispersion phenomena

To the best of our knowledge, nothing has yet been published on zero-dispersion phenomena in quantum systems. At the same time, such studies would be interesting both for their intrinsic interest and because many zero-dispersion systems may operate in the quantum or quasi-classical regimes (cf. for example local vibrations in doped crystals [27] and underdamped torsional motion in axial molecules [23]).

We briefly review below two unpublished incomplete theoretical studies [147,148] undertaken in 1995-1996, presenting initial results and discussing possible approaches for further studies. We hope that these notes will be stimulating for other researchers.

6.1 Quantum zero-dispersion peaks

The present sub-section is based on [147].

6.1.1 Qualitative analysis

In the purely quantum regime, when the extremal energy (i.e. the energy E_m at which $\omega(E)$ possesses an extremum) is comparable with the lowest energy level, zero-dispersion behaviour is unlikely to be manifested to any significant extent. On the other hand, if E_m lies in the range of energy levels with high quantum numbers so that the motion is quasi-classical, then zero-dispersion peaks may arise in various spectra. Consider a nonlinear oscillator (Fig. 67). The distance in energy between adjacent quasi-classical levels is equal to $\hbar\omega(E)$ [149]. Let the oscillator interact with a thermostat (whose temperature $T \gtrsim E_m$). All levels with energy $E \lesssim T$ are then populated. If the interaction with the thermostat is very weak, then the absorption spectrum contains separate spikes corresponding to transitions between different levels. For the sake of simplicity, let us consider transitions

between adjacent levels only [69] . They are distributed on the frequency axis with a density that, except in the immediate vicinity of ω_m, is given approximately by

$$D(\Omega) = \sum_i \frac{1}{[\mid d\omega/dE \mid \hbar\omega]\big|_{E_\Omega^{(i)}}}, \tag{6.1.1}$$

where $E_\Omega^{(i)}$ is an ith root of the equation

$$\omega(E_\Omega^{(i)}) = \Omega, \tag{6.1.2}$$

and the summation over i means the summation over all such roots (in the ZD case, typically two).

Thus, everywhere except the immediate vicinity of ω_m, the density of spikes on the frequency axis is related to the classical spectral densities $\mid d\omega(E_\Omega^{(i)})/dE_\Omega^{(i)} \mid^{-1}$ (cf. the subsection 3.2).

The interaction may be characterized by a parameter that in the classical limit reduces to the friction parameter Γ (cf. e.g. [2]). If Γ increases, then the spikes become broader (and lower). On further increase of Γ, the width of a partial spike calculated in the weak-interaction approximation becomes comparable with the distance between maxima of adjacent spikes. Interference between the corresponding transitions then comes into play and the weak-interaction approximation no longer provides a quantitative description of the spectrum. But it still allows us to draw some qualitative conclusions. Thus, if the width of the "partial spike" greatly exceeds the distance between the adjacent spikes, this indicates that a broad continuous spectrum is formed. Its value at each given frequency Ω is proportional to the number of significantly contributing transitions which, in turn, is proportional to the concentration of "spikes" calculated in the weak-interaction approximation i.e. to $D(\Omega)$ (6.1.1), which in turn is related to the spectral densities of classical oscillations. Obviously, the spectrum should reduce in this case to the classical limit. Just such a transformation of the quantum (with separate spikes) spectrum into the classical one as the interaction parameter grows was demonstrated in rigorous calculations for the Duffing oscillator [150,2].

In the ZD case, the evolution from the quantum-like spectrum to the classical-like one should possess distinctive features.

In the purely quantum stage, the distribution of the spikes on the Ω axis thickens as Ω approaches ω_m from within the spectrum of classical eigenfrequencies, and then abruptly vanishes as ω_m is crossed: see Fig. 68(a).

[69] The intensities of the corresponding spectral spikes are proportional to the square of the relevant matrix elements of coordinate, which are proportional, in turn, to the fundamental Fourier components of the classical oscillations [149]; the spikes resulting from transitions between non-adjacent levels relate to higher-order harmonics [149], which are typically much smaller in absolute value than the fundamental.

Let us estimate the width of an individual spike (this estimate is valid in all cases rather than in the ZD case only). Given that interaction with the thermostat is weak, we may describe it merely by introduction of a corresponding phenomenological random force in the Hamiltonian of the system

$$
\begin{aligned}
&H = H_0 + qf(t), \\
&H_0 = -\frac{\hbar^2}{2}\frac{d^2}{dq^2} + U(q), \\
&\langle f(t)\rangle = 0, \qquad \langle f(t)f(0)\rangle = 2\Gamma T\delta(t).
\end{aligned}
\tag{6.1.3}
$$

Here, q and $U(q)$ are respectively the coordinate and potential energy of the oscillator while, for the sake of similarity to the classical description in Sec. 3 (cf. e.g. Eq. (3.1.1)), its mass is normalized to unity here and in what follows. The random force $f(t)$ is white noise, where T is the temperature and Γ is an interaction parameter which corresponds in the classical limit to the friction parameter.

A description of the system in this way is analogous to neglect of the (dissipative) drift in comparison with the diffusion in the classical case, which may always be done in the limit $\Gamma \to 0$ (cf. Sec. 3).

Let us assume that at an arbitrarily chosen initial instant only the nth level of the oscillator is populated, i.e. the wave function of the system is

$$
\begin{aligned}
&\Psi(0) \equiv \Psi(q, t=0) = \psi_n(q), \\
&H_0\psi_n = E_n\psi_n.
\end{aligned}
\tag{6.1.4}
$$

As time passes, the wave function changes and other levels also start to become populated i.e. the initial state decays. Let us expand the time-dependent wave function $\Psi(t)$ over the full set of eigenfunctions of the oscillator,

$$
\begin{aligned}
\Psi(t) \equiv \Psi(q,t) = \sum_k c_k(t)\psi_k(q)\mathrm{e}^{-\frac{i}{\hbar}E_k t}, \\
c_k(0) = \begin{cases} 1 & \text{at} \quad k{=}n, \\ 0 & \text{at} \quad k{\neq}n. \end{cases}
\end{aligned}
\tag{6.1.5}
$$

Using standard time-dependent perturbation theory [149], averaging the result over the noise, and omitting terms $\propto t^l$ with $l \geq 2$, one can obtain for the initial stage of the decay of the population of the initial (i.e. nth) level:

$$
\begin{aligned}
&\langle \mid c_n(t) \mid^2 \rangle \approx 1 - t\frac{2\Gamma T \sum_{k\neq n} \mid q_{kn} \mid^2}{\hbar^2}, \\
&q_{kn} \equiv \int dq\ \psi_k^* q \psi_n.
\end{aligned}
\tag{6.1.6}
$$

If the nonlinearity is small, i.e. the potential is nearly parabolic, $U(q) \approx \omega^2 q^2/2$, then the matrix elements for transitions between non-adjacent levels are approximately equal to zero while $\mid q_{k(k-1)} \mid = \mid q_{(k-1)k} \mid \approx \sqrt{k\hbar/(2\omega)}$ [149], so that

$$\sum_{k \neq n} \mid q_{kn} \mid^2 \approx \mid q_{(n-1)n} \mid^2 + \mid q_{(n+1)n} \mid^2 \approx \frac{(2n-1)\hbar}{2\omega} \approx \frac{E}{\omega^2}, \tag{6.1.7}$$

$$U(q) \approx \frac{\omega^2 q^2}{2}, \qquad n \gg 1.$$

In the general case, (6.1.7) is not satisfied quantitatively but it can typically still be used as the basis for rough qualitative estimations.

Thus, as follows from (6.1.6) and (6.1.7), the initial state decays for a time of the order of

$$\Delta t = \frac{\hbar^2}{2\Gamma T \sum_{k \neq n} \mid q_{kn} \mid^2} \sim \frac{(\hbar\omega(E_n))^2}{\Gamma T E_n}. \tag{6.1.8}$$

Because of the uncertainty principle [149], the width of the level $\Delta E \sim \hbar/\Delta t$, so that the width of the spectral spike in the absorption spectrum

$$\Delta\omega \sim \frac{\Delta E}{\hbar} \sim \frac{1}{\Delta t} \sim \frac{\Gamma T E_n}{(\hbar\omega(E_n))^2}. \tag{6.1.9}$$

So, as the interaction with the thermostat grows, the widths of the spikes grow too and, when $\Delta\omega$ (6.1.9) becomes comparable with the separation between spikes, the interference of transitions between corresponding energy levels comes into play (cf. the case of the harmonic oscillator [151,152], where all energy levels are equidistant) so that the spikes merge and a united broader peak is formed (cf. Fig. 68(b)). In the ZD system, this process starts in the immediate vicinity of ω_m, where the distance between the spikes is minimal [70] (cf. Fig. 68(a)). As Γ (or T) grows further, the interference involves more and more spikes so that the resulting peak (i.e. ZDP) becomes broader and more intense, reducing in the end to the continuous classical form (cf. Fig. 68(c)). The distance between spikes in the immediate vicinity of ω_m is $\sim \mid d^2\omega(E_m)/dE_m^2 \mid (\hbar\omega_m)^2$. The condition for $\Delta\omega$ to become

[70] There may be doublets of spikes, both in the immediate vicinity of ω_m and beyond it, and the distance between the spikes in the doublets may be vanishing: this occurs if the energy levels on either side of E_m generate two very close sets of $\omega(E_n)$, which takes place either if E_m is very close to one of the levels or if E_m is situated very close to mid-way between some adjacent levels. In this case the overlap of spikes and the interference between the corresponding transitions may start at much smaller values of Γ than that one in (6.1.10). However, unlike Γ (6.1.10), the interference is limited in this case to only these two transitions while others are not involved. Such interference in a doublet does not relate to the formation of the major part of the ZDP, and we shall not discuss it further.

comparable with this distance may be written as

$$a \equiv \frac{\Gamma T E_m}{\mid \omega'' \mid (\hbar\omega_m)^4} \sim 1, \qquad \omega'' \equiv \frac{d^2\omega(E_m)}{dE_m^2}. \tag{6.1.10}$$

The above criterion (6.1.10) for the start of the formation of the ZDP as the interaction with the thermostat increases is the major result of this sub-section. It is worth noting that it can also be obtained in a different way, using results from the analysis of the classical ZDP. Indeed, it was shown in sub-section 3.3 that, in the vicinity of E_m, the classical correlation function decays for a time of the order of $t_{\rm zdp}$ (3.3.4); the energy diffusion during this time is of the order of $\Delta E_{\rm zdp}$ (3.3.5). Obviously, if $\Delta E_{\rm zdp}$ turns out to be less than or of the order of the distance between adjacent levels in the vicinity of E_m, then neither the classical approximation works nor will a ZDP arise in the spectrum. Comparing $\Delta E_{\rm zdp}$ with $\hbar\omega_m$ and allowing for $\overline{p^2}_m$ in (3.3.5) is typically $\sim E_m$, one derives that same criterion (6.1.10).

Thus, the qualitative analysis in this sub-section shows that, as the interaction with a thermostat grows, the onset of the ZDP in the spectrum and the start of the transformation of the purely quantum (spikes-like) spectrum into the classical (broad continuous) spectrum occur simultaneously, namely when criterion (6.1.10) is satisfied.

The quantitative description of how a ZDP is formed as the interaction grows turns out to be a very difficult problem. We briefly describe in the next sub-section two possible approaches and the corresponding difficulties encountered by the authors of [147].

6.1.2 Approaches for quantitative description

The quantum analogue of the classical correlation function $\langle\varphi(t)\varphi(0)\rangle$ may be introduced as (see e.g. [150,2]):

$$\begin{aligned} R_\varphi^{(\rm q)}(t) &= \frac{1}{2}{\rm Tr}\left\{\rho\left(\varphi_{\rm h}(t)\varphi_{\rm h}(0) + \varphi_{\rm h}(0)\varphi_{\rm h}(t)\right)\right\} \\ &\equiv \frac{1}{2}{\rm Tr}\left\{\rho\left(U^+\varphi_{\rm s}U\varphi_{\rm s} + \varphi_{\rm s}U^+\varphi_{\rm s}U\right)\right\}, \\ U &\equiv {\rm e}^{-\frac{i}{\hbar}Ht}, \qquad U^+ = U^{-1}, \end{aligned} \tag{6.1.11}$$

where ρ is the density matrix, $\varphi_{\rm h}$ and $\varphi_{\rm s}$ are respectively the Heisenberg and Schrödinger representations of the operator corresponding to a given physical quantity φ, and U is the evolution operator [149]. The Fourier transform of $R_\varphi^{(\rm q)}(t)$ may be called the *quantum spectrum of fluctuations* $Q_\varphi^{(\rm q)}(\Omega)$. It can be shown that $R_\varphi^{(\rm q)}(-t) = R_\varphi^{(\rm q)}(t)$, so that $Q_\varphi^{(\rm q)}(\Omega)$ may be expressed via the half-Fourier transform:

$$Q_\varphi^{(\rm q)}(\Omega) = \frac{1}{\pi}\int\limits_0^\infty dt\ {\rm e}^{-i\Omega t}R_\varphi^{(\rm q)}(t). \tag{6.1.12}$$

We shall describe below two different approaches to the calculation of the spectrum (6.1.12)-(6.1.11). For the sake of simplicity, only the case $\varphi = q$ will be considered.

1. Let us use the phenomenological Hamiltonian (6.1.3), in which the interaction with a thermostat is described by the phenomenological random force. It is then not difficult to show that

$$U = \mathrm{e}^{-\frac{i}{\hbar}H_0 t} T_\tau \exp\left\{-\frac{i}{\hbar}\int_0^t d\tau\ f(\tau)\ \hat{q}\ (\tau)\right\}, \tag{6.1.13}$$
$$\hat{q}\ (\tau) \equiv \mathrm{e}^{\frac{i}{\hbar}H_0 t} q \mathrm{e}^{-\frac{i}{\hbar}H_0 t},$$

where T_τ is the chronological-ordering operator.

Assuming that the temperature is high enough to exceed significantly the width of the energy range relevant to the ZDP (cf. Sec.3), ρ in (6.1.11) may be assumed constant within the relevant range of energies, so that the *shape* of the spectrum of the coordinate is entirely determined by the time evolution of $\langle \mathrm{Tr}\,\{U^+ qUq + qU^+ qU\}\rangle$ where $\langle ...\rangle$ denotes averaging over the random force. If $R_q^{(\mathrm{q})}(t)$ is formally expanded in a Taylor series over $\Gamma T/\hbar^2$, then it is possible in principle to average each term of the series over the random force in explicit form [147]. However, the main question is whether or not the series in the corresponding Fourier transform converges. Given that the classical spectrum (3.3.19) depends on ΓT non-analytically, and therefore that the Taylor series over ΓT diverges, one may expect that the quantum spectrum will also depend on ΓT non-analytically, given that it must reduce to the classical spectrum in the limit $\hbar \to 0$. It is therefore unlikely that the quantum spectrum can be found by the above approach.
2. Another possible approach is analogous to that used for the calculation of the spectrum (6.1.12)-(6.1.11) for a particular conventional nonlinear oscillator, namely the Duffing oscillator (DO), in the range of small energies when the nonlinearity is moderately weak [150,2]. The technique is quite complicated and its detailed description goes beyond the scope of the present review. So, we give below only a brief qualitative delineation of the work [150] (reproduced also in the review [2]) and indicate the main differences and complications that arise in the ZD case as well as possible ways of overcoming them.

   Thus, instead of using a phenomenological Hamiltonian (6.1.3), the authors of [150] start their consideration from the full system consising of a nonlinear oscillator interacting with a medium (thermostat) consisting of a quasi-continuous spectrum of harmonic vibrations. The Hamiltonian of the full system, expressed in terms of the creation and annihilation operators $\hat{a}^+$ and $\hat{a}$ for the oscillator and $\hat{a}_k^+$ and $\hat{a}_k$ for the quasi-continuous-spectrum of vibrations, takes the form:

$$H = H_0 + H_m + H_i, \tag{6.1.14}$$
$$H_0 = H_{\mathrm{DO}} \equiv \hbar\omega_0\, \hat{n} + \gamma\hbar^2\, \hat{n}^2, \qquad \hat{n} = \hat{a}^+ \hat{a},$$
$$H_m = \sum_k \hbar\omega_k\, \hat{a}_k^+ \hat{a}_k, \qquad H_i = \sum_k \epsilon_k (\hat{a} + \hat{a}^+)(\hat{a}_k + \hat{a}_k^+).$$

   It turns out to be possible to eliminate the vibrations of the continuous spectrum and to obtain for the operator acting only on the oscillator wave functions (which in a sense is

analogous to $q(t)$ in the classical case) a differential operator equation that may be considered as a generalized quantum kinetic equation. This operator equation is equivalent to a system of differential-difference equations for matrix elements. Introducing a generating function, the latter system of differential-difference equations can be transformed into a differential equation in partial derivatives of the *first*[71] order for the generating function. This equation is solved explicitly and, using it, the correlation function of the coordinate is also derived in explicit form. The Fourier transform can then easily be calculated numerically. As the parameters of nonlinearity and interaction with the medium vary, the spectrum evolves from having pronounced fine structure (the predominently quantal regime) to being relatively smooth and broad (the predominently classical regime).

In order to include the ZD case within this framework, one has to consider instead of the Duffing oscillator the tilted Duffing oscillator (TDO), whose Hamiltonian contains in addition the cubic nonlinearity:

$$H_0 = H_{\rm TDO} \equiv \hbar\omega_0 \hat{n} + \gamma\hbar^2 \hat{n}^2 + \beta\hbar^3 \hat{n}^3 . \tag{6.1.15}$$

It is then easy to see that the dependence of the energy level E_n on its quantum number n is

$$E_n = \hbar\omega_0 n + \hbar^2\gamma n^2 + \hbar^3\beta n^3, \tag{6.1.16}$$

so that, if $\gamma\beta < 0$, then $\omega(E_n)$, which is $\approx dE_n/dn$, possesses as a function of $n \approx E_n/\hbar\omega_0$ an extremum (local minimum or maximum) at

$$n = n_m \equiv \left[-\frac{\gamma}{3\hbar\beta}\right]. \tag{6.1.17}$$

The case of the TDO may be treated similarly to that of the DO, described above. However, unlike the DO case, partial derivatives of up to the *second* order appear in the equation for the generating function, because of the presence of the cubic nonlinearity in $H_{\rm TDO}$ (6.1.15). It may not be possible to derive a solution of this equation in explicit form. Then, instead of a numerical solution of the second-order equation in partial derivatives for the generating function (which is in itself far from trivial), it would probably be easier to go one step backwards, and to solve numerically the system of the differential-difference equations for the matrix elements, restricting oneself to those elements corresponding to the energy levels lying in the relevant vicinity of n_m: the number N of the equations should significantly exceed the ratio of the width $\Delta E_{\rm zdp}$ (3.3.5) of the energy range responsible for the formation of the classical ZDP to the distance between adjacent levels ($\approx \hbar\omega_0$),

$$N \gg \frac{1}{\hbar\omega_0}\left(\frac{\Gamma T E_{n_m}}{|d^2\omega(E_{n_m})/dE_{n_m}|}\right)^{1/4}, \tag{6.1.18}$$

[71] That the partial derivatives are not higher than of first order is because the nonlinearity in the Hamiltonian of the Duffing oscillator $H_{\rm DO}$ (6.1.14) is not higher than quadratic in terms of $\hat{n}$.

$$\frac{d^2\omega(E_{n_m})}{dE_{n_m}^2} \approx \frac{1}{\hbar^3\omega_0^2}\frac{d^3E_{n_m}}{dn_m^3} = \frac{6|\beta|}{\omega_0^2},$$

$$\Gamma = \frac{\pi}{4}g_\epsilon(\omega_0), \qquad g_\epsilon(\omega)d\omega \equiv \sum_{k\to[\omega\le\omega_k\le\omega+d\omega]}\frac{\epsilon_k^2}{\omega_k^2},$$

where Γ is an effective parameter of dissipation arising due to the interaction with the medium [150,2].

6.2 Quantum zero-dispersion nonlinear resonance

The resonant interaction of a periodic perturbation (e.g. light) with a quantum nonlinear oscillator (e.g. an atom or molecule) may have two limiting regimes. One of these, which may be described as purely quantum, occurs when the perturbation is resonant with a transition between only one pair of energy levels, while the frequencies of transitions between any other energy levels are distinctly different. In this case, only two energy levels are involved in the quantum dynamics caused by the periodic perturbation.

The other limiting regime, which relates typically to high-quantum-number (i.e. quasi-classical) energy levels, occurs if the distance between adjacent energy levels varies relatively slowly with quantum number, so that a large number of transitions are approximately resonant to the perturbation, and therefore a large number of levels are involved in the dynamics of repopulation caused by the periodic perturbation. It is this latter regime that is called *quantum nonlinear resonance* [153,154]. The first rigorous quantum (rather than quasi-classical [153]) approach was developed in [154] for quantum nonlinear resonance in a conventional nonlinear oscillator. In what follows, we shall denote it as QNR. It has many similarities to classical NR. In particular, the energy width of the QNR (or, equivalently, the number of levels involved in the QNR) is proportional to the square root of the ratio of the amplitude of the perturbation to the absolute value of the dispersion of the classical eigenfrequency [154]. In addition, there are quantum analogues of: the separatrix [155]; maps exhibiting chaos [156]; and the fast decay of correlations as different QNRs overlap [155]. But even for these analogues, there are many distinctions between the quantum and classical cases, and the quantum case possesses some properties that are absent in the classical case. A review of QNR properties and a fuller list of relevant references are given in [83].

It is obvious that, in a ZD system, where the distance between quasi-classical energy levels changes with quantum number even more slowly than in the conventional case, quantum nonlinear resonance may be expected to be much more pronounced, as well as possessing features absent in the conventional case. Initial results on isolated quantum zero-dispersion nonlinear resonance (QZDNR) are presented in an as yet unpublished work [148]. Sec. 6.2.1 below reviews the studies of the isolated QNR [154,155] and QZDNR [148]. Sec. 6.2.2 lists unsolved problems for the QZDNR.

6.2.1 Isolated resonance

While considering a single resonance, we shall use an approach similar to that developed in [154]. So, let a nonlinear oscillator characterized by the Hamiltonian operator H_0 be perturbed by a weak sinusoidal force $F\cos(\Omega t)$, i.e. the perturbation of the Hamiltonian is $V_{int} \equiv dF\cos(\Omega t)$ where d is a relevant operator of the oscillator [72]. We shall seek the wave function as an expansion over the full set of eigenfunctions $\psi_n(q)$ of the unperturbed oscillator:

$$\psi(q,t) = \sum_n c_n(t)\psi_n(q), \qquad H_0\psi_n(q) = E_n\psi_n(q). \tag{6.2.1}$$

The numbers of relevant energy levels are assumed to be high so that the corresponding levels are quasi-classical and as a consequence [149]

$$E_{n+1} - E_n \approx \hbar\omega(E_n), \tag{6.2.2}$$

where $\omega(E)$ is a classical eigenfrequency as a function of energy.

6.2.1.1. Conventional case.

Consider first the conventional case [154,155,157] when $d\omega/dE$ is distinctly non-zero in the relevant range of energies, for which [73] $\omega(E) \approx \Omega$. Let us denote by n_r the quantum number of the energy level closest to the classical resonant energy E_r defined by the relation $\omega(E_r) = \Omega$. It then follows from (6.2.2) that $dE_n/dn|_{n=n_r}$ is very close to $\hbar\Omega$. It will be sufficient for us to keep only three first terms in the Taylor expansion of E_n as a function of n:

$$E_n \approx E_{n_r} + \left.\frac{dE_n}{dn}\right|_{n=n_r}(n-n_r) + \frac{1}{2}\left.\frac{d^2E_n}{dn^2}\right|_{n=n_r}(n-n_r)^2. \tag{6.2.3}$$

It is convenient to separate out the fast-oscillating factor in $c_n(t)$. There are slightly different ways of doing this, but we follow that of [155]:

$$c_n(t) = A_m(t)\exp\left\{-\frac{i}{\hbar}\left(E_{n_r} + \left.\frac{dE_n}{dn}\right|_{n=n_r} m\right)t\right\}, \tag{6.2.4}$$
$$m \equiv n - n_r.$$

Substituting (6.2.1), (6.2.4) into the Schrödinger equation

$$i\hbar\frac{\partial\psi}{\partial t} = H\psi, \tag{6.2.5}$$

[72] For example, in the case of a dipole interaction, $d \propto q$ is the operator of a dipole moment.
[73] For the sake of simplicity, we consider only the resonance of 1st order.

$$H = H_0 + V_{int}, \qquad H_0\psi_n = E_n\psi_n, \qquad V_{int} = dF\cos(\Omega t),$$

multiplying the resulting equation by $\psi_n^*(q)$ with a given n, integrating over q and neglecting fast-oscillating terms, one obtains equations describing the dynamics of the "slow" amplitudes A_m:

$$i\frac{dA_m}{d\tau} = \mu m^2 A_m + \frac{1}{2}V\left(\mathrm{e}^{i\nu\tau}A_{m+1} + \mathrm{e}^{-i\nu\tau}A_{m-1}\right), \tag{6.2.6}$$

$$\tau \equiv \Omega\tau, \quad \mu \equiv \frac{1}{2\hbar\Omega}\left.\frac{d^2E_n}{dn^2}\right|_{n=n_r}, \quad \nu \equiv \frac{\Omega - \frac{1}{\hbar}\left.\frac{dE_n}{dn}\right|_{n=n_r}}{\Omega}, \quad V \equiv F\frac{\int dq\ \psi^*_{n_r}\ d\ \psi_{n_r+1}}{\hbar\Omega},$$

$$m \ll n_r.$$

Here we have also neglected for simplicity the difference between matrix elements for transitions from different relevant levels to adjacent ones, which is justifiable on account of the strong inequality in (6.2.6).

Introducing the auxiliary angle θ and periodic function $\varphi(\theta,\tau)$,

$$\varphi(\theta,\tau) = \sum_{m=-\infty}^{\infty} A_m(\tau)\mathrm{e}^{im\theta}, \tag{6.2.7}$$

$$A_m \equiv \int_0^{2\pi} d\theta\ \varphi\mathrm{e}^{-im\theta},$$

and using (6.2.6), one obtains the equation

$$i\frac{\partial\varphi}{\partial\tau} = -\mu\frac{\partial^2\varphi}{\partial\theta^2} + V\cos(\theta - \nu\tau)\varphi. \tag{6.2.8}$$

Given that ν is necessarily much smaller than the relevant "slow frequency" of the resonance $\sim\sqrt{|V\mu|}$ (see below), ν may be put to zero in the zeroth-order approximation [74] so that the resulting equation for φ is equivalent to the Schrödinger equation in the auxiliary cosine potential. The problem of its eigenfunctions and eigenvalues is the well known Mathieu equation [49,158]:

$$(-\mu\frac{d^2}{d\theta^2} + V\cos(\theta))\chi_z = \lambda_z\chi_z. \tag{6.2.9}$$

The spectrum λ_z has a band structure, but only periodic solutions χ_z are relevant (see Eq.(6.2.7)); such solutions correspond [154] to λ_z which lie on the boundaries of the bands (see [157,158] for more details).

[74] Note however that, for the sake of generality, the computer simulations [155] of eqs.(6.2.6) shown in Fig. 69 are for nonzero ν.

Taking account of (6.2.7)-(6.2.9) and of a property following from the orthogonality and periodicity of the relevant eigenfunctions χ_z,

$$\sum_k \tilde{\chi}_z^*(k)\tilde{\chi}_{z'}(k) = \delta_{zz'}, \tag{6.2.10}$$

$$\tilde{\chi}_z(k) \equiv \frac{1}{2\pi}\int_0^{2\pi} d\theta\ \chi_z(\theta)\mathrm{e}^{-ik\theta}, \qquad \tilde{\chi}_z^*(k) = \tilde{\chi}_z(-k),$$

one can obtain (cf. [154]) the following expression for $A_m(\tau)$ via the set of initial amplitudes $\{A_k(0)\}$ in the zero-order approximation ($\nu = 0$):

$$A_m(\tau) = \sum_z \sum_k A_k(0)\tilde{\chi}_z(m)\tilde{\chi}_z(-k)\mathrm{e}^{-i\lambda_z\tau}. \tag{6.2.11}$$

Using (6.2.11), and taking into account the relation [149] between the number of zeros in an eigenfunction of a Schrödinger equation and the quantum number of the energy level corresponding to this eigenfunction, it can be shown that the levels trapped in the resonance, i.e. levels with mixed dynamics, are those with quantum numbers m in the interval $[-\delta n/2, \delta n/2]$. Here δn is of the order of the number of levels in a single (isolated) well of the auxiliary cosine potential (6.2.9), which is [75] itself of the order of the ratio of the potential barrier $|V|$ to the eigenfrequency in the bottom of the potential well $\Omega_b = \sqrt{2|\mu V|}$, i.e. $\delta n \sim \sqrt{|V/\mu|} \propto \sqrt{F/|d\omega(E_r)/dE_r|}$. The latter dependence is similar to that of the width of classical NR on driving amplitude. A more accurate estimate, based on the properties of periodic Mathieu functions [158], is suggested in [155]:

$$\delta n \approx 4\sqrt{\left|\frac{V}{\mu}\right|}. \tag{6.2.12}$$

The paper [155] presents results of computer simulations of the dynamics of populations based on Eqs. (6.2.6) for a given set of parameters and various initial distributions of the amplitudes A_m. One of the main features of QNR is the formation of a steady regime after some transient period. If initially populated levels possess quantum numbers m within the interval $[-\delta n/2, \delta n/2]$, then the wave packet is spread over the whole interval during some time τ^*. The spreading then stops and the subsequent dynamics is reduced to an oscillatory redistribution between levels trapped in the QNR, possessing a characteristic "return" time τ_r. E.g. for the set of parameters $V = 5 \times 10^{-2}$, $\mu = 10^{-3}$, $\nu = 10^{-3}$ (the latter corresponds to exact resonance with the transition between the levels $m = 0$ and $m = 1$) and for the single populated level $m = 0$ (i.e. $A_m(\tau = 0) = \delta_{m0}$), the transient time $\tau^* \approx 200$ and the number of trapped levels $\delta n = 22$. The latter matches quite well the analytic estimate (6.2.12) which gives $\delta n = 28$. The return time in simulations, $\tau_r \approx 360$, also well matches the analytic estimate, i.e. the half-period of the eigenoscillation in the bottom of the auxiliary potential (6.2.9) $\pi/\Omega_b = \pi/\sqrt{2|\mu V|} \approx 314$.

[75] Note that (6.2.9) is written in normalized units and, in particular, that Planck's constant is normalized to unity.

Fig. 69 presents results of simulations [155] demonstrating in QNR the analogue of a separatrix. If the absolute value of the quantum number m of the initially populated level exceeds the critical value $m^* \approx \delta n/2$, then only few levels around $m(0)$ become populated in the steady regime (see Fig. 69(a)) and the formation time of the steady regime is relatively small. The situation drastically changes if $|m(0)| < m^*$ (see Figs. 69(c-e)): the distribution of populated levels is significantly wider, extending approximately over the interval $[-m^*, m^*]$, while the formation time of the steady regime significantly increases. The "boundary" case $|m(0)| \approx m^*$ is illustrated by Fig. 69(b).

6.2.1.2. Zero-dispersion case.

Let $\omega(E)$ possess a local minimum or maximum at some $E = E_m$, i.e. $d\omega(E)/dE|_{E=E_m} = 0$. Let us denote by n_m the number of the energy level closest to E_m, so that $d^2E_n/dn^2|_{n=n_m} \approx 0$ as follows from (6.2.2). Unlike the conventional case, it will be necessary for us to keep four terms in the Taylor expansion of E_n:

$$E_n \approx E_{n_m} + \left.\frac{dE_n}{dn}\right|_{n=n_m} (n-n_m) + \frac{1}{2}\left.\frac{d^2E_n}{dn^2}\right|_{n=n_m} (n-n_m)^2 + \frac{1}{6}\left.\frac{d^3E_n}{dn^3}\right|_{n=n_m} (n-n_m)^3. \tag{6.2.13}$$

The driving frequency Ω is assumed to be close to $\omega(E_m) \approx dE_n/dn|_{n=n_m}$. We shall separate out the fast-oscillating factor in $c(t)$ (6.2.1) in the following way:

$$c_n(t) = A_l(t) \exp\left\{-\frac{i}{\hbar}\left(E_{n_m} + \hbar\Omega l\right) t\right\}, \tag{6.2.14}$$
$$l \equiv n - n_m.$$

Substituting (6.2.1), (6.2.14) into the Schrödinger equation (6.2.5) and carrying out the same operations as in the conventional case (6.2.6), we obtain:

$$i\frac{dA_l}{d\tau} = (-\nu_m l + \eta_m l^3)A_l + \frac{1}{2}V_m\left(A_{l+1} + A_{l-1}\right), \tag{6.2.15}$$
$$\tau \equiv \Omega\tau, \quad \nu_m \equiv \frac{\Omega - \frac{1}{\hbar}\left.\frac{dE_n}{dn}\right|_{n=n_m}}{\Omega}, \quad \eta \equiv \frac{1}{6\hbar\Omega}\left.\frac{d^3E_n}{dn^3}\right|_{n=n_m}, \quad V_m \equiv F\frac{\int dq\ \psi^*_{n_m}\ d\ \psi_{n_m+1}}{\hbar\Omega},$$
$$l \ll n_m,$$

where we have also neglected the deviation of $d^2E_n/dn^2|_{n=n_m}$ from zero.

Then the equation for the auxiliary function $\phi(\theta, \tau)$ (6.2.7) is as follows:

$$
\begin{aligned}
& i\frac{\partial\varphi}{\partial\tau} = H^{(\mathrm{zd})}\varphi, \\
& H^{(\mathrm{zd})} = i\nu_m\frac{\partial}{\partial\theta} + i\eta_m\frac{\partial^3}{\partial\theta^3} + V_m\cos(\theta), \\
& \varphi(\theta+2\pi) = \varphi(\theta).
\end{aligned}
\tag{6.2.16}
$$

The operator $H^{(\mathrm{zd})}$ can be shown [148] to be Hermitian (self-conjugated), so that its eigenvalues are real while the eigenfunctions are orthogonal each other and constitute a complete set [149]. Thus, like periodic Mathieu functions, the eigenfunctions of $H^{(\mathrm{zd})}$ possess the property (6.2.10) and the amplitudes $A_l(\tau)$ may formally be expressed via the set of initial conditions $\{A_l(0)\}$ by means of Eqs. (6.2.11),(6.2.10) in which the periodic Mathieu functions χ_z are exchanged for periodic eigenfunctions of the operator $H^{(\mathrm{zd})}$.

It is worth pointing out that both in the conventional and ZDNR cases the corresponding operators (6.2.9) and (6.2.16) could be obtained from the classical asymptotic Hamiltonians (4.1.10) and (4.1.11) through the exchange of respectively $(I - I_r)$ and $(I - I_m)$ by the operator $-i\partial/\partial\theta$ and of the interaction amplitude by the corresponding matrix element. This is a consequence of the correspondence principle valid in the quasi-classical regime for classical action-angle variables and their properly introduced quantum analogues [159,157].

6.2.2 Unsolved problems

1. Though the formal solution of the problem of the QZDNR has been obtained, in terms of the periodic eigenfunctions of the operator $H^{(\mathrm{zd})}$, explicit expressions for the latter eigenfunctions have not so far been found. Operators of this kind, i.e. odd functions of the momentum operator, are not studied in quantum mechanics, so that the solution of the corresponding eigenvalue problem is a difficult task, even methodologically.
2. Simulations of the dynamics of the amplitudes $A_l(\tau)$ and populations $|A_l(\tau)|^2$ have not yet been carried out. In analogy with the classical cases, one may expect that the energy width of the QZDNR will be $\propto (|V_m/\eta_m|)^{1/3} \propto F^{1/3}$, therefore exceeding typically that of conventional QNR which is $\propto F^{1/2}$ (see Eqs.(6.2.12),(6.2.6)).
3. It was found in [155] by means of simulations that the overlap in energy between different QNRs drastically changes the population dynamics, in analogy with the onset of global chaos associated with the overlap of classical NRs. But the overlap in energy between classical ZDNRs of the same order does not result in the onset of global chaos (see Sec. 4). Even the overlap in phase space (the ZDNR/NR transition) results in a change of the phase space structure rather than in the onset of global chaos in the conventional sense. Therefore, it will be very interesting to study, at least by means of simulations, how the dynamics of the populations changes with decreasing distance in energy between two resonances of the *same* order.
4. In order to describe explicitly the dynamics of amplitudes $A_l(\tau)$, instead of the introduction of the auxiliary function $\varphi(\theta,\tau)$, one may exchange the discrete energy level number l for its continuous approximation: $A_{l+1} + A_{l-1} - 2A_l$ in the discrete description is exchanged for $\partial^2 A/l^2$ in the continuous one. Given that the number of levels trapped in the nonlinear resonance is large, such an approach should provide a good

approximation, at least in the steady regime (i.e. at large time-scales). The equation of motion for $A_l(\tau)$ reduces then to the Schrödinger-like equation:

$$-i\frac{\partial A}{\partial \tau} = \left[-\frac{1}{2m_{\rm a}}\frac{\partial^2}{\partial l^2} + U_{\rm a}(l)\right] A, \tag{6.2.17}$$

$$m_{\rm a} = \begin{cases} V^{-1} & \text{for the QNR,} \\ V_m^{-1} & \text{for the QZDNR,} \end{cases}$$

$$U_{\rm a}(l) = \begin{cases} -V-\mu l^2 & \text{for the QNR,} \\ -V_m+\nu_m l-\eta_m l^3 & \text{for the QZDNR.} \end{cases}$$

Such an approach may be especially advantageous for the QZDNR since the problem (6.2.17) is equivalent to conventional quantum-mechanical motion in the auxiliary potential $U_{\rm a}$, while methods for the solution of conventional quantum-mechanical problems are much better developed than those for solution of the eigenvalue problem for such non-conventional operators as $H^{(\rm zd)}$ (6.2.16).

5. It would be interesting to extend studies of quantum chaos related to QNR (see [83] and references therein) to the case of the QZDNR. Given that manifestations of chaos related to classical ZDNR have many distinctions from classical NR (see Sec. 4), one may expect that quantum chaos related to the QZDNR will differ significantly from that related to the QNR.

6.3 Conclusions

If the system operates in the range of quasi-classical energies, i.e. at high quantum numbers n of energy levels E_n, then the spacing between adjacent levels in this range changes with the quantum number very smoothly and is $\approx \hbar\omega(E_n)$ where $\omega(E)$ is a frequency of classical eigenoscillation with energy E. Then even a weak perturbation may cause a repopulation of a *large* number of levels due to a strong interference between corresponding transitions, which is analogous in a sense to long-lasting classical correlations. This effect is especially pronounced in zero-dispersion systems in the range of extreme energy E_m, where the spacing between levels changes with n especially slowly. This results in a number of effects which are either much less pronounced in, or completely absent from, non-ZD systems.

Thus, if the quantum ZD system is subject to an external noise, e.g. of thermal origin, a *quantum zero-dispersion peak* arises in the spectrum of fluctuations if the interaction parameter is larger than, or of the same order as, some small critical value [147] (see Eq. (6.1.10) in Sec. 6.1.1 above as well as the schematic Fig. 67). The phenomenon has not yet been described quantitatively but a reasonable modification of the corresponding approach used for the conventional case [150,2] was suggested [147] for the case of interaction with a thermostat of the quasi-continuous spectrum of vibrations (see Sec. 6.1.2).

If the quantum ZD system is periodically driven at a frequency close to $\omega(E_m)$ or one of its harmonics, then the phenomenon of *quantum zero-dispersion nonlinear resonance* (QZDNR) may occur [148]. It is expected to have many distinctive features compared to conventional quantum nonlinear resonance (QNR) [154]. In particular, QZDNR promises to be wider than the QNR, and the dynamics of repopulation of the quantum levels at the overlap of two QZDNRS of the *same* order promises to be very different from that at the

overlap of QNRs, which are necessarily of different orders. A very preliminary quantitative study [148] of QZDNR was reviewed in Sec. 6.2.1, and it would be interesting to extend these investigations in the ways discussed in Sec. 6.2.2.

It is also worth noting that the *simultaneous* action of noise and a periodic force on the quantum ZD system has not yet been studied at all. It would be interesting to do so, given that in classical cases such simultaneous action gives rise to many interesting phenomena (see Sec. 5), in particular to zero-dispersion stochastic resonance (see Sec. 5.1). Note that an analogue of conventional stochastic resonance in some non-ZD quantum system has been considered in [160].

7 Concluding remarks

We hope that we have managed to demonstrate in this review that zero-dispersion systems are rather widespread in nature and form a distinct class of systems with characteristic properties. If subject to external action, they may manifest resonant behaviour in a much more pronounced way than conventional systems and, moreover, some of the phenomena can occur only in ZD systems.

We have reviewed three characteristic types of action on classical ZD systems: noise (additive white, mostly), a sinusoidal force, and their combination (additive, mostly). Some of the resulting phenomena, such as zero-dispersion peaks in fluctuation spectra, zero-dispersion nonlinear resonance and zero-dispersion stochastic resonance, have already been well established, which provides a good base for a realization in a near future of their practical applications, apart from a good understanding of various relevant physical phenomena. Others are either barely studied or in the midst of being investigated, and we have given our view of the major unsolved problems for each of them.

We have also touched the subject of quantum ZD phenomena, which has barely been studied to date and would certainly be interesting for future investigations.

We hope that, apart from the reviewed phenomena and systems, there exist many other ZD phenomena and systems whose identification and study be in the future, and that our review may help to stimulate the further development of this interesting field.

Acknowledgements

We very much appreciate the contributions to many of our works on ZD phenomena by our coauthors. This concerns, first of all, M.I. Dykman, D.G. Luchinsky, A.B. Neiman, N.J. Stein, and N.G. Stocks, as well as M. Arrayas, I.Kh. Kaufman, V. Isaia, K. Richter, Yu.G. Rubo, A.N. Silchenko, O.M. Yevtushenko.

We are also grateful to T.L. Linnik, A.B. Neiman, K. Richter, V.I. Sheka, A.N. Silchenko and O.M. Yevtushenko for their patience while the completion and submission of our joint papers were postponed because of our work on the review.

We acknowledge also the financial support by the INTAS (grants 97-574, 00-00867).

S.M.S. acknowledges also the hospitality of Lancaster and Pisa Universities during his stay there, when some parts of the review were prepared.

A Appendix. Transformation to slow-fast variables

We present here the transformation between the momentum-coordinate and energy-angle or action-angle variables, as well as the dynamical equations for the latter variables in the case of non-Hamiltonian motion.

Let the $(p-q)$ variables obey the following equations

$$\begin{aligned}\dot{q} &= \frac{\partial H(q,p)}{\partial p} + f_q(q,p,t),\\ \dot{p} &= -\frac{\partial H(q,p)}{\partial q} + f_p(q,p,t),\end{aligned} \tag{A.1}$$

where f_q and f_p are some functions of q, p, t.

One may need to use canonical transformation between $(p-q)$ and $I-\psi$ (or a closely related pair of variables $E-\psi$). Let us first express E, ψ, I via p, q.

$$E = H(q,p), \tag{A.2}$$

$$\psi = \left[\omega(E)\int \frac{dq}{p(q,E)}\right]_{E=H(q,p)}, \tag{A.3}$$

where $\omega(E)$ is the frequency of eigenoscillation in the Hamiltonian system at the energy E, while $p(q,E)$ is to be found from (A.2).

The action I is related to energy E by the relation [1]

$$I \equiv I(E) = \int\limits_{E_{min}}^{E} d\tilde{E}\, \omega^{-1}(\tilde{E}), \tag{A.4}$$

where E_{min} is a relevant local minimum of E in (A.2).

On the other hand, q and p may be expressed via E and ψ:

$$\begin{aligned}q &= \sum_{n=-\infty}^{\infty} q_n(E)\exp(-in\psi),\\ p &= -i\omega(E)\sum_{n=-\infty}^{\infty} n q_n(E)\exp(-in\psi).\end{aligned} \tag{A.5}$$

Now, let us derive from (A.1) the dynamical equations for $E-\psi$. Differentiating (A.2)

with respect to t and using (A.1), one derives

$$\dot{E} = \frac{\partial H}{\partial p} f_p + \frac{\partial H}{\partial q} f_q. \tag{A.6}$$

To derive the equation for ψ, we use a more sophisticated method since the straightforward differentiation of (A.3) does not immediately lead to a simple result. We formally differentiate ψ as a function of q, p and use (A.1):

$$\begin{aligned} \dot{\psi} &= \frac{\partial \psi}{\partial q}\dot{q} + \frac{\partial \psi}{\partial p}\dot{p} = \frac{\partial \psi}{\partial q}\frac{\partial H}{\partial p} - \frac{\partial \psi}{\partial p}\frac{\partial H}{\partial q} + \frac{\partial \psi}{\partial q} f_q + \frac{\partial \psi}{\partial p} f_p \\ &= \omega(E) + \frac{\partial \psi}{\partial q} f_q + \frac{\partial \psi}{\partial p} f_p. \end{aligned} \tag{A.7}$$

We used in the derivation of the last equality in (A.7) the fact that the case of $f_q = f_p = 0$ corresponds to conservative motion, when $d\psi/dt = \omega(E)$ [1], whereas the form of the first two terms in the middle equality in (A.7) is independent of f_q, f_p.

In order to find $\partial\psi/\partial q \equiv (\partial\psi/\partial q)_p$, the partial derivative of ψ with respect to q at a constant p, we use the following trick. On the one hand,

$$\left(\frac{\partial p}{\partial q}\right)_p = 0, \tag{A.8}$$

while, on the other hand,

$$\left(\frac{\partial p}{\partial q}\right)_p = \left(\frac{\partial p}{\partial \psi}\right)_E \left(\frac{\partial \psi}{\partial q}\right)_p + \left(\frac{\partial p}{\partial E}\right)_\psi \left(\frac{\partial E}{\partial q}\right)_p. \tag{A.9}$$

Taking into account that

$$\left(\frac{\partial E}{\partial q}\right)_p \equiv \left(\frac{\partial H}{\partial q}\right)_p = -\left(\frac{dp}{dt}\right)_E = -\left(\frac{\partial p}{\partial \psi}\right)_E \left(\frac{d\psi}{dt}\right)_E = -\left(\frac{\partial p}{\partial \psi}\right)_E \omega(E), \tag{A.10}$$

we obtain from (A.9)

$$\left(\frac{\partial \psi}{\partial q}\right)_p = \omega(E) p_E. \tag{A.11}$$

Similarly, analysing $(\partial q/\partial p)_q$, one can obtain

$$\left(\frac{\partial \psi}{\partial p}\right)_q = -\omega(E) q_E. \tag{A.12}$$

Putting (A.11),(A.12) into (A.7), we finally obtain

$$\dot{\psi} = \omega(E) + \omega(E) p_E f_q - \omega(E) q_E f_p. \tag{A.13}$$

Thus, Eqs. (A.6),(A.13) are dynamical equations in terms of $E - \psi$ variables. For the case

$$\begin{aligned} H &= \frac{p^2}{2} + U(q), \\ f_q &= 0, \\ f_p &= -\Gamma p + f(t), \end{aligned} \tag{A.14}$$

most often used in the review, equations (A.6),(A.13) reduce to

$$\begin{aligned} \dot{E} &= -\Gamma p^2 + p f(t), \\ \dot{\psi} &= \omega(E) + \Gamma \omega(E) p q_E - \omega(E) q_E f(t). \end{aligned} \tag{A.15}$$

References

[1] L.D. Landau, E.M. Lifshitz, Mechanics (Pergamon, London, 1976).

[2] M.I. Dykman, M.A. Krivoglaz, Theory of nonlinear oscillator interacting with a medium, in: Soviet Physics Reviews, ed. I.M. Khalatnikov (Harwood, New York, 1984) v.5, pp. 265–441.

[3] M.I. Dykman, M.A. Krivoglaz, S.M. Soskin, Transition probabilities and spectral density of fluctuations of noise driven bistable systems, in: Noise in nonlinear dynamical systems, eds F. Moss, P.V.E. McClintock (Cambridge University Press, Cambridge, 1989) v.2, pp. 347–380.

[4] M.I. Dykman and P.V.E. McClintock, Power spectra of noise-driven nonlinear systems and stochastic resonance, Physica D 58 (1992) 10–30.

[5] B.V. Chirikov, A universal instability of many-dimensional oscillator systems, Phys. Rep. 52 (1979) 263–379.

[6] S.M. Soskin, Low-frequency spectral peak for systems thermalized in a periodic potential, Report No. 87/7 (Institute of Physics, Kiev, 1987), in Russian.

[7] ** S.M. Soskin, Fluctuation spectrum peaks for systems where the oscillator frequency dependence on energy has an extremum, Physica A 155 (1989) 401–429.

[8] * J.E. Howard, S.M. Hohs, Stochasticity and reconnection in Hamiltonian systems, Phys. Rev. A 29 (1984) 418–421.

[9] J.E. Howard, J. Humpherys, Nonmonotonic twist maps, Physica D 80 (1995) 256–276.

[10] D. del-Castillo-Negrete, J.M. Greene, P.J. Morrison, Area-preserving nontwist maps: Periodic orbits and transition to chaos, Physica D 61 (1996) 1–23.

[11] * M.I. Dykman, R. Mannella, P.V.E. McClintock, S.M. Soskin, N.G. Stocks, Noise-induced narrowing of peaks in the power spectra of underdamped nonlinear oscillators, Phys. Rev. A 42 (1990) 7041–7049.

[12] N.W. Ashcroft, N.D. Mermin, Solid State Physics (Holt, Reinhardt and Winston, New York, 1976).

[13] L.D. Landau, E.M. Lifshitz, Statistical Physics (Pergamon, New York, 1980).

[14] R. Barone, G. Paterno, Physics and Applications of the Josephson Effect (Wiley, New York, 1982).

[15] K.K. Likharev, Dynamics of Josephson Junctions and Circuits (Gordon and Breach, Philadelphia, 1986).

[16] H.A. Carmona, A.K. Geim, A. Nogaret, P.C. Main, T.J. Foster, M. Henini, S.P. Beamont, M.G. Blamire, Two dimensional electrons in a lateral magnetic superlattice, Phys. Rev. Lett. 74 (1995) 3009–3012.

[17] P.D. Ye, D. Weiss, R.R. Gerhardts, M. Seeger, K. Von Klitzing, G. Weimann, Electrons in a periodic magnetic field induced by a regular array of micromagnets, Phys. Rev. Lett. 74 (1995) 3013–3016.

[18] G.J.O. Shmidt, Deterministic diffusion and magnetotransport in periodically modulated magnetic fields, Phys. Rev. B 47 (1993) 13007–13010.

[19] P. Shmelcher, D.L. Shepelyansky, Chaotic and ballistic dynamics for two–dimensional electrons in periodic magnetic fields, Phys. Rev. B 49 (1994) 7418–7423.

[20] O.M. Yevtushenko, K. Richter, Effect of an ac electric field on chaotic electronic transport in a magnetic superlattice, Phys. Rev. B 57 (1998) 14839–14842.

[21] O.M. Yevtushenko, K. Richter, AC-driven anomalous stochastic diffusion and chaotic transport in magnetic superlattices, Physica E 4 (1999) 256–276.

[22] L.D. Landau, E.M. Lifshitz, The Classical Theory of Fields (Pergamon, Oxford, 1975).

[23] D. Brown, J.H.R. Clarke, A direct method of studying reaction rates by equilibrium molecular dynamics: Application to the kinetics of isomerization in liquid n-butane, J. Chem. Phys. 92 (1990) 3062–3073.

[24] G.J. Moro, A. Polimeno, Multi-barrier crossing regulated by the friction, Chem. Phys. Lett. 189 (1992) 133–137.

[25] C. Hayashi, Nonlinear Oscillations in Physical systems (McGraw-Hill, New York, 1964).

[26] K.R. Symon, A.M. Sessler, in: Proceedings of the International Conference on High-Energy Accelerators and Instrumentation (CERN, Geneva, 1956), pp 44–58.

[27] A.S. Barker, Jr. A.J. Sievers, Optical studies of the vibrational properties of disordered solids, Rev. Mod. Phys 47, Suppl. No. 2 (1975) S1–S179.

[28] J.H. Kim, H.W. Lee, Nonlinear resonance and chaos in the relativistic phase space for driven nonlinear systems, Phys. Rev. E 52 (1995) 473–480.

[29] M.I. Dykman, S.M. Soskin, M.A. Krivoglaz, Spectral distribution of a nonlinear oscillator performing Brownian motion in a double-well potential, Physica A 133 (1985) 53–73.

[30] D.G. Luchinsky, P.V.E. McClintock, S.M. Soskin, N.D. Stein, A.B. Neiman, Comment on "Nonlinear resonance and chaos in the relativistic phase space for driven nonlinear systems", Phys. Rev. E 53 (1996) 4240–4241.

[31] J.H. Kim, H.W. Lee, Reply to "Comment on 'Nonlinear resonance and chaos in the relativistic phase space for driven nonlinear systems ' ", Phys. Rev. E 53 (1996) 4242.

[32] W.P. Leemans, C. Joshi, W.B. Mori, C.E. Clayton and T.W. Johnston, Nonlinear dynamics of driven relativistic electron plasma waves, Phys. Rev. A, 46 (1992) 5112–5122.

[33] C. Chen, R.C. Davidson, Nonlinear resonances and chaotic behaviour in a periodically focused intense charge-particle beam, Phys. Rev. Lett 72 (1994) 2195–2198.

[34] P.G. Harper, Single band motion of conduction electrons in a uniform magnetic field, Proc. Phys. Soc. A 68 (1955) 874–878.

[35] G.M. Zaslavsky, R.D. Sagdeev, D.A. Usikov and A.A. Chernikov, Weak Chaos and Quasi-Regular Patterns (Cambridge University Press, 1991).

[36] P. Leboeuf, J. Kurchan, M. Feingold, D.P. Arovas, Phase-space localization: topological aspects of quantum chaos, Phys. Rev. Lett. 65 (1990) 3076–3079.

[37] I. Dana, Kicked Harper models and kicked charge in a magnetic field, Phys. Lett. A 197 (1995) 413–416.

[38] H. Risken, The Fokker-Planck Equation, 2nd ed. (Springer-Verlag, Berlin, 1992).

[39] H. Risken, H.D. Volmer, Susceptibilities for the Brownian motion in a cosine potential with application to the rotation of a dipole in a constant external field, Mol. Phys. 46 (1982) 555–576.

[40] M. Born, K. Huang, Dynamical Theory of Crystal Lattices (Clarendon, Oxford, 1954).

[41] N.N. Bogolyubov, Yu. A. Mitropolsky, Asymptotic Methods in the Theory of Nonlinear Oscillators (Gordon and Breach, New York, 1961).

[42] H.A. Kramers, Brownian motion in a field of force and diffusion model of chemical reactions, Physica 7 (1940) 284–304.

[43] M.I. Dykman, M.A. Krivoglaz, Time correlation functions and spectral distributions of the Duffing oscillator in a random force field, Physica A 104 (1980) 495–508.

[44] R.P. Feynman, Statistical Mechanics (Reading, Mass.: Benjamin, 1972).

[45] N.G. Stocks, P.V.E. McClintock, S.M. Soskin, Observation of zero-dispersion peaks in the fluctuation spectrum of an underdamped single-well oscillator, Europhys. Lett. 21 (1993) 395–400.

[46] P.V.E. McClintock, S.M. Soskin, N.D. Stein, N.G. Stocks, Universality of zero-dispersion peaks in the fluctuation spectra of underdamped nonlinear oscillators, Phys. Rev. E 48 (1993) 147–156.

[47] ** I.Kh. Kaufman, D.G. Luchinsky, P.V.E. McClintock, S.M. Soskin, N.D. Stein, Zero-dispersion stochastic resonance in a model for a superconducting quantum interference device, Phys. Rev. E 57 (1998) 78–87.

[48] S.M. Soskin, Evolution of zero-dispersion peaks in fluctuation spectra with temperature, Physica A 180 (1992) 386–406.

[49] M. Abramovitz, I. Stegun, Handbook of Mathematical Functions (Dover, New York, 1970).

[50] M.I. Dykman, R. Mannella, P.V.E. McClintock, S.M. Soskin and N.G. Stocks, Zero-frequency spectral peaks of underdamped nonlinear oscillators with asymmetric potentials, Phys. Rev. A 43 (1991) 1701–1708.

[51] S.M. Soskin, Zero-frequency spectral peak in multi-stable underdamped oscillators, unpublished.

[52] L. Fronzoni, Analogue simulations of stochastic processes by means of minimum component electronic devices, in Noise in Nonlinear Dynamical Systems, ed. F. Moss, P.V.E. McClintock (Cambridge University Press, Cambridge, England, 1989), Vol. 3, pp 222–242.

[53] P.V.E. McClintock, F. Moss, Analogue techniques for the study of problems in stochastic nonlinear dynamics, in Noise in Nonlinear Dynamical Systems, ed. F. Moss, P.V.E. McClintock (Cambridge University Press, Cambridge, England, 1989), Vol. 3, pp 243–272.

[54] D.G. Luchinsky, P.V.E. McClintock, M.I. Dykman, Analogue studies of nonlinear systems, Rep. Prog. Phys. 61 (1998) 889–997.

[55] M.I. Dykman, R. Mannella, P.V.E. McClintock, S.M. Soskin, N.G. Stocks, Noise-induced spectral narrowing in nonlinear oscillators, Europhys. Lett. 13 (1990) 691–696.

[56] I.Kh. Kaufman, D.G. Luchinsky, P.V.E. McClintock, S.M. Soskin, N.D. Stein, High-frequency stochastic resonance in SQUIDs, Phys. Lett. A 220 (1996) 219–223.

[57] I.Kh. Kaufman, D.G. Luchinsky, P.V.E. McClintock, S.M. Soskin, N.D. Stein, Zero-dispersion stochastic resonance in underdamped SQUIDs, International Journal of Bifurcation and Chaos 8 (1998) 843–848.

[58] N.G. Stocks, N.D. Stein, P.V.E. McClintock, Stochastic resonance in monostable systems J. Phys. A 26 (1993) L385–L390.

[59] B.V. Chirikov, Resonance processes in magnetic traps, Atomnaya Energiya 6 (1959) 630–638. (in Russian).

[60] A.J. Lichtenberg, M.A. Liebermann, Regular and Stochastic Motion (Springer, New York, 1992).

[61] J.B. Taylor, Relaxation of toroidal plasma and generation of reverse magnetic fields, Phys. Rev. Lett. 33 (1974) 1139–1141.

[62] C.F.F. Karney, Stochastic ion heating by a lower hybrid wave, Phys. Fluids. 21 (1978) 1584–1589.

[63] A.B. Langdon, B.F. Lasinsky, Filamentation and subsequent decay of laser light in plasmas, Phys. Rev. Lett. 34 (1975) 934–937.

[64] J.B. Weiss, Transport and mixing in traveling waves, Phys. Fluids A 3 (1991) 1379–1384.

[65] D. del-Castillo-Negrete, P.J. Morrison, Chaotic transport by Rossby waves in shear flow, Phys. Fluids A 5 (1993) 948–965.

[66] S.S. Abdullaev, Two–dimensional model of a kicked oscillator: Motion with intermittency, Chaos 4 (1994) 569–581.

[67] * S.M. Soskin, Nonlinear resonance for the oscillator with a nonmonotonic dependence of eigenfrequency on energy, Phys. Rev. E 50 (1994) R44–R46.

[68] S.M. Soskin, D.G. Luchinsky, Zero-dispersion nonlinear resonance, Nuovo Cimento D 17 (1995) 915–924.

[69] ** D.G. Luchinsky, R. Mannella, P.V.E. McClintock, S.M. Soskin, Zero-dispersion nonlinear resonance in dissipative systems, Phys. Rev. Lett. 76 (1996) 4453–4456.

[70] * R. Mannella, S.M. Soskin, P.V.E. McClintock, Bifurcation analysis of zero-dispersion nonlinear resonance, International Journal of Bifurcation and Chaos 8 (1998) 701–712.

[71] S.M. Soskin, D.G. Luchinsky, R. Mannella, A.B. Neiman, P.V.E. McClintock, Zero-dispersion nonlinear resonance, International Journal of Bifurcation and Chaos 7 (1997) 923–936.

[72] S.M. Soskin, R. Mannella, V. Isaia, A.B. Neiman, P.V.E. McClintock, Chaos in periodically driven dissipative zero-dispersion systems, in: Noise in physical systems and 1/f Fluctuations, eds. C. Claeys, E. Simoen (World Scientific, Singapore, 1997) pp 351–354.

[73] S.M. Soskin, R. Mannella, A.B. Neiman, A.N. Silchenko, D.G. Luchinsky, P.V.E. McClintock, A criterion for the onset of chaos in weakly dissipative periodically driven systems, in: Stochaos: Stochastic and Chaotic Dynamics in the Lakes, eds. D.S.Broomhead, E.A.Luchinskaya, P.V.E.McClintock, T.Mullin (American Institute of Physics, Melville, NY, USA, 2000), pp 443–449.

[74] S.M. Soskin, R. Mannella, A.B. Neiman, A.N. Silchenko, P.V.E. McClintock, "An onset of chaos in weakly dissipative periodically driven systems and the overlap of resonances", unpublished.

[75] A.B. Neiman, S.M. Soskin, P.V.E. McClintock, Dynamical chaos in zero-dispersion nonlinear resonance, in: Noise in Physical Systems and 1/f Fluctuations, eds. V. Bareikis, R. Katilius (World Scientific, Singapore, 1995) pp 701–704.

[76] S.M. Soskin, O.M. Yevtushenko, R. Mannella, K. Richter, "Drastic facilitation of the onset of global chaos in a Hamiltonian system due to an extremum vs energy", submitted to Phys. Rev. Lett.

[77] D.G. Luchinsky, R. Mannella, P.V.E. McClintock, S.M. Soskin, Fluctuations in zero-dispersion nonlinear resonance, in: Noise in Physical Systems and 1/f Fluctuations, eds. V. Bareikis, R. Katilius (World Scientific, Singapore, 1995) pp 705–708.

[78] S.M. Soskin, R. Mannella and P.V.E. McClintock, "Noise-induced transitions in a periodically driven tilted Duffing oscillator", unpublished.

[79] S.M. Soskin, P.V.E. McClintock, N.D. Stein, A.B. Neiman, R. Mannella, V. Isaia, Zero-dispersion nonlinear resonance in underdamped SQUIDs, in: Noise in physical systems and 1/f Fluctuations, eds. C. Claeys, E. Simoen (World Scientific, Singapore, 1997) pp 333–336.

[80] J. Guckenheimer, P. Holmes, Nonlinear Oscillations, Dynamical Systems and Bifurcations of Vector Fields (Springer-Verlag, New York, 1983).

[81] A. Politi, G.L. Oppo, Coexistence of conservative and dissipative behaviour in reversible dynamical systems, Phys. Rev. A 33 (1986) 4055–4060.

[82] G.A. Korn, T.M. Korn, Mathematical Handbook for scientists and engineers (McGraw-Hill, New York, 1961).

[83] G.P. Berman, A.R. Kolovsky, Quantum chaos in interactions of multilevel quantum systems with a coherent radiation field, Soviet Phys. Uspekhi 35 (1992) 303–326.

[84] S.M. Soskin, R. Mannella, M. Arrayás and A.N. Silchenko, Strong enhancement of noise-induced escape by transient chaos, Phys. Rev. E 65 (2001) 051111-1–051111-6.

[85] C. Hayashi, M. Abe, K. Oshima, H. Kawakami, The method of mapping as applied to the solution for certain types of nonlinear differential equations, in : Proceedings of the IX International conference on nonlinear oscillations, Kiev, 1981 (Naukova Dumka, Kiev, 1984), v.1, p.40-44.

[86] S. Watanabe and S.H. Strogatz, Integrability of a globally coupled oscillator array, Phys. Rev. Lett. 70 (1993) 2391–2394.

[87] S. Watanabe and S.H. Strogatz, Constants of motion for superconducting Josephson arrays, Physica D 74 (1994) 197–253.

[88] Y. Braiman and K. Wiesenfeld, Global stabilization of a Josephson-junction array, Phys. Rev. B 49 (1994) 15223–15226.

[89] S. Nichols and K. Wiesenfeld, Non-neutral dynamics of splay states in Josephson-junction arrays, Phys. Rev. E 50 (1994) 205–212.

[90] G. M. Zaslavsky, Chaotic Dynamics and the Origin of Statistical Laws, Physics Today, August 1999, pp. 39-45.

[91] B.V. Chirikov and D.L. Shepelyansky, Statistics of Poincaré returns and a structure of the chaotic layer of nonlinear resonance (in Russian), in : Proceedings of the IX International conference on nonlinear oscillations, Kiev, 1981 (Naukova Dumka, Kiev, 1984), v.2, p.421–424 (English translation: Princeton University Report No.PPPL-TRANS-133, 1983).

[92] B.V. Chirikov and D.L. Shepelyansky, Asymptotic Statistics of Poincaré Recurrences in Hamiltonian Systems with Divided Phase Space, Phys. Rev. Lett. 82 (1999) 528–531.

[93] M.I. Dykman, D.G. Luchinsky, R. Mannella, P.V.E. McClintock, N.D. Stein, N.G. Stocks, Stochastic Resonance in Perspective, Nuovo Cimento D 17 (1995) 661–683.

[94] L. Gammaitoni, P. Hänggi, F. Marchesoni, Stochastic resonance, Rev. Mod. Phys. 70 (1998) 223–287.

[95] M.I. Dykman, H. Rabitz, V.N. Smelyanskiy, B.E. Vugmeister, Resonant Directed Diffusion in Nonadiabatically Driven Systems, Phys. Rev. Lett. 79 (1997) 1178–1181.

[96] I.A. Khovanov, V.S. Anishchenko, D.G. Luchinsky, P.V.E. McClintock, Noise Induced Escape from Different Types of Chaotic Attractors, in "Stochaos: Stochastic and chaotic dynamics in the Lakes", eds. D. Broomhead, E. Luchinskaya, P.V.E. McClintock, T. Mullin (AIP, Melville, NY, USA, 2000) pp. 48–53.

[97] I.A. Khovanov, D.G. Luchinsky, R. Mannella and P.V.E. McClintock, Fluctuations and the energy-optimal control of chaos, Phys. Rev. Lett. 85 (2000) 2100–2103.

[98] R. Benzi, A. Sutera, A. Vulpiani, The mechanism of stochastic resonance, J. Phys. A 14 (1981) L453–457.

[99] B. McNamara, K. Wiesenfeld, R. Roy, Observation of stochastic resonance in a ring laser, Phys. Rev. Lett. 60 (1988) 2626–2629.

[100] B. McNamara, K. Wiesenfeld, Theory of stochastic resonance, Phys. Rev. A 39 (1989) 4854–4869.

[101] M.I. Dykman, R. Mannella, P.V.E. McClintock, N.G. Stocks, Comment on stochastic resonance in bistable systems, Phys. Rev. Lett. 65 (1990) 2606.

[102] M.I. Dykman, P.V.E. McClintock, R. Mannella, N.G. Stocks, Stochastic resonance in the linear and nonlinear response of a bistable system to a periodic field, JETP Lett. 52 (1990) 141–144.

[103] * N.G. Stocks, N.D. Stein, S.M. Soskin and P.V.E. McClintock, Zero-dispersion stochastic resonance, J. Phys. A 25 (1992) L1119–1125.

[104] A.D. Hibbs, A.L. Singsaas, E.W. Jacobs, A.R. Bulsara, J.J. Bekkedahl, F. Moss, Stochastic resonance in a superconducting loop with a Josephson junction, J. Appl. Phys. 77 (1995) 2582–2590.

[105] M.I. Dykman, D.G. Luchinsky, R. Mannella, P.V.E. McClintock, N.D. Stein, N.G. Stocks, Nonconventional Stochastic Resonance, J. Stat. Phys. 70 (1993) 479–499.

[106] M.I. Dykman, D.G. Luchinsky, R. Mannella, P.V.E. McClintock, N.D. Stein, N.G. Stocks, Supernarrow spectral peaks and high-frequency stochastic resonance in systems with coexisting periodic attractors, Phys. Rev. E 49 (1994) 1198–1215.

[107] L. Alfonsi, L. Gammaitoni, S. Santucci, A.R. Bulsara, Intrawell stochastic resonance versus interwell stochastic resonance in underdamped bistable systems, Phys. Rev. E 62 (2000) 299–302.

[108] S.M. Soskin, unpublished.

[109] C. Pegrum, private communication.

[110] S. Ramo, J.R. Whinnery and T. Van Duzer, Fields and Waves in Communication Electronics, 3rd edn. (Wiley, New York, 1994).

[111] A. Bulsara and G. Schmera, Stochastic resonance in globally coupled nonlinear oscillators, Phys. Rev. E 47 (1993) 3734–3737.

[112] J.F. Lindner, B.J. Breen, M.E. Wills, A.R. Bulsara, and W.L. Ditto, Monostable array-enhanced stochastic resonance, Phys. Rev. E 63 (2001) 051107-1–051107-6.

[113] J.F. Lindner, B.J. Breen, M.E. Wills, A.R. Bulsara, and W.L. Ditto, Reply to 'Comment on "Monostable array-enhanced stochastic resonance"', submitted to Phys. Rev. E.

[114] S.M. Soskin and P.V.E. McClintock, Comment on "Monostable array-enhanced stochastic resonance", Phys. Rev. E, in press.

[115] Y.R. Shen, The Principles of Nonlinear Optics (Wiley, New York, 1984).

[116] * M.I. Dykman, D.G. Luchinsky, R. Mannella, P.V.E. McClintock, S.M. Soskin, and N.D. Stein, Resonant Subharmonic absorption and second-harmonic generation by a fluctuating nonlinear oscillator, Phys.Rev. E 54 (1996) 2366-2377.

[117] M.I. Dykman, D.G. Luchinsky, R. Mannella, P.V.E. McClintock, H.E. Short, N.D. Stein and N.G. Stocks, "Simulation of critical phenomena in nonlinear optical systems", in *Modern Nonlinear Optics, Part 3*, ed M W Evans and S Kielich, Adv. Chem. Phys. **LXXXV** (1994) 265–378.

[118] H. Yoshida, Construction of higher-order sympletic integrators, Phys. Lett. A 150 (1990) 262–268.

[119] * S.M. Soskin, R. Mannella and A.N. Silchenko, "Noise-induced escape assisted by periodic driving in zero-dispersion systems and zero-dispersion ratchets", unpublished.

[120] M.H. Devoret, J. M. Martinis, D.Esteve, and J. Clarke, Resonant activation from the zero-voltage state of a current biased Josephson jucction, Phys. Rev. Lett. 53 (1984) 1260–1263.

[121] B. Carmeli and A. Nitzan, Non-Markovian theory of activated rate processes. V. External periodic forces in the low-friction limit, Phys. Rev. A 32 (1985) 2439–2454.

[122] A.I. Larkin and Yu.N. Ovchinnikov, Resonance Reduction of the Lifetime of the Metastable State of Tunnel Junctions, J. Low Temp. Phys. 63 (1986) 317–329.

[123] B.I. Ivlev and V.I. Mel'nikov, Effect of resonant pumping on activated decay rates, Phys. Lett. A 116 (1986) 427–428.

[124] S. Linkwitz and H. Grabert, Enhancement of the decay rate of a metastable state by an external driving force, Phys. Rev. B 44 (1991) 11901–11910.

[125] R.L. Kautz, Noise, chaos and the Josephson voltage standard, *Rep. Prog. Phys.* **59** (1996) 935–992.

[126] D.G. Luchinsky, M.J. Greenall, P.V.E. McClintock, Resonant rectification of fluctuations in a Brownian ratchet, Phys. Lett. A 273 (2000) 316–321.

[127] A.N. Cleland and M.L. Roukes, A nanometre-scale mechanical electrometer, Nature 392 (1998) 160–162.

[128] M.O. Magnasco, Forced Thermal Ratchets, Phys. Rev. Lett. 71 (1993) 1477–1481.

[129] M.I. Dykman and M.A. Krivoglaz, Theory of fluctuational transitions between the stable states of a nonlinear oscillator, Sov. Phys. JETP 50 (1979) 30–37.

[130] A.P. Dmitriev and M.I. D'yakonov, Activated and tunneling transitions between the two forced-oscillation regimes of an anharmonic oscillator, Sov. Phys. JETP 63 (1986) 838–843.

[131] S. Flach, O.Yevtushenko, Y. Zolotaryuk, Directed current due to broken time-space symmetry, Phys. Rev. Lett. 84 (2000) 2358–2361.

[132] M.I. Freidlin and A.D. Wentzell, Random Perturbations of Dynamical Systems, 2nd ed. (Springer, New York, 1998).

[133] R. Graham and T. Tel, Nonequilibrium potential for coexisting attractors, Phys. Rev. A 33 (1986) 1322–1337.

[134] L.E. Elsgolc, Calculus of Variations (Pergamon Press, London, 1961).

[135] I.S. Gradshtein and I.M. Ryzhik, Table of Integrals, Series, and Products, 5th edition (Academic Press, London, 1994)

[136] G.M. Zaslavsky, Physics of Chaos in Hamiltonian systems (Imperial Colledge Press, 1998).

[137] S. Kraut, U. Feudel, C. Grebogi, Preference of attractors in noisy multistable systems, Phys. Rev. E 59 (1999) 5253–5260.

[138] S.M. Soskin, Large fluctuations in multi-attractor systems and the generalized Kramers problem, J. Stat. Phys. 97 (1999) 609–676.

[139] M.I. Dykman, M.M. Millonas, V.N. Smelyanskiy, Observable and hidden singular features of large fluctuations in nonequilibrium systems, Phys. Lett. A 195 (1994) 53–58.

[140] M.I. Dykman and V.N. Smelyanski, Fluctuational transitions between stable states of a nonlinear oscillator driven by random resonant force, Physical Review A 41 (1990) 3090–3102.

[141] M. Lax, Fluctuation and Coherence Phenomena in Classical and Quantum Physics, edited by M. Chretien, E.P. Gross and S. Deser (Gordon and Breach, New York, 1968).

[142] R.P. Feinman and A.R. Hibbs, Quantum Mechanics and Path Integrals (McGraw-Hill, New York, 1965).

[143] M. Arrayás, I.Kh. Kaufman, D.G. Luchinsky, P.V.E. McClintock, and S.M. Soskin, Kramers Problem for a Multiwell Potential, Phys. Rev. Lett. 84 (2000) 2556–2559.

[144] D.G. Luchinsky, R.S. Maier, R. Mannella, P.V.E. McClintock and D.L. Stein, Observation of saddle-point avoidance in noise-induced escape, Phys. Rev. Lett. 82 (1999) 1806–1809.

[145] M.I. Dykman, R. Mannella, P.V.E. McClintock, F. Moss and S.M. Soskin, Spectral density of fluctuations of a double-well Duffing oscillator driven by white noise, Phys. Rev. A 37 (1988) 1303-1313.

[146] M.I. Dykman, R. Mannella, P.V.E. McClintock and N.G. Stocks, Fluctuation-induced transitions between periodic attractors: Observation of supernarrow spectral peaks near a kinetic phase transition, Phys. Rev. Lett. 65 (1990) 48–51.

[147] S.M. Soskin and Yu.G. Rubo, Formation of zero-dispersion peaks in the fluctuation spectra of quasi-classical systems, unpublished.

[148] S.M. Soskin, Quantum zero-dispersion nonlinear resonance, unpublished.

[149] L.D. Landau and E.M. Lifshitz, Quantum Mechanics: Non-Relativistic Theory (Pergamon, Oxford, 1977).

[150] M.I. Dykman and M.A. Krivoglaz, Quantum theory of nonlinear oscillators interacting with a medium, Sov. Phys. JETP 37 (1973) 506–511.

[151] B.Ya. Zeld'ovich, A.M. Perelomov, and V.S. Popov, Relaxation of a quantum oscillator, Sov. Phys. JETP 28 (1969) 308–316.

[152] B.Ya. Zeld'ovich, A.M. Perelomov, and V.S. Popov, Relaxation of a quantum oscillator in the presence of external force, Sov. Phys. JETP 30 (1970) 111–116.

[153] E.V. Shuryak, Nonlinear resonance in quantum systems, Sov. Phys. JETP 44 (1976) 1070–1080.

[154] G.P. Berman and G.M. Zaslavsky, The theory of quantum nonlinear resonance, Phys. Lett. A 61 (1977) 295–296.

[155] G.P. Berman, G.M. Zaslavsky and A.R. Kolovsky, Interaction of quantum nonlinear resonances, Sov. Phys. JETP 54 (1981) 272–277.

[156] G.P. Berman and G.M. Zaslavsky, Condition of stochasticity in quantum nonlinear systems, Physica A 91 (1978) 450–460.

[157] G.P. Berman, G.M. Zaslavsky and A.R. Kolovsky, Nonlinear resonance and stochasticity in a system of surface electrons, Sov. Phys. JETP 61 (1985) 925–929.

[158] E. Jahnke, F. Emde, and F. Lösch, Tables of higher functions (McGraw-Hill Book Co., New York, 1960).

[159] G.P. Berman and A.R. Kolovsky, Correlation function behaviour in quantum systems which are classically chaotic, Physica D 8 (1983) 117–141.

[160] M. Grifoni and P. Hänggi, Coherent and incoherent quantum stochastic resonance, Phys. Rev. Lett. 76 (1996) 1611–1614.

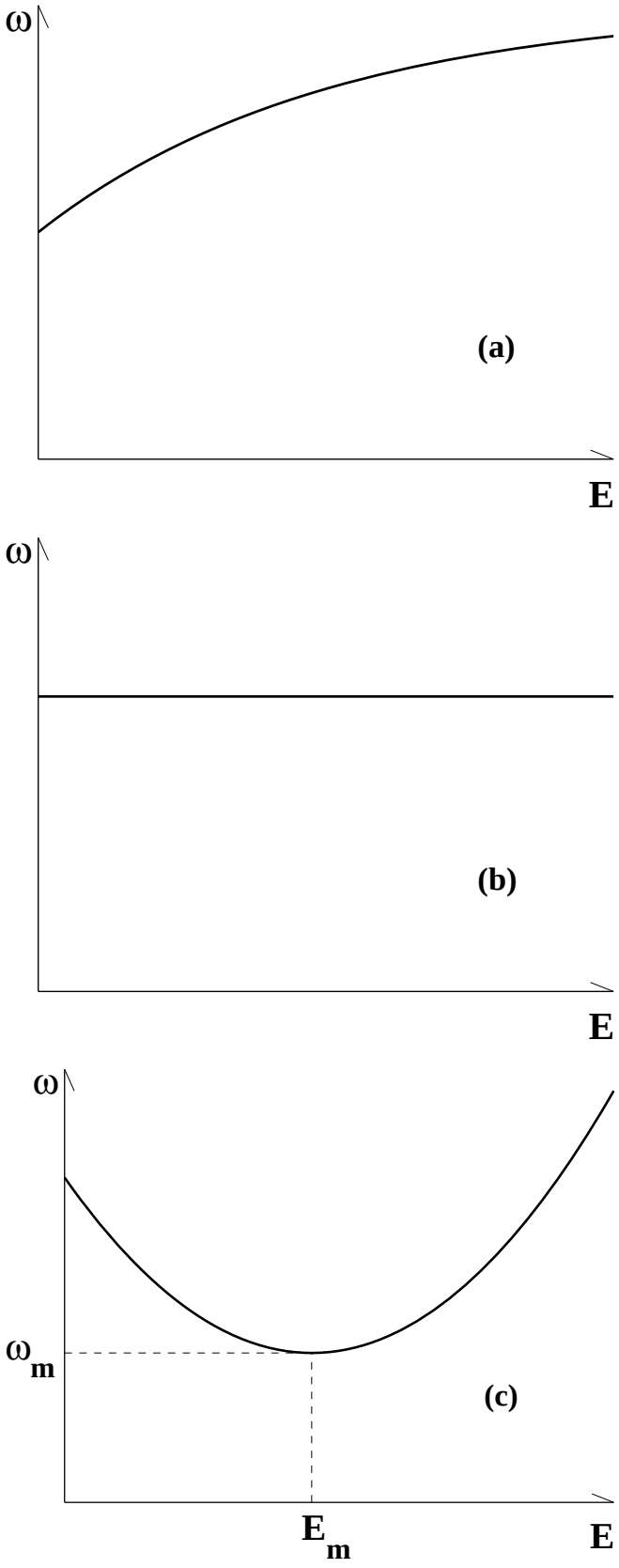

Fig. 1. Examples of the dependence of the frequency of eigenoscillation on energy for: (a) a conventional nonlinear oscillator; (b) a harmonic (linear) oscillator; (c) a zero-dispersion oscillator.

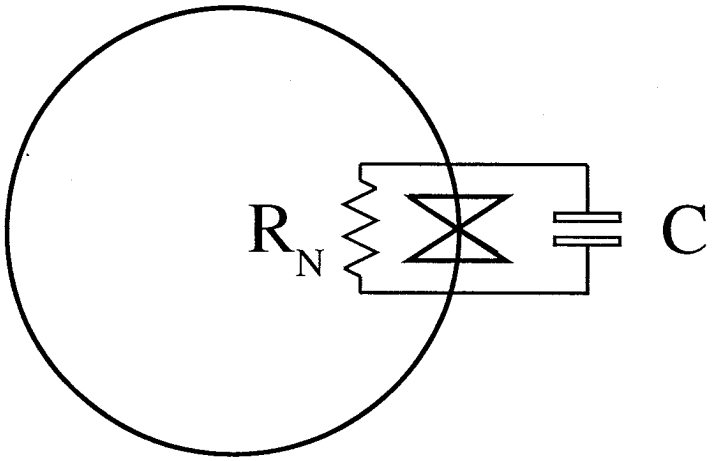

Fig. 2. Schematic plot of a Josephson junction closed with a superconducting loop.

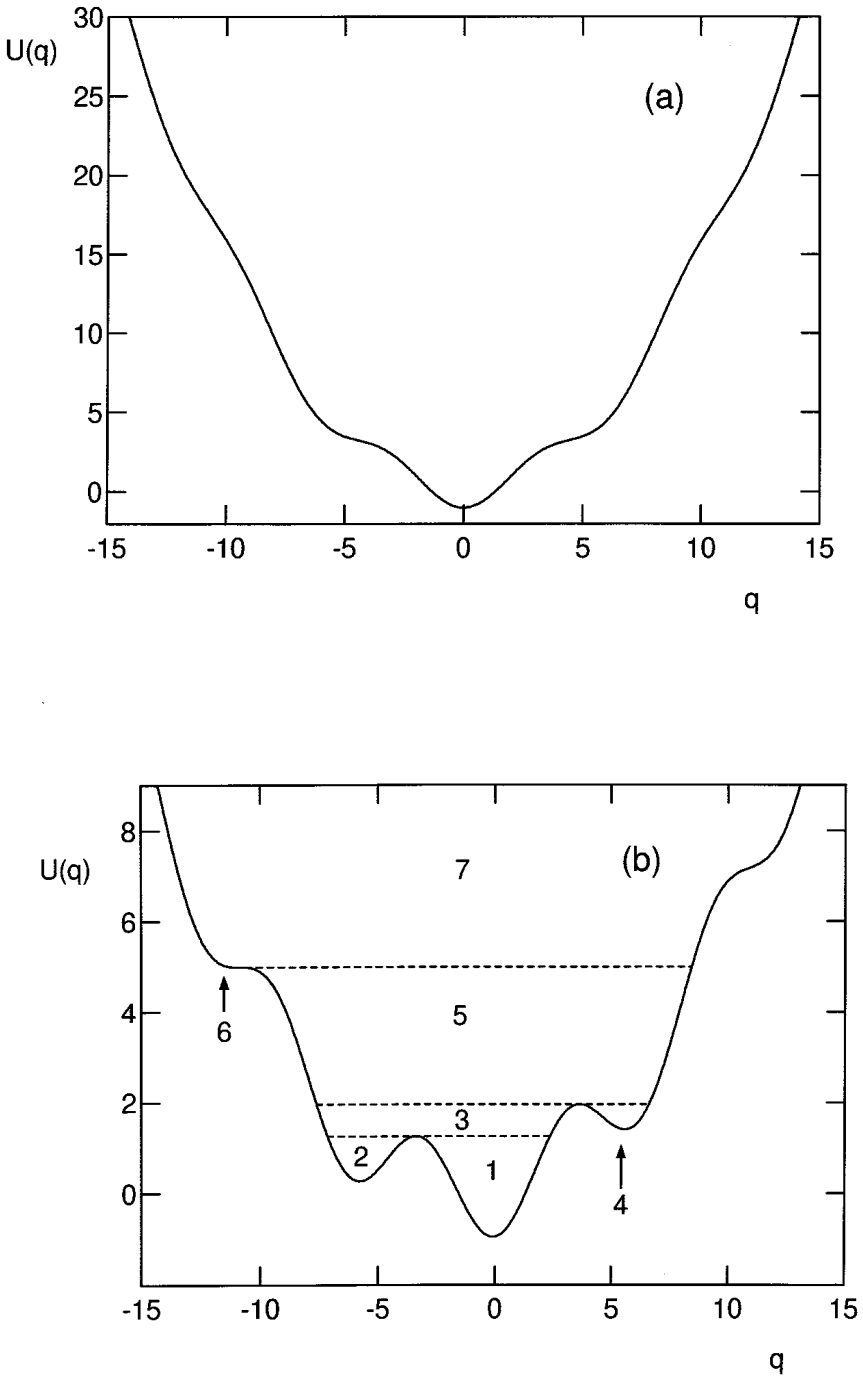

Fig. 3. The effective potential for a SQUID, Eq. (2.1.5), plotted for: (a) $B = 0.3, q_e = 0$; (b) $B = 0.1, q_e = -1.0$. Dashed lines in (b) show the barrier levels while the corresponding numbers identify different regions of phase space corresponding to motion confined within energy ranges of three different kinds, separated by the dashed lines: between local energy maxima adjacent in height; between a local maximum and the local minimum adjacent in coordinate; or between the highest local maximum and infinity. After [**?**].

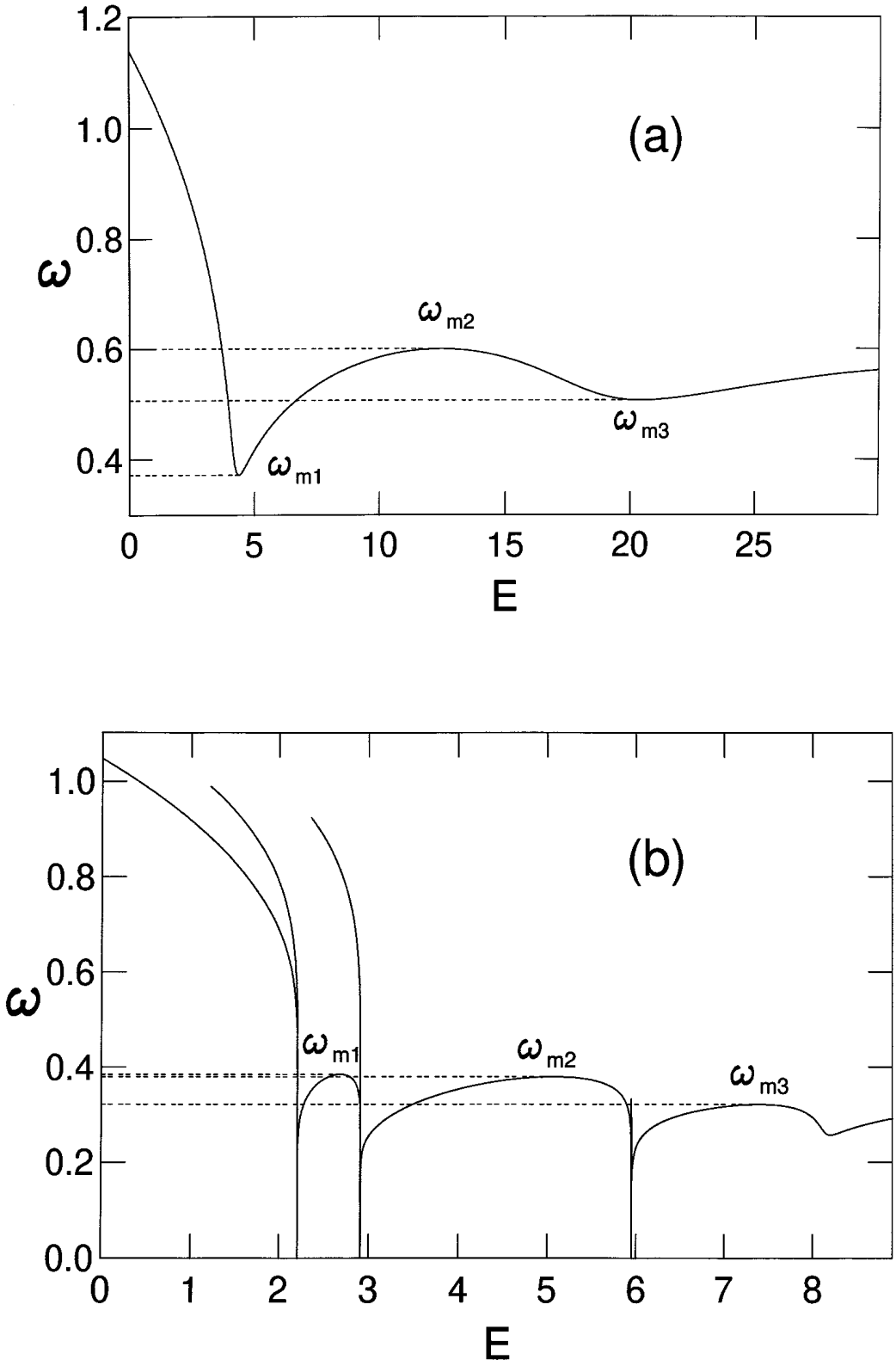

Fig. 4. Dependences of the frequency $\omega(E)$ of eigenoscillation on energy E for the potentials shown in Fig. 3: (a) $B = 0.3, q_e = 0$; (b) $B = 0.1, q_e = -1.0$. Dashed lines indicate the positions of the first three extrema in each case: (a) $\omega_{m1} = 0.372$, $\omega_{m2} = 0.600$, $\omega_{m3} = 0.506$; (b) $\omega_{m1} = 0.385$, $\omega_{m2} = 0.380$, $\omega_{m3} = 0.321$. After [**?**].

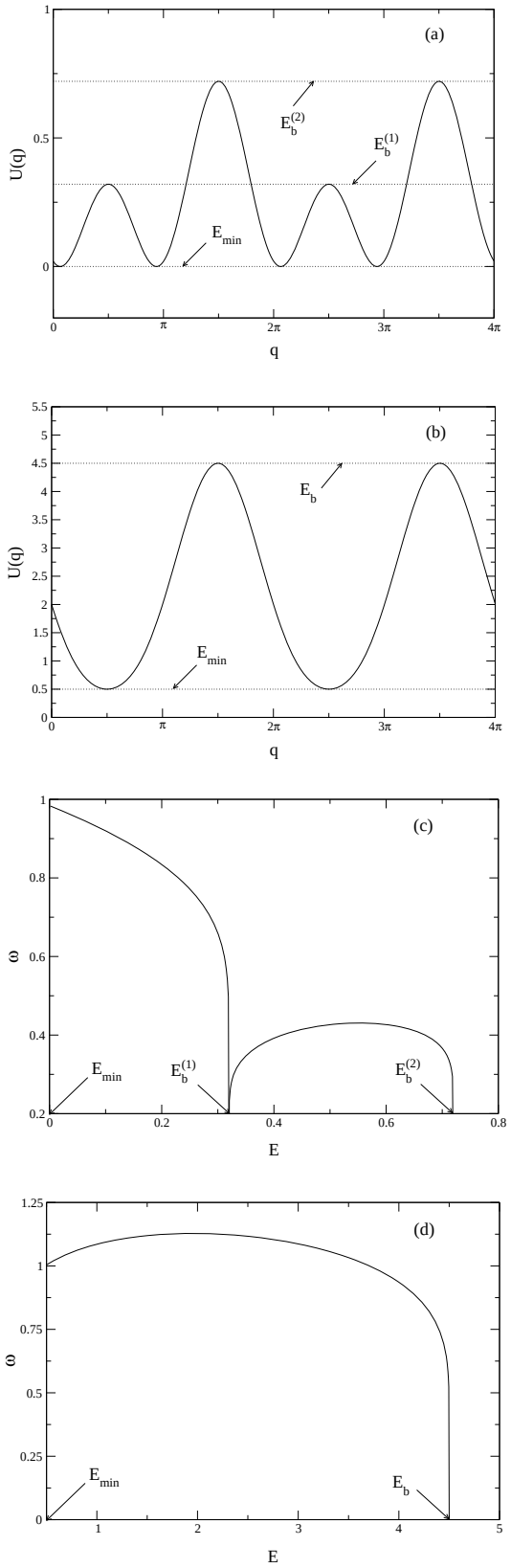

Fig. 5. The potential $U(q)$ (2.2.6) at (a) $\Phi = 0.2$, (b) $\Phi = 2.0$, and the corresponding (for H given by (2.2.5)-(2.2.6)) dependences of the frequency $\omega(E)$ of oscillation on energy: (c) for $\Phi = 0.2$, (d) for $\Phi = 2.0$. After [**?**].

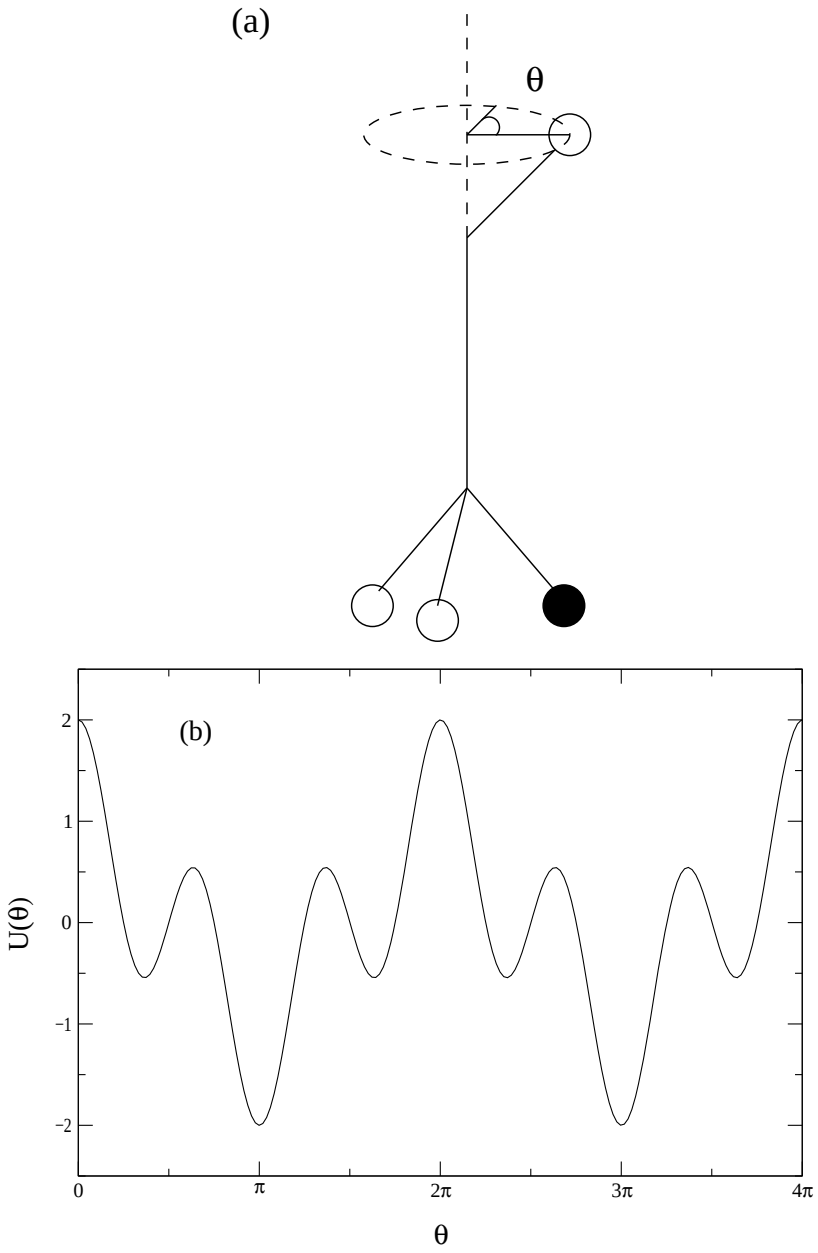

Fig. 6. (a) Schematic plot of an axial molecule in which an atom (or a group of atoms) may rotate around a rigid axis in the plane perpendicular to the axis. (b) The corresponding dependence of the effective potential on the angle of the rotation: within a 2π period, there are two equal barriers and a third barrier of a different height.

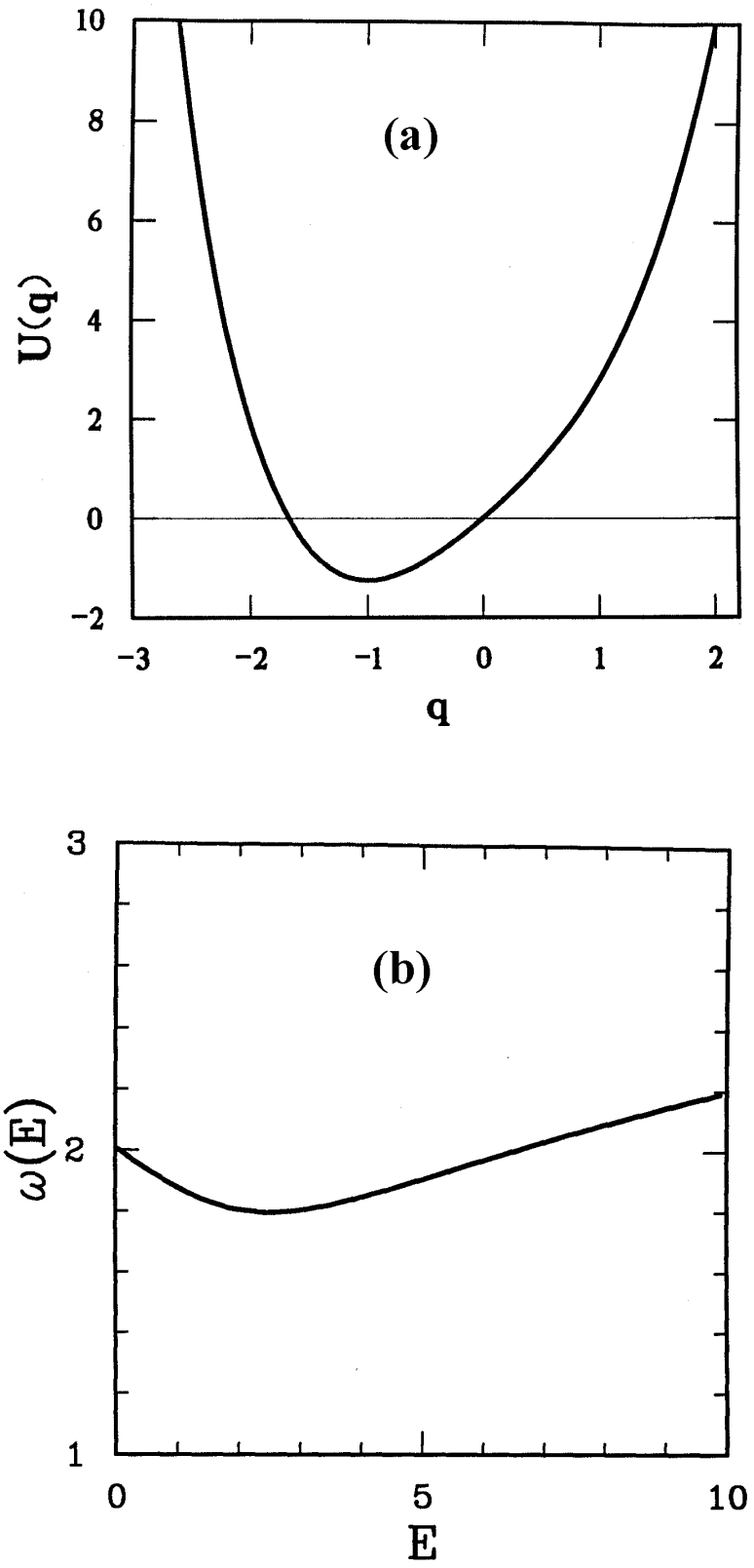

Fig. 7. (a) The tilted Duffing potential (2.3.1) for $\omega_0 = \gamma = 1, A = 2$; (b) the corresponding dependence of the frequency of eigenoscillation on energy. After [**?**].

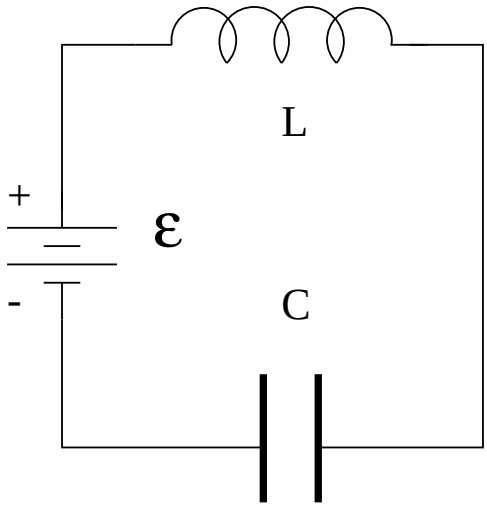

Fig. 8. An oscillatory electric circuit including a battery.

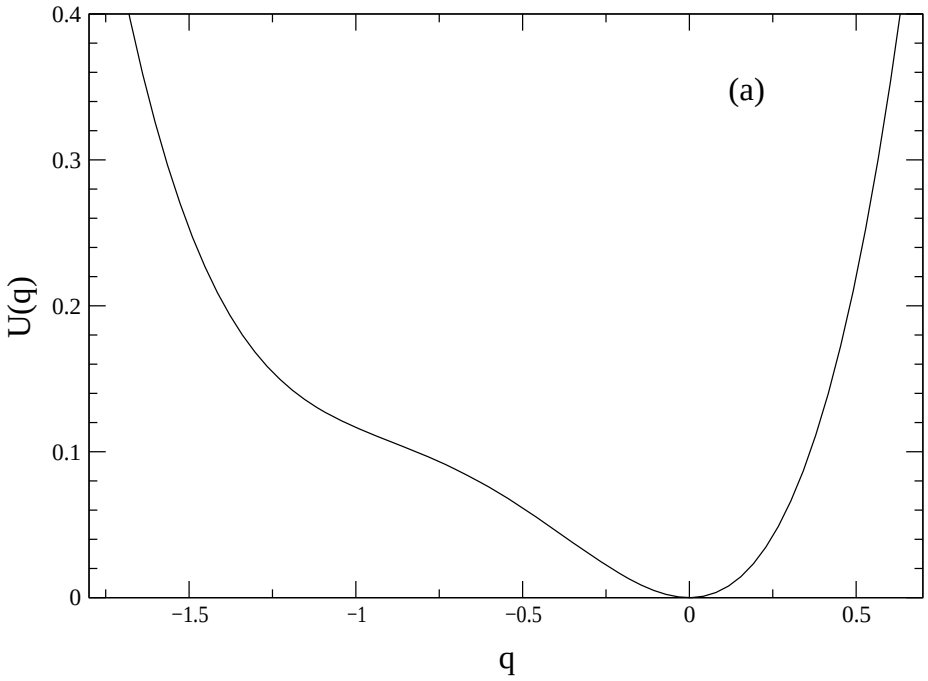

Fig. 9. (a) The cubic potential (2.3.5) with $\omega_0 = 1, \beta = 1.9, \gamma = 1$ and (b) the corresponding dependence of eigenfrequency $\omega(E)$ on energy.

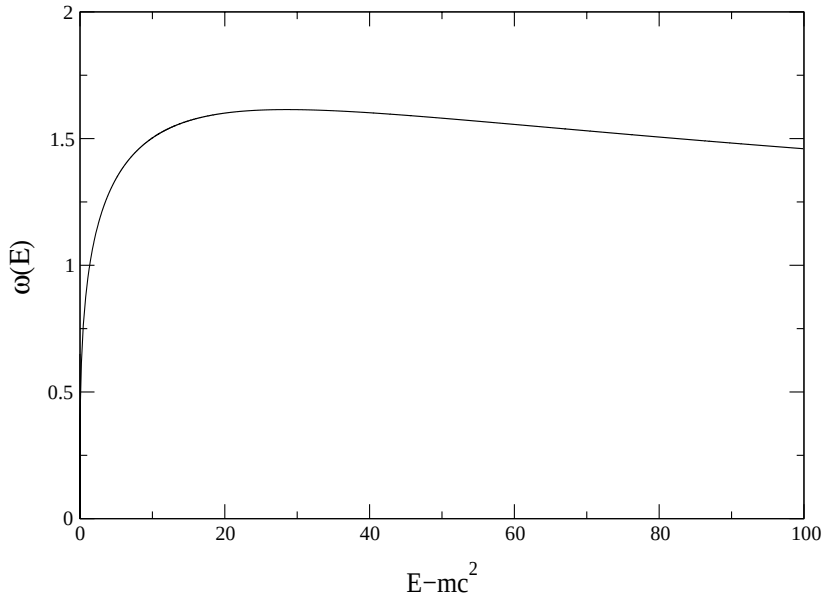

Fig. 10. The dependence of eigenfrequency on energy for a relativistic double-well Duffing oscillator (2.4.1) with $U(q) = -q^2/4 + q^4/8$, $m = 1$ and $c = 5.5$ (the parameters being chosen to be the same as in [**?**]).

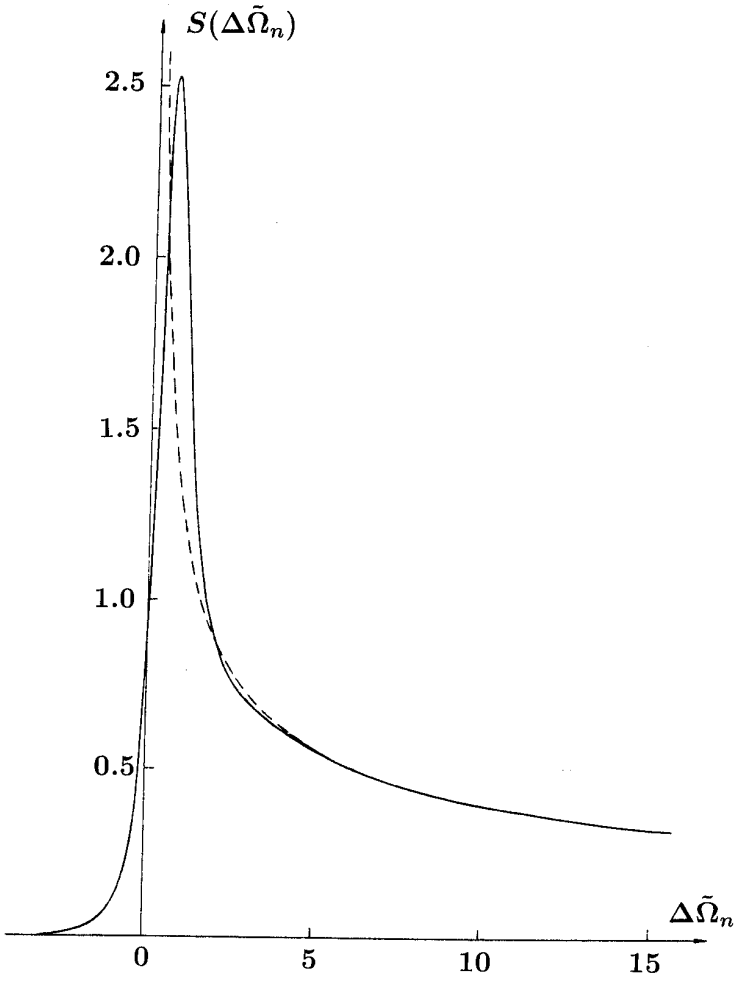

Fig. 11. The universal function describing the shape of a ZDP in the asymptotic limit $\Gamma \to 0$. After [**?**].

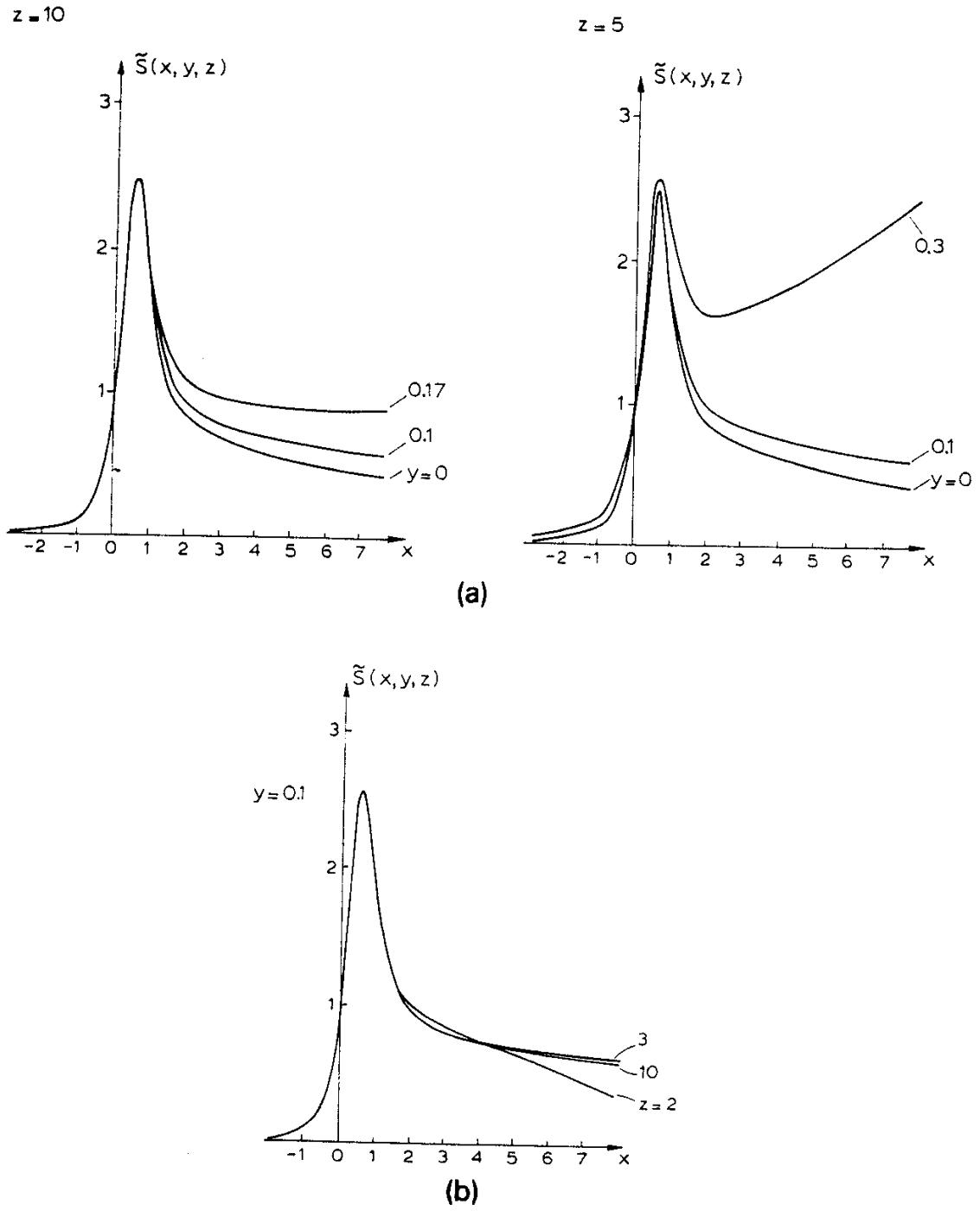

Fig. 12. The evolution of the dependence of $\tilde{S}$ on x:(a) for different y at two different z; (b) for different z, at $y = 0.1$. After [**?**].

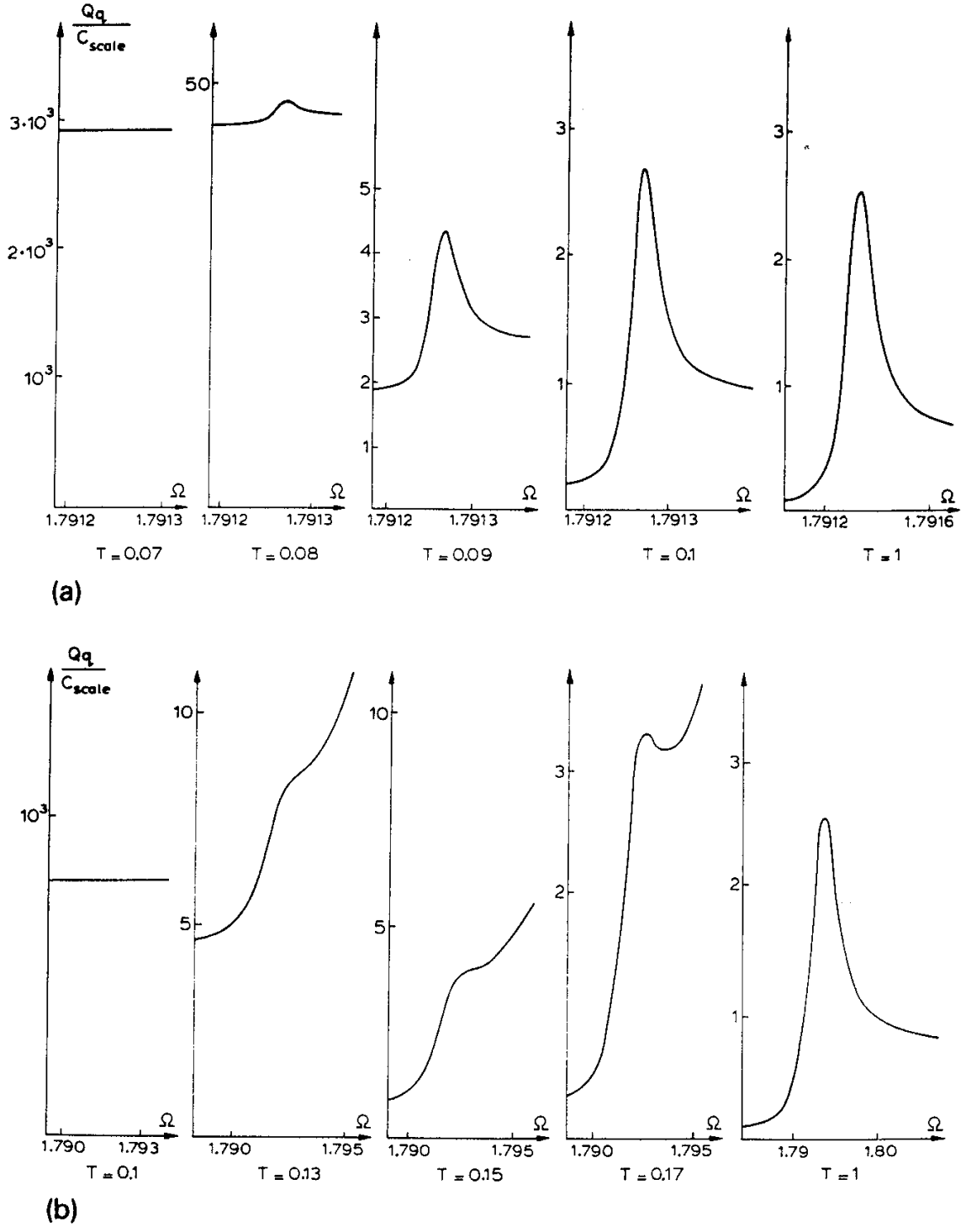

Fig. 13. The evolution with increasing temperature T of the scaled fluctuation spectrum $Q_q(\Omega)$ calculated from Eqs. (3.4.12), (3.4.13) for the same TDO model as in Fig. 7 ($U(q) = q^2/2 + q^4/4 + 2q$) and: (a) $\Gamma = 10^{-7}$; (b) $\Gamma = 10^{-4}$. After [?].

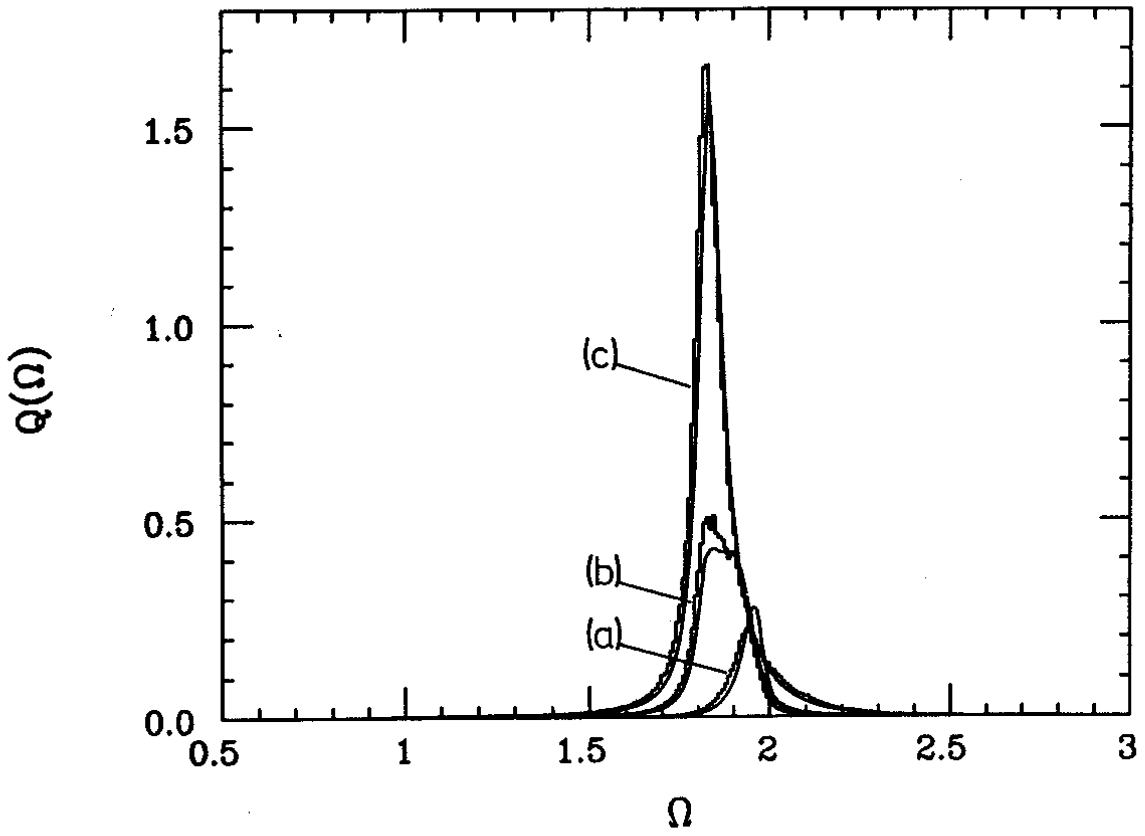

Fig. 14. Evolution of the fluctuation spectrum $Q_q(\Omega)$ calculated from Eqs. (3.4.12), (3.4.13) for the same TDO model as in Figs. 7 and 13 but with $\Gamma = 0.0286$, as the temperature increases: (a) $T = 0.078$; (b) 0.687; (c) 3.04. The histograms show measurements while solid lines show calculations based on the algorithm described in sub-section 3.5. After [**?**].

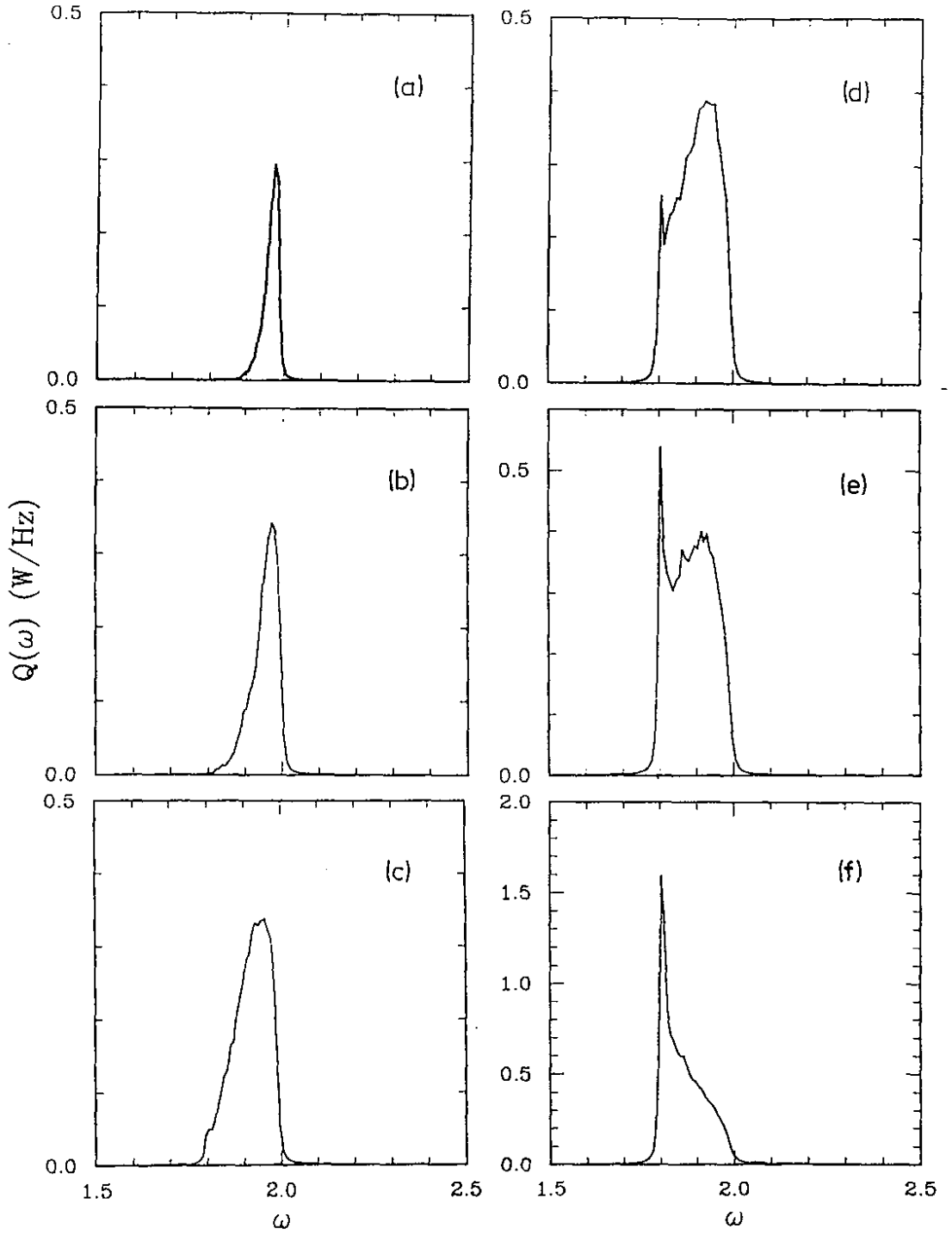

Fig. 15. The evolution of the measured spectrum for the same TDO model as in Figs. 7, 13 and 14 but with $\Gamma = 0.0017$, as the temperature increases: (a) $T = 0.100$; (b) 0.203; (c) 0.320; (d) 0.409; (e) 0.485; (f) 0.742. The onset of the ZDP and its evolution are seen in (c)-(f). After [**?**].

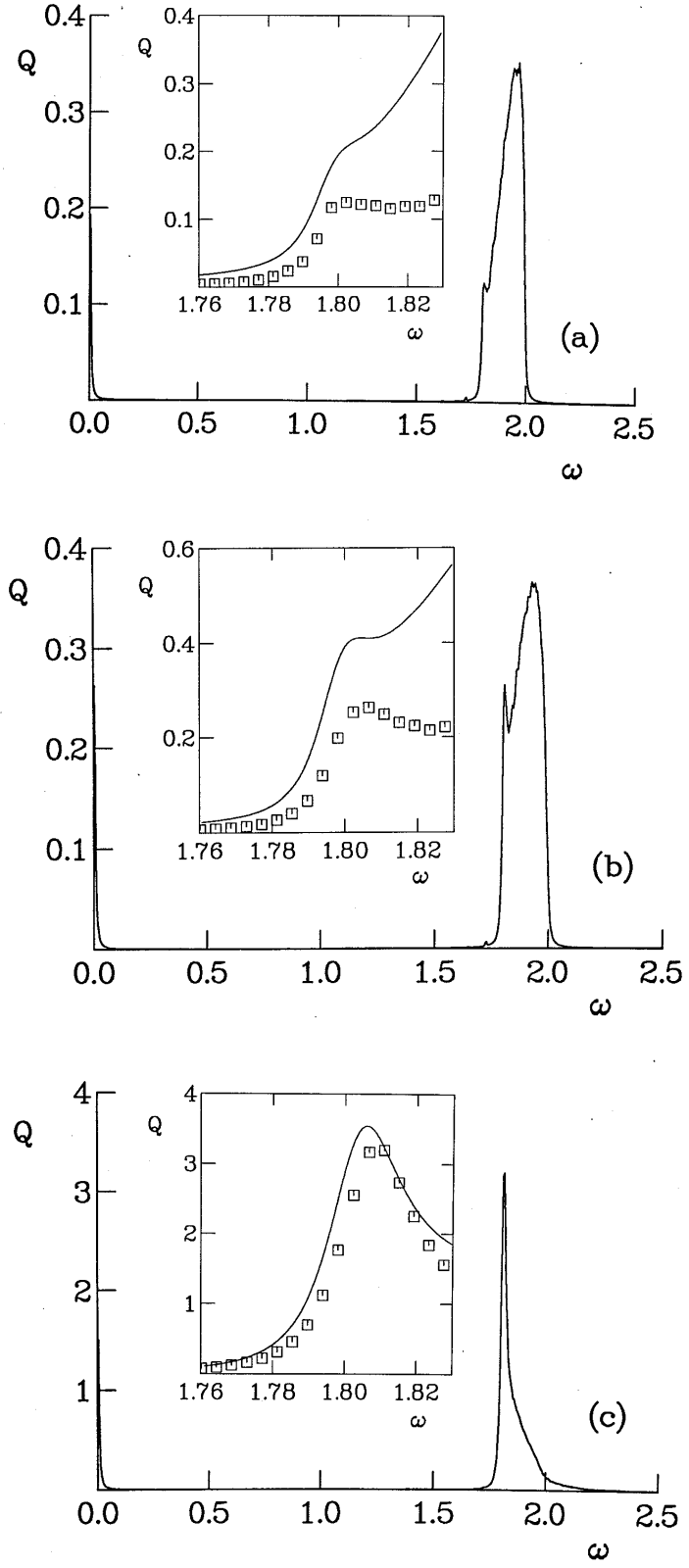

Fig. 16. The spectrum $Q_q(\Omega)$ measured for the same TDO model as in Figs. 7, 13–15 but with $\Gamma = 2.4 \times 10^{-3}$, as temperature grows: (a) $T = 0.370$; (b) 0.445; (c) 1.5. The insets in each case show a comparison, on expanded scales, of the experimentally measured fundamental ZDP (squares) with the theoretical prediction of Eq. (3.4.9) (solid line). After [**?**].

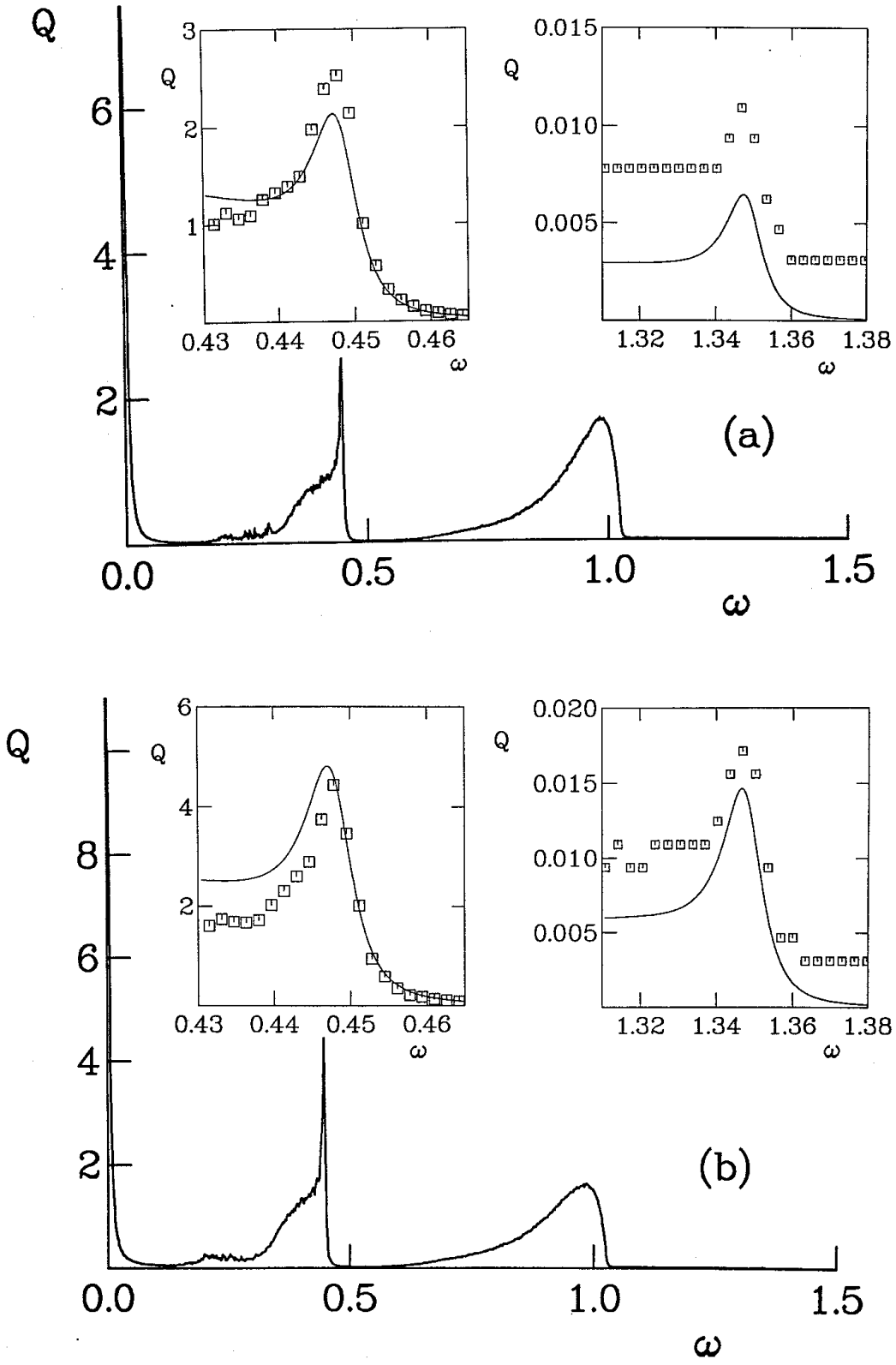

Fig. 17. The spectrum $Q_q(\Omega)$ measured for the SQUID model $U(q) = \cos(q) + 0.05q^2$ with $\Gamma = 2.8 \times 10^{-4}$), as temperature grows: (a) $T = 0.394$; (b) 0.463; (c) 1.3. The insets in each case show a comparison, on expanded scales, of the experimentally measured ZDP (squares) with the theoretical prediction of Eq. (3.4.9) (solid line), for the fundamental (left-hand insets) and third-harmonic (right-hand insets) peaks. After [**?**].

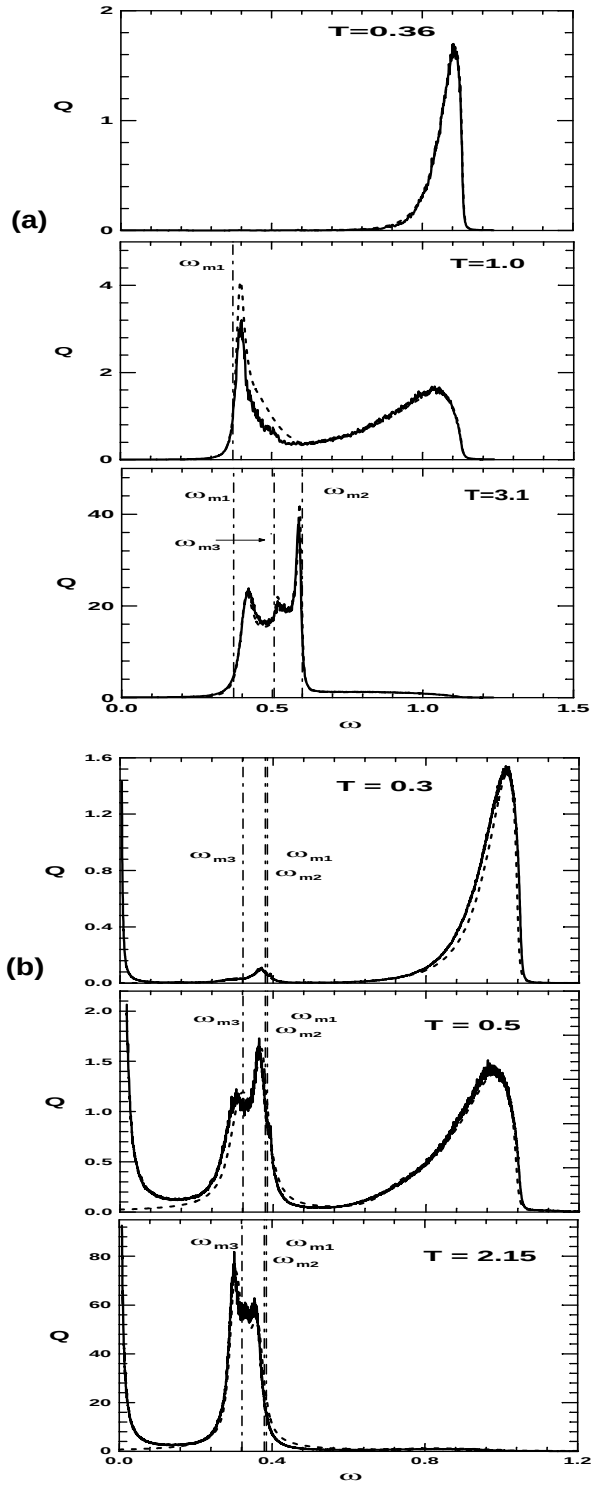

Fig. 18. Evolution of the fluctuation spectra with increasing noise intensity T, measured (jagged full curves) and calculated using the numerical algorithm described in sub-section 3.5 (dashed curves) for: (a) the single-well SQUID potential of Fig. 3(a); and (b) the multiwell SQUID potential of Fig. 3(b). Dash-dotted lines mark the positions of the relevant extrema of $\omega(E)$ (see Fig. 4). After [**?**].

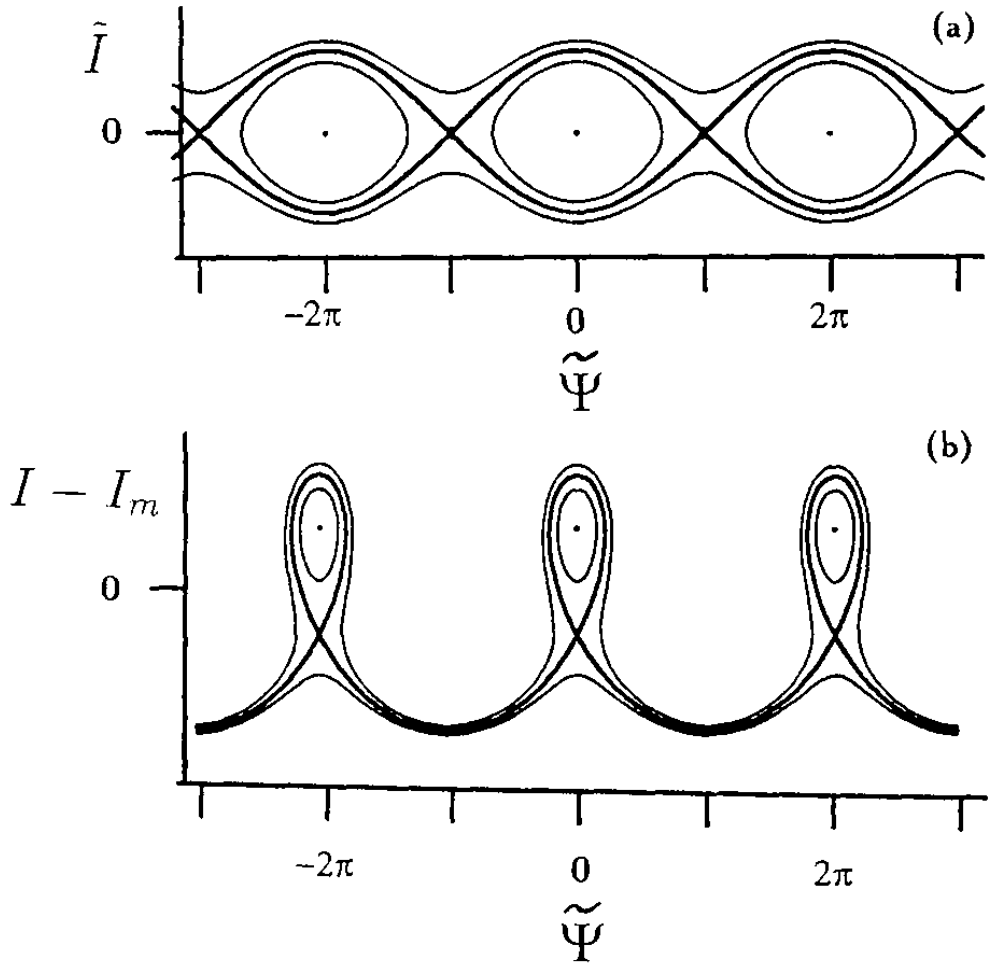

Fig. 19. Typical trajectories in the absence of dissipation: (a) for conventional nonlinear resonance; (b) for zero-dispersion nonlinear resonance. The separatrices are shown by thicker lines and the stable states by dots. After [?].

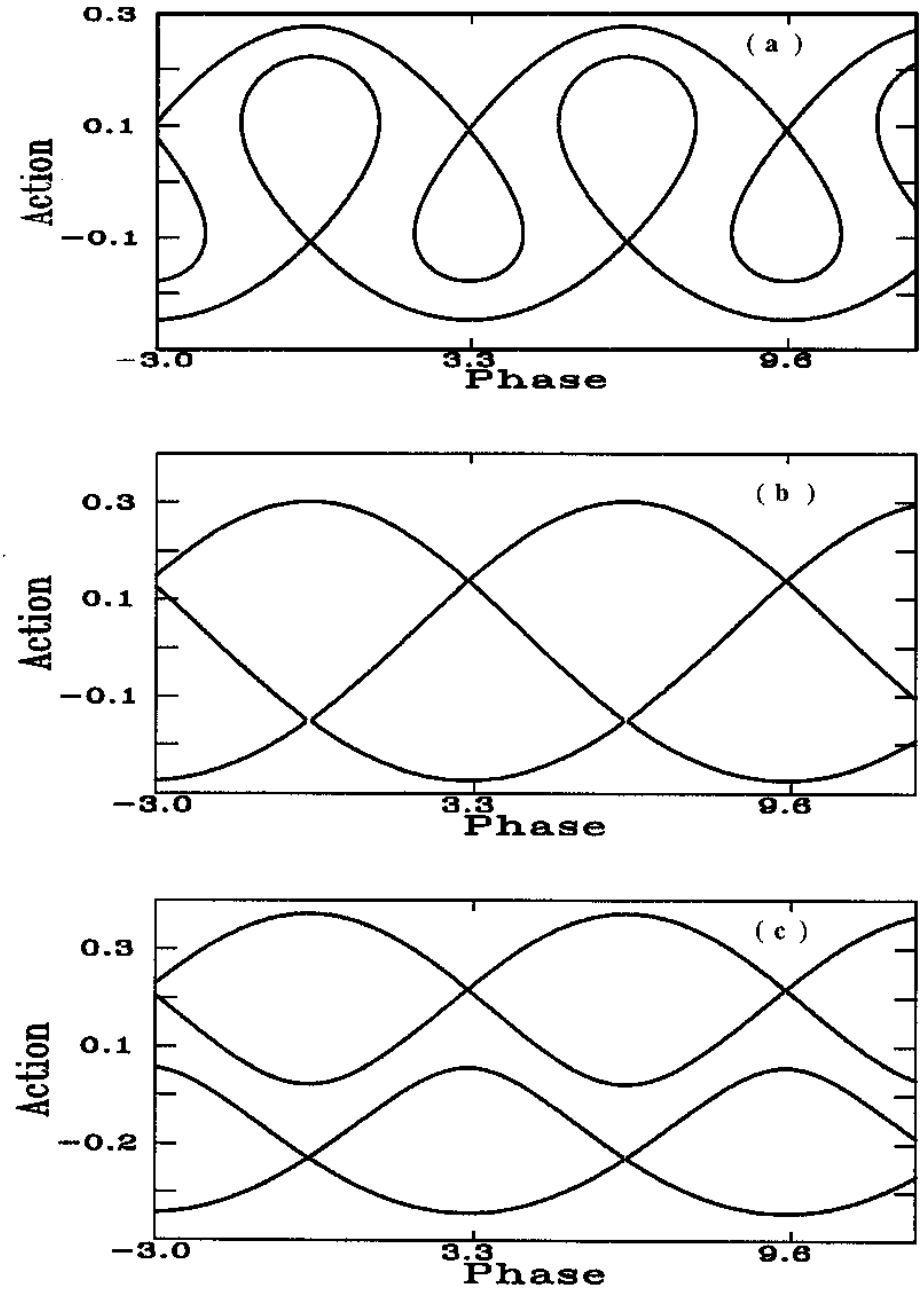

Fig. 20. Evolution of separatrices in the phase space as parameters are varied: (a) zero-dispersion nonlinear resonance; (b) at the transition between zero-dispersion and conventional nonlinear resonances; (c) conventional nonlinear resonance. After [?].

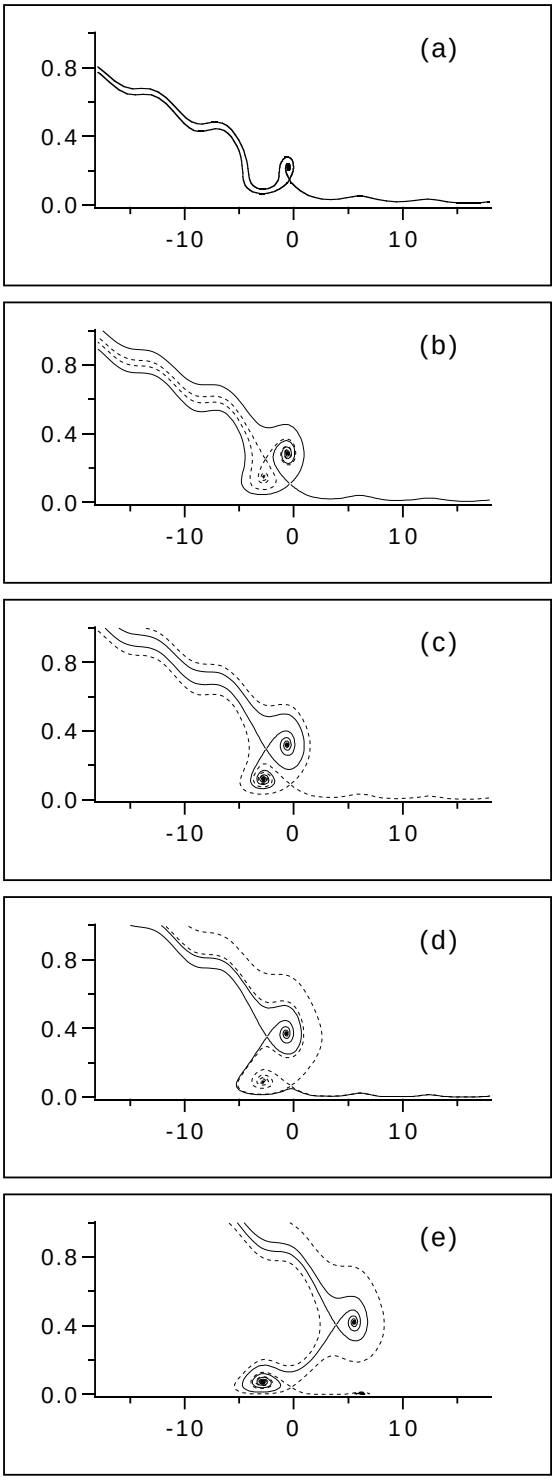

Fig. 21. Evolution with driving frequency ω_f of the basins of attraction of nonlinear resonances in a 2π band of the phase space of the slow variables (I ordinate, $\tilde{\psi}$ abscissa) for the system (4.2.3) averaged over the high-frequency oscillations (Eqs. (4.2.4)) for $\omega_0 = 1$, $\beta = 5/3$, $\gamma = 1$, $\Gamma = 0.011$, h=0.0143 and: (a) ω_f=0.8, (b) 0.83, (c) 0.85, (d) 0.88, (e) 0.92. The boundaries of basins of attraction of the larger (smaller) action nonlinear resonance, and trajectories emerging from the corresponding saddle point, are drawn by full (dashed) lines. One can obtain the complete phase space by repeating the above picture with a period 2π in $\tilde{\psi}$. After [**?**].

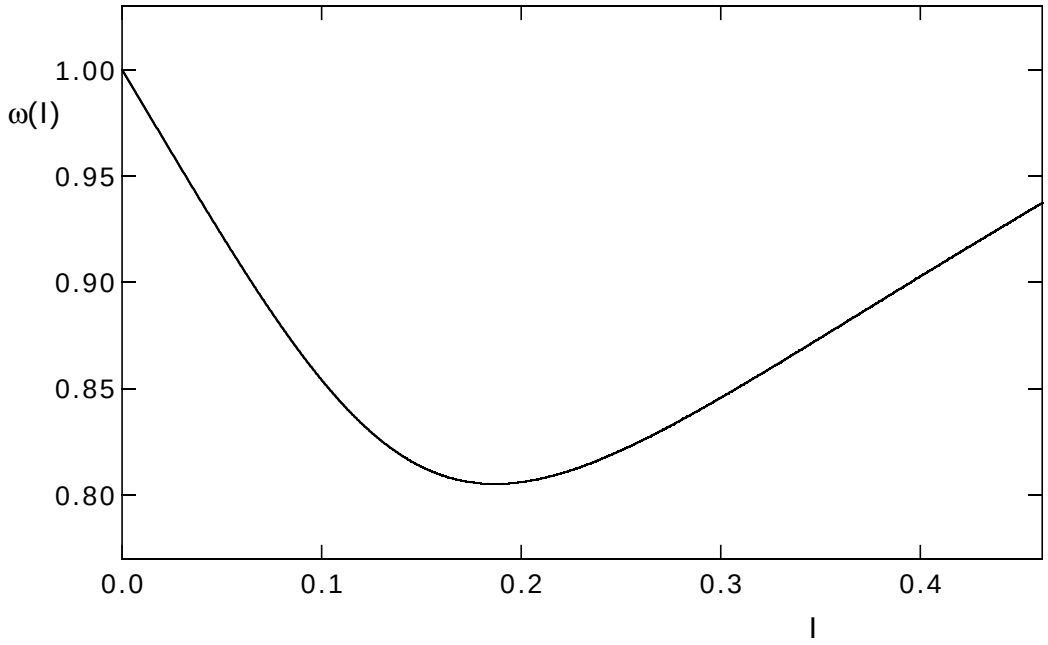

Fig. 22. Frequency of eigenoscillation $\omega(I)$ of the system (4.2.1) as a function of its action I at $\omega_0 = 1$, $\beta = 5/3$, $\gamma = 1$ ($\omega_m = 0.805, I_m = 0.1870$). After [**?**].

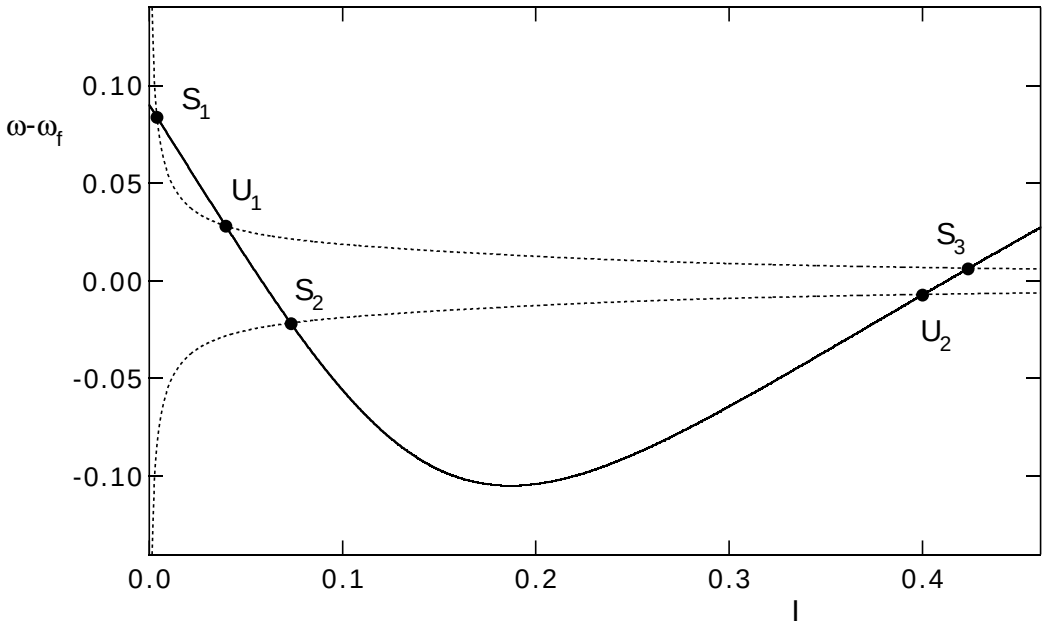

Fig. 23. Example of the graphical solution of (4.2.7) for $\Gamma = 0.011$ and $\omega(I), q_1(I)$ for the system (4.2.1), with the same parameter values as in Fig. 22, driven by a periodic force with arbitrarily chosen h and ω_f. The full line represents the dependence of $(\omega - \omega_f)$ on I. The dotted line represents $\pm hq_1'[1 - (\Gamma I/(hq_1))^2]^{1/2}$. The intersections corresponding to stable and unstable points are labelled S1-3 and U1-2 respectively. After [**?**].

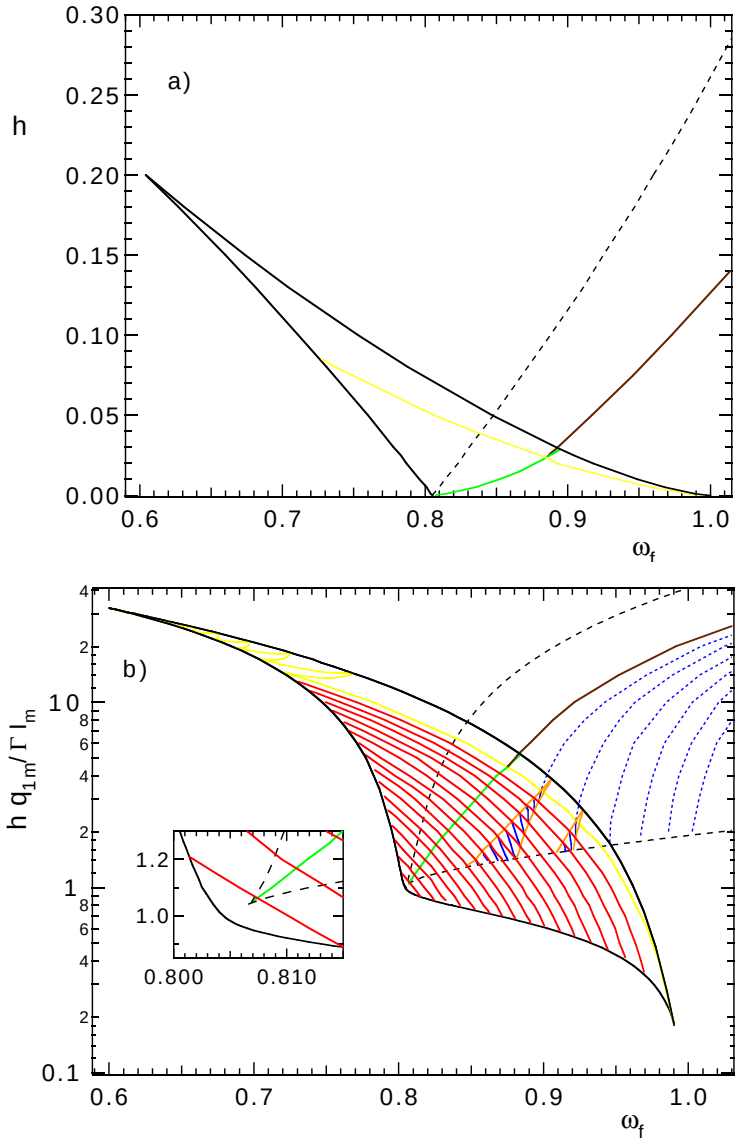

Fig. 24. The bifurcation diagrams for (4.2.4), (4.2.1) with $\omega_0 = 1$, $\beta = 5/3$, $\gamma = 1$ and: (a) $\Gamma = 0$; (b) $\Gamma = 0.011$. Note in (b) the logarithmic vertical scale and the ordinate scaling factor of $q_{1m}/(\Gamma I_m) = 159$. Black lines indicate local bifurcations: the full line bounds the region within which both the linear (S1) response and one or both of the nonlinear (S2, S3) responses can exist. The upper part of this line marks the boundary of linear response, and the lower part that for nonlinear response. Both nonlinear responses coexist in the region to the right of the dashed black line in (a), or between the upper and lower parts of the dashed black line in (b). The full green lines mark the ZDNR/NR transition, which corresponds to either the $o \leftrightarrow g$ separatrix reconnection (cf. Figs. 25(a,b)) in the non-dissipative case (a), or to the $o \to g$ heteroclinic orbit in the dissipative case (b). The yellow line corresponds to the $y \leftrightarrow o$ separatrix reconnection (cf. Figs. 25(b,c)) in the non-dissipative case (a), or to the $y \to o$ heteroclinic orbit (cf. Figs. 26(b,c)) in the dissipative one (b). The brown line corresponds to the $y \leftrightarrow g$ separatrix reconnection in the non-dissipative case (a), or to the $y \to g$ heteroclinic orbit in the dissipative one (b). Red and orange lines correspond to $o \to y$ and $g \to o$ heteroclinic orbits respectively (the transition between Figs. 26(a,b) occurs just via the connection $o \to y$). Blue lines correspond to the $g \to y$ heteroclinic orbit: the full line corresponds to a slip of the end of a trajectory emerging from the green saddle between adjacent linear responses, while the dashed line corresponds to slip of the trajectories emerging from green saddles between adjacent nonlinear responses. The inset in (b) shows an enlargement of the vicinity of the cusp point of the dashed black line. After [**?**].

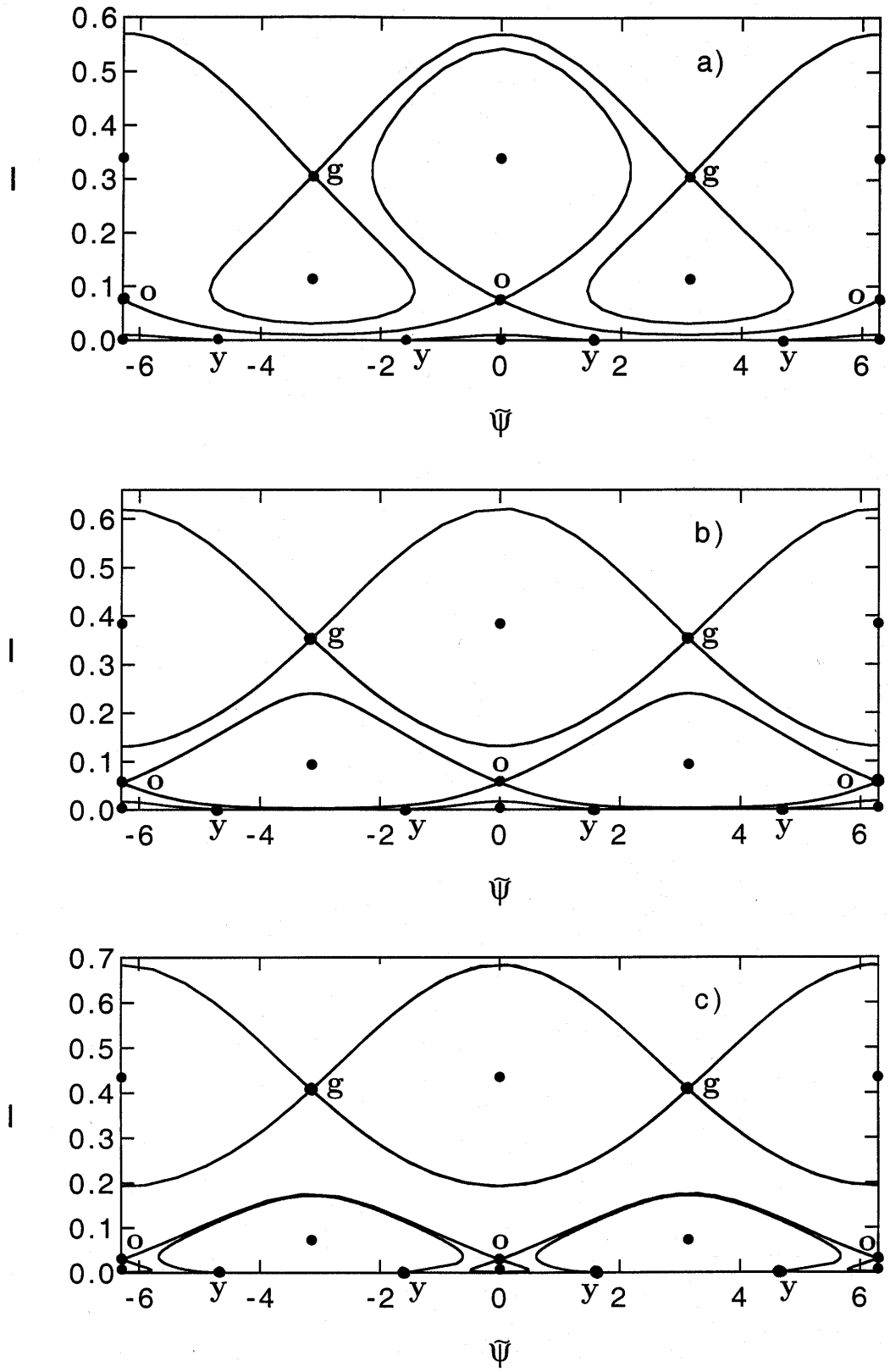

Fig. 25. Typical evolution of the phase space structure for the non-dissipative case, with parameters as in Fig. 24(a) and h =0.018, as the driving force frequency increases: (a) ω_f=0.860; (b)0.885; (c)0.915. Lines show separatrices. The different types of unstable fixed points are indicated by dots with different labels (g, o and y, which correspond to the unstable fixed points drawn in the original [?] color figure in green, orange and yellow respectively). Stable points are shown as black dots without any labels. After [?].

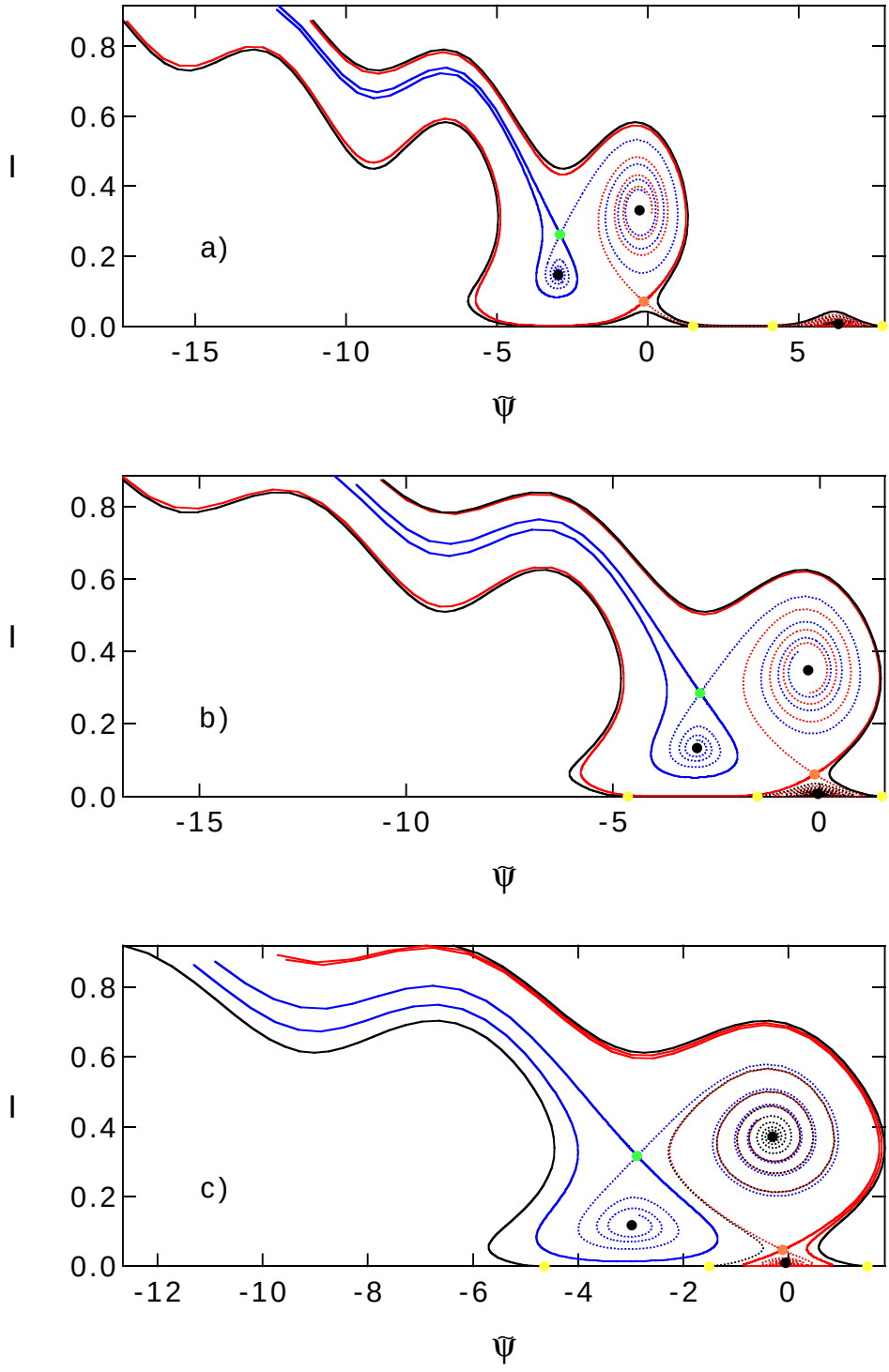

Fig. 26. Typical evolution of a 2π band of the phase space structure for the dissipative case, with parameters as in Fig. 24(b) and $hq_{1m}/(\Gamma I_m) = 5$, as the driving force frequency increases: (a) $\omega_f = 0.847$; (b) 0.857; (c) 0.872. Note that the phase space is periodic in angle, with a period of 2π. Black dots mark the locations of the attractors. Trajectories coming to/from the yellow, orange and green unstable fixed points are drawn as full/dotted black, red and blue lines, respectively. Trajectories coming to unstable fixed points form the boundaries of the basins of attraction; those leaving these points go to attractors, with the exception of those emanating from one of the two types of yellow point (with $\tilde{\psi} = \pi/2 + 2n\pi$), which go to a yellow point of another type (with $\tilde{\psi} = \pi(1/2 \pm 1) + 2n\pi$). After [**?**].

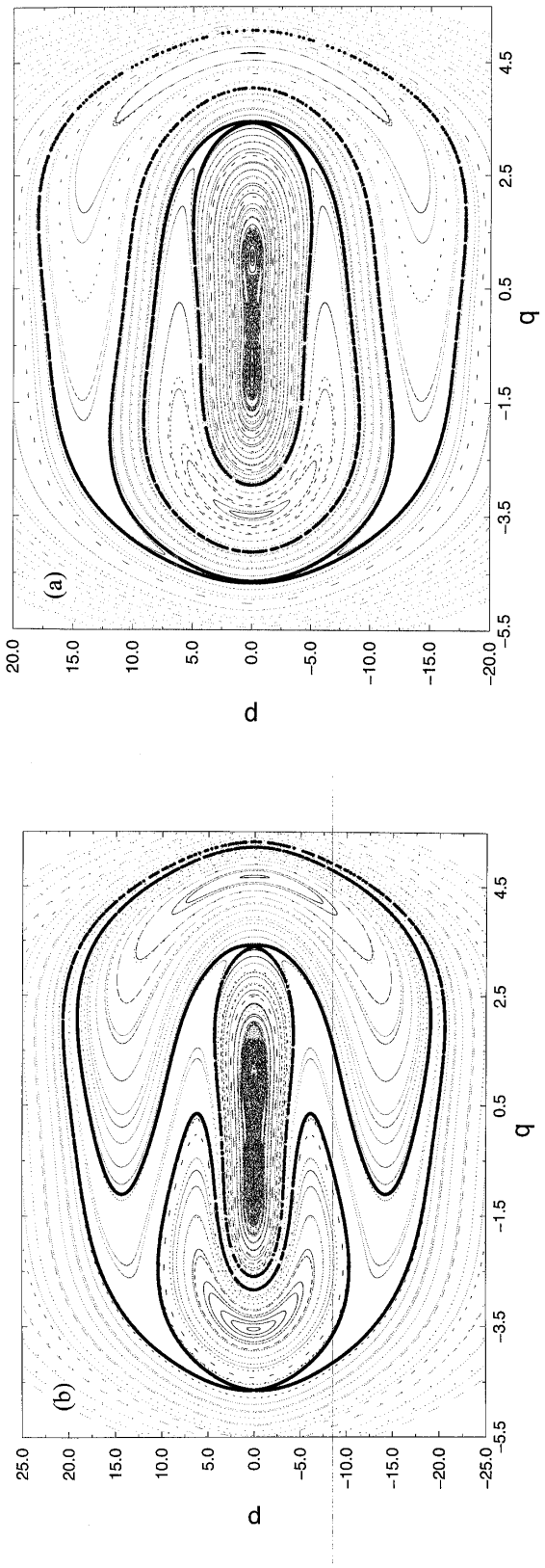

Fig. 27. Poincaré sections for the relativistic double-well Duffing oscillator (2.4.1) (with $U(q)$ and parameters as in Fig. 10) with the periodic perturbation $qF_0\cos(\pi t/2)$ added, for: (a) $F_0 = 0.1$, (b) $F_0 = 0.3$. Exponentially narrow chaotic layers, separating nonlinear resonances from other regions of the phase space, are indicated by larger dots (the gaps are due to a finite integration time). There are two nonlinear resonances in each figure: of the NR and ZDNR type, in (a) and (b) respectively. After [**?**].

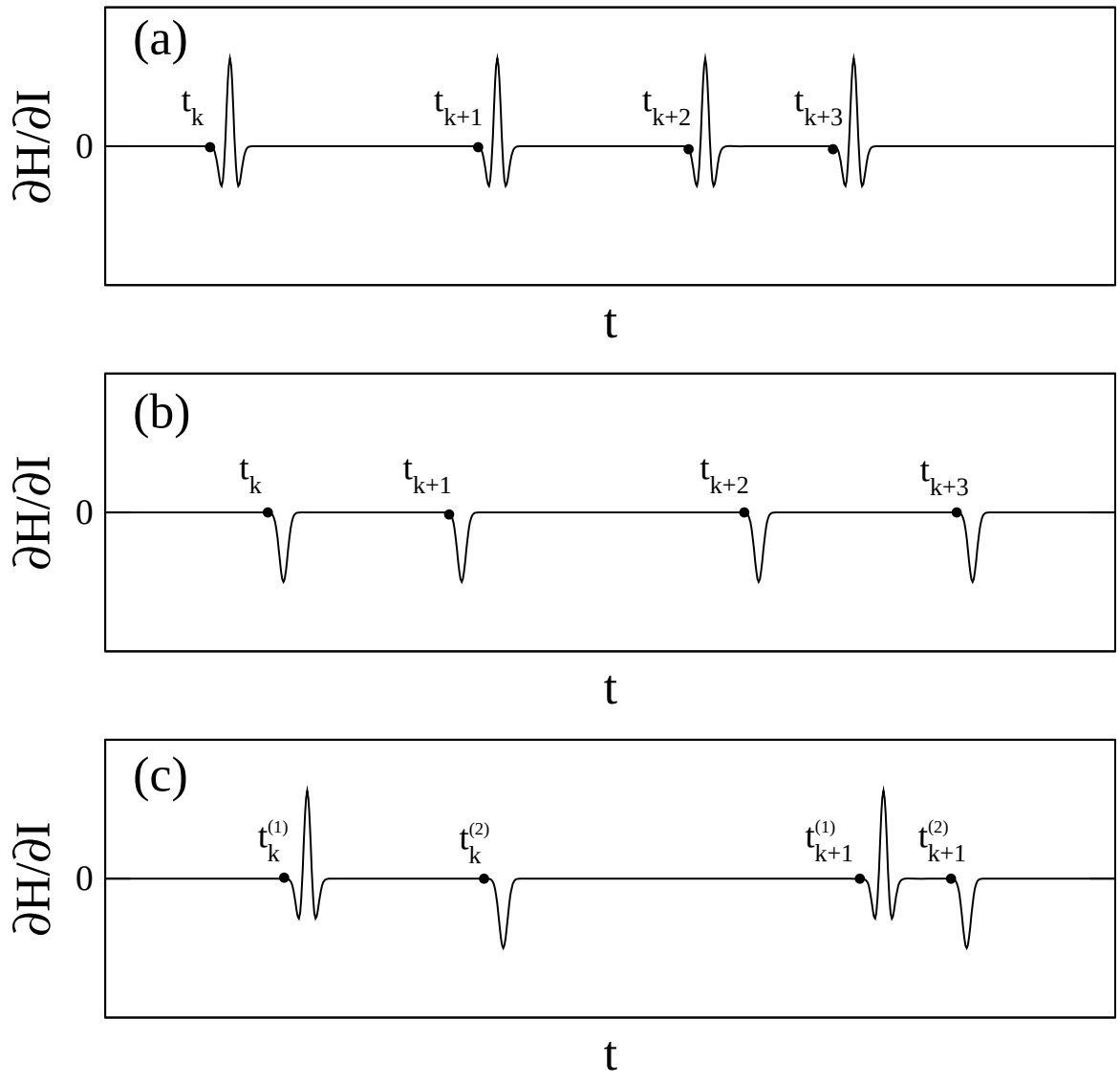

Fig. 28. Schematic dependence $\partial\overline{H}/\partial I(t)$ along a trajectory in the vicinity of the separatrix (relevant to $\overline{H}(I,\tilde{\psi})$) shown in Fig. 19(b), for three characteristic trajectories (cf. Fig. 19(b)): (a) inside one of the loops; (b) below the loops; (c) above the loops. Instants preceding successive pulses of $\partial\overline{H}/\partial I(t)$ are marked by dots with corresponding labels.

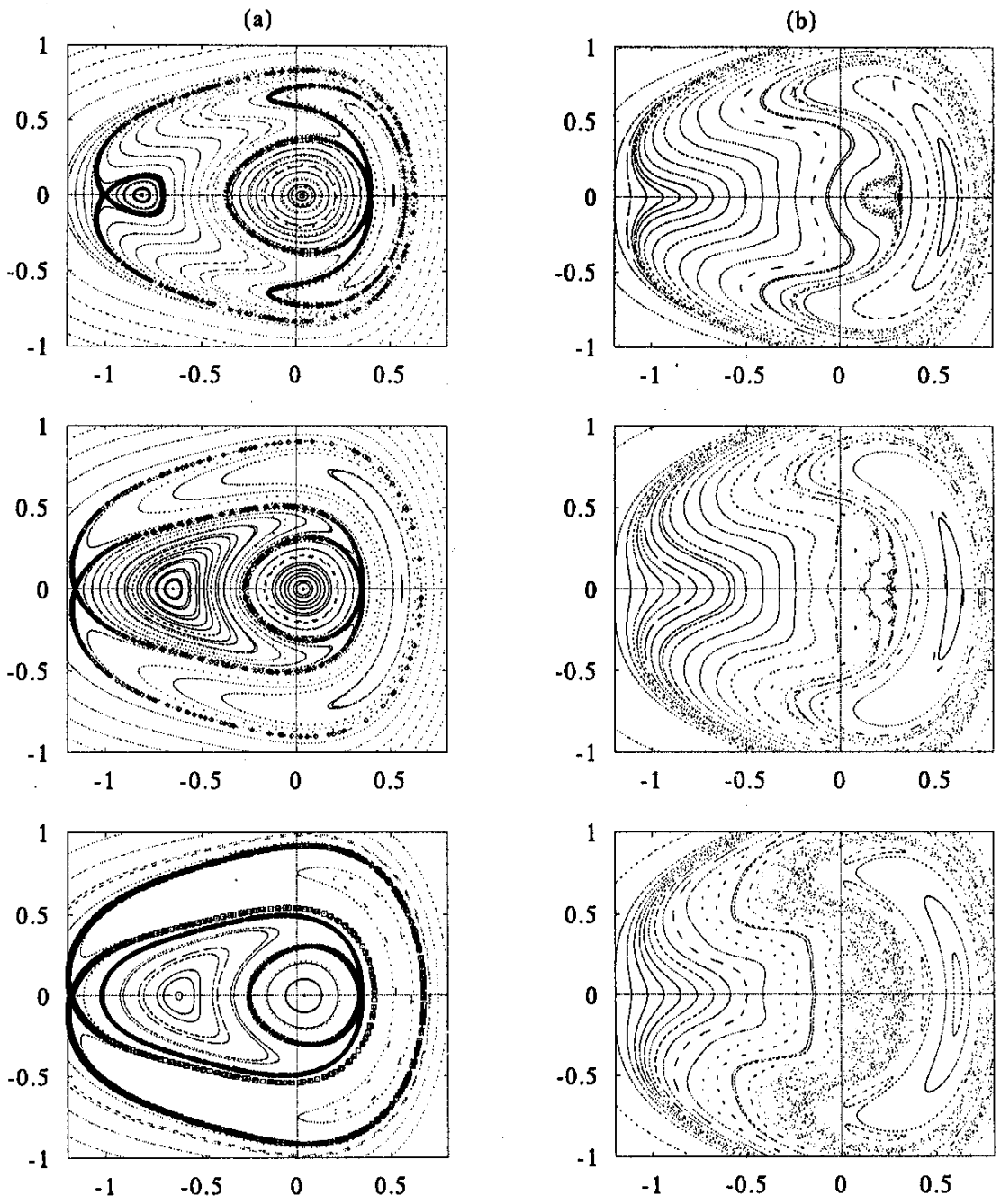

Fig. 29. Stroboscopic Poincaré sections of the periodically driven non-dissipative TDO (see (4.2.3) at $\Gamma = 0$) at $\omega_0 = 1, \beta = 5/3, \gamma = 1$. (a) For h=0.01, with driving frequencies, from top to bottom: ω_f=0.82; 0.85258; 0.86. Chaotic layers (which are so narrow that cannot be seen on this scale of the figure, but are clearly evident in enlarged figures) are indicated with bigger dots (whose discreteness is due to the finite integration time). (b) For ω_f=0.84 and, from top to bottom: h=0.05; 0.07; 0.09. After [**?**].

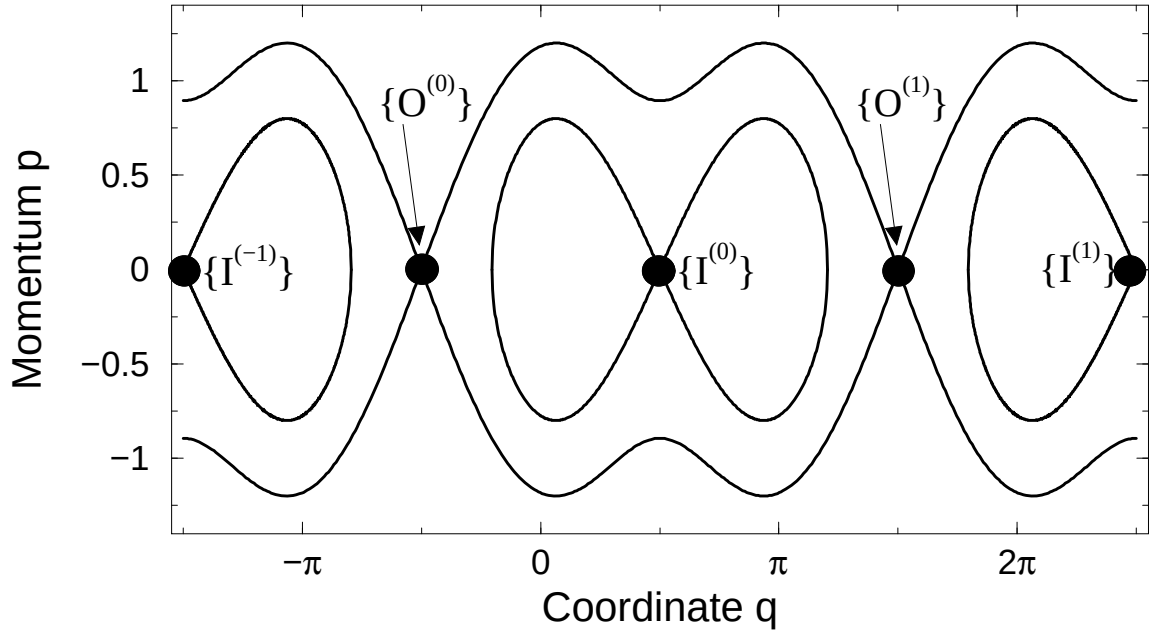

Fig. 30. The separatrices in the p–q plane for the unperturbed Hamiltonian, $H(p,q) = p^2/2 + (0.2 - \sin(q))^2/2$ (the corresponding potential $U(q)$ is drawn in Fig. 5(a)). The inner and outer saddles are indicated by dots and labels $\{I^{(l)}\}$ and $\{O^{(l)}\}$ respectively. After [**?**].

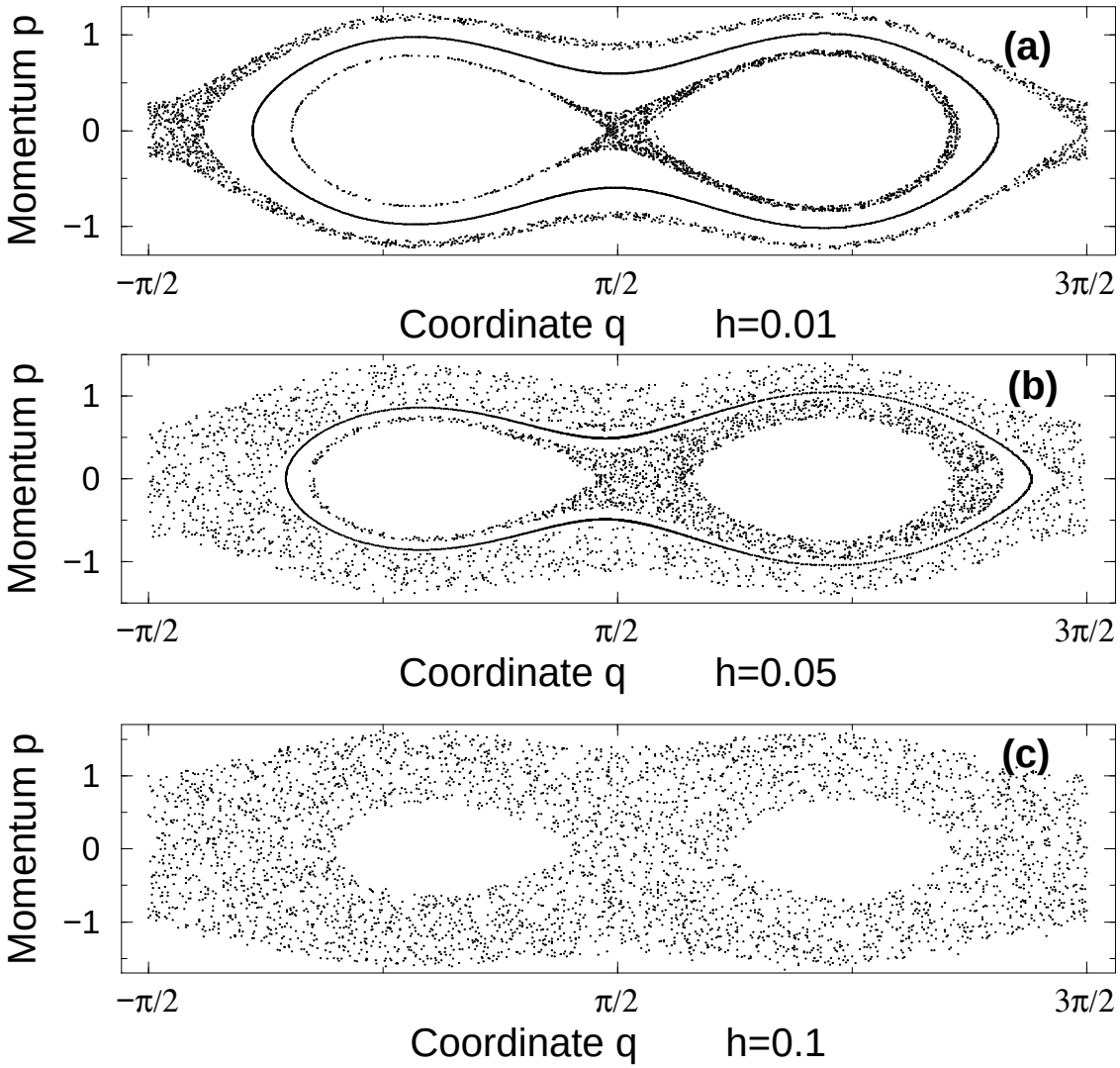

Fig. 31. The evolution of the stroboscopic (for instants $n2\pi/\omega_f$ with $n = 0, 1, 2, ...$) Poincaré sections of the system (4.3.14) with $\omega_f = 0.3$ while h grows from the top to the bottom: (a) 0.01, (b) 0.05, (c) 0.1. The number of points in each trajectory is 2000 (i.e. the integration time is $4000\pi/\omega_f$). In parts (a) and (b), three characteristic trajectories are shown: the inner trajectory starts from the state $\{I^{(0)}\} \equiv \{p = 0, q = \pi/2\}$ (which corresponds to the inner saddle of the unperturbed system), and is chaotic but bounded in the space; the outer trajectory starts from $\{O^{(0)}\} \equiv \{p = 0, q = -\pi/2\}$ (which corresponds to the outer saddle of the unperturbed system), and is chaotic and unbounded in coordinate; the third trajectory represents an example of a regular (KAM) trajectory separating the above chaotic ones. In (c), only one, chaotic and unbounded, trajectory exists in the relevant region of the Poincaré section. After [**?**].

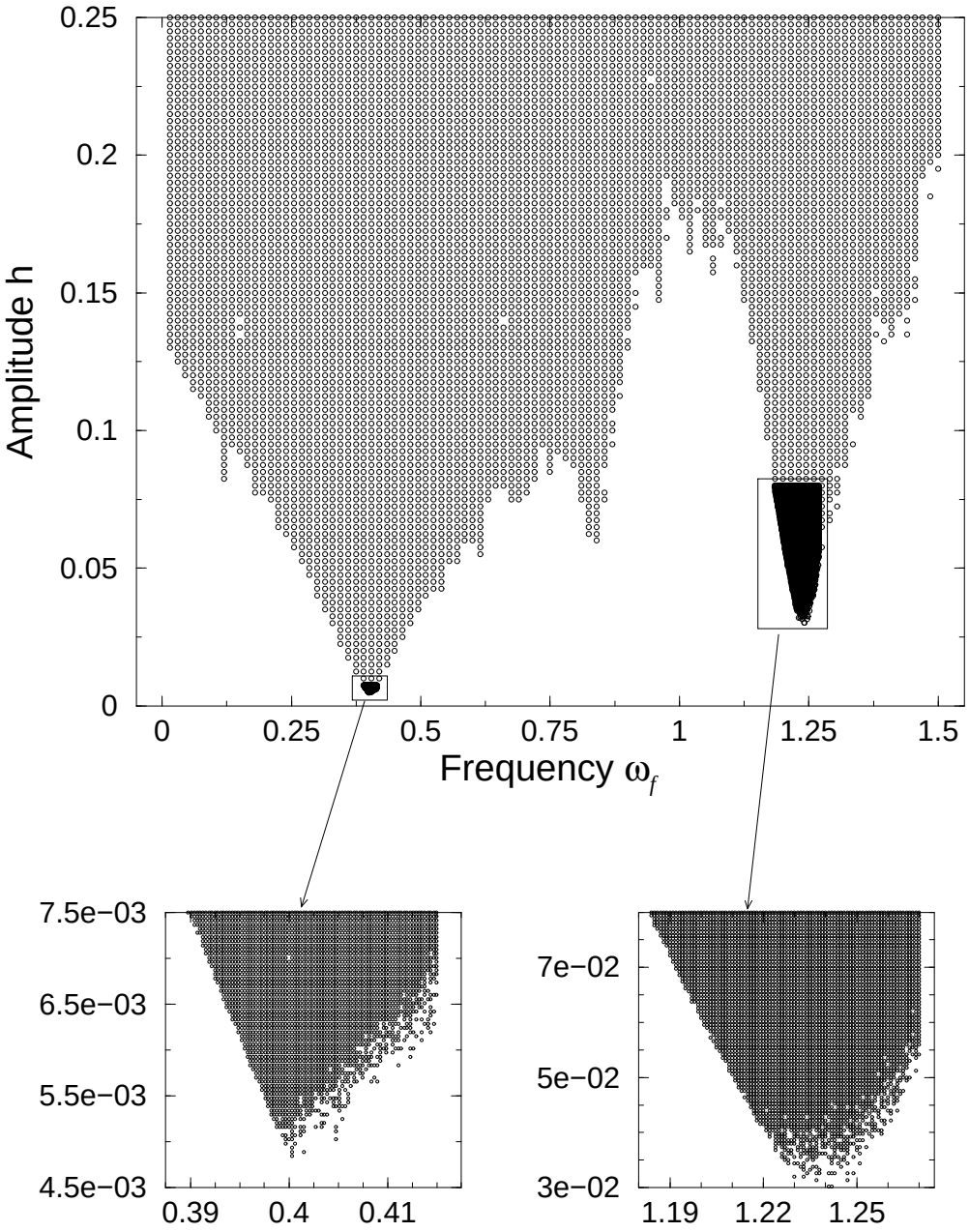

Fig. 32. The bifurcation diagram indicating (by shading) the parameter ranges for which there is global chaos: the latter is tested in simulations by noting whether the system can be transported from the state $\{I^{(0)}\} \equiv \{p = 0, q = \pi/2\}$ (the inner saddle) beyond the neighbouring outer saddles, $\{O^{(0)}\}$ and $\{O^{(1)}\}$, i.e. if the coordinate reaches either $-\pi/2$ or $3\pi/2$. The grid in the regions bounded by the rectangles was made significantly denser than beyond them in order to find more accurately the boundaries of the "chaotic" spikes. The integration time for each point of the grid is 12000π. After [**?**].

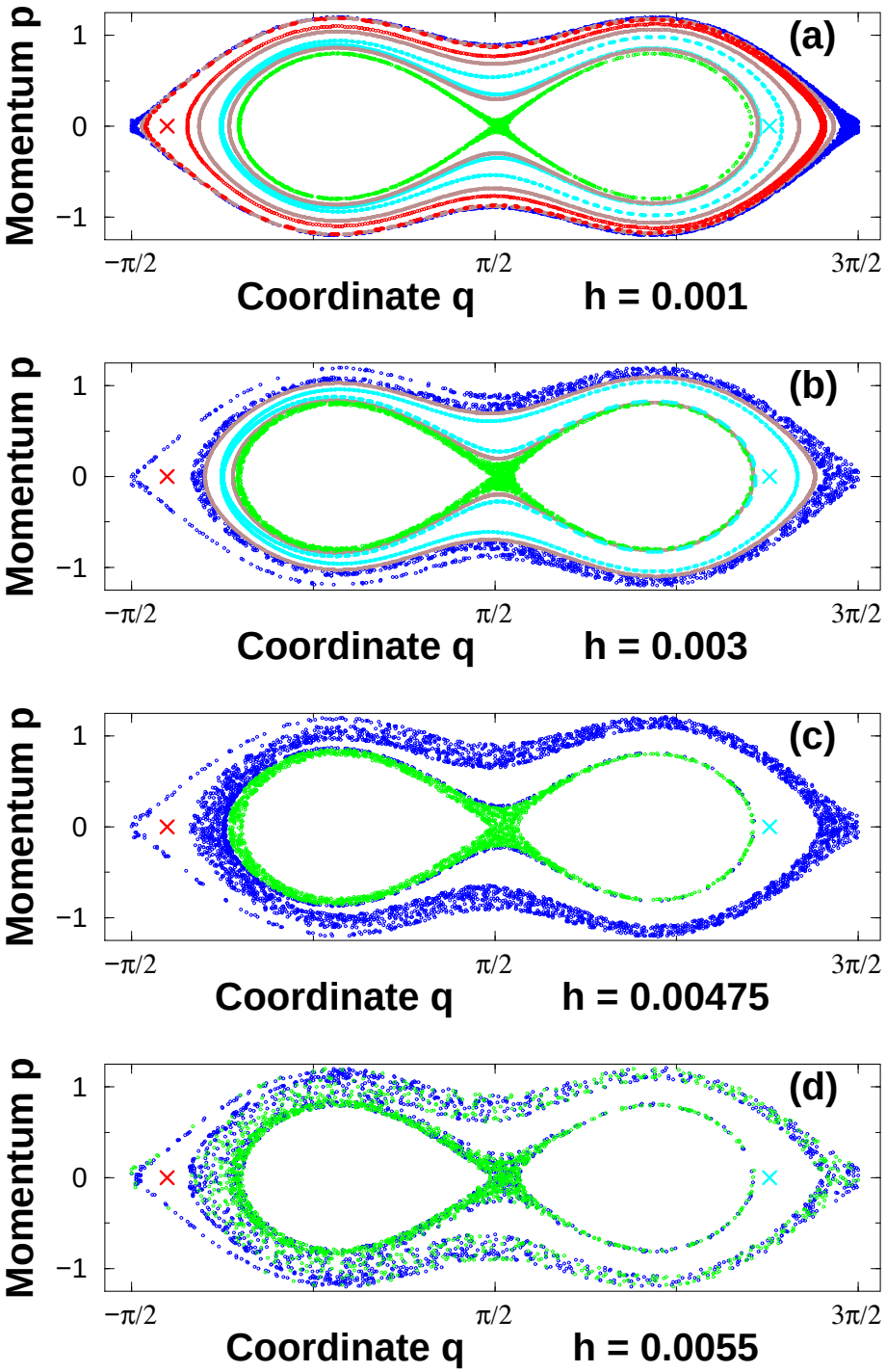

Fig. 33. The evolution of the stroboscopic (for instants $n2\pi/\omega_f$ with $n = 0, 1, 2, ...$) Poincaré section of the system (4.3.14) as the amplitude of the perturbation h grows while the frequency is fixed at $\omega_f = 0.401$. The number of points in each trajectory is 2000. The chaotic trajectories starting from the states $\{I^{(0)}\}$ and $\{O^{(0)}\}$ are drawn in green and blue respectively. The stable stationary points (the 1st-order nonlinear resonances) are indicated by the red and cyan crosses. The chaotic trajectories associated with the resonances, in those cases when they do not merge with the green/blue chaotic trajectories, are indicated in red and cyan respectively (their real width is exponentially small and much less than the width of the line as drawn). Examples of KAM trajectories embracing the state $\{I^{(0)}\}$ while separating various chaotic trajectories are shown in brown. After [**?**].

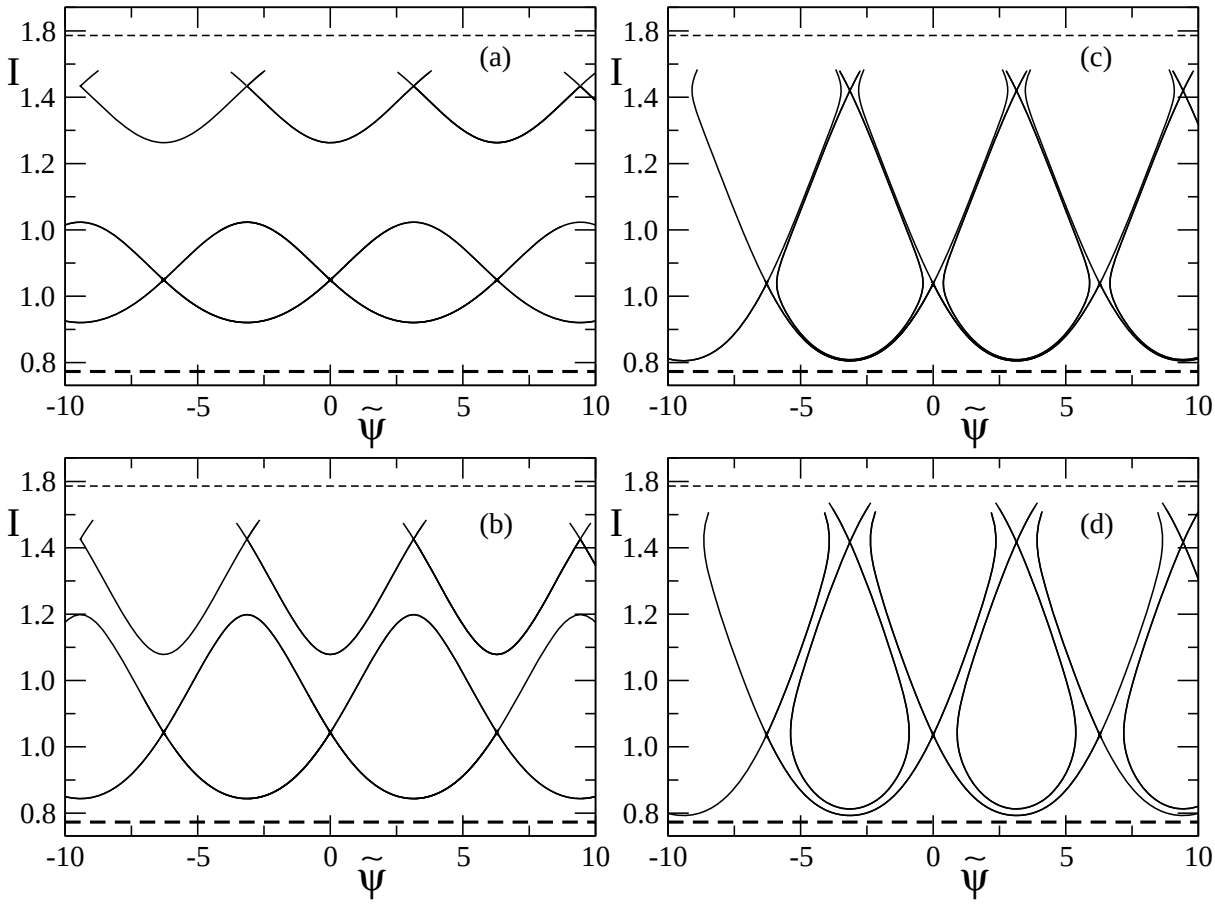

Fig. 34. The evolution of the separatrices (full lines) of the 1st-order resonances within the resonance approximation (cf. (4.2.4) at $\Gamma = 0$) in the action-angle plane, for the same parameters as in Fig. 33. The dashed lines show the levels of the barriers. After [**?**].

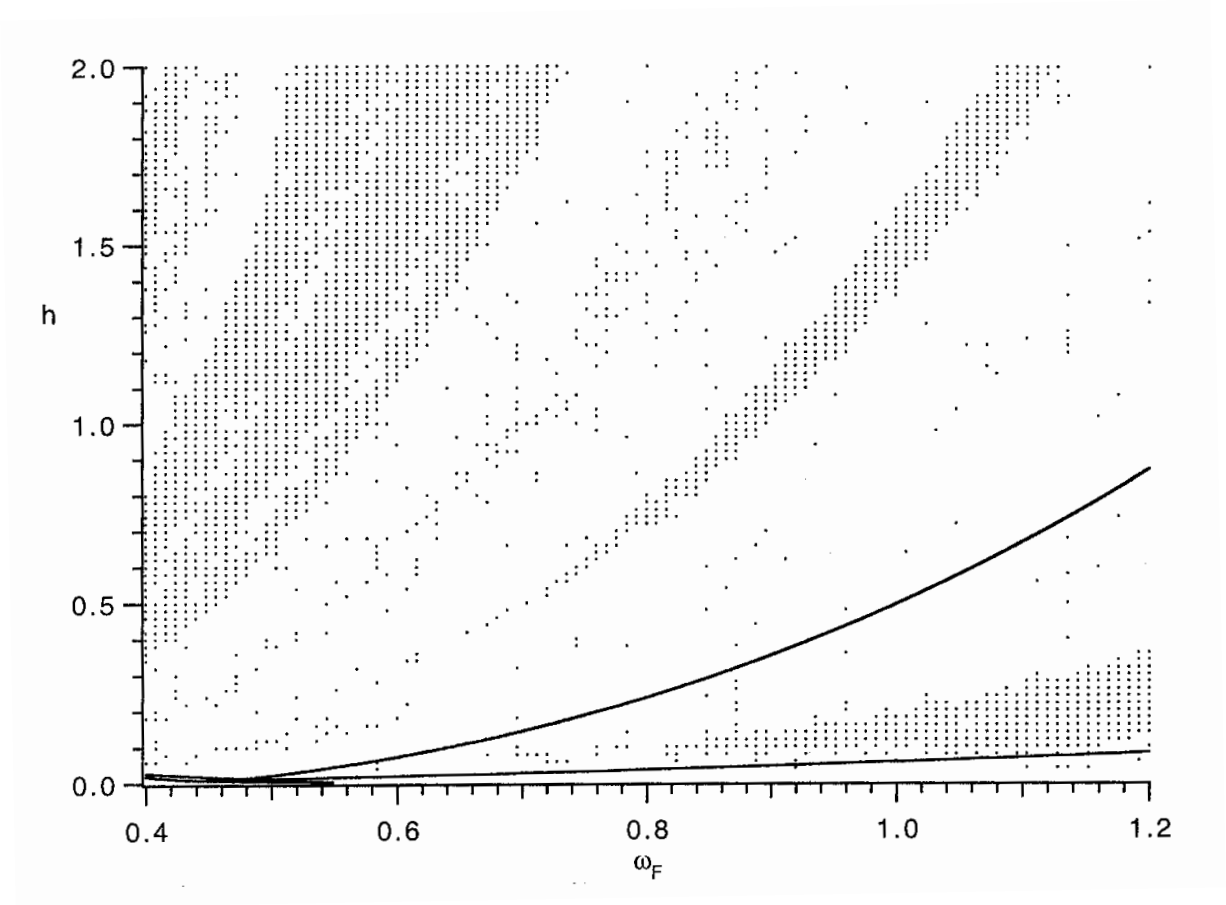

Fig. 35. Regions of chaos (shaded), i.e. where positive Lyapunov exponents exist, in the plane of the driving force parameters, for the system (4.2.3) with Γ =0.05, ω_0 =0.5924, β =1.026, γ =1. Local bifurcations of the corresponding reduced system (4.2.4) with $n = 1$ (1st-order resonance) are indicated by full curves. After [**?**].

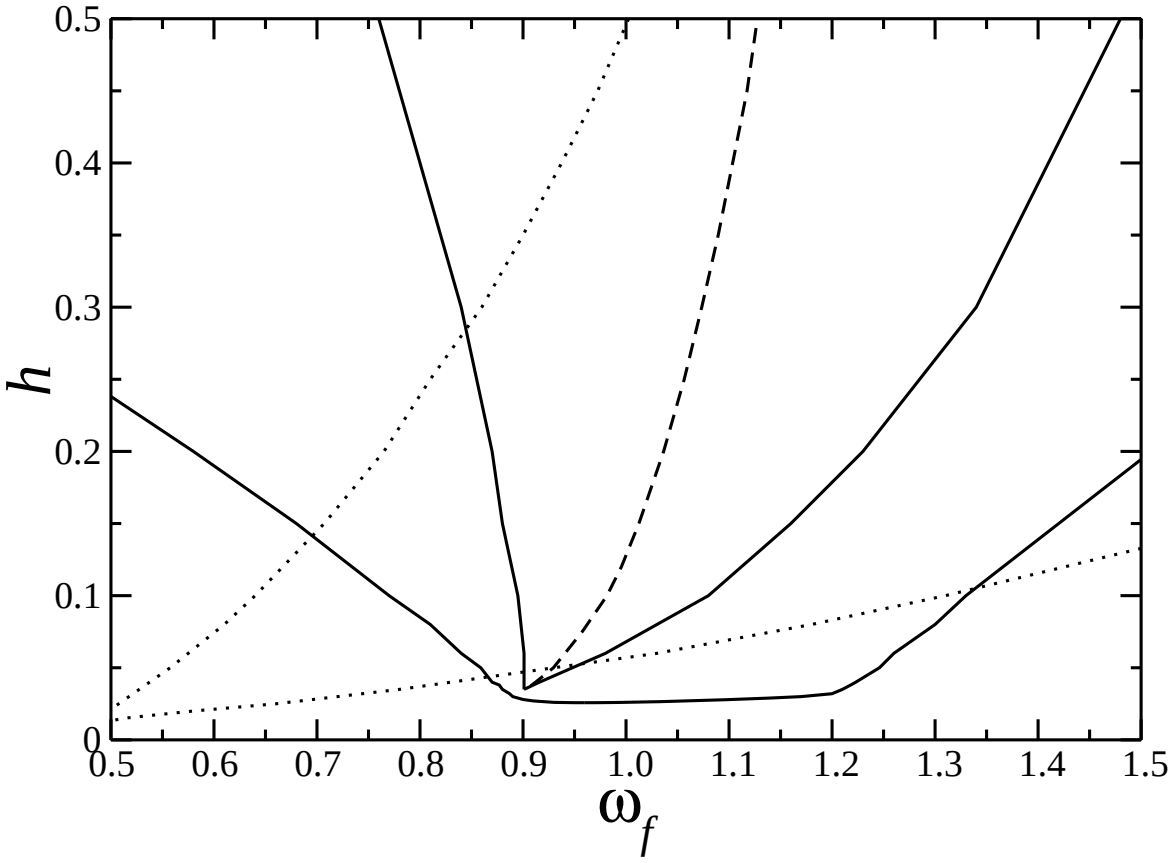

Fig. 36. Some of the bifurcation lines of the resonance approximation (4.2.4) at $n = 1, 2$ for the system (4.2.3) with the same parameters as in Fig. 35. The region where the two attractors with $n = 1$ coexist lies between the dotted lines. There are two (one) attractors corresponding to $n = 2$ between the inner (inner and outer) full lines. The dashed line marks the ZDNR/NR transition at $n = 2$ (see Fig. 37). After [**?**].

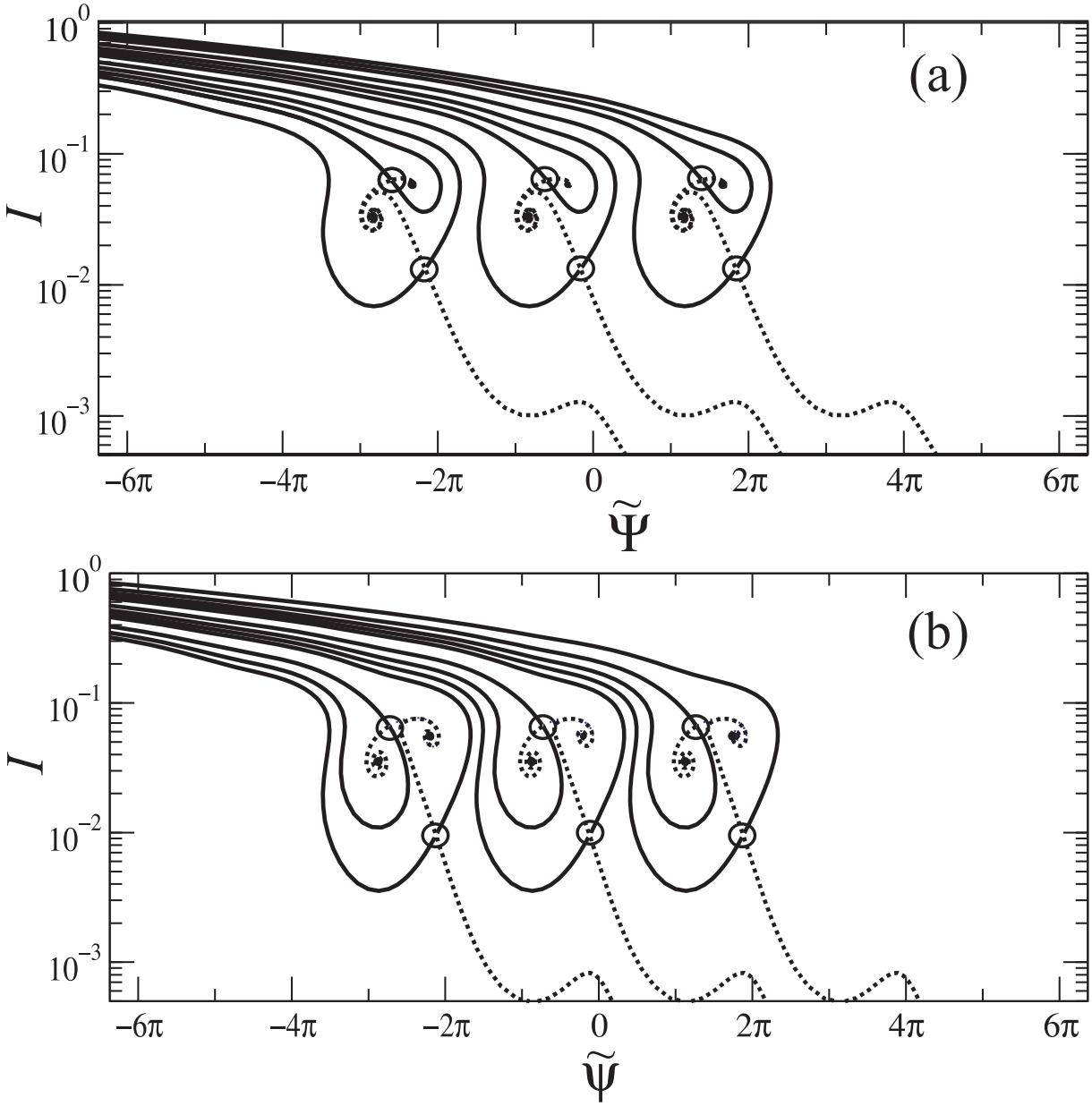

Fig. 37. Typical evolution of three 2π bands of the phase space structure for the reduced system (4.2.4) at $n = 2$, with the same parameters as in Fig. 35 and $\omega_f = 0.95$ for (a) $h = 0.055$, (b) 0.075; note that the phase space is periodic in angle, with a period of 2π but, in the interests of clarity, we draw only three 2π bands. Dots and open circles mark attractors and saddles respectively. Trajectories coming to/from saddles are drawn as full/dotted lines. Trajectories coming to saddles form the boundaries of the basins of attraction. After [**?**].

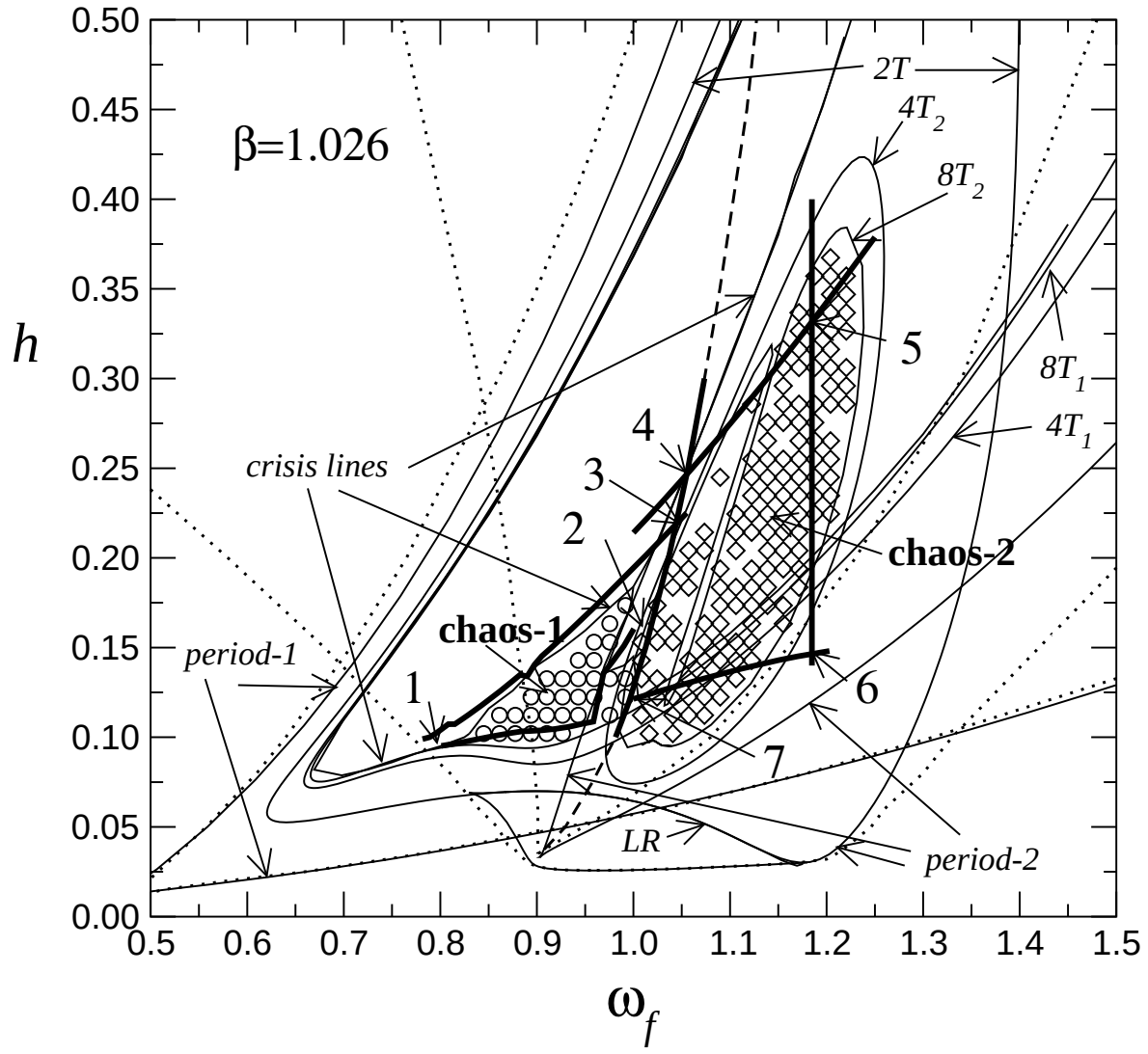

Fig. 38. The bifurcation diagram for the full system (4.2.3) with the same parameters as in Fig. 35. Various bifurcations, found from the analysis of Poincaré sections, are indicated by thin full lines and by the corresponding labels (to simplify a little the visual perception of the figure, we do not show the lines of period-3 bifurcations since they lie entirely to the right from $\omega_f = 1.2$ and seem to be irrelevant to the onset of chaos). Regions where strange attractors exist match well the regions where positive Lyapunov exponents exist. The latter regions are shaded. To resolve the two different types of chaotic attractor (see text) labelled chaos–1 and chaos–2, we use different markers (circles and rhombuses) for shading the corresponding regions; note that there is a slight overlap of the regions (where both types of chaotic attractors coexist). Dotted lines mark the local bifurcations calculated in the resonance approximation for resonances $n = 1, 2$ (cf. Fig. 36). The dashed line marks the (calculated in the resonance approximation) ZDNR/NR transition for $n = 2$ (cf. Figs. 36 and 37). Thick full lines are related to the interaction between oscillations of different frequency, and their intersections are indicated by the arrows and corresponding numbers. After [**?**].

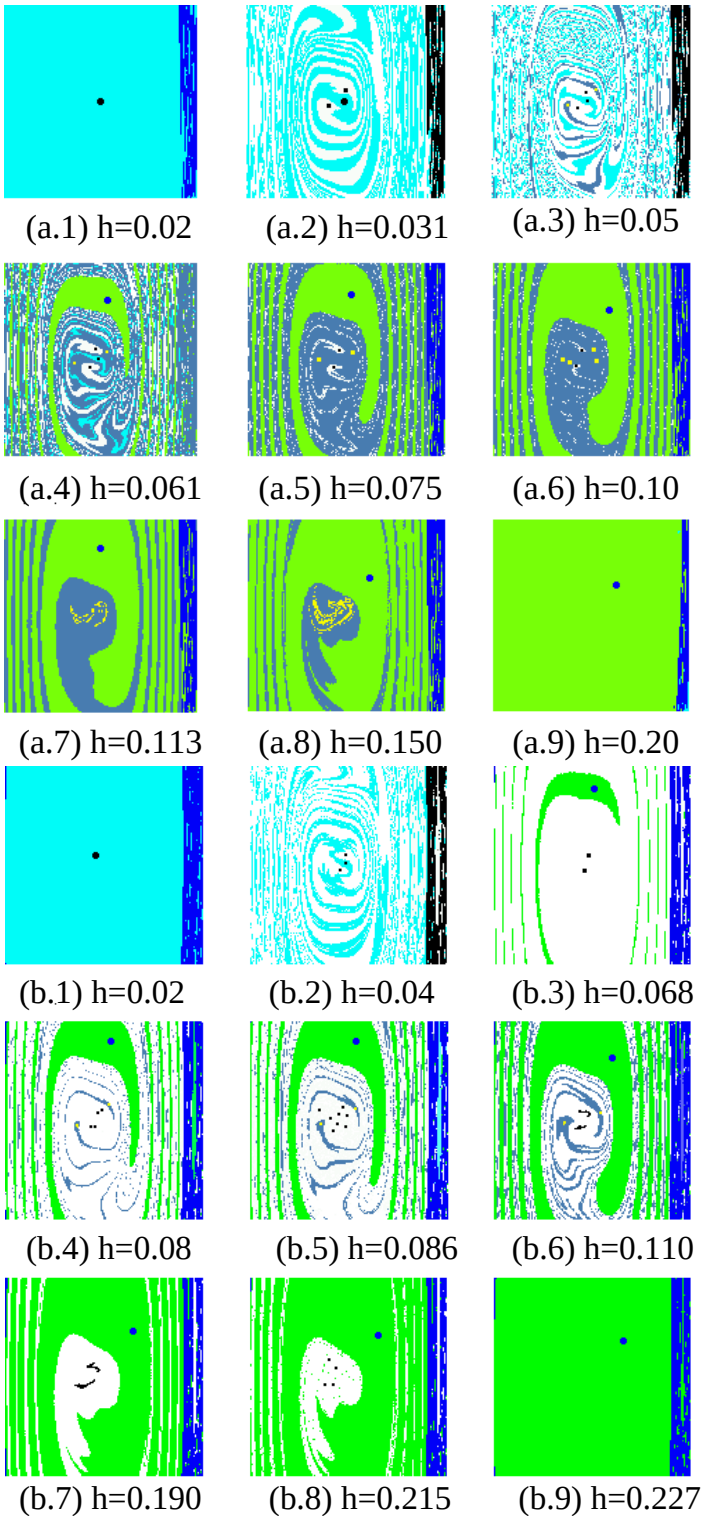

Fig. 39. An evolution of the stroboscopic $(t = 0, 2\pi, ...)$ Poincaré section $p - q$, for the same system as in Fig. 35, for: (a) $\omega_f = 0.95$, (b) $\omega_f = 1.05$, as h increases. It demonstrates how *chaos-1*(a) and *chaos-2*(b) are born. Regular attractors are indicated by dots; chaotic attractors are shown by grey in (a.7), (a.8) and by black in (b.6), (b.7). Basins of attraction are shown by different shades. After [**?**].

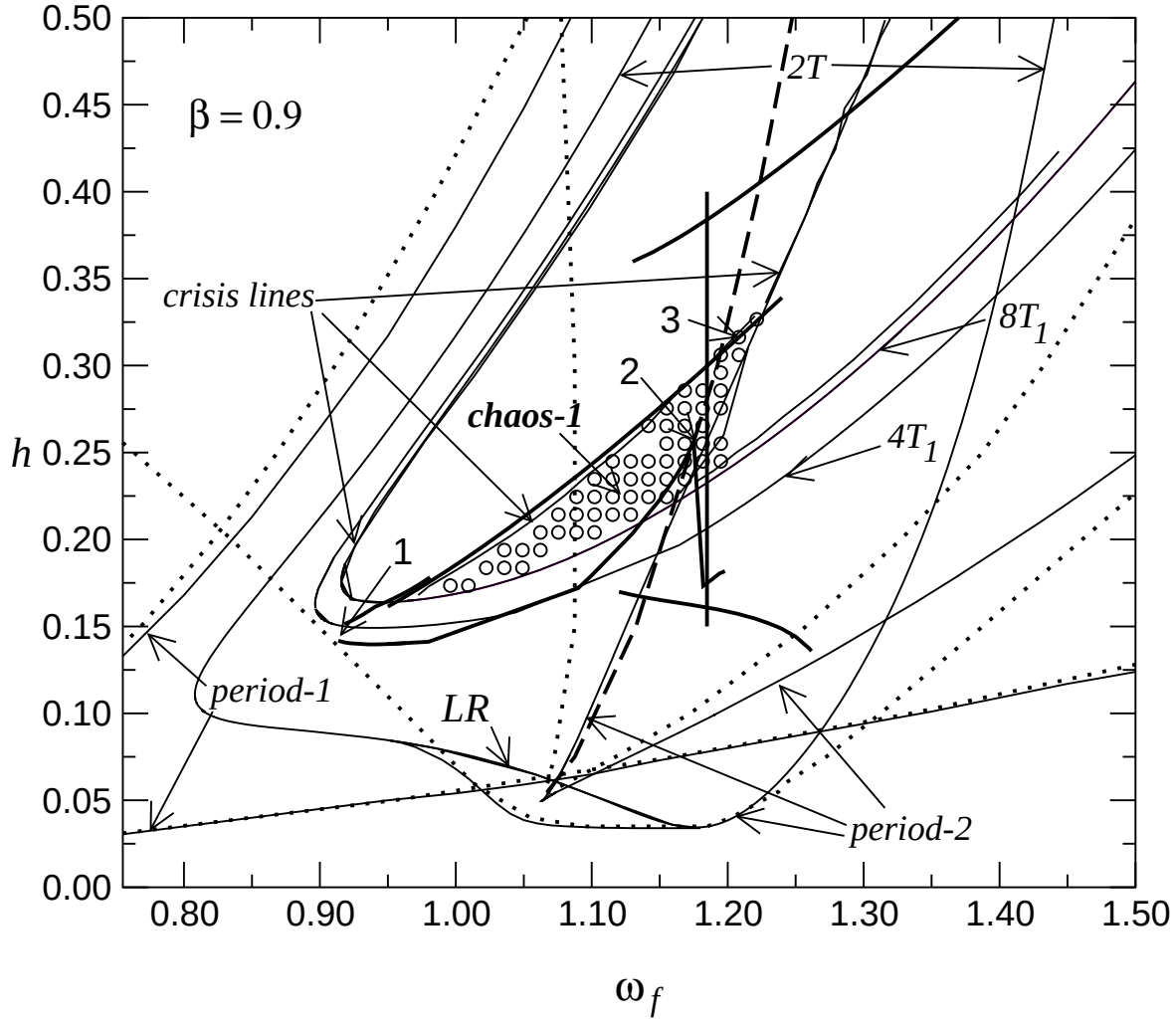

Fig. 40. Bifurcation diagram similar to that in Fig. 38 but for the case $\beta = 0.9$ (Γ, ω_0 and γ are the same as in Fig. 38: $\Gamma = 0.05$, $\omega_0 = 0.5924$ and $\gamma = 1$). After [**?**].

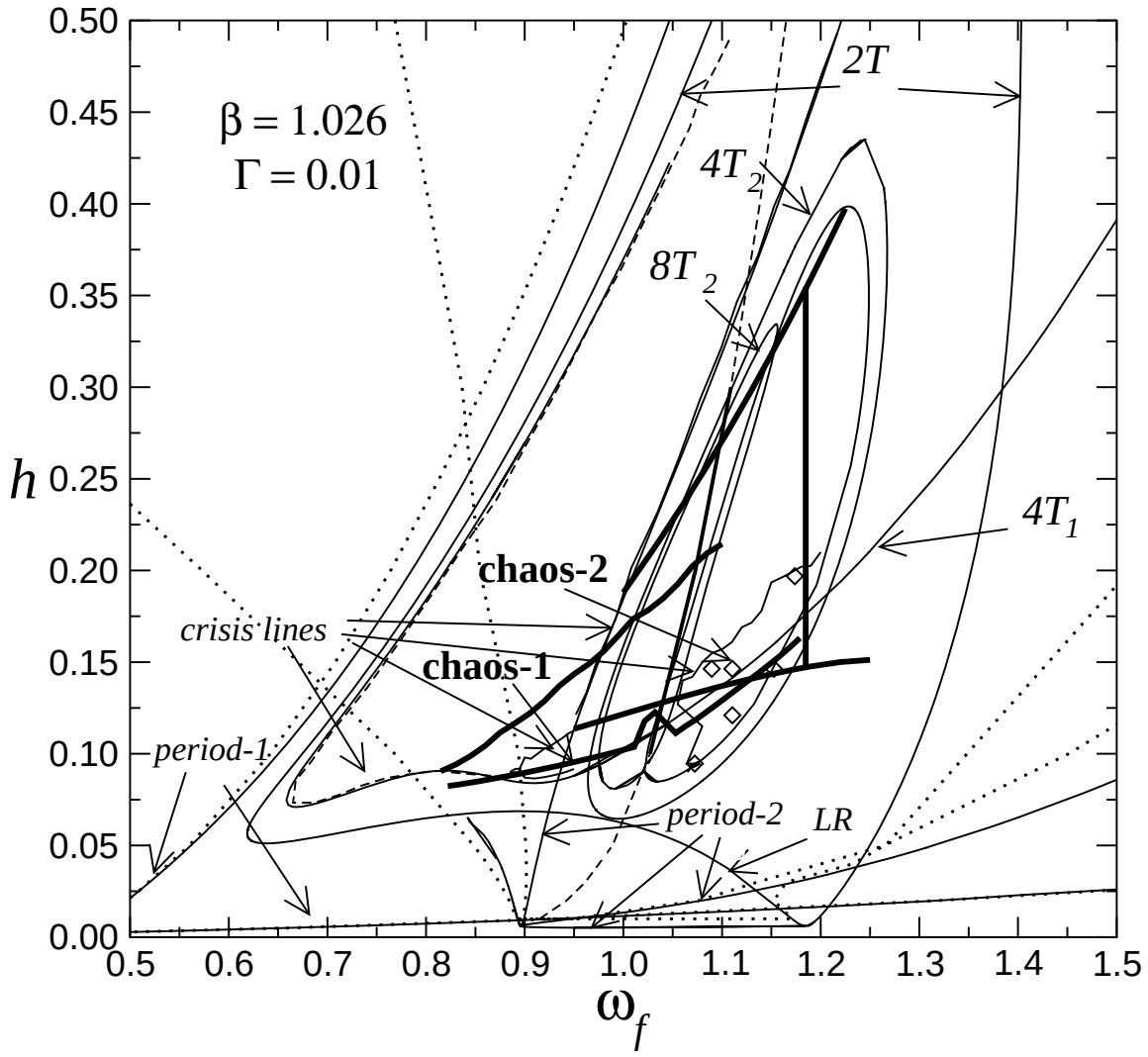

Fig. 41. Bifurcation diagram similar to that in Fig. 38 but for the case $\Gamma = 0.01$ (ω_0, β and γ are the same as in Fig. 38: $\omega_0 = 0.5924$, $\beta = 1.026$ and $\gamma = 1$). After [**?**].

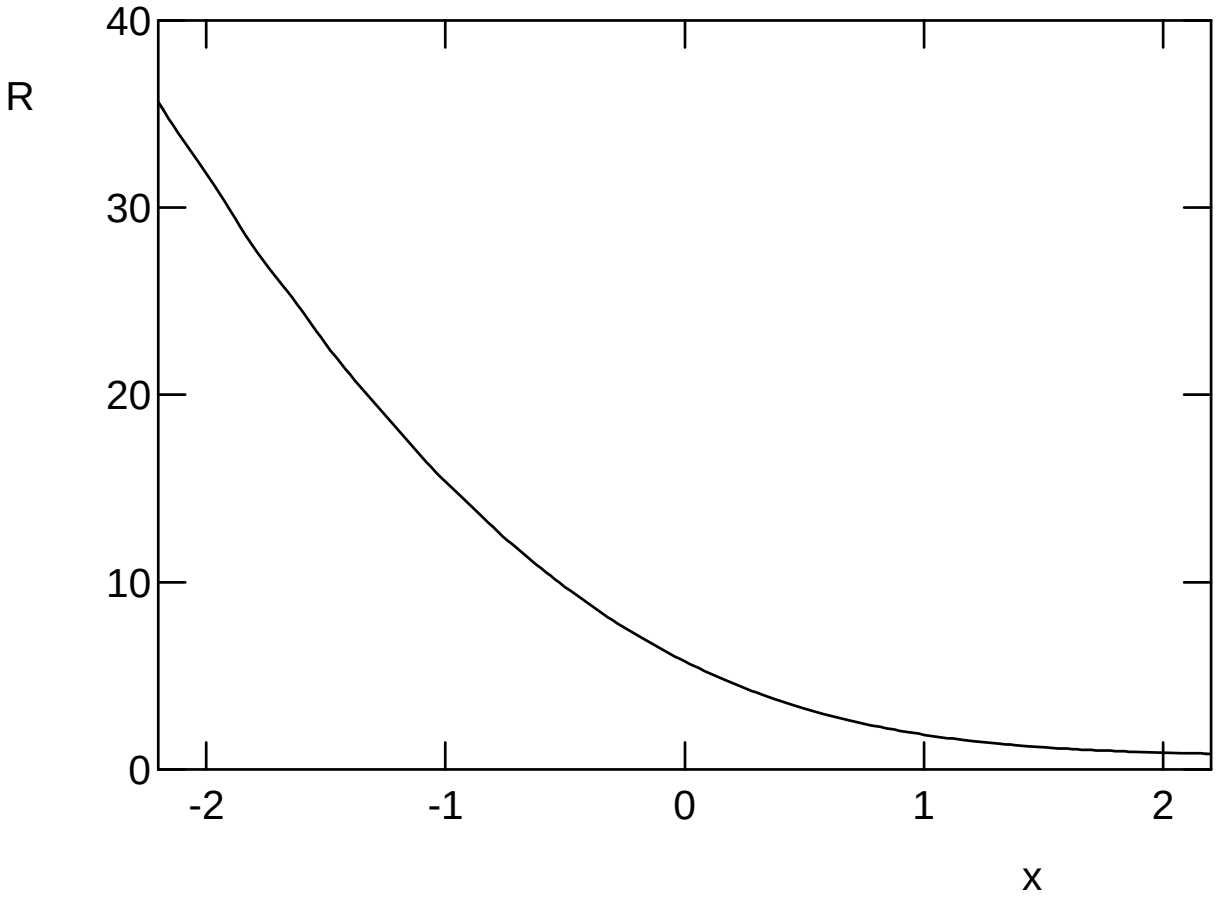

Fig. 42. The normalized frequency-dependence of the signal-to-noise ratio in the asymptotic limit of small dissipation, as given by the function $R(x)$ defined in Eqs.(5.1.9),(3.3.19). After [**?**].

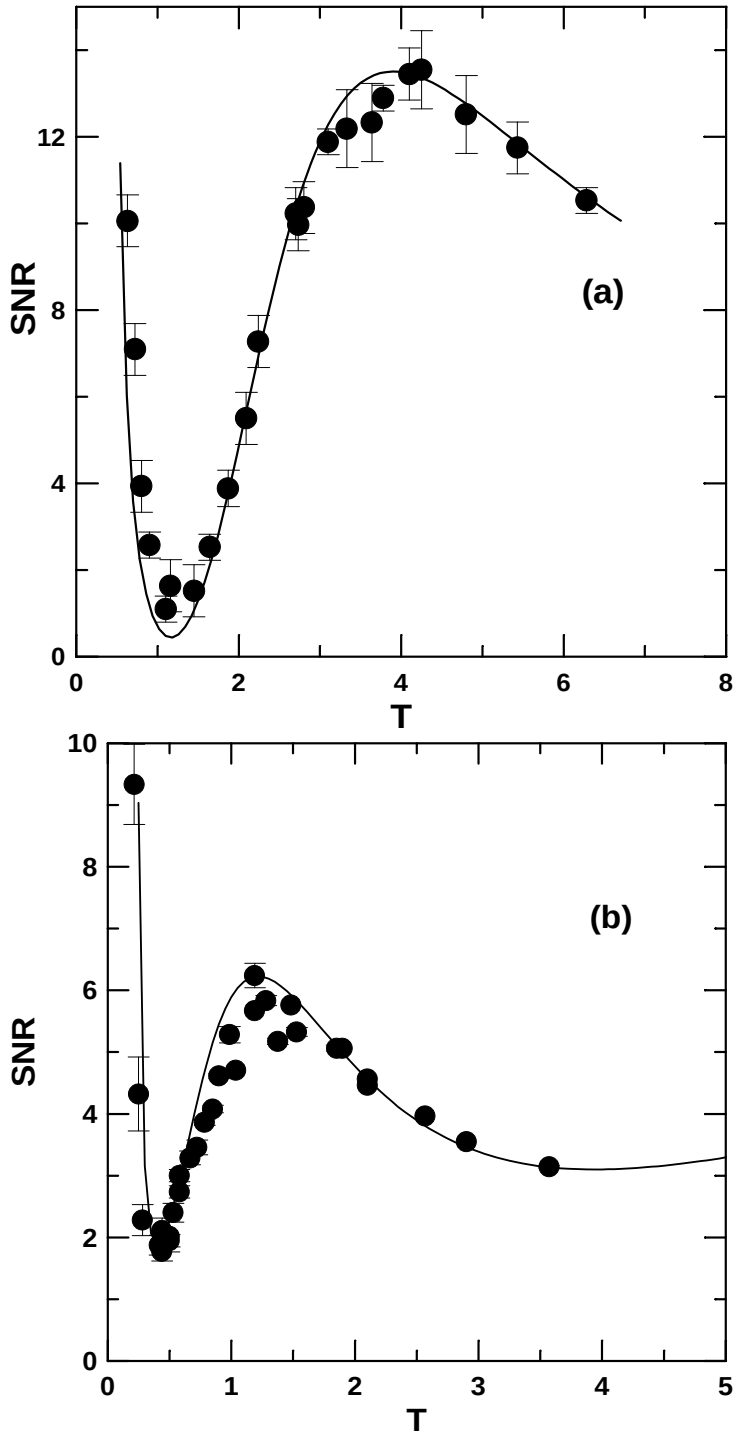

Fig. 43. The dependence of the signal-to-noise ratio on noise intensity for: (a) the single-well SQUID potential of Fig. 3(a), with $\Omega = 0.62$ and $A = 0.016$; and (b) the multiwell SQUID potential of Fig. 3(b), with $\Omega = 0.39$ and $A = 0.005$. The results of the electronic experiments and numerical calculations are shown respectively by the circles and the solid lines. After [**?**].

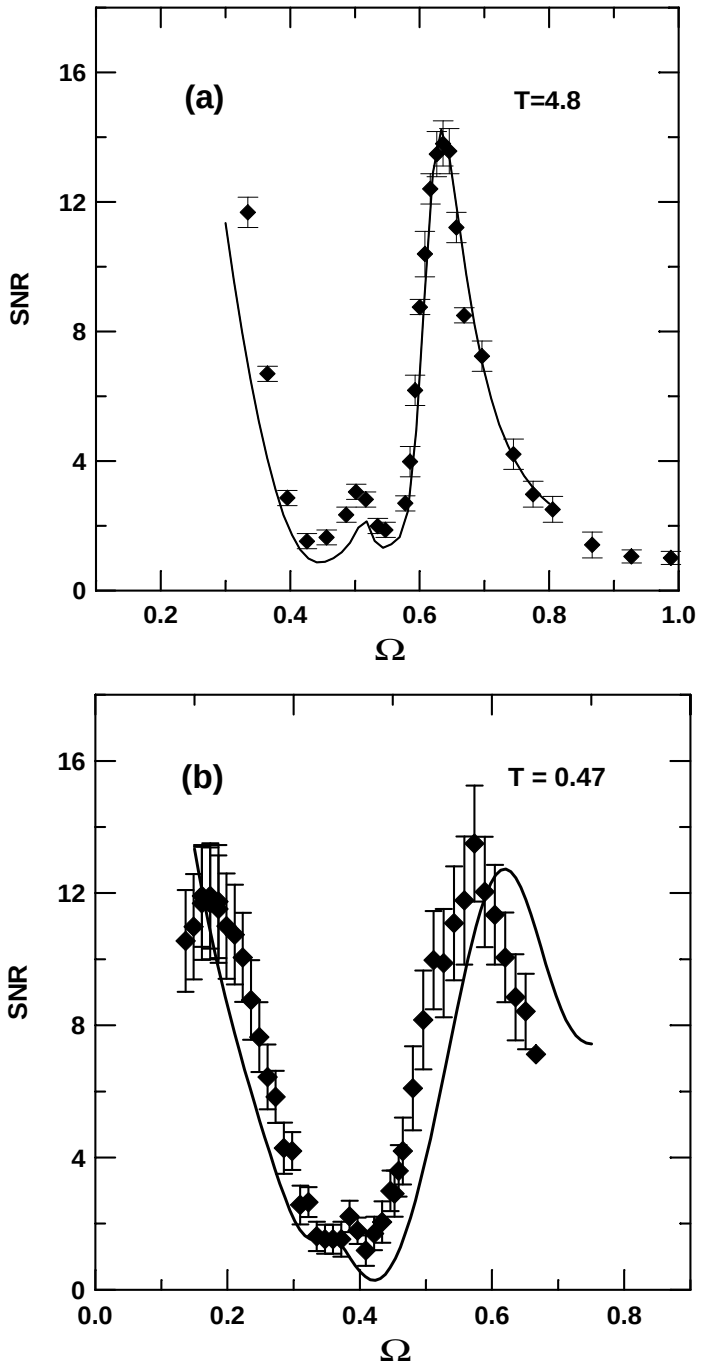

Fig. 44. The experimental (data points) and numerically calculated (solid line) frequency dependence of the SNR at fixed noise intensity for (a) the single-well SQUID potential of Fig. 3(a), with $T = 4.8$ and $A = 0.016$; and (b) the multiwell SQUID potential of Fig. 3(b), with $T = 0.47$ and $A = 0.005$. Dash-dotted lines mark the positions of the relevant extrema of $\omega(E)$ (see Fig. 4). After [**?**].

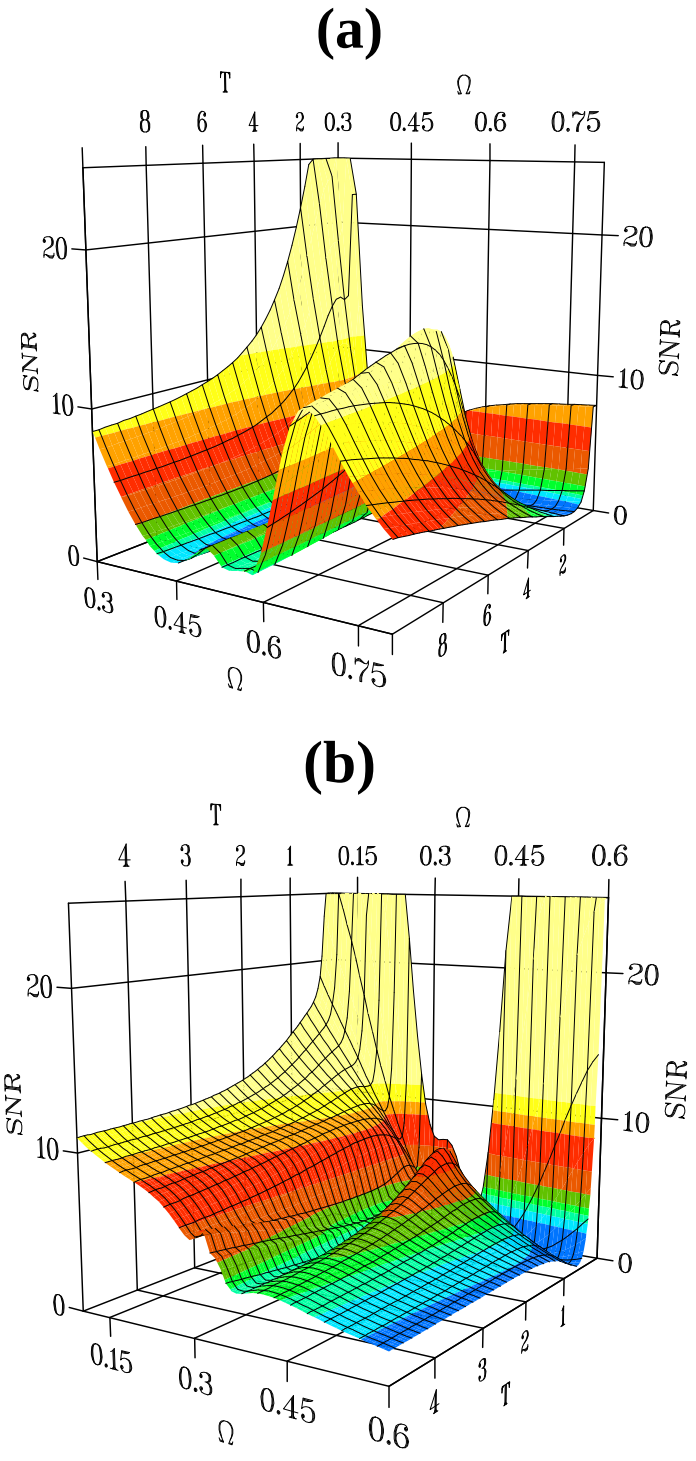

Fig. 45. The dependence of the signal-to-noise ratio (normalized by a squared signal amplitude) on the noise intensity T and the signal frequency Ω, calculated using (5.1.4) and the numerical algorithm described in sub-section 3.5, for: (a) the single-well SQUID potential of Fig. 3(a); and (b) the multiwell SQUID potential of Fig. 3(b). After [**?**].

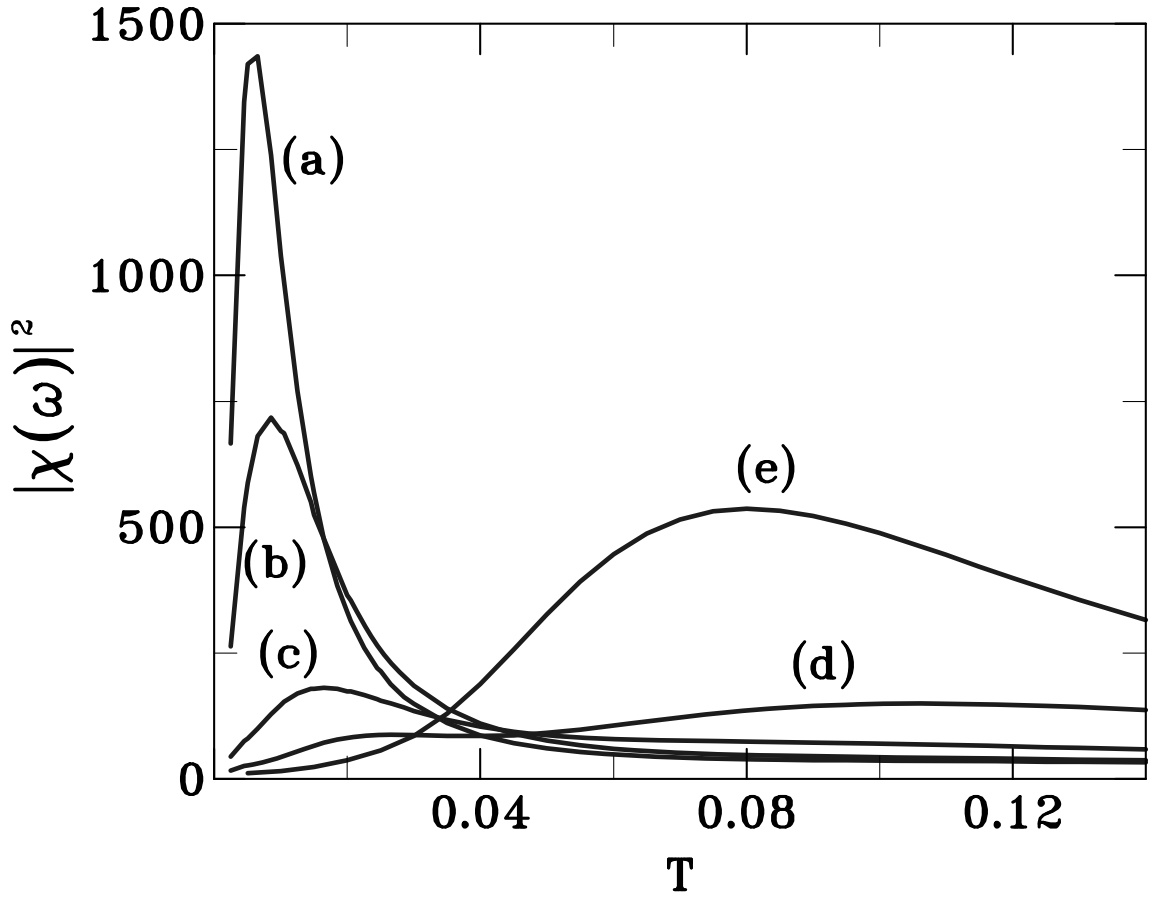

Fig. 46. Dependence of the squared modulus of the susceptibility on temperature, for the TDO (5.2.2) with parameters of the potential as in Fig. 22 and $\Gamma = 0.0122$. The curves represent the calculated $|\chi(\omega)|^2$ at the second harmonic ($\omega = 2\Omega$) of the field frequency Ω in the model (5.2.2). The frequencies for different curves are (a) $\Omega/\omega_0 = 0.490$, (b) $\Omega/\omega_0 = 0.483$, (c) $\Omega/\omega_0 = 0.463$, (d) $\Omega/\omega_0 = 0.440$, (e) $\Omega/\omega_0 = 0.415$. After [**?**].

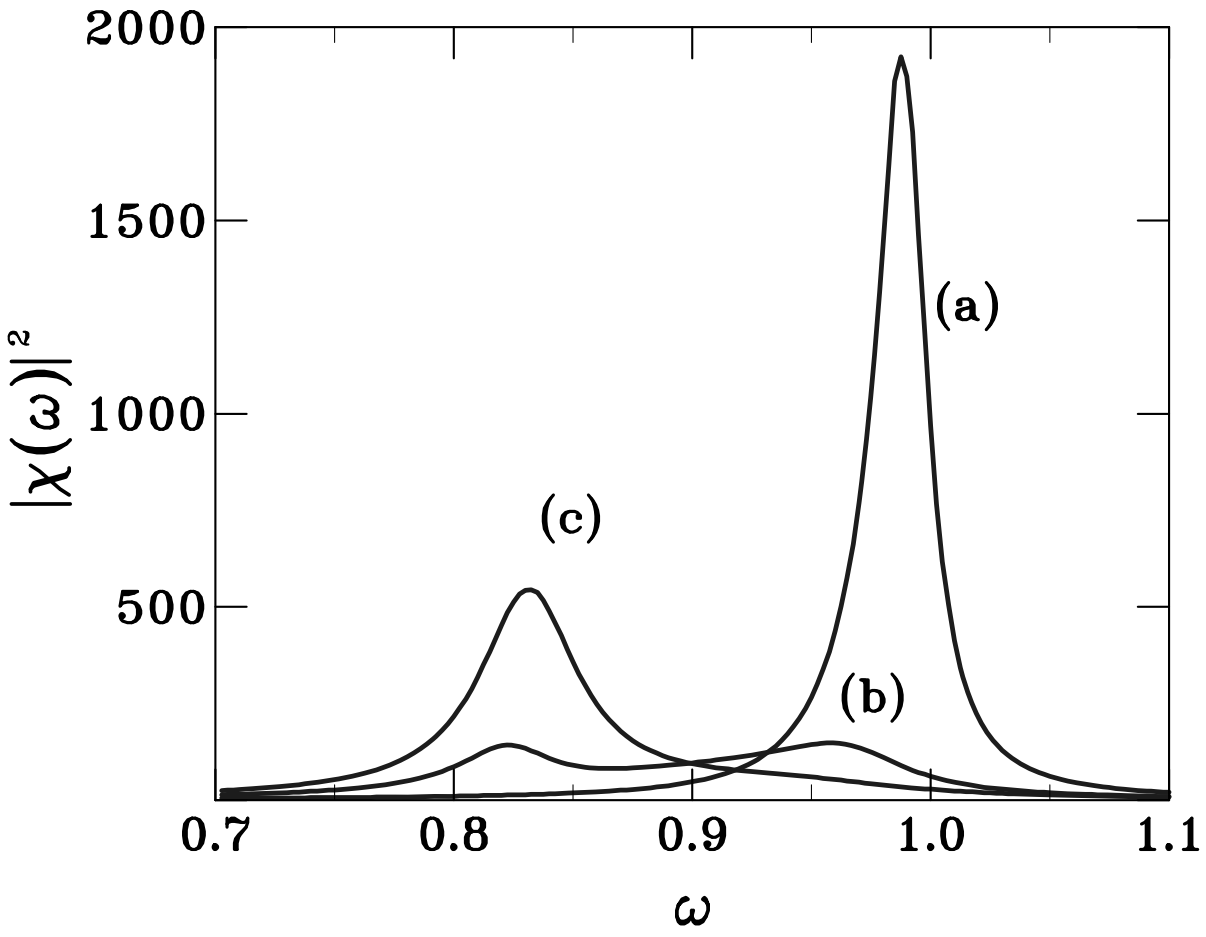

Fig. 47. Frequency dependence of $|\chi|^2$ for the same model as in Fig. 46, for different values of temperature: (a) $T = 0.0065$, (b) 0.035, (c) 0.080. After [**?**].

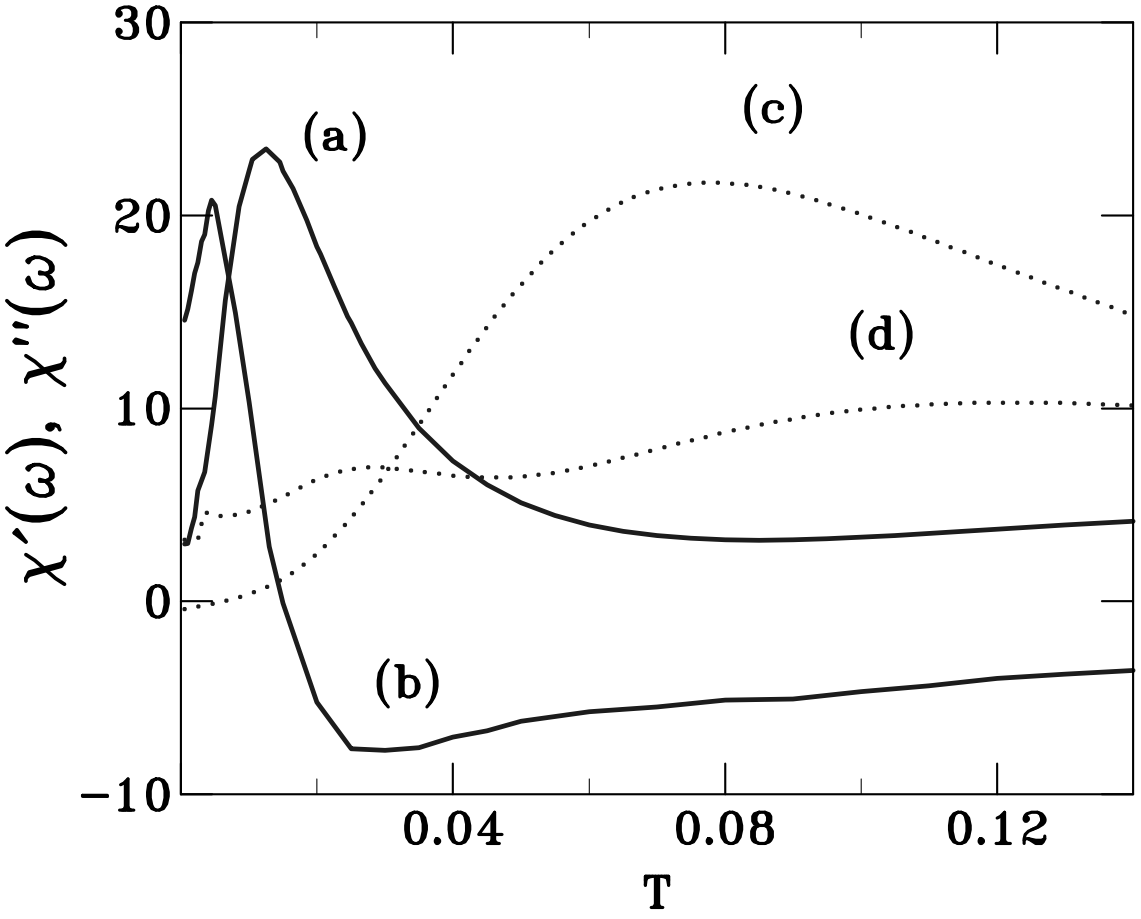

Fig. 48. Dependence on temperature T of the susceptibility at the second harmonic ($\omega = 2\Omega$) for the same model as in Fig. 46, for two different frequencies: $\Omega/\omega_0 = 0.483$ (solid curves) and $\Omega/\omega_0 = 0.415$ (dotted curves). The real parts χ' are shown by (b) and (d), and the imaginary parts χ'' by (a) and (c). After [**?**].

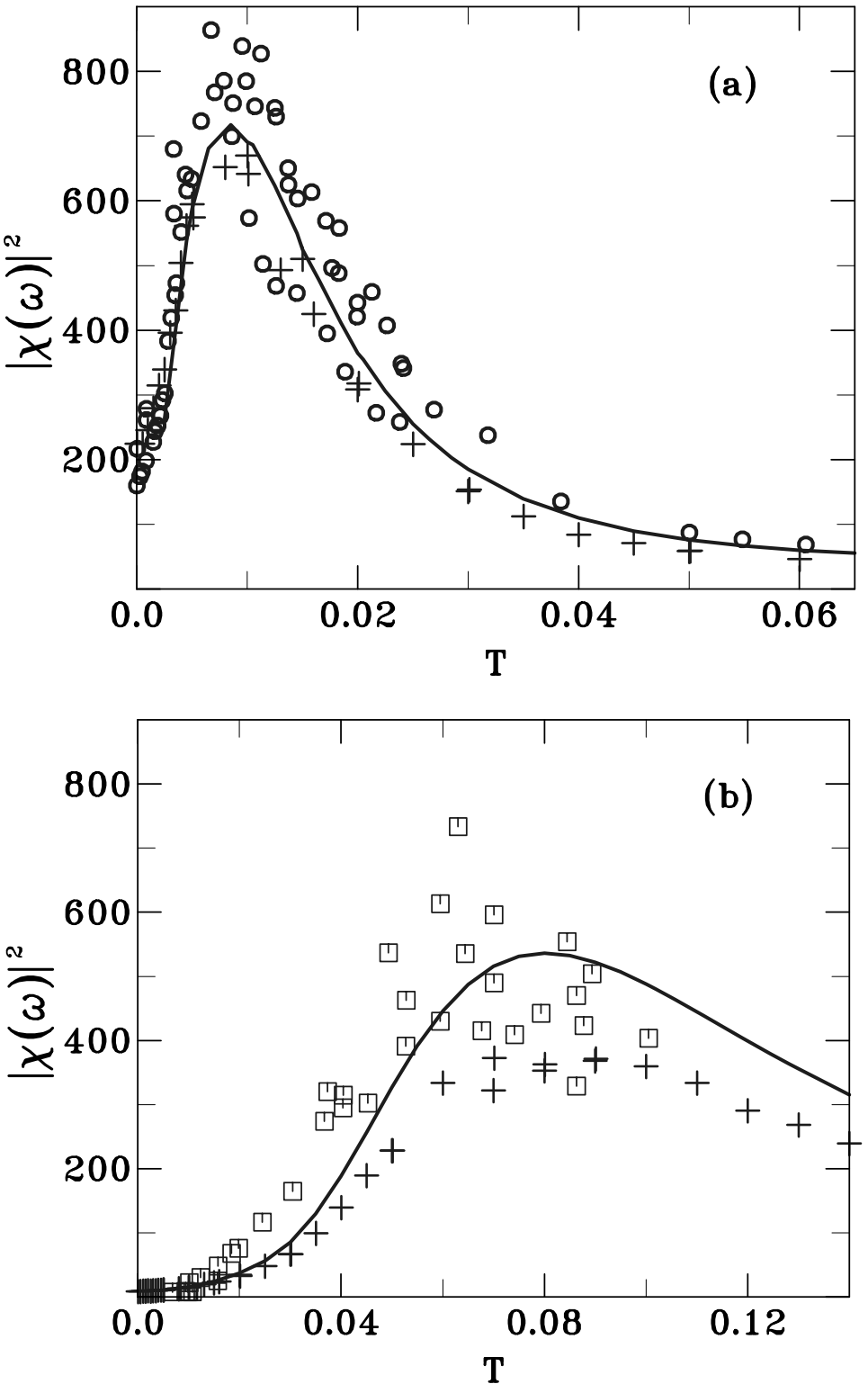

Fig. 49. Comparison of signal intensities measured for the analog electronic model (for Eq. (5.2.2)) with susceptibilities calculated from (5.1.4), as a function of temperature T in units of ω_0^4/γ. The measured values (circles and squares) have been scaled by $\beta^2 A^4/(16(\omega_0^2 - \Omega^2)^4)$ with $\beta = 5/3$ and $A = 0.0176$ to facilitate direct comparison with the relevant theoretical curves from Fig. 46. The pluses also represent calculated susceptibilities, but using in (5.1.4) fluctuation spectra derived from digital simulations of the dynamics. The frequencies used were (a) $\Omega/\omega_0 = 0.483$ and (b) $\Omega/\omega_0 = 0.415$. After [**?**].

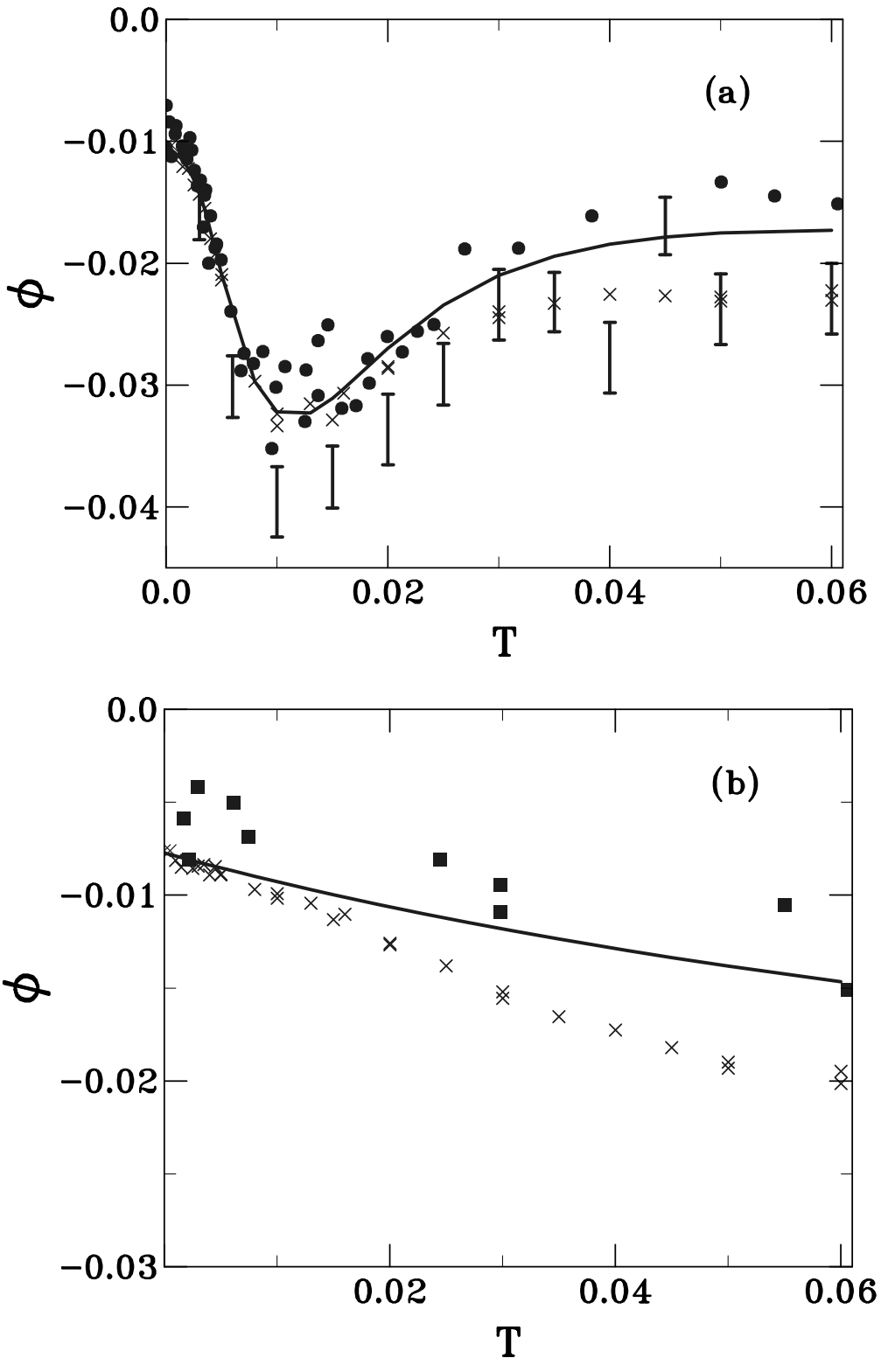

Fig. 50. (a) Dependence on temperature T (in units of ω_0^4/γ) of the angle ϕ of the response at the frequency Ω of the driving force for $\Omega/\omega_0 = 0.483$ and the reduced field amplitude $A = 0.0176$ measured for the analogue model of (5.2.2) (solid circles). The results are compared to the theory (solid line) for ϕ (see text), to the values of ϕ obtained from computer simulations of the spectrum of fluctuations (crosses), and to direct computer simulations of ϕ for these parameters (bars). (b) As in (a) but with squares in place of circles, without direct computer simulations, and with $A = 0.0044$ i.e. four times smaller than in (a), so that $\chi \approx \chi^{(1)}$. After [**?**].

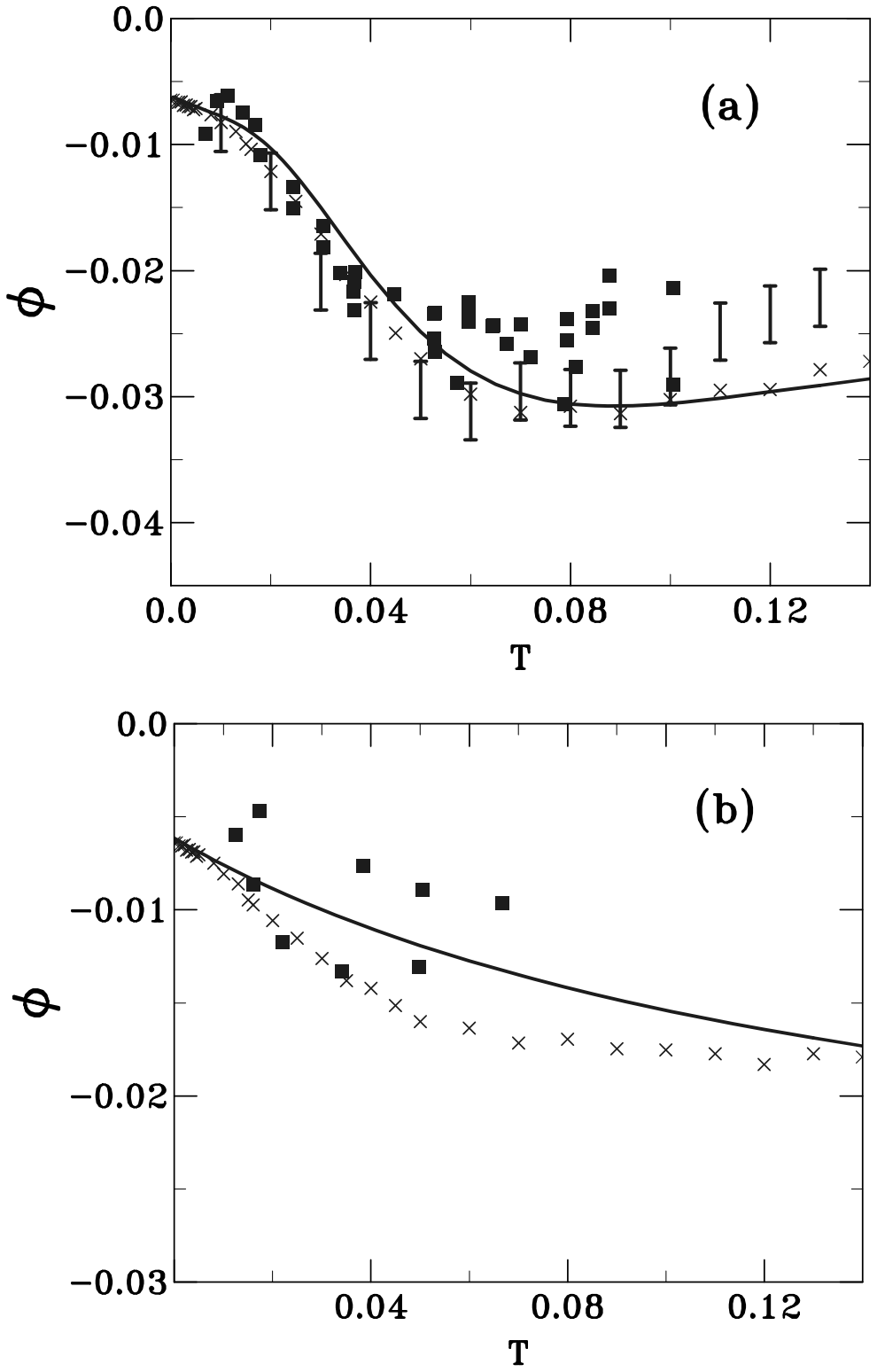

Fig. 51. As in Fig. 50(a),(b) but for $\Omega/\omega_0 = 0.415$ and with squares in place of the circles in Fig. 50(a). After [**?**].

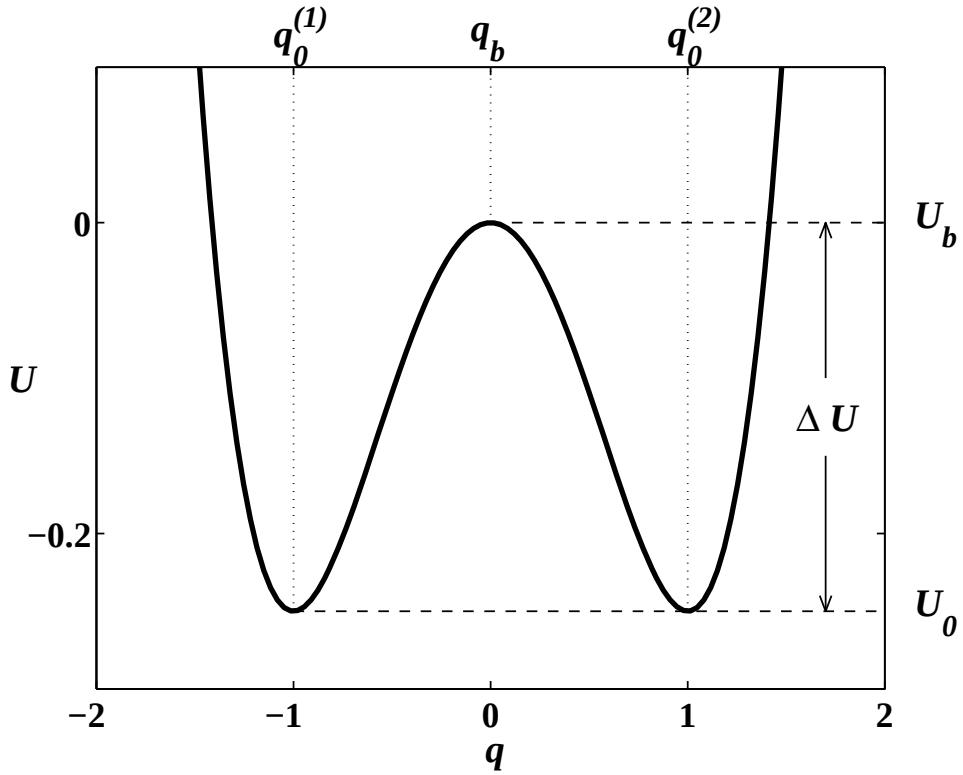

Fig. 52. The Duffing potential $U(q) = -q^2/2 + q^4/4$.

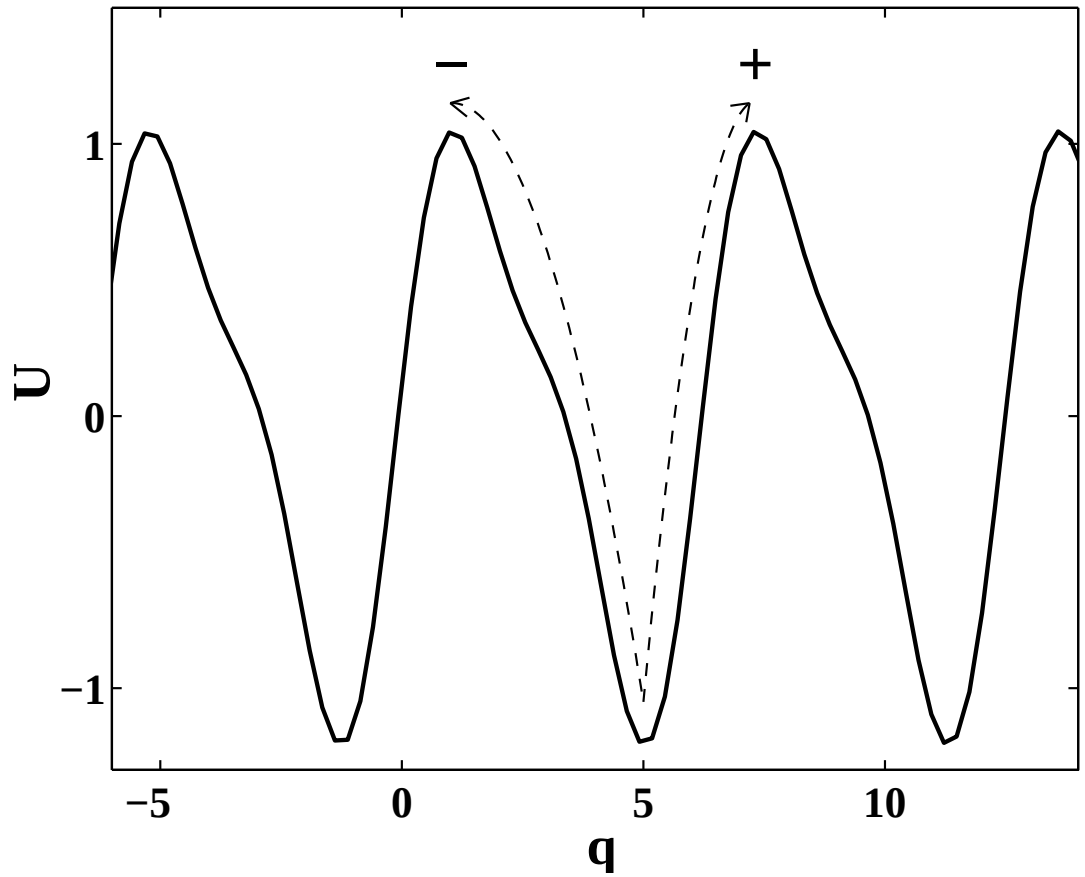

Fig. 53. The asymmetric periodic potential $U(q) = \sin(q) + 0.3\sin(2q + 0.4)$. Noise-induced escapes from the bottom of one of the wells are shown schematically by dashed lines with arrows labelled + and − for escapes over the right or left barrier respectively.

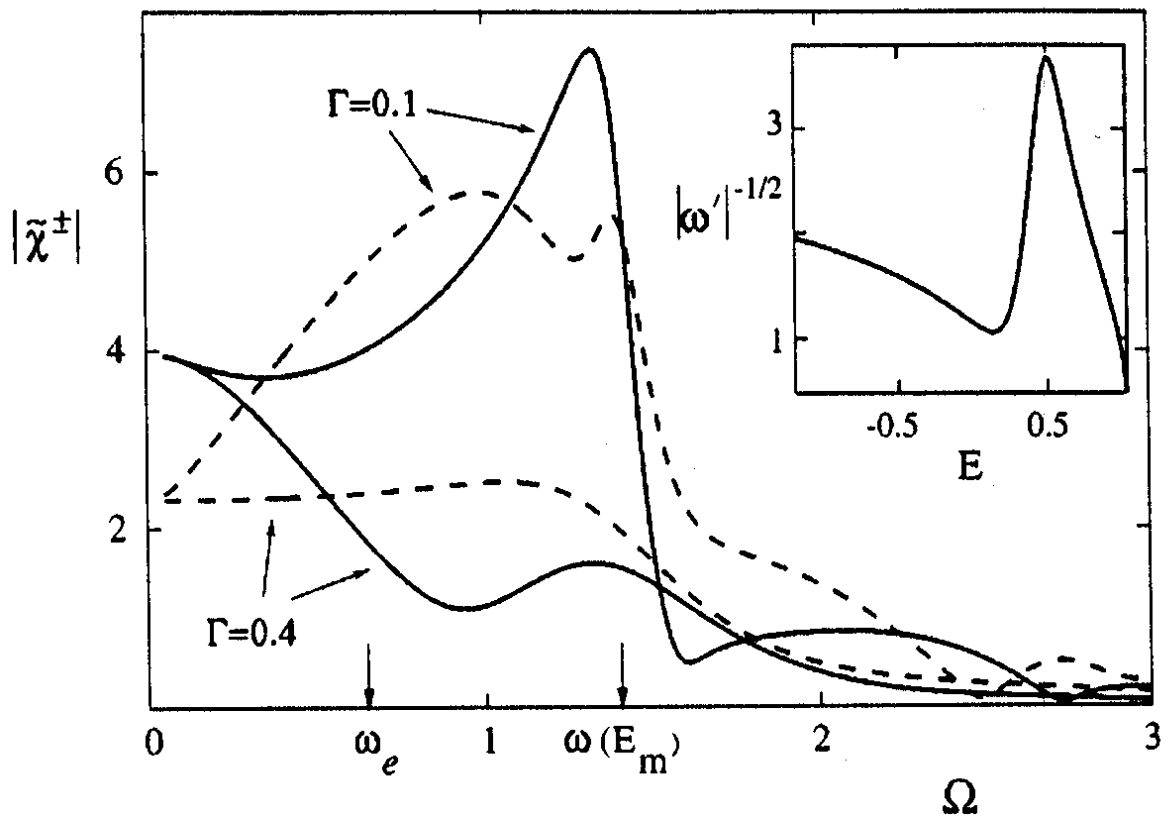

Fig. 54. Moduli of the spectral densities $|\tilde{\chi}^{+}(\Omega)|$ (solid curves) and $|\tilde{\chi}^{-}(\Omega)|$, related to the escape respectively to the right or to the left from any of the minima of $U(q)$ shown in Fig. 53. The two pairs of curves related to different values of Γ are indicated. The inset shows $(|d\omega/dE|)^{-1/2}$ as a function of energy E. After [?].

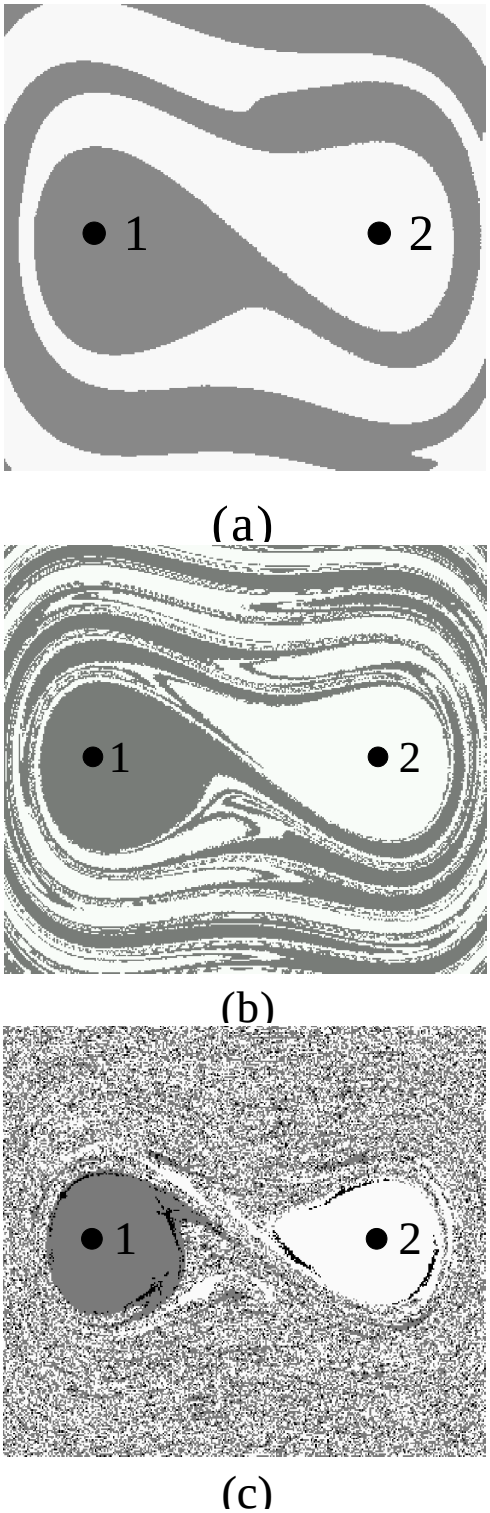

Fig. 55. Stroboscopic ($\Omega t = 0, 2\pi, 4\pi, ...$) Poincaré section $\dot{q} - q$ of the noise-free ($T = 0$) system (5.3.1) for $A = 0.07$, $\Omega = 1.7$ as Γ decreases: (a) $\Gamma = 0.07$, (b) $\Gamma = 0.025$, (c) $\Gamma = 0.005$. Attractors corresponding to $q_{st}^{(1,2)}$ are marked by dots and labels $1, 2$. Their basins of attraction are shown by different shades of grey (small black areas in (c) are basins of attraction of period-3 orbits). The mixing of basins is: (a) absent, (b) already significant, (c) well developed. After [**?**].

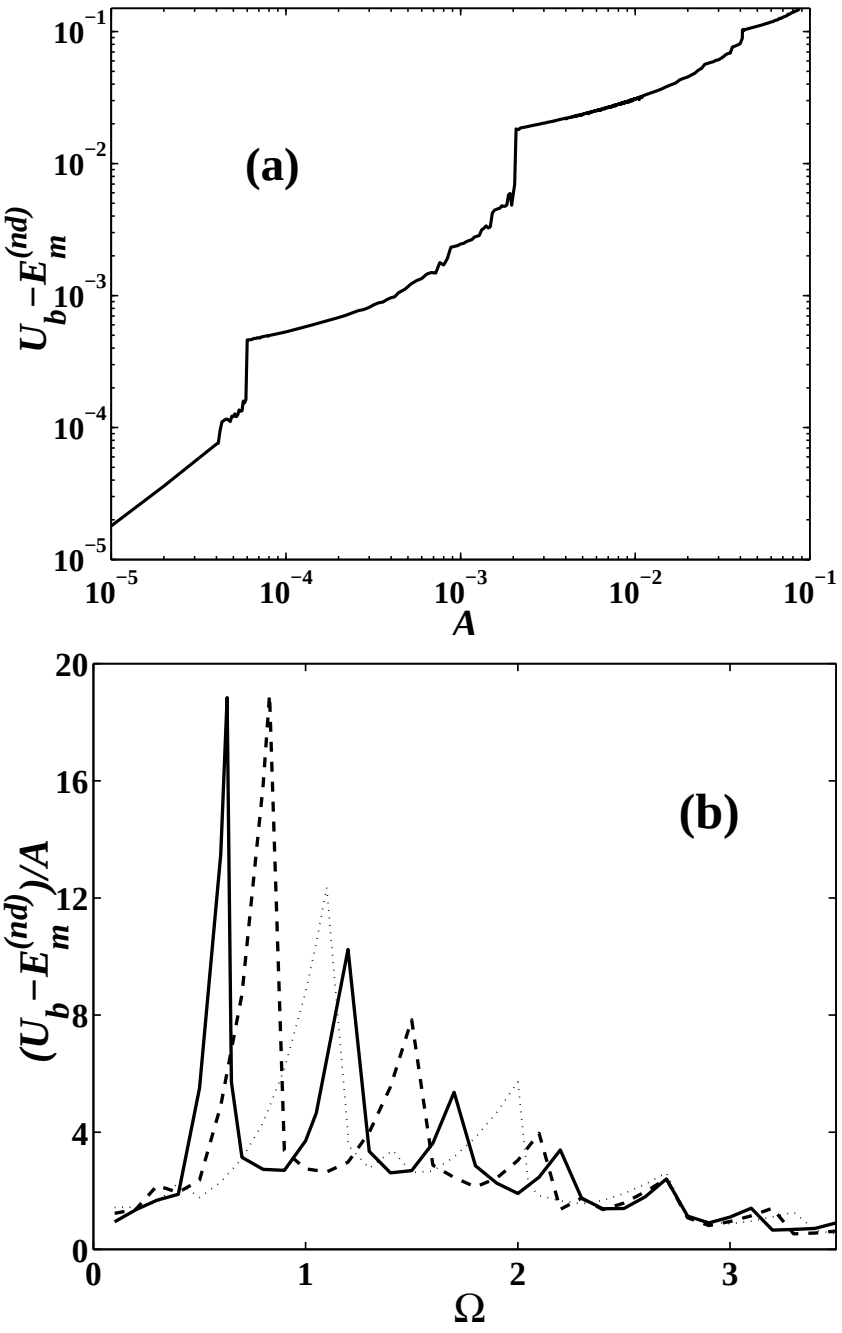

Fig. 56. (a) $U_b - E_m^{(nd)}$ as a function of A (note logarithmic scales) for $\Omega = 1.7$, (b) $(U_b - E_m^{(nd)})/A$ as a function of Ω for $A = 0.0001$, 0.001, and 0.01 (solid, dashed, and dotted lines respectively). $E_m^{(nd)}$ is the minimal energy in the chaotic layer in the Poincaré section of the *non-dissipative* system (cf. Fig. 57). After [**?**].

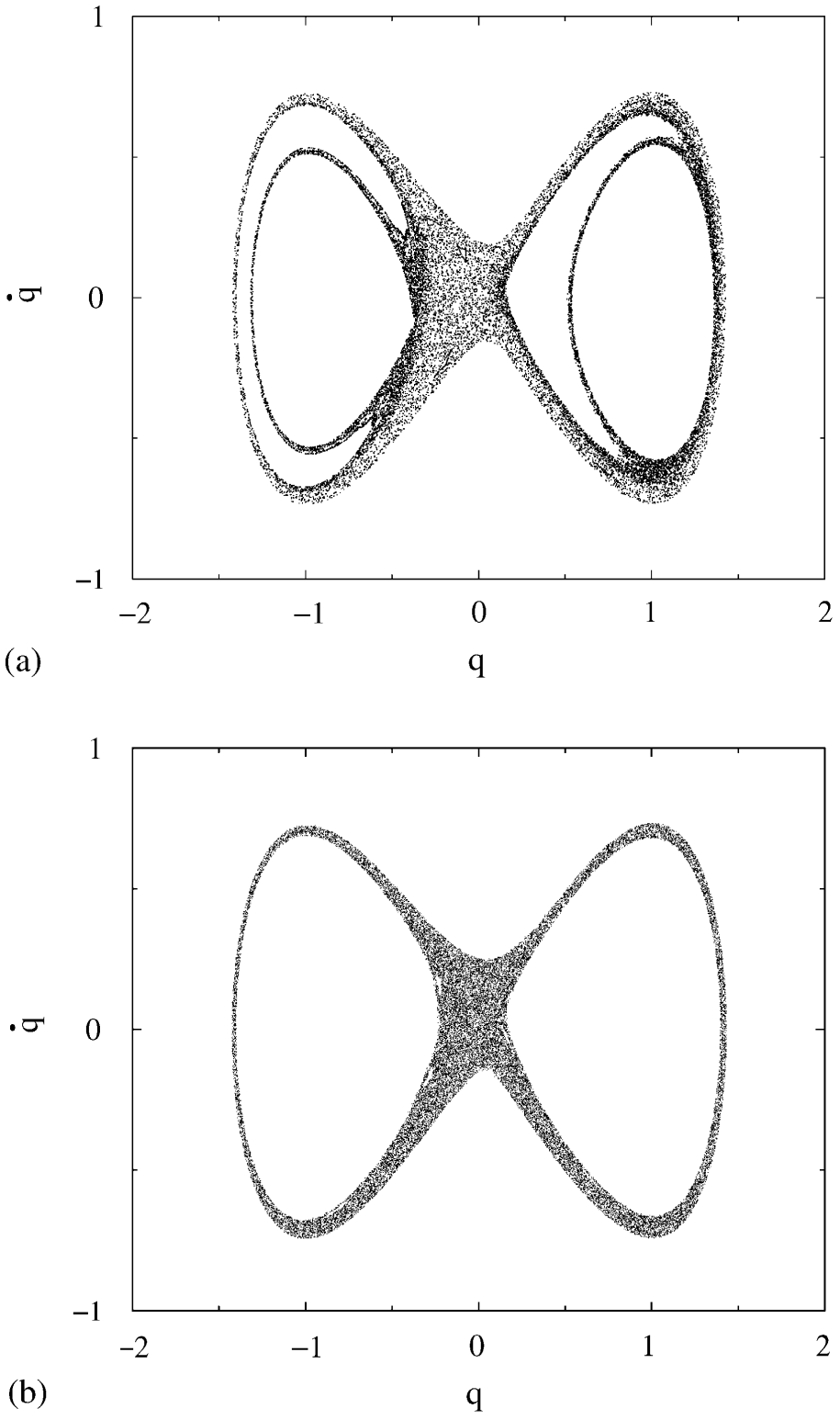

Fig. 57. The chaotic layer (black) which provides the *inter-well* chaotic transport in the non-dissipative noise-free system (Eq. (5.3.1) with $\Gamma = 0$ and $\xi(t) \equiv 0$), for $A = 0.01$ and (a) $\Omega = 1.1$, (b) $\Omega = 1.2$. After [**?**].

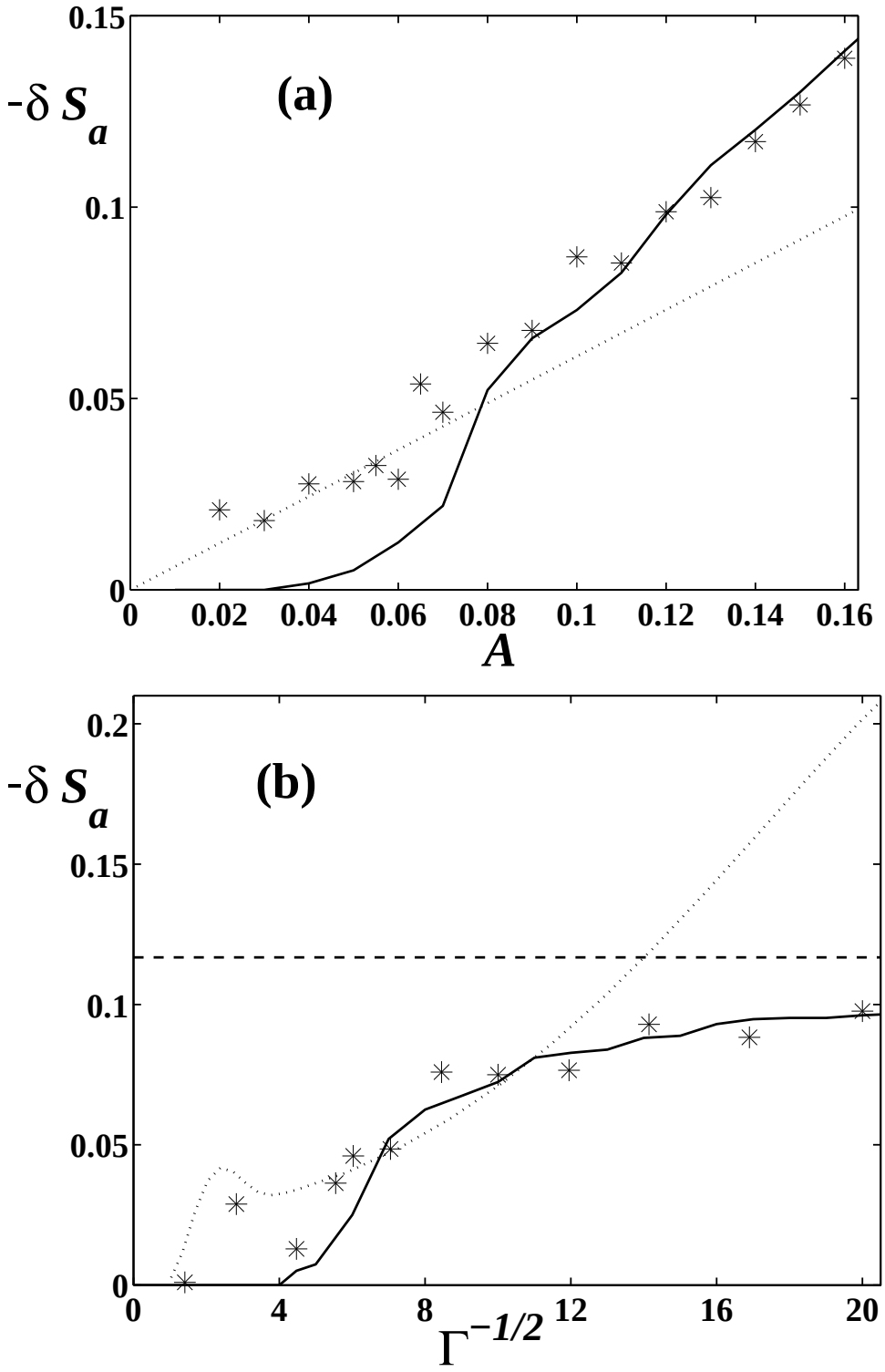

Fig. 58. $-\delta S_a$ (a) as a function of A for $\Gamma = 0.025$, and (b) as a function of $\Gamma^{-1/2}$ for $A = 0.07$; $\Omega = 1.7$ in both cases. Stars correspond to data extracted from computer simulations of (5.3.1) (for details of this procedure see footnote 50); dotted lines are theory for $-\delta S_a^{(r)}$, based on the resonant mechanism [**?**] (see (5.3.4)); solid lines are theory, based on the layer mechanism (5.3.13), for $U_b - E_{min}$. The dashed line in (b) shows $U_b - E_m^{(nd)}$, which is our theoretical non-dissipative asymptote for the solid line. After [**?**].

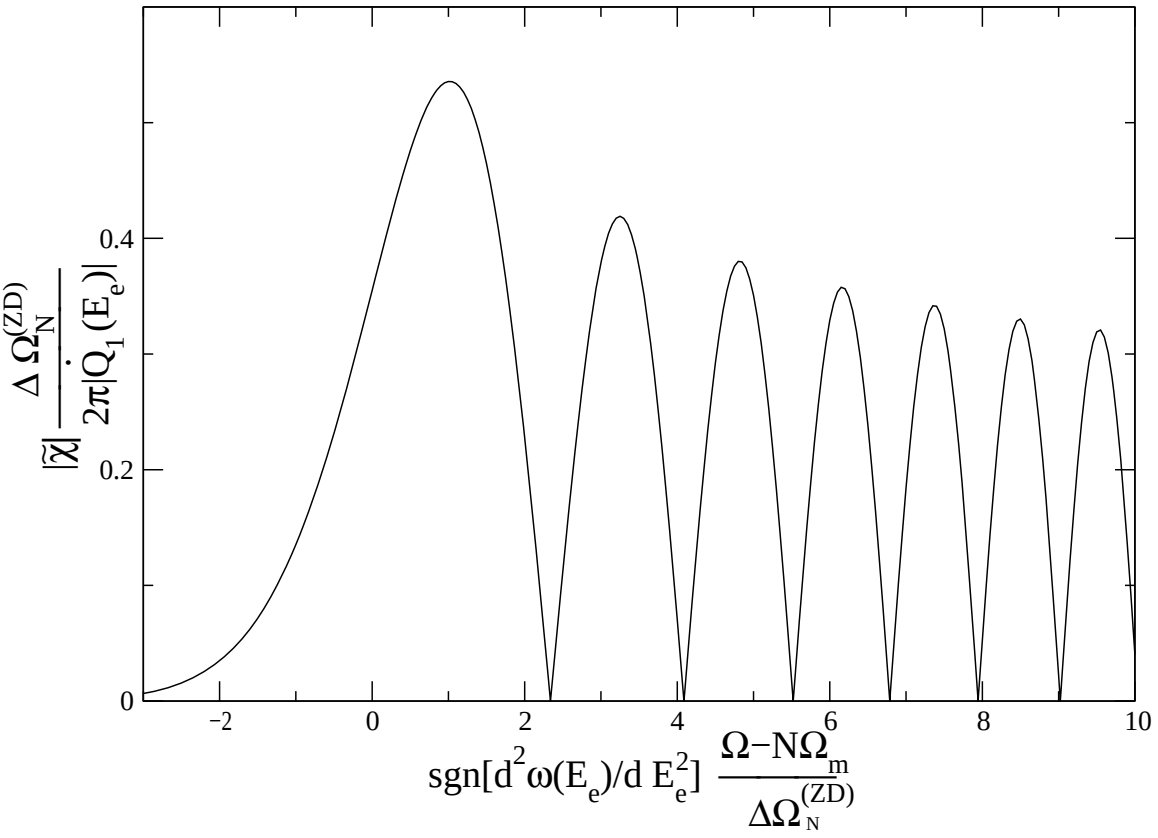

Fig. 59. The universal asymptotic shape of the zero-dispersion peak in the absolute value of the spectral density of logarithmic susceptibility, $|\tilde{\chi}(\Omega)|$, presented in dimensionless units. After [**?**].

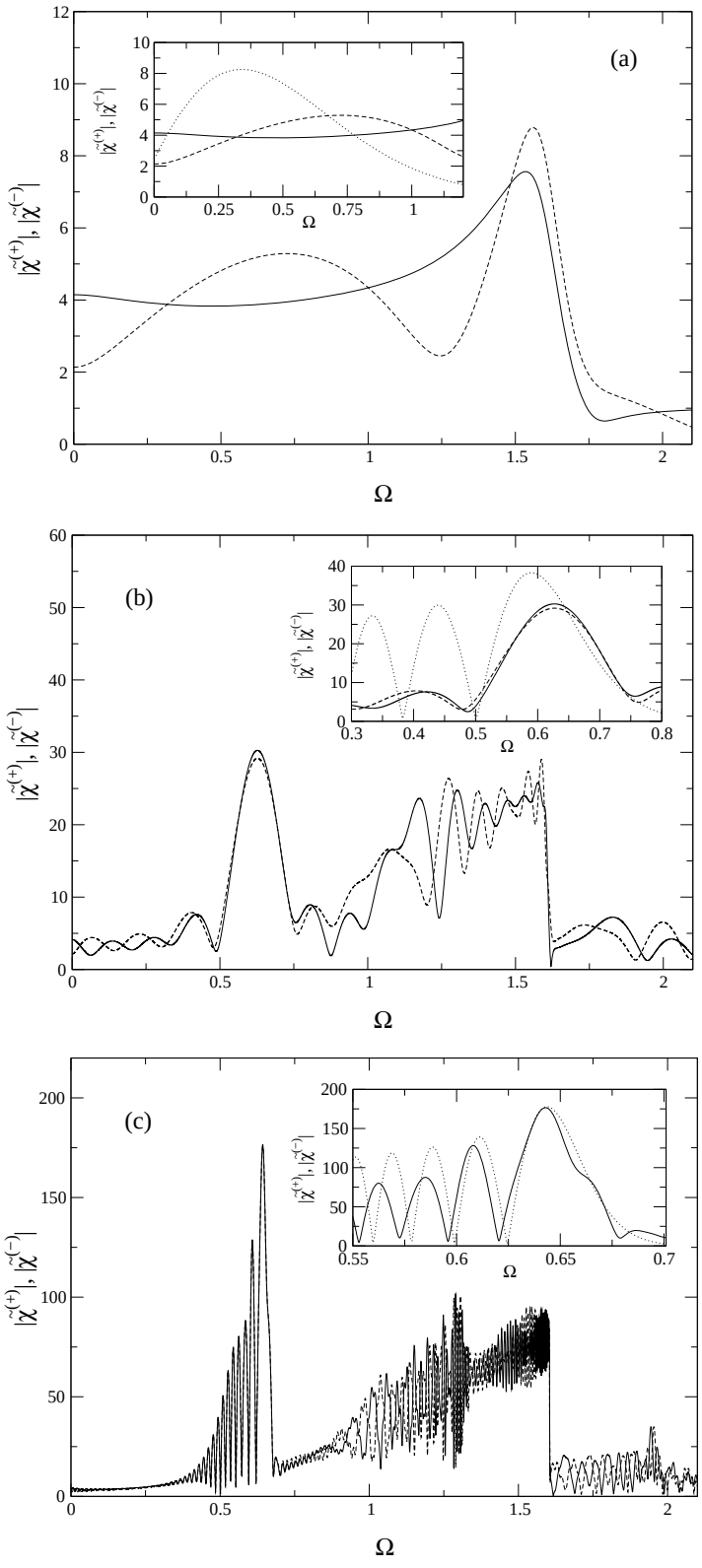

Fig. 60. Absolute values of the spectral densities $\tilde{\chi}^{(+)}(\Omega)$ (solid lines) and $\tilde{\chi}^{(-)}(\Omega)$ (dashed lines), for escape to the right and to the left respectively, calculated numerically from Eqs. (5.3.3) and (5.3.4) for the potential shown in Fig. 61(a) while Γ is: (a) $\Gamma = 0.1$, (b) $\Gamma = 0.01$, (c) $\Gamma = 0.001$. The insets compare the results of numerical calculations based on the exact equations (5.3.3)–(5.3.4) with the explicit asymptote formula (5.3.28), for the 1st ZD harmonic; the relevant parameters in (5.3.28) are: $E_e = 0.70496$ ($E_m = -1.3413$), $\Omega_m = 0.65836$, $d^2\omega(E_e)/dE_e^2 = -0.8460$, $I(E_e) = 2.039$, $\dot{Q}_1(E_e) = 0.7670$. After [**?**].

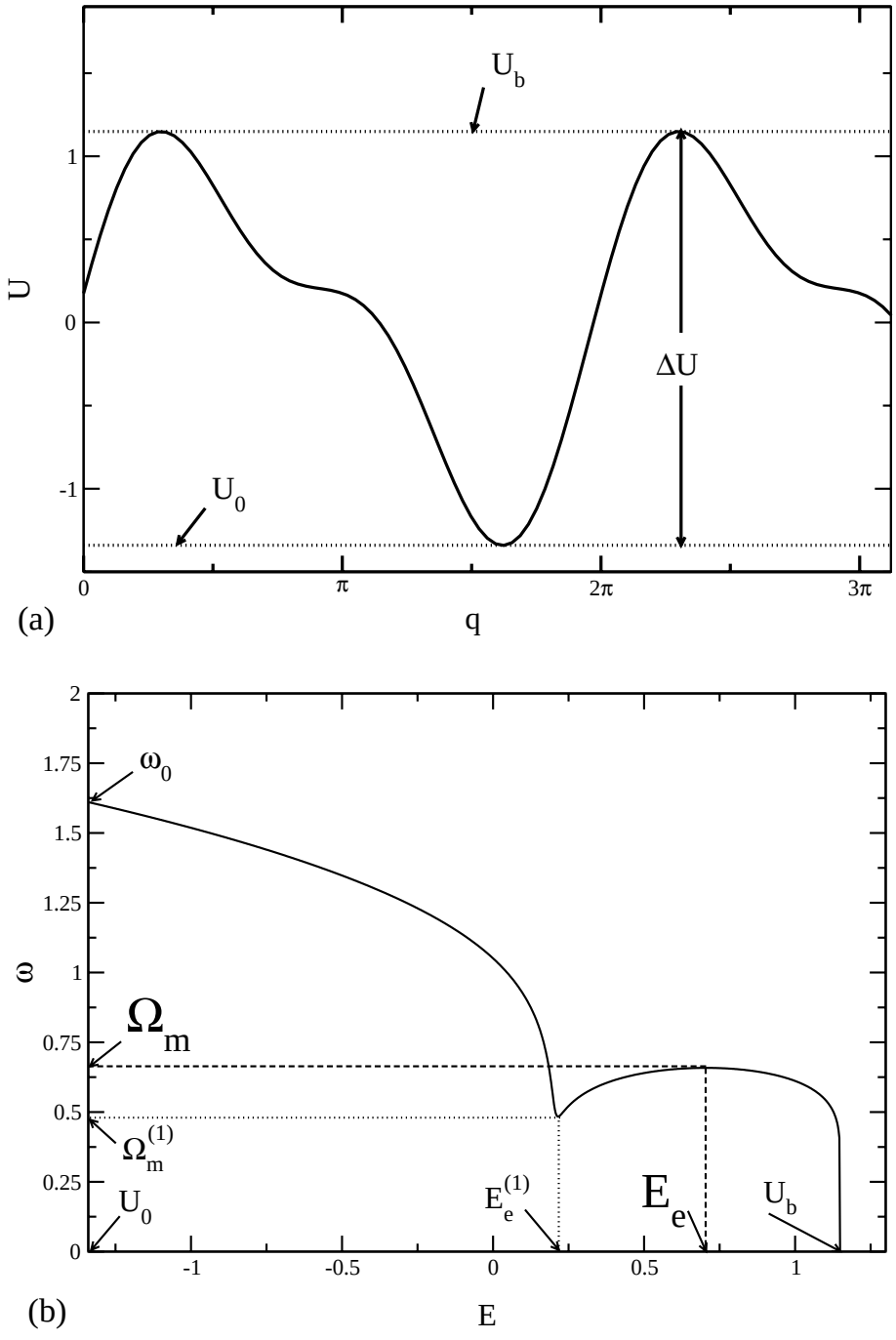

Fig. 61. (a) The potential $U(q) = \sin(q) + 0.45\sin(2q + 0.4)$. Note that the potential shown in Fig. 53 differs only in the magnitude of the second harmonic, but the latter is enough for the latter system to lack the zero-dispersion property. (b) The corresponding dependence of eigenfrequency on energy in between the minimum and maximum values of the potential: the maximum and the minimum of $\omega(E)$ are indicated by the dashed and dotted lines respectively. After [**?**].

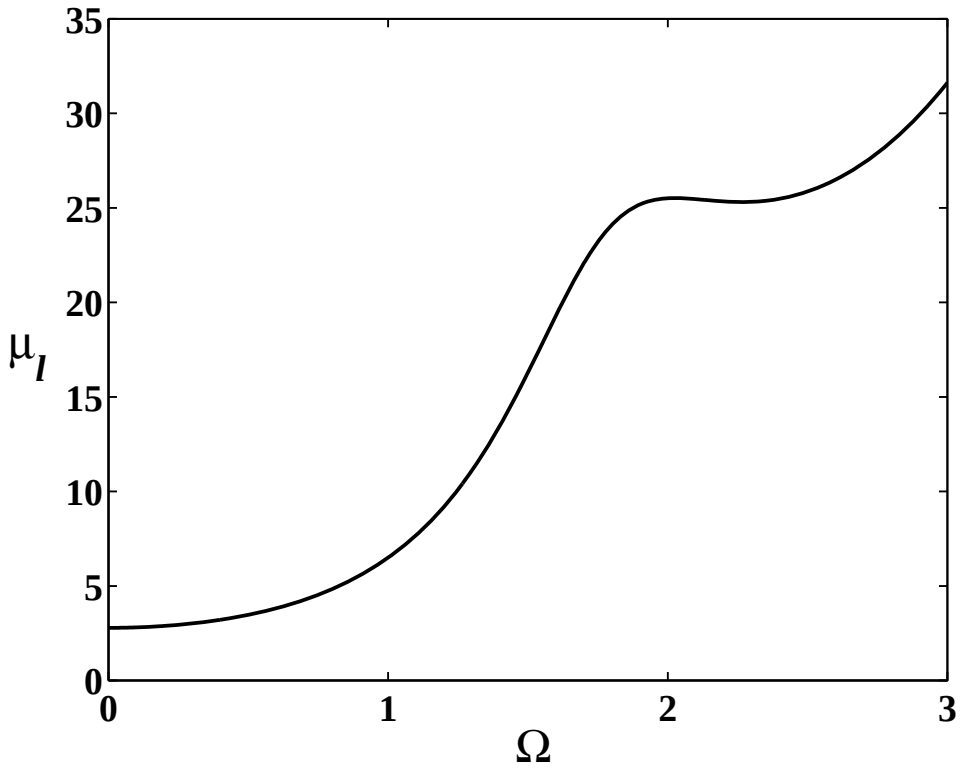

Fig. 62. The critical value A/Γ at which the homoclinic tangle arises, as given by the asymptotic formula (5.3.30), for the potential shown in Fig. 61(a), as a function of driving frequency. After [**?**].

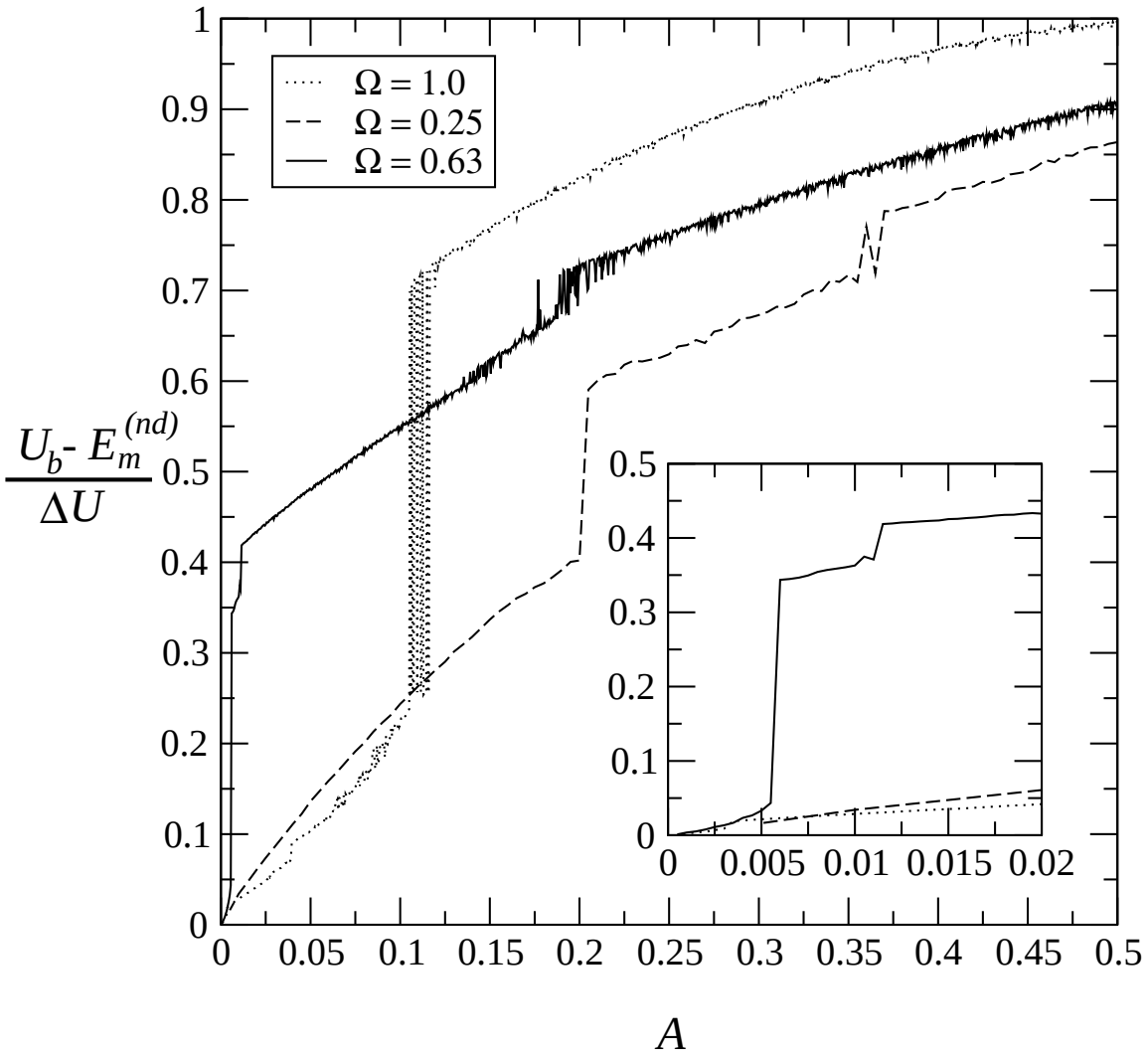

Fig. 63. The normalized lowering of the minimal energy in the relevant chaotic layer, i.e. in the layer which provides unbounded transport in the noise-free ($T = 0$) non-dissipative ($\Gamma = 0$) system similar to (5.3.1) but with the potential $U(q)$ as in Fig. 61(a) (the corresponding $\omega(E)$ possesses extrema: see Fig. 61(b)), as a function of the amplitude of the driving force, for three values of the driving frequency. The inset presents on an enlarged scale the range of small A, where the large jump-wise increase of the lowering occurs for the case $\Omega = 0.63 \approx \Omega_m$. After [**?**].

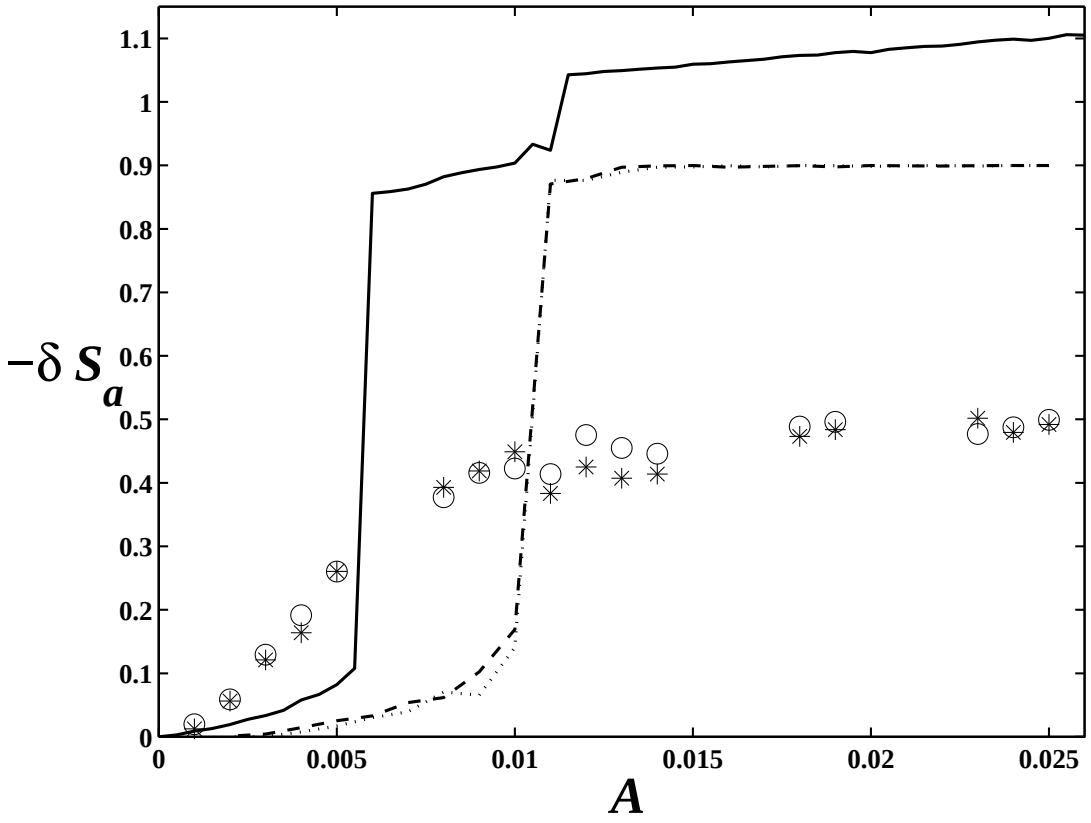

Fig. 64. The decrease of activation energies from simulations in the periodic potential system shown in Fig. 61(a) driven by the periodic force $A\cos(\Omega t)$ with $\Omega = 0.63$ and friction $-\Gamma\dot{q}$ with $\Gamma = 5 \times 10^{-4}$: stars and circles correspond to escape over the barrier respectively to the left or right of the initial well. The theoretically calculated quantities $U_b - E_m$ for the layers related to all attractors situated to the left/right from the barrier to the left/right from an initial well are shown by the dotted/dashed line. The non-dissipative approximation, $U_b - E_m^{(nd)}$, is shown by the solid line. After [**?**].

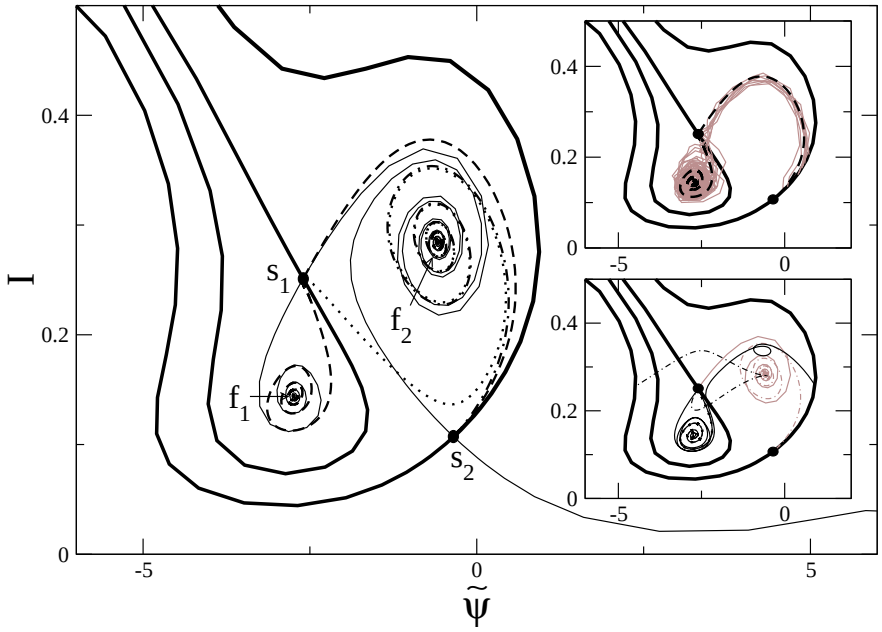

Fig. 65. Most probable escape paths (MPEPs), calculated as projections onto the plane of mechanical action I and slow angle $\tilde{\psi}$ of the proper solutions of Eqs. (5.4.13)–(5.4.15), with $\overline{H}$ given by (5.4.2); $\omega(I)$ and $q_1(I)$ are respectively the eigenfrequency and modulus of the first Fourier harmonic of the coordinate (see (A.5)) as functions of I for the tilted Duffing oscillator as in Fig. 21, and h and ω_f are respectively amplitude and frequency of the driving force as in Fig. 21(b); $\Gamma = 0.011$ as in Fig. 21. The foci and saddles are indicated by dots and labels f_1, f_2 and s_1, s_2 respectively. The boundaries of the basins of attraction are shown by the thick solid lines while the noise-free paths emanating from the saddles are shown in the main figure by the thin solid lines. For escape from a single basin of attraction, and for a transition to the basin of attraction of a neighbouring attractor, the initial and final conditions were specified as the corresponding focus and saddle respectively: see (5.4.9) and (5.4.16). The paths $[f_1 \to s_1]$, and $[f_2 \to s_1]$ $[f_2 \to s_2]$ are shown in the main figure by the bold-dashed, dotted, and dash-dotted lines respectively; the action S along them (i.e. the activation energy (5.4.7)) is respectively $S^{(12)}_{\min} = 0.00293$, $S^{(21)}_{\min} = 0.0118$ and $S^{(23)}_{\min} = 0.01$. The MPEP from the inner nonlinear resonance beyond the nonlinear resonance area as a whole (i.e. from f_1 beyond the outer thick solid line) is shown by the bold-dashed line and consists of two distinct sections, the first of which coincides with $[f_1 \to s_1]$, while the second $[s_1 \to s_2]$ connects the saddles by the projection of a smooth solution of Eqs. (5.4.13)–(5.4.15) such as to avoid intersections with itself and with the noise-free path $[s_1 \to f_2]$ and with the MPEP $[f_2 \to s_2]$; the activation energy is $S^{(13)}_{\min} = 0.007$. The upper inset shows a few direct, i.e. avoiding a relaxation into the close vicinity of f_2, first-passage paths (jagged lines) from f_1 to the boundary of the nonlinear resonance area as a whole, derived sequentially (i.e. not selected from a larger group of direct first-passage paths) by digital simulation of Eq. (5.4.2) with noise $f(t)$ defined in (5.4.1) of intensity $D = 0.00035$: the paths concentrate nicely near the theoretical MPEP $[f_1 \to s_1 \to s_2]$ (dashed line). The lower inset shows two "edge" smooth paths i.e. projections of such smooth solutions of Eqs. (5.4.13)–(5.4.15) whose projections emanate from f_1 while ending on the outer boundary as close to the saddle s_2 as possible: the black thin solid and dash-dotted lines show the right and left edge paths respectively; the noise-free path $[s_1 \to f_2]$ and the MPEP $[f_2 \to s_2]$ are shown by the grey solid and dash-dotted lines respectively. Note that actions along the right and left edge paths are 0.0376 and 0.173 respectively, which are much larger than that along the true MPEP $[f_1 \to s_1 \to s_2]$ (which possesses a cusp in s_1), so that their role in relation to real escapes is negligible (cf. the upper inset). After [**?**].

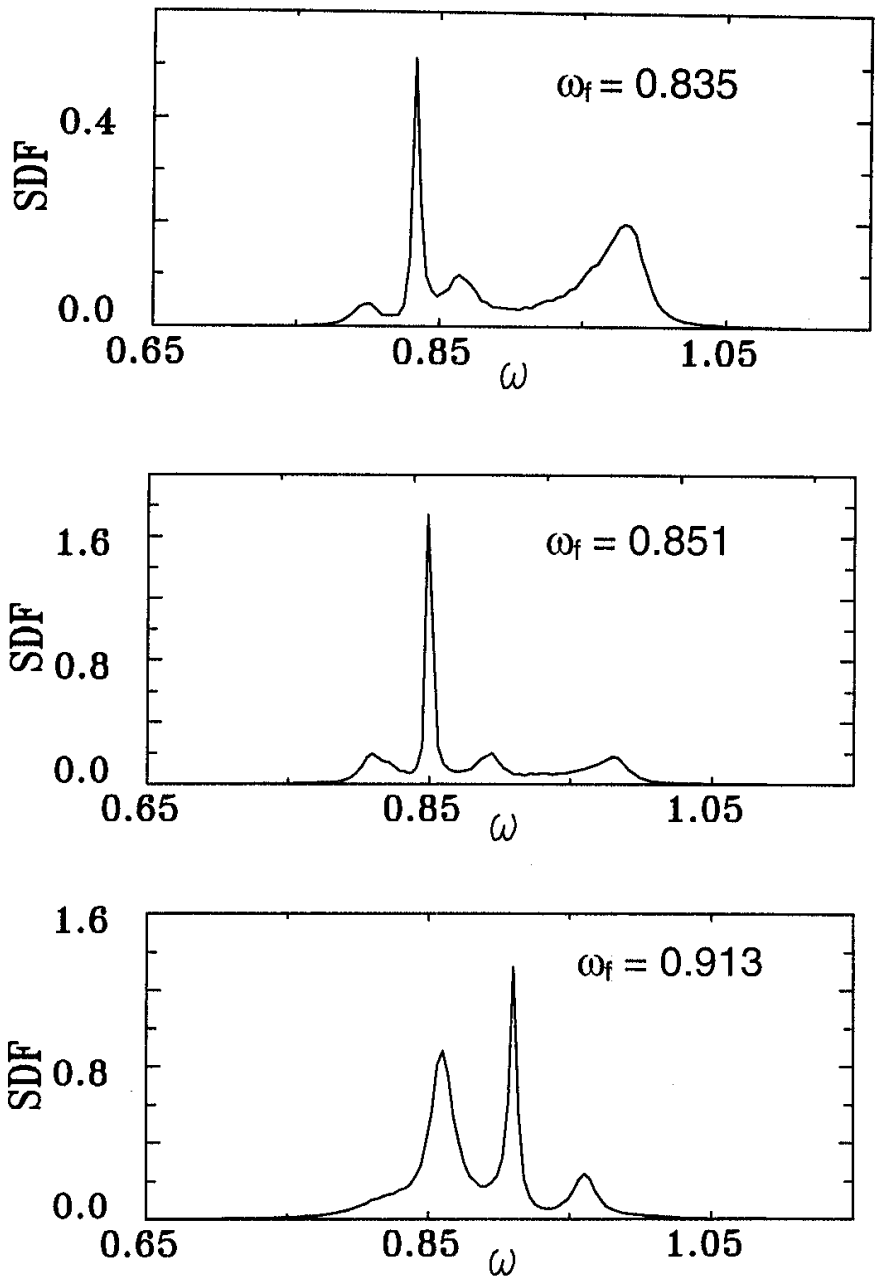

Fig. 66. An example evolution of the spectral density of fluctuations (SDF) of coordinate $Q_q(\omega)$, for the periodically driven TDO (with parameters, friction and the driving amplitude as in Fig. 21) subjected to additive white noise (cf. Eq. (5.2.2)), as the driving frequency ω_f increases, measured for an analogue electronic model for three values of ω_f. The Stokes and anti-Stokes peaks (arising from slow oscillations in nonlinear resonances) lie immediately to the right and left, respectively, of the sharp spectral peak at the driving frequency; the broad peak on the far right arises from fluctuations about linear response. The normalisation of the ordinate axis is arbitrary. After [?].

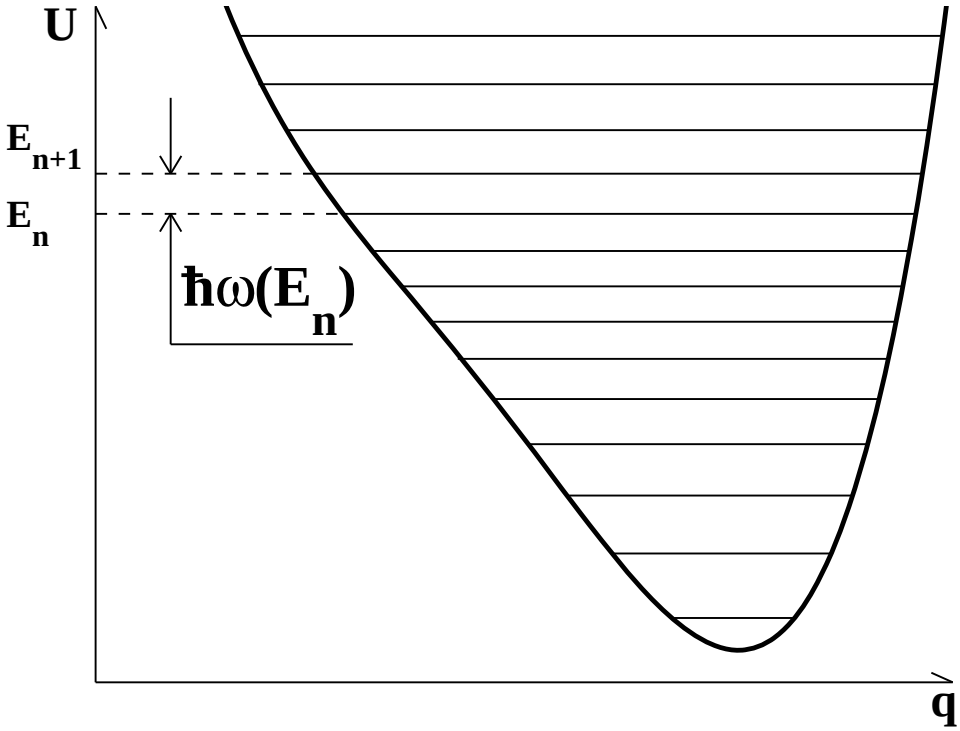

Fig. 67. A schematic plot of energy levels in a nonlinear oscillator: the distance in energy between adjacent levels, $E_{n+1} - E_n$, with high n (quasi-classical levels) is approximately equal to $\hbar\omega(E_n)$ where $\omega(E_n)$ is the frequency of a classical eigenoscillation of energy E_n. After [**?**].

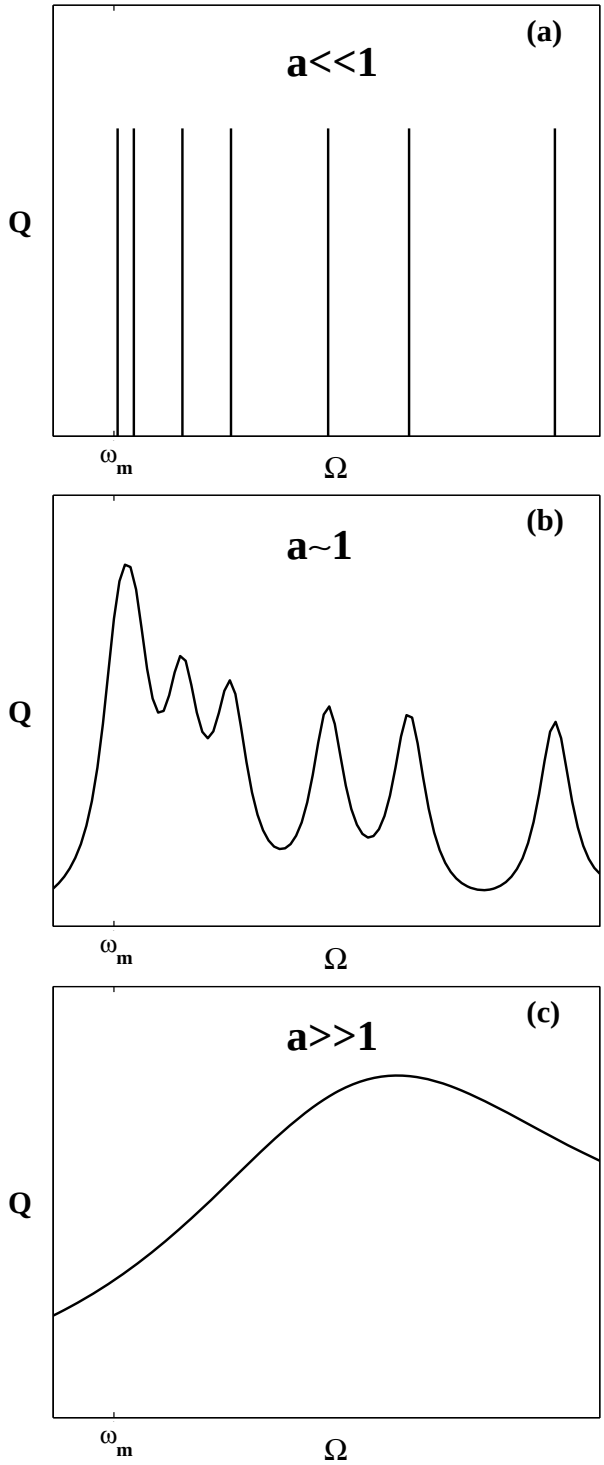

Fig. 68. Parts (a)–(c) of the figure show the schematic evolution of an absorption spectrum near the extremal eigenfrequency ω_m as the interaction with the thermostat increases: the formation of the ZDP is associated with a transformation from the quantum spectrum to the classical one in the vicinity of ω_m. The major features of the evolution depend on the only parameter, namely $a \equiv \Gamma T E_m/(|\omega''|(\hbar\omega(E_m))^4)$. After [**?**].

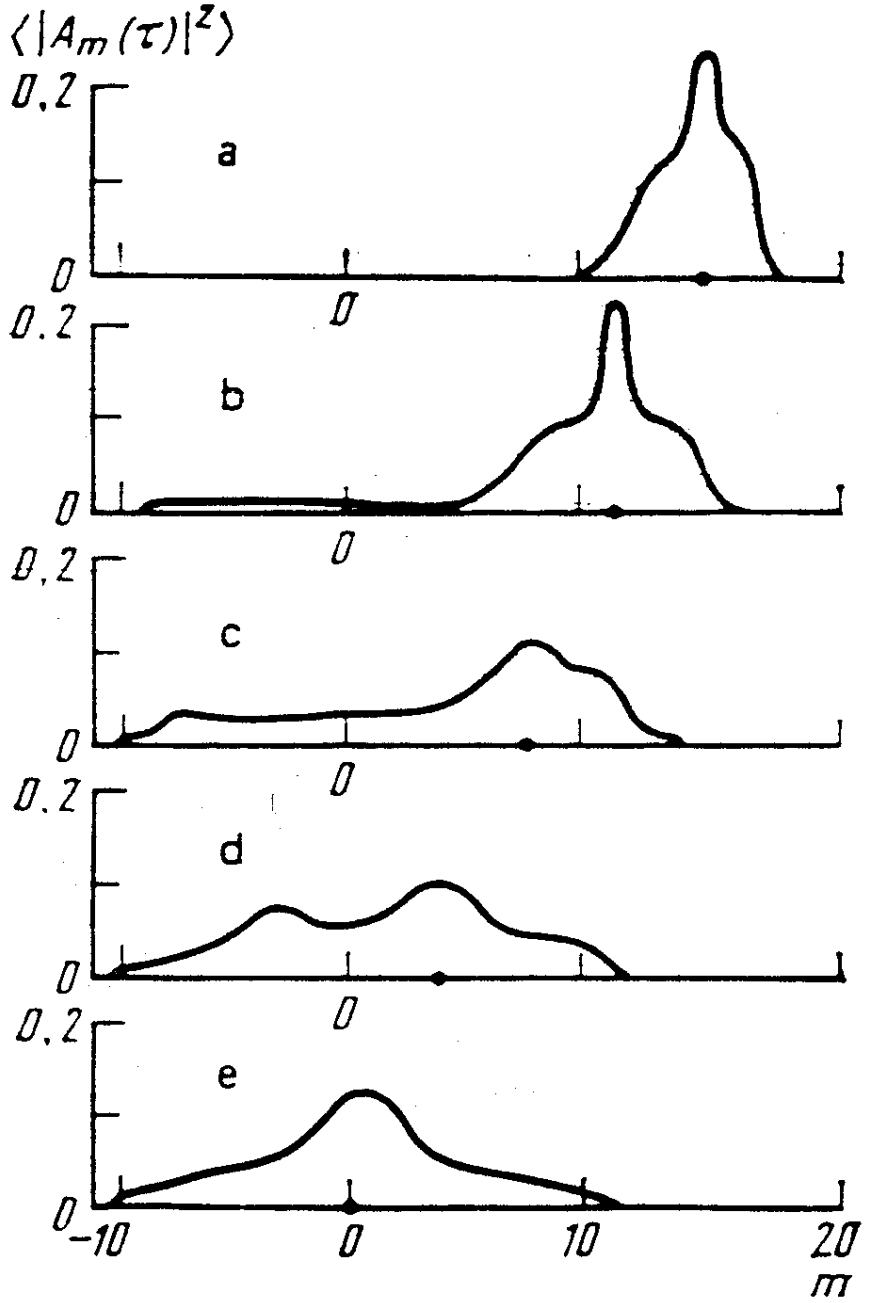

Fig. 69. The average distribution of the population as a single initially populated level (indicated by the dot on the abscissa axis) varies: (a) $m(\tau = 0) = 16$, (b) 12, (c) 8, (d) 4, (e) 0. The amplitudes A_m were simulated by Eqs. (6.2.6) with $V = 5 \times 10^{-2}$, $\mu = 10^{-3}$, $\nu = 10^{-3}$ and $A_m(\tau = 0) = \delta_{mm(0)}$. The quantity $\langle |A_m(\tau)|^2 \rangle$ is calculated on long time-scales, after the steady regime has been formed, by averaging $|A_m|^2$ over a time $T = 720$ that is equal to the period $2\tau_r$ of the phase oscillations. After [**?**].